VARIATIONAL STUDY OF STRONGLY CORRELATED ELECTRONIC MODELS

THÈSE N^{O} 3892 (2007)

PRÉSENTÉE LE 21 DÉCEMBRE 2007
À LA FACULTÉ DES SCIENCES DE BASE
CHAIRE DE PHYSIQUE NUMÉRIQUE DE LA MATIÈRE CONDENSÉE
PROGRAMME DOCTORAL EN PHYSIQUE

ÉCOLE POLYTECHNIQUE FÉDÉRALE DE LAUSANNE

POUR L'OBTENTION DU GRADE DE DOCTEUR ÈS SCIENCES

PAR

Cédric WEBER

ingénieur physicien diplômé EPF
de nationalité suisse et originaire de Hohenrain (LU)

acceptée sur proposition du jury:

Prof. R. Schaller, président du jury
Prof. F. Mila, Prof. T. Giamarchi, directeurs de thèse
Dr F. Becca, rapporteur
Prof. C. Gros, rapporteur
Prof. D. Ivanov, rapporteur

ÉCOLE POLYTECHNIQUE
FÉDÉRALE DE LAUSANNE

Suisse
2007

Abstract

The discovery of high-T_c superconductivity in the cuprates, and the observation that strong correlations are important in connection with these compounds has led to a tremendous interest in understanding the physics of strongly correlated electronic models. In particular the two simplest models for strongly correlated electrons, namely the Hubbard and $t-J$ models, have been the subject of intensive studies. In a milestone paper of 1987, P.W. Anderson proposed that a resonating valence bond (RVB) wave-function, which consists of a superposition of valence-bond states, contains the ingredients to account for a consistent theory of the Hubbard and $t-J$ models. Motivated by the success of variational Monte-Carlo to describe some of the peculiar properties of the cuprates, we propose in this dissertation, on one hand, to extend the method to further strongly correlated models to describe other compounds such as graphene, carbon nanotube or the cobaltite compounds, and on the other hand we propose to focus on the pseudo-gap phase of the cuprates, which is still prompting for a consistent theory. In particular, the issue of checkerboard spatial modulations in the density of states in the low temperature regime of the cuprates is addressed. Finally, we have studied the possibility for spontaneous orbital currents in the cuprates, that might play a key role in the theory of high T_c superconductors.

Keywords : Superconductivity, Electronic correlation, Cuprates, Lattice Theories, Variational Methods, Low Energy Physics, Monte-Carlo simulations.

Version abrégée

La découverte de la superconductivité à haute température dans les cuprates, et l'observation que les corrélations électroniques pourraient jouer un rôle crucial dans ces composés, a généré un intérêt et une activité intense dans la communauté de la physique théorique. En particulier, les deux modèles les plus élémentaires pour étudier les fortes corrélations (les modèles dits $t-J$ et Hubbard) ont été étudiés par de nombreux théoriciens. Notamment, dans un papier remarquable de 1987, P.W. Anderson a proposé qu'une fonction du type liens de valence rśonnants (RVB), qui consiste en une superpositions des pavages du réseau en termes de dimères, contient les ingrédients cruciaux pour décrire la physique de ces modèles. Motivé par le succès des méthodes variationelles Monte-Carlo pour décrire quelques unes des plus interpellantes propriétés des cuprates, nous proposons dans cette dissertation d'une part d'étendre cette méthode aux théories décrivant d'autres matériaux, comme le graphène, les nanotubes de carbone et les composés cobaltites; d'autre part nous proposons d'étudier plus en détail la phase pseudo-gap des cuprates, qui interpelle encore actuellement les scientifiques par la richesse de sa physique. En particulier, nous nous intéressons à la question des modulations spatiales à géometrie en damier observées dans la densité d'état à basse température dans les cuprates. Finalement, nous discutons la possibilité de la présence de courants orbitaux générés spontanément dans la phase pseudo-gap des cuprates, qui pourrait être étroitement lié à la présence de la superconductivité dans ces matériaux.

Mots clefs : Superconductivité, Corrélation Electronique, Cuprates, Théories sur Réseaux, Méthodes Variationelles, Physique des Basses Energies, Simulations Monte-Carlo.

Acknowledgments

The biggest thank goes to Frédéric Mila and Thierry Giamarchi, who gave me the opportunity to engage a doctoral thesis at IRRMA. Special thanks goes also to Andreas Martin Lauechli. I am grateful not only for their scientific guidance, but also for their effort to make our discussions very alive and more generally for the nice time that I spent in the respective groups of Irrma, UniGe and ITP-EPFL.

During these four years and a half, they were particularly involved in all the work done in the chapters presented in this dissertation. Moreover, I had also the chance to collaborate and discuss with other distinguished physicists. I am especially thinking to Michel Ferrero and Federico Becca, with whom I spent some nice time at the Sissa (Trieste, Italy). I also enjoyed working in collaboration with Didier Poilblanc and Sylvain Caponi (Irsamc, Toulouse, France), that have hosted me very nicely in Toulouse for a short visit. I also thank a lot Claudius Gross and Walter Hofstetter (Frankfurt, Germany) that have allowed me to come and visit them in Frankfurt. The scientific discussions were very motivating. Special thanks also to Werner Krauth (Paris) who explained to me the scientific activity of his group. Finally, I would like to thank Chandra Varma (Irvine, USA) for past and ongoing discussions related to the presence of orbital currents in the pseudogap phase of the cuprates. I detail here further who was involved in the work of the chapters of the dissertation:

Chapter 3: I am very grateful to Michel Ferrero and Federico Becca for discussions about the Pfaffians, that are used to sample the wave-function having non-collinear magnetism.

Chapter 4: The credits of the RVB mean field theory in this chapter is entirely due to Thomas Gloor. Moreover, the quantum Monte-Carlo results, shown in this chapter as a comparison with the variational Monte-Carlo results, were done by the work of Thomas Gloor and Andreas Martin Laeuchli.

Chapter 5: This was a collaboration with Didier Poilblanc and Sylvain Caponi. Everything related to the mean-field calculations done in this chapter is due to their impressive work.

Chapter 6: I could profit from the experience of Andreas Laeuchli, who helped me to understand in details the exact diagonalization calculations. We could also check that our different codes were giving identical results. These discussions were certainly motivating. I would like to especially thank Chandra Varma, who visited us in Lausanne, and gave us many very clever comments on our numerical results.

Certainly I enjoyed the discussions with the present and former PhD students and postdocs in the different group, I am thinking in particular to Thomas Gloor, François Vernay, Julien Dorier, Jean-Baptiste Fouet, Arnaud Ralko, Stéphane Dommange, David Eichenberger, Maged Elhajal, Yannis Burnier, and many other people that will certainly excuse me.

I thank finally at most my wife, Allison Weber, for sharing my life during this thesis.

I am especially grateful to my parents for their love and their support.

In the memory of Stéphane Dommange and Alexandre Yakini ...

Contents

Chapter 1

Introduction

1.1 History of high temperature superconductivity

In 1986 superconductivity was found in a range of temperature which was well above all previous signature: Bednorz and Müller found a transition temperature of about 30K [1] in the layered copper-oxide material $La_{2-x}Ba_xCuO_4$, for which they won the Nobel Prize in Physics. The psychological barrier of the liquid Nitrogen condensation temperature was crossed shortly after with $YBaCu_3O_7$ and the hope was growing that one might find an increasing number of every-day life applications.

Since then, copper-oxide superconductors, which are structural derivatives of the class of perovskites, have been at the center of a tremendous scientific activity. A number of high-temperature superconducting compounds has been reported. Starting out at $T_c = 30K$ for $La_{2-x}Ba_xCuO_4$ in 1986 the transition temperatures have climbed to $T_c = 156K$ in members of the $HgBa_2CuO_{4+x}$ family which are among the recently discovered compounds. Moreover, new materials found more recently like the mercury-type copper-oxides still increased accessible transition temperatures without any obvious upper bound, and a critical temperature as high as $164K$ was reported [2], though it was obtained for a compound under pressure. In the meantime, progress in the preparation of high-quality single crystals has allowed to remove many of the uncertainties in the interpretation of experimental data obtained from polycrystals. In Fig. 1.1 we show the lattice structure of an YBCO perovskite structure. Despite the apparent complexity of the structures of the different cuprates compounds, they all have two dimensional CuO_2 planes. In essence all the high-temperature superconductors (HTCS) consist of two-dimensional CuO_2 planes which are sandwiched between intervening atomic layers. These layers are composed mostly out of alkaline-earths, rare-earths, oxygen and halogenides. Depending on the number of CuO_2 planes per unit cell the materials have a single , a double-, or a triple-plane form as in

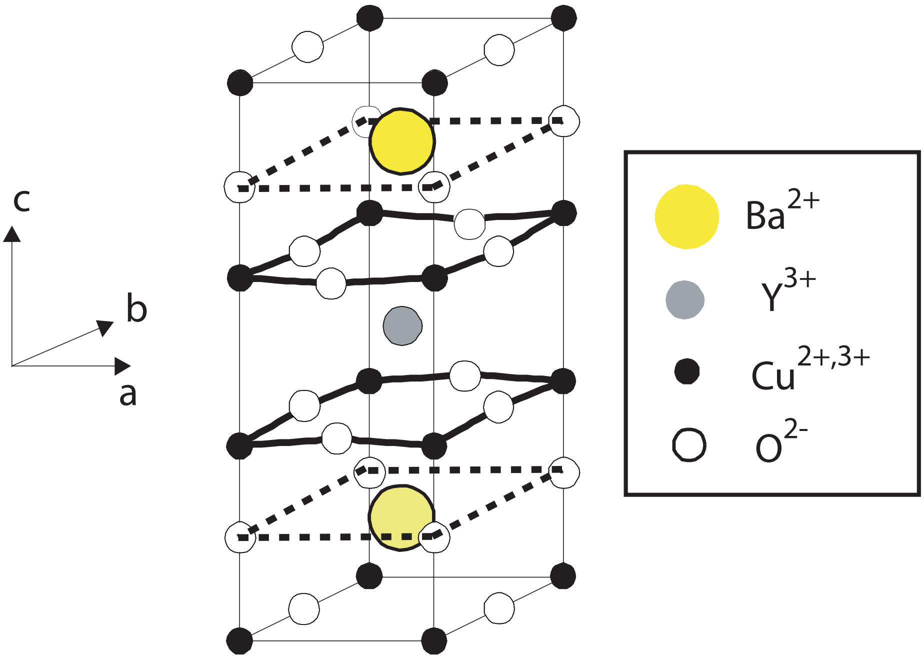

Figure 1.1: A single unit cell of $YBa_2Cu_3O_6$ (YBCO) is illustrated. The dimensions of the cell are $a = 3.8227$, $b = 3.8872$, and $c = 11.6802$. The lattice is composed of double perovskite layers, separated by CuO chains.

La_2CuO_4 , in $YBa_2Cu_3O_6$, or in $Bi_2Sr_2YCu_3O_8$, respectively.

It is widely accepted that the CuO_2 planes host electronic excitations which are most relevant to the superconductivity. The intervening layers are viewed as *inert* charge reservoirs. However, there is still some controversy about the role of the co-called apical oxygen atoms, which are located above and below the CuO_2 plane.

Moreover, it is experimentally well established that the parent compounds [1] La_2CuO_4 and $YBa_2Cu_3O_6$ are charge transfer insulators and ordered antiferromagnetically below a Néel temperature T_N. Below the Néel temperature T_N, the unpaired holes of the Cu^{2+} ions are antiferromagnetically coupled via super-exchange through the oxygen O^{2-}. The maximum Néel temperature is of the order of several hundred Kelvin (in $YBa_2Cu_3O_6$ $T_N \approx 420K$).

The picture of a magnetic insulator contradicts the simple band-structure point of view. In fact, the formal valencies of lanthanum, oxygen, and copper in La_2CuO_4 are La_3^+, O_2^-, and Cu_2^+, respectively. Hence the planar copper constitutes the only open shell atomic configuration. It is in a $3d_9$ state which contains a single d-hole. This hole is expected to be mainly located in a planar d_{x2-y2} orbital. Therefore, a naive argument would suggest that the parent compounds are simple metals with the charge carriers moving in the planes. But the localized copper spins provide the magnetic moments for the antiferromagnetic order. The in-plane antiferromagnetic exchange coupling J is generated by a copper spin super-exchange and the undoped CuO_2 plane is well described by a two-dimensional spin$-1/2$ antiferromagnetic Heisenberg model.

Typically, J is of the order of a few hundred meV and depends on the parent compound. Let us note that long-range AFM order at finite temperature requires an inter-plane coupling $J_\perp$, since a pure two dimensional long-range magnetic order is ruled out by the Mermin-Wagner theorem [3], which forbids any continuous symmetry breaking at a finite temperature in one and two dimensions.

1.2 The phase diagram

Besides the question of the nature of the parent compound, one of the early questions was whether there are Cooper pairs in these materials or some new exotic form of superconductivity that takes place when the system is doped with electrons or holes. In this regards, it is quite remarkable that the cuprate perovskites allow for a continuous variation of the in-plane carrier concentration by doping which leads to a complex phase diagram. The parent compounds can be *doped* by adding or removing holes, which eventually leads to metallic behavior and superconductivity. Doping is achieved either by hetero-valent substitution as in $La_{2-x}Sr_xCuO_4$ and in $Bi_2Sr_2Cy_{1-x}YxCu_2O_8$ or by a variation of the total oxygen content as in $YBa_2Cu_3O_{6+x}$. Doping introduces additional charge carriers into

---

[1] Undoped materials are for historical reasons usually referred to as *parent compounds*.

the CuO_2 planes. Since none of this is accompanied by any major structural change of the materials, it is quite natural to expect electronic correlations to play a significant role in these systems. The notion of overdoped or underdoped cuprates is frequently used to define the region of doping above, or below the so-called optimal doping concentration at which the superconducting transition temperature T_c is highest. Obviously, holes and electrons doped into the antiferromagnetic insulators are very efficient in destroying the magnetic order. In $La_{2-x}Sr_xCuO_4$ only 2% of holes are sufficient to achieve this. Therefore, the charge carriers seem to couple strongly to the spin systems. However, there is an apparent asymmetry between the electron and the hole-doped systems regarding the stability of antiferromagnetism as well as that of superconductivity, since the magnetic order is stable up to 30% in the electron doped side of the phase diagram.

1.3 Theoretical approaches to superconductivity

Regarding theory, despite the huge research efforts and tremendous scientific activity, the current understanding of both the normal state properties of the cuprates as well as the nature of the superconducting phase remains incomplete.

Early on, it has been argued that many of the unusual properties of the cuprates are related to the electronic structure of the CuO_2 planes. It is widely believed that this structural unit supplies the carriers which form the superconducting condensate. At present time, it is commonly accepted that the relevant degrees of freedom in the perovskites are confined to the two dimension plans, though the role of the out-of-plane oxygens, the so called apical oxygens, remains unclear. Therefore, low dimensionality is one of the challenging aspects of the carrier dynamics in the cuprates which is directly related to their layered crystal structure.

Another challenging aspect from the theoretical point of view is that the electron correlations constitute the key issue in the description of the elementary excitations in the cuprates. Ab initio LDA calculations (Local Density Approximations) corroborate the picture of strong local Coulomb correlations and give an onsite electronic repulsion of about $10eV$ in the d_{x2-y2} orbitals [4], which are located in the copper-oxide planes.

More importantly, the Fermi level in La_2CuO_4 is located such that at half-filling we get one hole per unit cell, which would exactly satisfy the valencies of La_2^+, O_2^- , and Cu_2^+. Therefore, any picture within a simple band structure theory would predict that at half-filling the cuprates have a metallic ground state and fail to reproduce the insulating behavior of undoped La_2CuO_4 . The inconsistency of LDA is a direct consequence of an improper treatment of strong

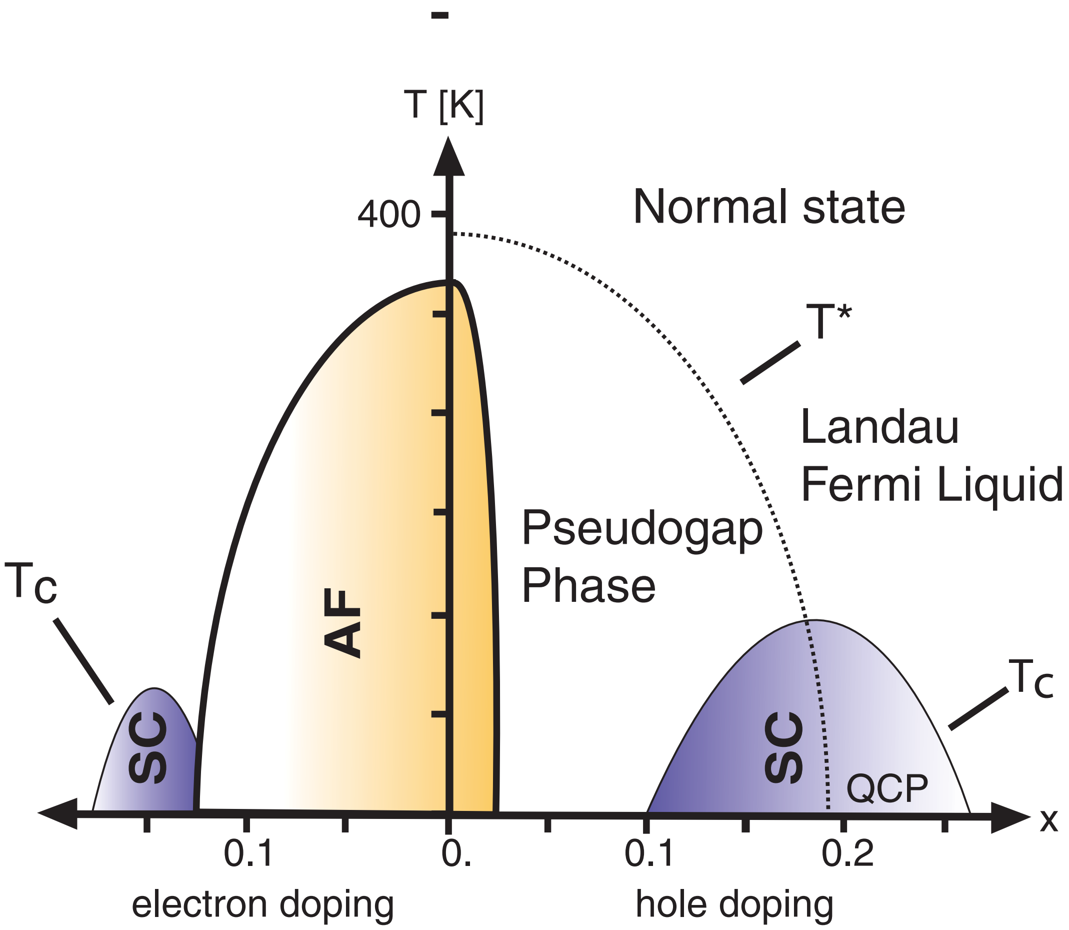

Figure 1.2: Simple Sketch of the phase diagram of the copper oxide superconductors. The system is a Mott insulator at half-filling ($x = 0$) and the ground-state is antiferromagnetic. The antiferromagnetism is progressively destroyed when additional holes are put in the two dimensional planes ($x > 0$) or when holes are removed from the planes ($x < 0$). In $\mathrm{La}_{2-x}\mathrm{Ba}_x\mathrm{CuO}_4$, the system becomes superconducting at low temperature for hole doping $x \approx 0.1$. On top of the superconducting phase, the compounds show many peculiar behaviors and do not behave like a normal metal. This phase is called the *pseudo-gap* phase. In the high doping limit, the ground sate is again a normal metal. Wether T^* falls inside the superconducting dome or not is an interesting question : it was proposed that the pseudo-gap phase would be still present if the superconducting instability would not exist. On the other hand, it was also proposed that the pseudo-gap phase is strongly connected to the SC instability and would not exit alone. The possibility for a quantum critical point (QCP) is also a controversial open question.

local Coulomb correlations. To incorporate electronic correlations, one has to map the complicated band structure onto effective microscopic models which treat in a better way the electron-electron interactions.

The importance of the strong correlations in these materials is corroborated by the vicinity of the metal-insulator transitions, of the antiferromagnetism instability, and also by the presence of superconductivity in this phase diagram. These phases are frequently attributed to electron interaction effects in the context of doped Mott insulators.

Indeed, the low-energy charge and spin dynamics of the cuprates displays many features which defy an interpretation in terms of normal Fermi-liquid theory. In the compounds, most noteworthy are the *unconventional* temperature and frequency dependencies of various scattering rates and cross sections, which allow to think that strong correlation might be responsible for these unconventional electronic behaviors. Various theoretical scenari have been proposed which speculate on the complete breakdown of Fermi-liquid theory including new and exotic quantum ground states of the spin and charge carriers.

Nevertheless, despite many unexpected features and unconventional behaviors in the high T_c compounds, a number of electronic properties remain which are quite conventional and thereby constrain possible theories. In particular, the angular resolved photo-emission (ARPES) reveals the presence of a normal Fermi surface in the metallic compounds [5]. Moreover, photoemission data identifies dispersive single-particle states which seem related to the predictions of the LDA although they exhibit significant mass enhancement [6].

In conclusion, the compounds are expected to be highly correlated, with an effective bandwidth roughly equal to the effective local Coulomb interaction. The undoped materials are antiferromagnetic charge transfer insulators at half-filling, and upon doping the antiferromagnetism is destroyed and the system becomes superconducting. At small doping, in the proximity of the antiferromagnetic phase, the normal state physics cannot be described in terms of Fermi liquid theory and is characterized by the presence of a pseudo-gap.

An essential requirement of any successful theory is to capture all these fundamental features at the same time.

1.4 Microscopic models for the cuprates

1.4.1 Three band Hubbard model

The electronic properties of oxide high-Tc superconductors have been extensively investigated over the last decade. The mechanism of superconductivity (SC) has been studied using various two-dimensional (2D) models of electronic interactions. One of the models proposed to describe the physics of high Tc materials was the so-called three-band Hubbard model introduced by Varma et al. [7] and Emery et al [8]. This Hamiltonian considers only the in-plane oxygen p_σ and d_{x2-y2} orbitals, and is defined in hole notations:

$$H = \sum_{\langle i,j\rangle\sigma} \left(S_{i,j} t_{i,j} d^\dagger_{i\sigma} p_{j\sigma} + c.c.\right) + \sum_{\langle i,j\rangle\sigma} \left(S_{i,j} t_{i,j} p^\dagger_{i\sigma} p_{j\sigma} + c.c.\right) + \\ U_p \sum_p \hat{n}_{p\uparrow}\hat{n}_{p\downarrow} + U_d \sum_d \hat{n}_{d\uparrow}\hat{n}_{d\downarrow} + \Delta_p \sum_{p,\sigma} \hat{n}_{p\sigma} + V_{dp} \sum_{d,p} \hat{n}_d \hat{n}_p \quad (1.1)$$

where $t_{i,j}$ is the hopping matrix, and contains copper-oxygen (oxygen-oxygen) transfer integrals t_{dp} (t_{pp}). The parameters of the three-band Hubbard model are given by the energy of the atomic level of the p electrons Δ_p, by U_d and U_p the respective on-site repulsion at the d_{x2-y2} and p_σ orbitals, and V_{dp} is the nearest neighbor repulsion between the d and p orbitals. Realistic sets of parameters were found by LDA calculations [8, 9, 10], though it is generally argued that the parameters should not be taken too seriously, that is within 30%. The cuprate compounds have one hole per Cu site at half-filling, and usually it is easier to work in hole notations, hence $d^\dagger$ ($p^\dagger$) creates one hole on a copper (oxygen) site. The matrix $S_{i,j}$ contains the phase factor that comes from the hybridization of the p-d orbitals [2].

In the limit $t_{dp} \ll U_d - \Delta_p$, $t_{dp} \ll \Delta_p$ and $\Delta_p < U_d$, the dp model can be mapped onto the $t-J$ model with [11]:

$$J = 4t^2_{eff} \left(\frac{1}{U_d} + \frac{2}{2\Delta_p + U_p}\right), \quad (1.2)$$

where $t_{eff} \approx t^2_{dp}/\Delta_p$ and $J_K = 4t_{eff}$ is the antiferromagnetic exchange coupling between the d and p holes. Since Δ_p/t_{pd} is not so large in real materials, the mapping to the $t-J$ model is not necessarily justified in this simple limit, though the mapping would still be relevant by considering the full canonical transformation.

Zhang and Rice [12] argued that the low-energy physics of the hole-doped three-band model can be described by a simpler one-band $t-J$ model. Starting from the three-band model and neglecting the oxygen dispersion, Zhang and Rice showed in perturbation theory that an additional hole put into the oxygen band binds strongly with a hole on the Copper atom, forming an on-site singlet. This singlet state can be thought of as moving through the lattice like a hole in an antiferromagnetic background. Therefore the physics can be described by a one-band $t-J$ model, which contains a kinetic part which describes in the three-band language the hopping of the singlet state. Pertinent criticism to this simplified model were raised by different authors. For instance, it was stressed

---

[2] In hole notations the bonding orbitals enter the Hamiltonian with a positive transfer integral sign, and the anti-bonding orbitals with a negative sign. In electron notations, the signs are reversed.

that the other d and p orbitals might be important and should be considered in the theory. Nevertheless, the Zhang-Rice theory is widely accepted nowadays, probably the most serious critique to it is the neglect of the t_{pp} transfer integral.

1.4.2 Hubbard and t-J models

One of the most studied one band model which takes into account the strong correlations is the Hubbard model :

$$H_{Hubbard} = -t \sum_{\langle i,j \rangle,\sigma} \left(c^{\dagger}_{i\sigma} c_{j\sigma} + h.c. \right) + U \sum_{i} n_{i\uparrow} n_{i\downarrow} \tag{1.3}$$

where $c^{\dagger}_{i\sigma}$ creates an electron at site i and $\langle i,j \rangle$ are nearest neighbors site of the lattice. The first term is a kinetic energy term, that takes into account the hopping of the electrons and the second term is an on-site Coulomb repulsion term. This model leads to the free-particle tight-binding case when $U = 0$, and we get in this limit the usual band structure theory, whereas when $t = 0$ the model is fully localized and the ground state is an insulator. At half-filling, the model has one electron per site of the lattice, and by increasing the on-site Coulomb repulsion U the ground state moves from a metal to a Mott insulator (Metal-Insulator transition).

Starting from the Hubbard model, which contains doubly occupied sites, and performing a canonical transformation, it is straightforward to get an effective $t{-}J$ model within the subspace of the Hilbert space that contains no doubly occupied site :

$$\begin{aligned} H_{t-J} = -t \sum_{\langle i,j \rangle,\sigma} \left(c^{\dagger}_{i\sigma} c_{j\sigma} + h.c. \right) + J \sum_{\langle i,j \rangle} \left(\mathbf{S}_i \cdot \mathbf{S}_j - \frac{1}{4} n_i n_j \right) + \\ J_3 \left(\sum_{\langle i,j,k \rangle \sigma} t_{ij} c^{\dagger}_{i\sigma} c_{j\sigma} c^{\dagger}_{j-\sigma} c_{k-\sigma} + t_{ij} n_k c^{\dagger}_{i\sigma} c_{j\sigma} + c.c. \right) \end{aligned} \tag{1.4}$$

The $t{-}J$ model describes, like the Hubbard model, electrons hopping with an amplitude t and interacting with an antiferromagnetic exchange term J. The first term describes the nearest neighbor hopping between sites of the lattice allowing the electrons to delocalize. The second term represents the nearest neighbor exchange interaction between the spins of the electrons. The exchange interaction is considered for electrons lying on nearest neighbor sites (denoted $\langle i,j \rangle$). $\mathbf{S}_i$ denotes the spin at site i, $\mathbf{S}_i = \frac{1}{2} c^{\dagger}_{i,\alpha} \vec{\sigma}_{\alpha,\beta} c_{i,\beta}$, and $\vec{\sigma}$ is the vector of Pauli matrices. The J_3 term in the $t{-}J$ model is usually dropped out for simplicity, though its amplitude is not expected to be negligible. When $t = 0$, the $t{-}J$ model is equivalent to the Heisenberg model. H_{t-J} is restricted to the subspace where there are no doubly occupied sites.

The mapping of the Hubbard model on the $t{-}J$ model is done by using a unitary transformation e^{iS} that decouples the Hilbert space of the Hubbard Hamiltonian so that there are no connections between the subspaces with different numbers of doubly occupied sites. This transformation is an expansion in (t/U), so that the subspaces are decoupled at each order. At first order, the operator $\hat{S}$ is given by $\hat{S} = -\frac{1}{iU}\left(F_{+1} - F_{-1}\right)$, where F_1 (F_{-1}) is the part of the kinetic operator that increases (decreases) the number of doubly occupied sites by unity.

The spin operator in the fermionic language can be more easily understood by its effect on single-particle fermionic states. We consider first the dot product of the spin operators :

$$\mathbf{S}_i \cdot \mathbf{S}_j = \frac{1}{2}\left(S_i^+ S_j^- + S_i^- S_j^+\right) + S_i^z S_j^z \tag{1.5}$$

S_i^+, when applied a fermion with spin down, is equivalent to a spin-flip process :

$$S_i^+\left(c_{i\downarrow}^+ \left|0\right\rangle\right) = c_{i\uparrow}^+ \left|0\right\rangle \tag{1.6}$$

On the other hand, the up fermion state is contained in the Kernel of the S_i^+ operator:

$$S_i^+\left(c_{i\uparrow}^+ \left|0\right\rangle\right) = 0 \tag{1.7}$$

And finally S_i^z is diagonal and gives the spin of the fermion state:

$$S_i^z\left(c_{i\sigma}^+ \left|0\right\rangle\right) = \sigma\left(c_{i\sigma}^+ \left|0\right\rangle\right) \tag{1.8}$$

Finally, the exchange coupling J is obtained from the canonical transformation of the Hubbard model and is given by $J = 4t^2/U$. When the on-site repulsion is very large the exchange process of two neighbors up and down spins vanishes. This is intuitive, since the exchange of two fermions is a second order process that makes an up fermion hop on the same site than a down fermion. In the limit when U is small, the canonical transformation is no longer valid, since the Hilbert sector containing the single occupied site is no longer decoupled from the highest energy states. Finally, let us note that the exchange coupling J is antiferromagnetic.

To illustrate the physics of the $t{-}J$ model, we consider first a simple toy model of two Heisenberg spin coupled through an antiferromagnetic coupling J: $H = J \sum\limits_{\langle i,j \rangle} \mathbf{S}_i \cdot \mathbf{S}_j$. The ground-state for this model is a singlet with energy $E = -3J/4$, and the higher energy state is a triplet with energy $E = J/4$. A naive expectation, when dealing with antiferromagnetic quantum spin systems, is that the ground state in one or two dimensions might be therefore a singlet as well. It is worth looking at the energy of the singlet state in the one dimensional spin-1/2 case, since in this limit the exact solution is known (Bethe Ansatz). The spin-1/2 system is gapless, in contrary with the spin-1 chain that is gapped

(Haldane gap). In the one dimensional spin chain, a pure valence-bond [3] wavefunction is clearly not the ground state but it gives indeed an energy that is even better than the classical antiferromagnetic state:

- Classical antiferromagnetic state : $E = -0.25J$
- valence-bond of singlet states : $E = -0.375J$
- Exact ground state energy (Bethe Ansatz) : $E = -\sqrt{2}\log 2J \approx -0.43J$

Clearly the valence-bond state made of dimers is not close to the ground state of the one-dimensional chain, though it were the case if we introduce the coupling of the spin degrees of freedom to the lattice (there is an energy gain due to the elastic energy that is reduced by forming singlets, this is the so called Spin-Peierls instability). Nevertheless, it can still be expected, although the pure valence-bond state is not a good approximation of the ground-state, that a superposition of many valence-bond state (resonating valence-bond) will give a good Ansatz that keeps the key ingredient of the low energy physics. The valence-bonds are expected to give a good variational basis to describe the low energy physics of the model. This later argument is at the basis of the ideas of Anderson, and such a proposal was made for the triangular lattice in 1975 [13].

1.4.3 Anderson's Resonating valence-bond theory

The discovery of high-T_c superconductivity, and the observation [14] that strong correlations are important in connection with these compounds has led to a tremendous interest in understanding strongly correlated electron physics. In particular the two simplest models for strongly correlated electrons, namely the Hubbard and $t-J$ models, have been the subject of intensive studies. In a milestone paper of 1987, Anderson proposed [14] that a resonating valence-bond (RVB) wave function, which consists of a superposition of valence-bond states (see Fig. 1.3), contains the ingredient to account for a consistent theory of the Hubbard and $t-J$ models. The $t-J$ model on the square lattice has been discussed extensively in the context of high-T_c superconductivity, especially as a framework for the implementation of the resonating valence bond (RVB) scenario proposed by P.W. Anderson [15]. The $t-J$ model can be viewed as the large on-site repulsion limit of the Hubbard model, and therefore at half-filling it describes an antiferromagnetic insulator. An RVB theory for the insulating state predicts that the preexisting singlet pairs become superconducting when the insulator is doped sufficiently. In that case the superconductivity would be driven exclusively by strong electron correlations.

---

[3] A valence-bond state is a paving of the chain with nearest neighbors singlets.

To illustrate our future strategy, let us recall in more details the simple basis of the RVB theory. Anderson propose to write the exchange part of the $t-J$ model in terms of singlet creation operators:

$$b_{i,j}^{+}\left|0\right\rangle = \frac{c_{i\downarrow}^{+}c_{j\uparrow}^{+} - c_{i\uparrow}^{+}c_{j\downarrow}^{+}}{\sqrt{2}}\left|0\right\rangle = \frac{1}{\sqrt{2}}\left(\left|\downarrow_i\uparrow_j\right\rangle - \left|\uparrow_i\downarrow_j\right\rangle\right) \tag{1.9}$$

This leads to the following equivalent Hamiltonian :

$$H_{t-J} = -t\sum_{\langle i,j\rangle\sigma} c_{i\sigma}^{\dagger}c_{j\sigma} - J\sum_{\langle i,j\rangle} b_{i,j}^{\dagger}b_{i,j} \tag{1.10}$$

In this language, the exchange term of the $t-J$ model can be seen as a term that condenses singlets. A simple mean-field decoupling of the singlet creation operator was proposed by P.W. Anderson:

$$\Delta_{i,j} = \left\langle b_{i,j}\right\rangle_0 \tag{1.11}$$

The mean-field hamiltonian is:

$$H_{MF} = -t'\sum_{\langle i,j\rangle\sigma} c_{i\sigma}^{\dagger}c_{j\sigma} - J\left(\sum_{\langle i,j\rangle}\langle b_{i,j}^{\dagger}\rangle b_{i,j} + b_{i,j}^{\dagger}\langle b_{i,j}\rangle + \langle b_{i,j}^{\dagger}\rangle\langle b_{i,j}\rangle\right) \tag{1.12}$$

And if the quantum fluctuations around the mean-field value are small, the final mean-field Hamiltonian reads:

$$H_{MF} = \sum_{k}\varepsilon_k\left(c_{k\sigma}^{\dagger}c_{k\sigma} + c.c.\right) + \left(\Delta_k c_{k\uparrow}^{\dagger}c_{-k\downarrow}^{\dagger} + c.c.\right) \tag{1.13}$$

Therefore the BCS mean-field theory is recovered as a mean-field theory of the $t-J$ model. The pairing order parameter assumed above is defined in real space. For example, when Δ is isotropic the Fourier transform of the pairing leads to the so called s-wave symmetry, and for the square lattice we get $\Delta_k = \Delta\left(\cos(k_x) + \cos(k_y)\right)$. In the case when Δ_{ij} has alternating sign on the square lattice ($+1$ on the horizontal bonds and -1 on the vertical bonds) the Fourier transform gives the d-wave pairing symmetry $\Delta_k = \Delta\left(\cos(k_x) - \cos(k_y)\right)$. The BCS wave-function has the peculiar property that it is a superposition of different numbers of particle states. Even more relevant, the full projection that forbids doubly occupied sites in the $t-J$ model is not taken into account by the simple mean-field decoupling. Therefore, we have to remove the doubly occupied site of the wave-function. As a first step, the wave-function is written in real space :

$$\left|\psi\right\rangle = \prod_{k\in BZ}\left(u_k + v_k c_{k\uparrow}^{+}c_{-k\downarrow}^{+}\right)\left|0\right\rangle \propto \prod_{k\in BZ}\left(1 + \frac{v_k}{u_k}c_{k\uparrow}^{+}c_{-k\downarrow}^{+}\right)\left|0\right\rangle \tag{1.14}$$

This can be expanded in power of $c^{+}_{k\uparrow}c^{+}_{-k\downarrow}$, and we get:

$$|\psi\rangle = \prod_{k\in BZ}\left(1+\frac{v_k}{u_k}c^{\dagger}_{k\uparrow}c^{\dagger}_{-k\downarrow}+\left(\frac{v_k}{u_k}c^{\dagger}_{k\uparrow}c^{\dagger}_{-k\downarrow}\right)^2+..\right) = \exp\left(\sum_k \frac{v_k}{u_k}c^{\dagger}_{k\uparrow}c^{\dagger}_{-k\downarrow}\right) \tag{1.15}$$

In this representation, we can project the wave-function on a state with fixed number of particles. The variance of the number of particles in the BCS wave-function behaves like $1/\sqrt{N}$, and the projection of the wave-function on a state with a fixed number of particle is not inducing drastic changes when the system is large. Hence, the wave-function that we consider is:

$$|\psi'\rangle = P_N \exp\left\{\sum_{i,j}\left(\sum_k \frac{v_k}{u_k}e^{ik(R_{i\uparrow}-R_{j\downarrow})}\right)c^{\dagger}_{i\uparrow}c^{\dagger}_{j\downarrow}\right\}|0\rangle \tag{1.16}$$

And u_k and v_k are respectively the particle and the hole densities :

$$u_k = \frac{1}{\sqrt{2}}\sqrt{1-\frac{\gamma_k}{\sqrt{\gamma_k+|\Delta_k|^2}}} \tag{1.17}$$

$$v_k = \frac{1}{\sqrt{2}}\sqrt{1+\frac{\gamma_k}{\sqrt{\gamma_k+|\Delta_k|^2}}} \tag{1.18}$$

$$v_k/u_k = \Delta_k/\left(\xi_k+\xi_k^2+\Delta_k^2\right)^{1/2}) \tag{1.19}$$

Very interestingly, the obtained projected BCS wavefunction can be written as a superposition of dimer paving of the lattice:

$$|\psi'\rangle = P_N\,|\psi_{BCS}\rangle = \left(\sum_{i,j} f(i,j)c^{+}_{i\uparrow}c^{+}_{j\downarrow}\right)^{N/2}|0\rangle \tag{1.20}$$

where f_{ij} depends on the choice of the order parameters. In the case of BCS projected wave-function, we have:

$$f_{BCS}(i,j) = \sum_k \frac{v_k}{u_k}e^{ik(R_{i\uparrow}-R_{j\downarrow})} \tag{1.21}$$

The f_{ij} plays the role of a pairing amplitude between a pair of electrons. The wave-function (1.20) is actually a superposition of many valence-bond configurations (see Fig.1.3), and was named *resonating valence-bond* state (RVB). To summarize, at zero temperature, the RVB theory can be formulated in terms of a variational wavefunction obtained by applying the so called Gutzwiller projector, that removes the doubly occupied site of the BCS wavefunction. The projected

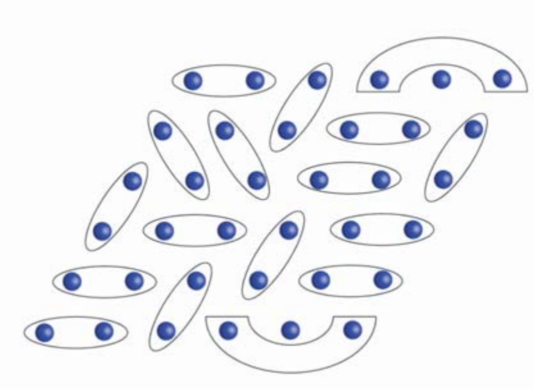

Figure 1.3: The projected BCS wave-function is a superposition of valence-bond states (resonating valence-bond state). A valence-bond state consist of a paving of the lattice with short-range dimers.

BCS wave-function is expected to be a good starting point to describe a doped Mott insulator. However, at half-filling the $t-J$ model reduces to the Heisenberg model, and it was pointed out that the magnetic order is not destroyed by the quantum fluctuations, though it is renormalized down to 60% of the classical value on the square lattice [16]. Therefore, we have to take into account an additional mean-field decoupling that allows to put back the long-range magnetic correlation in the wave-function. This can be done by considering additionally a spin decoupling of the exchange term in the $t-J$ model:

$$\begin{aligned} H_{t-J} \approx -t \sum_{\langle i,j \rangle \sigma} \left(c^{\dagger}_{i\sigma} c_{j\sigma} + c.c. \right) + \frac{J}{2} \left(\sum_{\langle i,j \rangle} \langle \mathbf{S_j} \rangle \mathbf{S_i} + \mathbf{S_j} \langle \mathbf{S_i} \rangle \right) \\ - \frac{J}{2} \left(\sum_{\langle i,j \rangle} \langle b^{\dagger}_{i,j} \rangle b_{i,j} + b^{\dagger}_{i,j} \langle b_{i,j} \rangle \right) \end{aligned} \tag{1.22}$$

As a matter of fact, the more general quadratic mean-field hamiltonian can be obtained after a mean-field decoupling of the $t-J$ model, where the decoupled exchange energy leads to the χ_{ij}, $\Delta_{i,j}$ and $\mathbf{h}_i$ order parameters:

$$\begin{aligned} H_{MF} = -t \sum_{\langle i,j \rangle \sigma} \left(\chi_{i,j} c^{\dagger}_{i\sigma} c_{j\sigma} + h.c. \right) + \\ \sum_{\langle i,j \rangle \sigma_i \sigma_j} \left(\Delta^{\sigma_i \sigma_j}_{i,j} c^{+}_{i\sigma_i} c^{\dagger}_{j\sigma_j} + h.c. \right) + \sum_i \mathbf{h}_i \mathbf{S_i} - \mu \sum_{i\sigma} n_{i\sigma} \end{aligned} \tag{1.23}$$

The first term in Hamiltonian (1.23) is a renormalized hopping term, that is allowed to take a complex phase. The phases are associated with a vector potential

$A(r)$ by the usual relation:

$$\chi_{ij} = |\chi_{ij}| \exp\left[i \frac{\pi}{\phi_0} \int_{r_i}^{r_j} \mathbf{A}(r) \cdot \mathbf{d}r \right], \tag{1.24}$$

and it describes an electron moving in an external magnetic field given by the gauge field $A(r)$. Consequently, the θ_{ij} order parameter breaks the time-reversal symmetry of the original $t{-}J$ model. The second term in H_{MF} is the usual BCS pairing order parameter, it can be singlet or triplet pairing. The pairing parameter breaks the one dimensional $U(1)$ symmetry. For the d-wave RVB phase, $\Delta_{i,j}$ is a nearest neighbor d-wave pairing with opposite signs on the vertical and horizontal bonds. Finally, the last term of the hamiltonian couples the spin operator to a classical external magnetic field. This latter term breaks the $SU(2)$ symmetry. When this latter order parameter is present, the ground state of Hamiltonian (1.23) is no longer a singlet. Finally, μ plays the role of a chemical potential and allows to control the number of particles in the non-projected wavefunction. We can expect that each of these instabilities could be stabilized in doped Mott-insulator, since the order parameter are obtained by natural decoupling of the exchange term of the $t{-}J$ Hamiltonian.

Although the $t{-}J$ is formulated in a very simple form, the nature of the quantum correlations makes its physics very rich. One question of crucial interest is the interplay between superconductivity and antiferromagnetism close to the insulating phase in the $t{-}J$ model. The ground state of this model on the square lattice is known to be antiferromagnetic at half-filling and one of the important questions is what happens upon doping. Although all the approaches to these strong coupling problems involve approximations, and it is sometimes difficult to distinguish the artefact due to approximations from the true features of the model, for the case of the square lattice, both the variational Monte Carlo method (VMC) [17, 18, 19] and mean-field theories [20] have found a d-wave superconducting phase in the the $t{-}J$ model and a phase diagram which accounts for most of the experimental features of the high-T_c cuprates [21, 22].

In the limit of vanishing doping (half-filling), the d-wave RVB state can be viewed as an (insulating) resonating valence bond (RVB) or *spin liquid* state. In fact, such a state can also be written (after a simple gauge transformation) as a staggered flux state (SFP) [20, 23], i.e. can be mapped to a problem of free fermions hopping on a square lattice thread by a staggered magnetic field.

Upon finite doping, although such a degeneracy breaks down, the SFP remains a competitive (non-superconducting) candidate with respect to the d-wave RVB superconductor [24]. In fact, it was proposed by P.A. Lee and collaborators [25, 26, 27] that such a state bears many of the unconventional properties of the pseudo-gap *normal* phase of the cuprate superconductors. This simple mapping connecting a free fermion problem on a square lattice under magnetic field [28] to a correlated wave-function (see later for details) also enabled to construct more exotic flux states (named *commensurate flux states*) where the fictitious flux could be uniform and commensurate with the particle density [29, 30]. In this particular case, the unit-cell of the tight-binding problem is directly related to the rational value of the commensurate flux.

Eventually, we expect that the wave-function given by (1.23) is a good starting point to approximate the ground state of the $t-J$ model. However, such a wave-function obviously does not fulfill the constraint of no-doubly occupied site (as in the $t-J$ model). This can be easily achieved, at least at the formal level, by applying the full Gutzwiller operator [31] $\mathcal{P}_{\mathcal{G}} = \prod_i (1 - n_{i\uparrow} n_{i\downarrow})$ to the BCS wave-function $|\psi_{\mathrm{BCS}}\rangle$:

$$|\psi_{\mathrm{RVB}}\rangle = \mathcal{P}_{\mathcal{G}} \, |\psi_{\mathrm{BCS}}\rangle \ . \tag{1.25}$$

The main difficulty to deal with projected wave-functions is to treat correctly the Gutzwiller projection $\mathcal{P}_{\mathcal{G}}$. Indeed, the full Gutzwiller projection cannot be treated exactly analytically and none of the observables can be easily calculated. Actually, the properties of the projected wavefunction can be evaluated in several ways, e.g. by using a Gutzwiller approximation to replace the projector by a numerical renormalization factor. Alternatively the properties of the projected wavefunctions can be obtained numerically using the Variational Monte Carlo method. The numerics, using the variational Monte Carlo (VMC) technique [32, 18,19,21] on large clusters, allow to treat exactly the Gutzwiller projection within the residual statistical error bars of the sampling. It has been shown that the magnetic energy of the variational RVB state at half-filling is very close to the best exact estimate for the Heisenberg model. Such a scheme also provides, at finite doping, a semi-quantitative understanding of the phase diagram of the cuprate superconductors and of their experimental properties.

Finally, a projected wavefunction combining antiferromagnetism and superconductivity was proposed for the Hubbard and $t-J$ models [33, 32], allowing to reconcile the variational results between these two models. This wavefunction allowed for an excellent variational energy and order parameter and a range of coexistence between superconductivity and anti-ferromagnetism was found. Further investigations of this class of wavefunctions has been very fruitful for the square lattice. This allowed to successfully compare to some of the experimental features with the high-T_c cuprates [21, 34], even if of course many questions remain regarding the nature of the true ground state of the system.

1.5 Scope of the Dissertation

Motivated by the success of variational Monte Carlo to describe some of the peculiar properties of the cuprates, we propose, on one hand to extend the method to other strongly correlated models for other compounds, and on the other hand we will focus on the pseudo-gap phase of the cuprates. The thesis is organized as follows:

- In Chapter 2 the variational method and its extension are described.
- Chapter 3 is devoted to the study of superconductivity and magnetism in the context of the cobaltites.
- In Chapter 4 we study strongly correlated properties of graphene and carbon nanotubes.
- Chapter 5 is devoted to the study of possible checkerboard patterns in the pseudo-gap phase of the cuprates, which is showing very peculiar properties and is a very challenging phase to understand at the theoretical level.
- Chapter 6 is devoted to the investigation of the possibility for spontaneous orbital currents in the cuprates, that might be candidates to describe the pseudo-gap phase of the cuprates.
- Finally, in Chapter 7, a summary of the work is given and the outlooks and extensions related to the present work are discussed.

Chapter 2

Numerical Methods

2.1 Variational Monte Carlo

In order to propose a good variational Ansatz for strongly correlated models, the starting point consists the considering a rich enough mean-field Hamiltonian that contains the main physical ingredients of the original model. The most general quadratic fermionic Hamiltonian is given in equation (1.23). The ground-state of this simple Hamiltonian is given by the usual Bogoliubov canonical transformation:

$$\sum_j \begin{pmatrix} K_{\uparrow,i,j} & \Delta_{i,j} \\ \Delta^\dagger_{i,j} & -K^*_{\downarrow,i,j} \end{pmatrix} \begin{pmatrix} u_\alpha(r_j) \\ v_\alpha(r_j) \end{pmatrix} = E_\alpha \begin{pmatrix} u_\alpha(r_i) \\ v_\alpha(r_i) \end{pmatrix} \tag{2.1}$$

where K_{ij} is the tight-binding part of the mean-field Hamiltonian and Δ_{ij} is the pairing. Here we have considered for clarity only the case of singlet pairing. The u_n^i and v_n^i are in this language the particle and hole densities and are coupled together by the above equations. This system of equation can be diagonalize numerically and the u_n and v_n coefficients can be extracted. The pairing, the current and the densities can be easily obtained from these coefficients by using the usual mean-field equations [35, 36, 37, 38, 39, 40]:

$$\Delta_{ij} = \langle c_{j,\downarrow} c_{i,\uparrow} \rangle = \sum_n \left(u_{ni} v^\dagger_{nj} + u_{nj} v^\dagger_{ni} \right) (1 - 2f(E_n)) \tag{2.2}$$

$$n_{i,\uparrow} = \left\langle c^\dagger_{i,\uparrow} c_{i,\uparrow} \right\rangle = \sum_\alpha |u_\alpha(r_i)|^2 f\left(E_\alpha\right) \tag{2.3}$$

$$n_{i,\downarrow} = \left\langle c^\dagger_{i,\downarrow} c_{i,\downarrow} \right\rangle = \sum_\alpha |v_\alpha(r_i)|^2 \left(1 - f\left(E_\alpha\right)\right) \tag{2.4}$$

$f(E)$ is the usual Fermi-Dirac distribution. The wavefunction can straightforwardly be built from the Bogoliubov quasi-particle operators (bogolons) that are defined by :

$$\alpha_\lambda = \sum_i \left(u_i^\lambda c_{i\uparrow} + v_i^\lambda c^\dagger_{i\downarrow} \right) \left(E^\lambda < 0 \right) \tag{2.5}$$

The ground state is obtained by the application of the bogolons on the vacuum of these operators :

$$|\psi\rangle = P_{N_e} \prod_{\lambda} \alpha^{\dagger}_{\lambda} |0_{bcs}\rangle \tag{2.6}$$

P_{N_e} projects the wavefunction on a state with N_e particles. The brute-force calculation of the latter equation is a generally non-trivial task, since the bogolons (the quasi-particle operator that are obtained after diagonalization of H_{MF}) contains both creation and destruction fermionic operators, and the product of the bogolons generates a series of terms with different number of fermions. The number of bogolon states increases with the size of the unit cell of the lattice and the brute force calculation can be done up to unit cell with size about 10 sites. Indeed, it was shown that the wavefunction can be obtained by [41]:

$$|\psi\rangle = P_{N_e} \exp\left(-\sum_{ij} \left(U^{-1}V\right)_{ij} c^{\dagger}_{i\uparrow} c^{\dagger}_{j\downarrow}\right) |0\rangle \tag{2.7}$$

where U and V are matrices defined by $(V_\lambda)_j = v^\lambda_j$ and $(U_\lambda)_j = u^\lambda_j$. In order to prove this result, let us assume that the ground state of the mean-field Hamiltonian has the following form:

$$|\psi\rangle = P_{N_e} \exp\left(\sum_{ij} \phi_{ij} c^{\dagger}_{i\uparrow} c^{\dagger}_{j\downarrow}\right) |0\rangle \tag{2.8}$$

Since the superconducting state satisfies $a_\lambda |\psi\rangle = 0$, we find :

$$\sum_i \left(u^\lambda_i c_{i\uparrow} + v^\lambda_i c^{\dagger}_{i\downarrow}\right) |\psi\rangle = 0 \tag{2.9}$$

Operating U^{-1} to this equation, the ground state $|\psi\rangle$ satisfies:

$$\left[c_{j\uparrow} + \sum_i \sum_\lambda \left(U^{-1}\right)_{j\lambda} V_{\lambda i} c^{\dagger}_{i\downarrow}\right] |\psi\rangle = 0 \tag{2.10}$$

On the other hand, using the anti-commutation relation of the bogolon operators, we derive from equation (2.8) :

$$\left(c_{j\uparrow} - \sum_i \phi_{ji} c^{\dagger}_{i\downarrow}\right) |\psi\rangle = 0 \tag{2.11}$$

which proves the identity (2.7). In conclusion, the ground-sate of the superconducting mean-field Hamiltonian is given by,

$$|\psi\rangle \approx \left[\sum_{ij} \left(U^{-1}V\right)_{ij} c^{\dagger}_{i\uparrow} c^{\dagger}_{j\downarrow}\right]^{Ne/2} |0\rangle \tag{2.12}$$

and additionally:

$$\phi_{ij} = -\sum_{\lambda}\left(U^{-1}\right)_{i\lambda}V_{\lambda j} = -\left(U^{-1}V\right)_{ij} \tag{2.13}$$

The Monte Carlo algorithm by Ceperley [42] is applicable to wavefunction of the form (2.7). These functions were extensively studied by variational Monte Carlo [43, 44, 18, 19, 21, 32].

To handle these functions, we have first to write them in terms of the real space fermionic configurations. A real space configuration of a fix number of fermions is defined as :

$$|\alpha\rangle = c^{+}_{R_1\uparrow}...c^{+}_{R_{N_e/2}\uparrow}c^{+}_{R'_1\downarrow}.....c^{+}_{R'_{N_e/2}\downarrow} \tag{2.14}$$

and we project the wavefunction in this basis:

$$|\psi\rangle = \sum_{\alpha}\langle\alpha|\psi\rangle|\alpha\rangle \tag{2.15}$$

The projection of the wavefunction on a configuration state $|\alpha\rangle$ is a sum of all the permutations of the fermions in this configuration:

$$|\psi\rangle = \left(\sum_{i,j} a(i,j)c^{+}_{i\uparrow}c^{+}_{j\downarrow}\right)^{N_e/2}|0\rangle = \sum_{i_1...i_{N_e/2}j_1...j_{N_e/2}}\left\{a(i_1,j_1)...a(i_{N_e/2},j_{N_e/2})\right\}c^{+}_{i_1\uparrow}c^{+}_{j_1\downarrow}......c^{+}_{i_{N_e}\uparrow}c^{+}_{j_{N_e}\downarrow}|0\rangle \tag{2.16}$$

It is straightforward to prove that the coefficient is indeed a determinant (see Appendix A):

$$\langle\alpha|\psi\rangle = \det\left\{Q = \{a_{i,j}\}\right\} \tag{2.17}$$

Now that the wavefunction is written in the real-space representation, the observables can be easily computed using Monte Carlo calculations. For instance, the variational energy is calculated as follows:

$$\frac{\langle\psi|H|\psi\rangle}{\langle\psi|\psi\rangle} = \sum_{\alpha,\beta}\frac{\langle\psi|\alpha\rangle}{\langle\psi|\psi\rangle}\langle\alpha|H|\beta\rangle\langle\beta|\psi\rangle \tag{2.18}$$

We can separate the sum in terms of a positive probability $P(\alpha)$ and of the local energy $e(\alpha)$:

$$\frac{\langle\psi|H|\psi\rangle}{\langle\psi|\psi\rangle} = \sum_{\alpha}\underbrace{\frac{|\langle\alpha|\psi\rangle|^2}{\langle\psi|\psi\rangle}}_{P(\alpha)}\left(\underbrace{\sum_{\beta}\langle\alpha|H|\beta\rangle\frac{\langle\beta|\psi\rangle}{\langle\alpha|\psi\rangle}}_{e(\alpha)}\right) \tag{2.19}$$

Since $P(\alpha)$ is a positive function, the sum can be sampled by Monte Carlo calculations and no spurious sign problem occurs. The probability of a transition from state X to a new state X' is given by:

$$P(X \to X') = min\left(1, \frac{|\det(A(X'))|^2}{|\det(A(X))|^2}\right) \tag{2.20}$$

Therefore, during a simulation the main task consists in calculating ratios of determinants. Although the brute force calculation of a determinant scales like N^3 numerical operations, we can reduce it to N operations [42] by considering optimized formulae that allow to compute directly ratios of determinants of two matrices A'/A, where the two matrices A and A' differ only the column j:

$$w_j = \frac{det(A')}{det(A)} = \sum_k A^{-1}_{j,k}\mathbf{v}_k \tag{2.21}$$

where $\mathbf{v}$ is the column j of the new matrix A'. Similar formula can be obtained when several lines and columns are updated at the same time in the new matrix A' (for further details see ref. [45]). However, the formula (2.21) involves the inverse of the matrix A. The matrix A^{-1} can be updated when a set of rows and/or columns are changed in the matrix A [1] each time that a Monte Carlo move is accepted, and the update can be done in N^2 numerical operation [42]. In the simple implementation of the Metropolis algorithm, the moves are often rejected and therefore the formula 2.21 is the bottleneck of the simulation. A even much improved algorithm, that updates directly the weights w_j and does not compute the inverse of the matrix A, is currently used by Sandro Sorella and collaborators. This latter algorithm computes the weight w_j in a single operation. However, the implementation of such an algorithm is much more involved and is beyond the scope of this dissertation.

2.1.1 Degenerate open shell

As discussed in the previous section, the variational wavefunction is built by piling the quasi-particle states up to the Fermi energy, in the case of a tight-binding wavefunction, or up to the chemical potential μ when the BCS pairing is considered. When the energy of the single-particle state is non-degenerate the resulting wavefunction is well defined. However, the wavefunction becomes ambiguous when the energies are degenerate. This happens in finite size clusters, due to the symmetry of the lattice: The $\mathbf{k}$ points are lying on shells of same energy. This gives artificial degeneracies related to the different filling possibilities.

---

[1] The hopping of one particle involves a change of row or a column in A, and the swap of an up and down particles involves the change of both a row and a column in A.

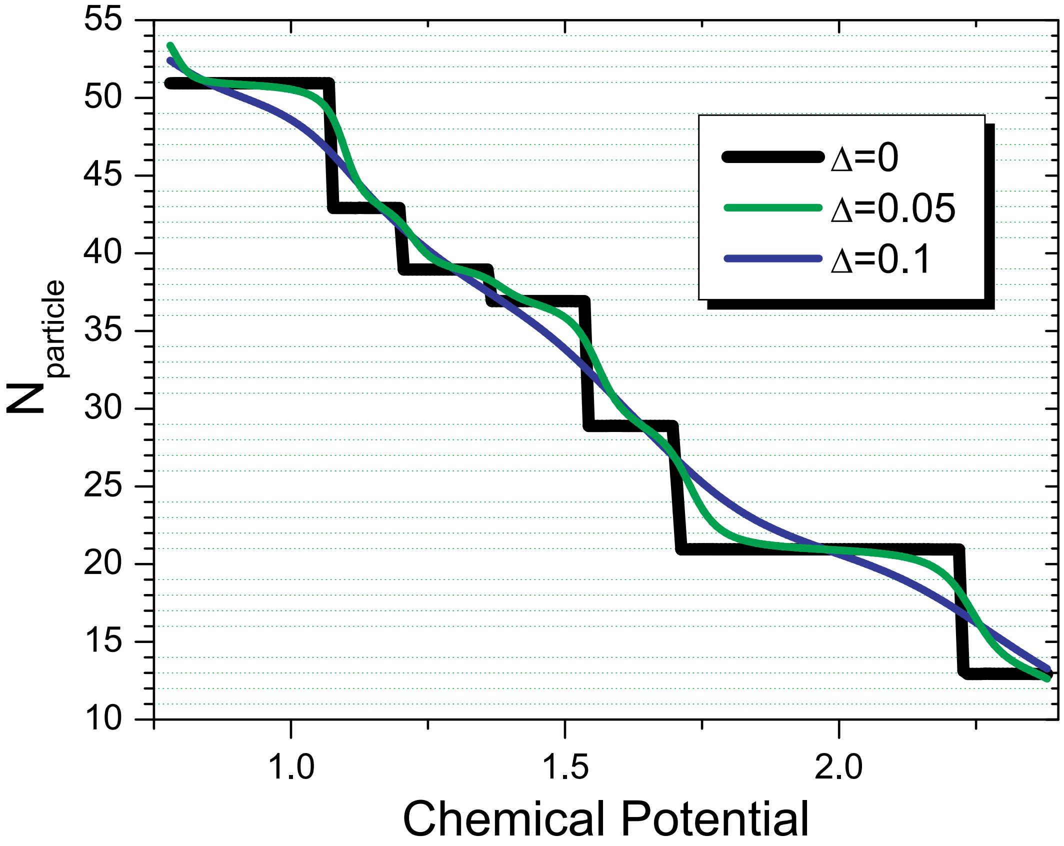

Figure 2.1: Number of particle in the non-projected RVB wavefunction versus the chemical potential when the pairing is $\Delta = 0$, and for finite pairing in a three band hubbard model. When $\Delta = 0^+$, some of the numbers of particle are forbidden due to the degenarate shells. In contrast, when $\Delta > 0$ the number of particles evolves smoothly with the chemical potential.

In the language of the non-projected RVB wavefunction this will give plateaus in the number of particles versus the chemical potential (see Fig. 2.1) when the pairing parameters vanish. Indeed, when the chemical potential reaches the energy of a degenerate shell, all the particles in the plateau are filled and the number of particles changes discontinuously. These spurious degeneracies can be left out for the case of one band theories by considering rotated lattices : for these lattices the k-vectors move out of the degenerate shells. This cannot be done for more complicated multi-band theories, like for the three-band Hubbard model discussed in Chapter 6. Nevertheless, when the pairing parameters are finite, the number of particles is moving continuously with the chemical potential and it is always possible to impose a fixed number of particles in the variational wavefunction. It is therefore often more efficient to consider a small residual pairing also when tight-binding wavefunctions are considered. Therefore, for open shells, we take $f_{i,j}$ with a small pairing in order to split the bare degeneracy, the resulting wavefunction being still a singlet. Finally, to avoid spurious and peculiar effects in the calculations, we impose that the non-projected wavefunction has the same number of particle than the projected wavefunction.

2.1.2 Pfaffian variational Monte Carlo

In this section we address the issue of collinear magnetism or triplet pairing in the mean-field Hamiltonian (1.23). In both cases, the exponent in (2.8) becomes spin dependant:

$$|\psi_{MF}\rangle = \exp\left(\frac{1}{2}\sum_{i,j,\sigma_i,\sigma_j} f_{i,j}^{\sigma_i,\sigma_j} c^{\dagger}_{i,\sigma_i} c^{\dagger}_{j,\sigma_j}\right)|0\rangle \tag{2.22}$$

We emphasize that $|\psi_{MF}\rangle$ has neither a fixed number of particles due to the presence of the pairing, nor a fixed total S^z due to the non-collinear magnetic order. Thus in order to use it for the VMC study we apply to it the following projectors: $\mathcal{P}_N$ which projects the wavefunction on a state with fixed number of electrons, and $\mathcal{P}_{S^z}$, which projects the wavefunction on the sector with total $S^z = 0$.

Expanding (2.22) we get:

$$\begin{aligned}
|\psi\rangle &= P_N|\psi_{MF}\rangle && (2.23)\\
&= \left\{\sum_{i,j}\lambda(i,j)c^{+}_{i\downarrow}c^{+}_{j\downarrow} + \omega(i,j)c^{+}_{i\uparrow}c^{+}_{j\uparrow} + \theta(i,j)c^{+}_{i\downarrow}c^{+}_{j\uparrow} + \chi(i,j)c^{+}_{i\uparrow}c^{+}_{j\downarrow}\right\}^{N/2} && (2.24)\\
&= \left\{\sum_{i,j,\sigma_i,\sigma_j} D_{(i,j,\sigma_i,\sigma_j)}c^{+}_{i\sigma_i}c^{+}_{j\sigma_j}\right\}^{N/2} && (2.25)
\end{aligned}$$

$$|\psi\rangle = \sum_{\left(R_1..,R_{N/2}\right)\left(R'_1..R'_{N/2}\right)} \left\{D_{(R_1,R'_1)}..D_{(R_{N/2},R'_{N/2})}\right\} c^{\dagger}_{R_1}c^{\dagger}_{R'_1}..c^{\dagger}_{R_{N/2}}c^{\dagger}_{R'_{N/2}} \tag{2.26}$$

where we used the notations $R_i = (x_i, \sigma_i)$. Then the projection on the real basis state $\langle\alpha| = \langle 0|\, c_{R_1}..c_{R_N}$ is given by :

$$\langle\alpha|\psi\rangle = \sum_{\mathcal{P}}\left\{D_{(P_{R_1},P_{R_2})}...D_{(P_{R_{N-1}},P_{R_N})}\right\}(-1)^{Signature(\mathcal{P})} \tag{2.27}$$

We introduced the notation $\mathcal{P}(R_i) = R_k, k = \mathcal{P}(i)$.

$$\sum_{\mathcal{P}}\left\{D_{(P_{R_1},P_{R_2})}...D_{(P_{R_{N-1}},P_{R_N})}\right\}(-1)^{Signature(\mathcal{P})} = P_f(A) \tag{2.28}$$

where we have defined : $A_{ij} = (D_{i,j} - D_{j,i})$. The Pfaffian of a skew matrix is related to the determinant [46]:

$$P_f(A)^2 = \det(A) \tag{2.29}$$

However, the sign of the Pfaffian is not given by this relation and further algorithms to compute the Pfaffian of a squew matrix must be used. In conclusion, we find that the wavefunction projected on a real basis state when collinear/triplet pairing are present is the Pfaffian of the real-space configuration anti-symmetrized matrix A:

$$\begin{aligned} \langle \alpha \mid \psi_{\text{var}} \rangle &= P_f\left(\mathbf{A}\right) \\ A_{i,j} &= f_{(k_i,k_j,\sigma_i,\sigma_j)} - f_{(k_j,k_i,\sigma_j,\sigma_i)} \end{aligned} \tag{2.30}$$

where $P_f(\mathbf{A})$ denotes the *Pfaffian* of the matrix **A**. Using this last relation, the wavefunction can now be evaluated numerically using a Monte Carlo procedure with Pfaffian updates, as introduced in Ref. [47]. In the particular case where $f_{k,l,\uparrow,\uparrow} = f_{k,l,\downarrow,\downarrow} = 0$ and at $S^z = 0$ (this happens if the BCS pairing is of singlet type *and* the magnetic order is collinear), the Pfaffian reduces to a simple determinant, and the methods becomes equivalent to the standard Variational Monte Carlo [42] technique.

However, in the simulation we have to calculate the ratio of the two Pfaffians of matrices Q and R that correspond to two different real-space configurations. One of the main problem is that the sign of the Pfaffian is not given by the general formula $P_f(Q)^2 = \det(Q)$. However, it was shown by the mathematician Arthur Cayley in 1849 that the ratio of the Pfaffian of two skew matrices, that differ only by the column and the line i, is given by [48]:

$$\frac{P_f(Q)}{P_f(R)} = \frac{\det(S)}{\det(R)} \tag{2.31}$$

Where the matrix R is distinct from the matrix Q only by the line and the column i, and the matrix S is distinct from the matrix R only by the column i. When moving the particle labeled by index i from one site to another site, the line and the column of the matrix A in equation (2.30) must be changed, and thus formula (2.31) can be used. The ratio of the determinants can still be calculated with the method of Ceperley [42]:

$$\frac{\det(S)}{\det(Q)} = \sum_{j=1,2N} c_j \left(Q^{-1}\right)_{j,i} \tag{2.32}$$

where $\mathbf{c}$ is the updated column of matrix Q. Finally, we note that in the case when $f_{ij\uparrow\uparrow} = f_{ij\downarrow\downarrow} = 0$, the matrix Q reduces to diagonal blocks:

$$A = \begin{pmatrix} 0 & B \\ -B^T & 0 \end{pmatrix} \Rightarrow P_f(A) = \det B \tag{2.33}$$

Where the matrix elements of B are the f_{ij} matrix of equation (2.8), and we get back the usual determinantal variational Monte Carlo calculations. We emphasize that the matrix that we need to update in the Pfaffian Monte Carlo simulations has linear sizes twice larger than in the calculations with determinants. In conclusion, the Pfaffian Monte Carlo procedure is nothing else but an extension of the usual variational wavefunction method. This procedure allows to treat generally every order parameter contained in the mean-field Hamiltonian (1.23). However, we considered up to now only the uncorrelated part of the wavefunction. It will likely contain many doubly occupied sites that will cost a lot of energy within the Hubbard model. To treat correctly the correlations, we need to introduce an additional projection that takes care of the doubly occupied site contained in the wavefunction.

2.2 Jastrow factors, Gutzwiller projection

In the simplest approximation of the ground-state of the Hubbard model, a simple Fermi sea can be considered, and a simple so-called Gutzwiller projection can be used to treat the on-site repulsion of the Hubbard model. This gives one of the simplest possible variational Ansatz :

$$|\psi\rangle = P_G|\psi\rangle \tag{2.34}$$

where ψ is the one-body wavefunction and the Gutzwiller projection P_G is defined as [49]:

$$P_G = \prod_i \left(1 - (1-g)\,\hat{n}_{i\uparrow}\hat{n}_{i\downarrow}\right) \tag{2.35}$$

The variational parameter g is running from 0 to unity and i labels the sites of the lattice in real space. The Gutzwiller projection is very well suited by the variational Ansatz described in the last section, since the numerical variational Monte Carlo samples the wavefunction in the real-space fermionic configurations, and therefore the Gutzwiller projector is a diagonal operator in this representation. The Gutzwiller projection can be extended by the incorporation of a Jastrow factor [50] which provides an additional powerful way to tune more precisely the correlations of the wavefunction. Some of the possible choices of the Jastrow term are the long-range charge Jastrow :

$$J_d = \exp\left(\frac{1}{2}\sum_{i,j} u_{ij}\hat{n}_i\hat{n}_j\right) \tag{2.36}$$

Another long-range spin Jastrow can also be considered :

$$J_s = \exp\left(\frac{1}{2}\sum_{i,j} v_{ij}\hat{S}^z_i\hat{S}^z_j\right) \tag{2.37}$$

The full variational wavefunction is, when all these projections are considered:

$$|\psi_{VMC}\rangle = J_s J_d P_N P_{S^z=0} |\psi_{MF}\rangle \tag{2.38}$$

Where P_N projects the wavefunction on a state with fixed number of particles N, and $P_{S^z=0}$ projects the wavefunction on the $S^z_{tot} = 0$ sector. We expect that the projections allow to improve significantly the wavefunction. Let us note that in the $t-J$ model the situation is somehow simplified, since the full projection contained in the model forbids any doubly occupied site. Therefore, the local Gutzwiller projection is not needed. Nevertheless, the Jastrow term between different site of the lattice might still play an important role. Finally, we emphasize that the Jastrow parameters change the wavefunction's energy on much larger scales than the variations of the parameters in the one-body part.

2.3 Stochastic minimization

Quantum Monte Carlo methods are some of the most accurate and efficient methods for treating many-body systems. The success of these methods is in large part due to the flexibility in the form of the trial wavefunctions, discussed in the previous section, that results from doing integrals by Monte Carlo calculations.

Since the capability to efficiently optimize the parameters in trial wavefunctions is crucial to the success of the variational Monte Carlo (VMC), a lot of effort has been put into inventing better optimization methods. Two recent works [51, 52] have put the limitations in the minimization procedure to even further grounds.

In our work, we are mainly interested in the energy minimization, instead of the possible variance minimization. Both minimization are not identical. The variance of the wavefunction measures basically its distance to a true eigenstate of the Hamiltonian, that might be an excited state and not the ground-state.

Therefore, one typically seeks the lowest energy by minimizing either the one-body uncorrelated part of the variational wavefunction, that consist mainly of a determinant or a Pfaffian of a matrix, or by minimizing the Jastrow variational parameter, that consists of the strongly correlated part of the wavefunction.

To carry out the minimization, we start therefore by expanding in quadratic order the wavefunction in a neighborhood of the parameters.

$$|\psi_{\alpha+\gamma}\rangle \simeq \left[1 + \sum_k \gamma_k \left(O_k - \langle O_k \rangle \right) + \frac{\beta}{2} \sum_{k,k'} \gamma_k \gamma_{k'} \left(O_k - \langle O_{k'} \rangle \right) \right] |\psi_\alpha\rangle \tag{2.39}$$

where $\psi_\alpha(x)$ is the variational wavefunction, with set of variational parameters $\alpha = (\alpha_1 ... \alpha_m)$, projected on the real space fermionic configuration x. The O_k operators are the logarithmic derivative of the wavefunction with respect to the variational parameters α_k, and γ_k are the finite variations of the variational parameters. The O_k operators are defined by:

$$O_k\left(x\right) = \frac{\partial_{\alpha_k}\psi_\alpha\left(x\right)}{\psi_\alpha\left(x\right)} \tag{2.40}$$

We measure the energy difference between the expanded wavefunction and the original function :

$$\Delta E = -\sum_k \gamma_k f_k + \frac{1}{2}\sum_{k,k'} \gamma_k \gamma_{k'} \left[S_h + \beta G\right]^{k,k'} \tag{2.41}$$

where we find, for complex evaluated functions [2]:

$$S_h^{k,k'} = \langle O_k^\dagger H, O_{k'}\rangle \tag{2.42}$$

$$G^{k,k'} = 2Re\left(\langle H\left(O_k - \langle O_k\rangle\right)\left(O_{k'} - \langle O_{k'}\rangle\right)\rangle\right) \tag{2.43}$$

$$f_k = -Re\left(\partial_{\alpha_k} E_\alpha\right) = -2Re\left(\langle\left(H - E_\alpha\right) O_k\rangle\right) \tag{2.44}$$

On one hand, the linear term f_k plays the role of a force on the variational parameters, on the other hand, the S_h matrix represent the excitation matrix elements corresponding to the operators O_k and the G matrix helps the wavefunction to converge when it is far from the ground-state. The minimum energy is obtained for:

$$\gamma = B^{-1}\mathbf{f} \tag{2.45}$$

B is given by:

$$B = S_h + \left(1 + \beta\right) G \tag{2.46}$$

If B is not positive definite, the procedure does not converge. This typically happens when the wavefunction is very far from the ground state and can be repaired by adding a positive definite matrix $S^{k,k'} = \langle\left(O_k - \langle O_k\rangle\right)\left(O_{k'} - \langle O_{k'}\rangle\right)\rangle$ to the matrix B. We choose μ such that the energy variation in equation (2.41) is optimal. The additional μS term allows also to control how much the wavefunction is changing at each iteration.

2.3.1 Implementation details of the stochastic minimization

The remaining task for minimizing the wavefunction is the measurement of the O_k operators. When Jastrow-like parameters are considered, O_k is diagonal in the real space representation, and it is therefore straightforward to have a precise estimation of the mean value of this operator. However, when the parameters

---

[2] Here the results are given for complex wavefunctions. In Ref. [51] the results are shown in a more elegant way, but limited to the case of real functions.

that vary are contained in the mean-field Hamiltonian (1.23), they enter in a non trivial way into the one-body part of the wavefunction :

$$O_k = \frac{\delta_{\alpha_k}\psi_\alpha(x)}{\psi_\alpha(x)} = \frac{\delta_{\alpha_k}det(Q(x,\alpha_k)))}{det(Q(x,\alpha_k))} \tag{2.47}$$

where Q is the matrix of equation (2.17). The derivative of a determinant is given by the well known formula

$$\frac{\delta_{\alpha_k}det(Q(x,\alpha_k))}{det(Q(x,\alpha_k))} = Trace\left[Q^{-1}\frac{\delta Q}{\delta\alpha_k}\right] \tag{2.48}$$

Moreover, the derivative of the Q matrix with respect to the variational parameters is still unknown, and prompts for further calculations. Indeed, we should recall that the matrix Q is obtained by the ϕ_{ij} coefficient of equation (2.8), and using equation (2.13)) we get :

$$\frac{\delta\phi_{ij}(x,\alpha_k)}{\delta\alpha_k} = \frac{\delta}{\delta\alpha_k}\left(U^{-1}V\right)_{ij} = \left(-U^{-1}U'U^{-1}V + U^{-1}V'\right)_{ij} \tag{2.49}$$

where the U and V matrices are composed by the quasi-particle states that diagonalize the mean-field Hamiltonian (1.23). The final step consists in obtaining the derivative of the eigenstate of H_{MF} that enters in the U' and V' matrices.

2.3.2 Derivative of degenerate eigenvectors

The problem for computing eigenvector derivatives has occupied many researchers in the past several decades. The reason why so many people are interested in this problem is that derivatives of eigenvectors play a very important role in optimal analysis and control system design, and may also be an expensive and time-consuming task.

However, when all the eigenvectors are non-degenerate, the derivative of the eigenvectors and eigenvalues is given by a very simple perturbation theory. Let us consider the following eigenproblem :

$$|K_0(p)|\, x_{0i} = \lambda_{0i} x_{0i} \tag{2.50}$$

The unperturbated Hamiltonian matrix $K_0(p)$ depends on some control parameter (or variational parameter) p that makes the system evolve. When the eigen problem is perturbed with a linear perturbation in p:

$$[K] = [K_0] + [\delta K] \tag{2.51}$$

And we define the matrix D as the derivative of the Hamiltonian matrix K with respect to p :

$$D = \frac{\delta K_0}{\delta p} \tag{2.52}$$

The following change in the eigenvalues are obtained with first order perturbation theory:

$$\lambda_i = \lambda_{0i} + \mathbf{x}_{0i}^{\mathrm{T}} \left([\delta K] \right) \mathbf{x}_{0i}, \tag{2.53}$$

and the eigenvectors are given by:

$$\mathbf{x}_i = \mathbf{x}_{0i} + \sum_{j \neq i} \frac{\mathbf{x}_{0i}^{\mathrm{T}} \left([\delta K] \right) \mathbf{x}_{0j}}{\lambda_{0i} - \lambda_{0j}} \mathbf{x}_{0j} \tag{2.54}$$

The derivatives are easily obtained from these formulae. In the case of degenerate eigenvectors, the above formulae are no longer valid, and a more general degenerate perturbation theory should be considered.

Research on the derivative of degenerate eigenvectors has been an area of significant interest in recent years. Engineer have focused on the study of the so called *sensitivities*, that are simply the derivatives of eigenvalues and eigenvectors with respect to design parameters that make the matrix evolve. Degenerate eigenvalues are unavoidable in practice, and, for instance, appear in the calculation of the derivatives of the eigenvectors of the BCS Hamiltonian.

We sketch only here the main results obtained for the derivate of a degenerate eigenvector (for more details the reader is referred to Ref. [53, 54, 55, 56]). Let us assume without loss of generality that the first eigenvalue λ_1 is degenerate with multiplicity r. We define Φ as the matrix containing all the eigenvectors, Φ_1 as the matrix of the degenerate eigenvectors, and Φ_2 as the matrix containing the other vectors. With this definitions we have the trivial identity:

$$\Phi^{\mathrm{T}} K_0 \left(p \right) \Phi = \Lambda = \begin{bmatrix} \lambda_1 1_r & 0 \\ 0 & \Lambda_2 \end{bmatrix}, \tag{2.55}$$

It can be proved that the derivative of the degenerate eigenvectors ϕ_1 is :

$$\Phi_1' = \Phi_2 \left(\lambda_1 I - \Lambda_2 \right)^{-1} \Phi_2^{\mathrm{T}} D_j \Phi_1 \tag{2.56}$$

Knowing the derivative of the U and V matrices allows to measure the O_k observables of equation (2.40) and the stochastic minimization procedure is now well defined.

2.3.3 Correlated measurement minimization

One limitation of the stochastic minimization method, in our present implementation, is that the formulae obtained for the derivation of a determinant are not valid for the more general Pfaffian wavefunction, since there is no simple formula for the derivative of a Pfaffian (see equation (2.48)). Therefore, in the case of a Pfaffian Monte Carlo simulations, the gradients of the energy with respect to the variational parameters have to computed numerically. This task is very heavy and limits the minimization to a few parameters (about 10 parameters at most). Nonetheless, it is very difficult to get a precise estimation of a derivative of a curve obtained by a set of points that have error bars due to the Monte Carlo sampling. To overcome this problem, Umrigar has proposed [52] a correlated measurement method to extrapolate the energy, starting from a given set of variational parameters α, to the other parameters α' lying in the vicinity of α. The method is very simple, and consists in running a long simulation for the α parameters, book-keeping in the memory every accepted and rejected Monte Carlo moves. The mean-value of the energy of this simulation is given by:

$$\frac{\langle\psi|H|\psi\rangle}{\langle\psi|\psi\rangle} = \sum_{x,y} \frac{|\langle\psi|x\rangle|^2}{\langle\psi|\psi\rangle} \langle x|H|y\rangle \frac{\langle y|\psi\rangle}{\langle x|\psi\rangle} \tag{2.57}$$

The energy for a another set of parameter (and another wavefunction ψ') can be obtained by using the same run, if the statistics is large enough, by [3]:

$$\langle\psi'|H|\psi'\rangle = \sum_{x,y} |\langle\psi|x\rangle|^2 \left(\langle x|H|y\rangle \frac{\langle y|\psi'\rangle}{\langle x|\psi'\rangle} \frac{|\langle\psi'|x\rangle|^2}{|\langle\psi|x\rangle|^2} \right) \tag{2.58}$$

The normalization $\langle\psi'|\psi'\rangle$ also needs to be calculated:

$$\langle\psi'|\psi'\rangle = \sum_{x} |\langle\psi|x\rangle|^2 \left(\frac{|\langle\psi'|x\rangle|^2}{|\langle\psi|x\rangle|^2} \right) \tag{2.59}$$

This procedure was found to be very efficient when done on multiple computer nodes within parallel simulations. In these simulations, each of the computer node gives a value for the derivative that can be averaged to obtain a good approximation of the gradients.

2.3.4 Multi - Determinant/Pfaffian wavefunctions

The single determinant or Pfaffian wavefunction described previously breaks explicitly the original symmetries of the Hubbard or $t-J$ Hamiltonian. However, the true ground-states of the later Hamiltonian never breaks the corresponding symmetries when finite clusters are considered. The symmetry can be restored in the wavefunction by considering a superposition of variational functions that carry the order parameters:

$$|\psi\rangle = \sum_i \lambda_i |\phi_i\rangle \tag{2.60}$$

where $\{|\phi_i\rangle\}$ is a variational basis of determinants or pfaffians. The Hamiltonian matrix H_{ij} and the overlap matrix S_{ij} are defined as:

$$H_{ij} = \langle\psi_i|\hat{H}|\psi_j\rangle \tag{2.61}$$

$$S_{ij} = \langle\psi_i|\psi_j\rangle \tag{2.62}$$

---

[3] The method is however not applicable, for a reasonable statistics, when the parameters α' are too far from the initial parameter α.

The variational energy is given by the lowest eigenvalue of the eigen-system:

$$\sum_j H_{ij} c_j = E \sum_j S_{ij} c_j \tag{2.63}$$

The expectation value of other observables is given by:

$$\langle \hat{O} \rangle = \frac{\sum\limits_{ij} c_i^\dagger c_j O_{ij}}{\sum\limits_{ij} c_i^\dagger c_j S_{ij}} \tag{2.64}$$

where $O_{ij} = \langle \phi_i | \hat{O} | \phi_j \rangle$. Moreover, we can follow similar steps as in section 2.3.3 to calculate the overlap matrix S_{ij} and the matrix element O_{ij} :

$$\langle \psi_2 | \hat{O} | \psi_1 \rangle = \sum_x |\langle \psi_1 | x \rangle|^2 \left(\sum_y \langle x | O | y \rangle \frac{\langle y | \psi_1 \rangle}{\langle x | \psi_1 \rangle} \right) \frac{\langle x | \psi_2 \rangle}{\langle x | \psi_1 \rangle} \tag{2.65}$$

By running a simulation for ψ_1, we can generate the configurations $\{x\}$ obtained by a Metropolis algorithm with the probability $p = min(1, |\langle x | \psi_1 \rangle|^2)$, and the matrix element $\langle \psi_2 | \hat{O} | \psi_1 \rangle$ are then easily obtained through the above equation.

2.4 Optimization of the wavefunction : Lanczos Step

Once the energy of the wavefunction is satisfactorily optimized, we can systematically [57] improve the quality of the energy and of the variance by considering the extended wavefunction $|\psi'\rangle = \left(1 + \lambda \hat{H}\right) |\psi\rangle$. This procedure is similar to what is done in a Lanczos calculation, though we apply here only one step of the full Lanczos calculation. The wavefunction ψ' can be sampled by using the following relations:

$$\frac{\psi'_\alpha(x')}{\psi'_\alpha(x)} = \frac{\langle x' | (1 + \alpha H) | \psi \rangle}{\langle x | (1 + \alpha H) | \psi \rangle} = \frac{\psi(x')}{\psi(x)} \left(\frac{1 + \alpha E_{x'}}{1 + \alpha E_x} \right) \tag{2.66}$$

$\psi_\alpha(x')/\psi_\alpha(x)$ is the only necessary quantity that we need to perform the variational calculations. These calculations are however relatively heavy, and the cpu time for further Lanczos steps increases very fast, such that a two-Lanczos step calculation can only be done on small ≈ 20 site clusters. The parameter α is an additional variational parameter, and a very powerful method was proposed in Ref. [58] to find the optimal α for one Lanczos step calculations. The one lanczos step applied on the optimized variational function is a further test for the reliability of the method. Indeed, the variational results will certainly not be well converged if the energy changes significantly after applying one Lanczos iteration onto the optimized wavefunction.

2.5 Physical observables

The strength of variational calculations is certainly that it is straightforward to measure any correlations or observable with a given wavefunction. In particular, we can sample wavefunction on very large system sizes and measure therefore long-range correlations. Therefore, once the wavefunction is converged and the variational energy is minimized, we measure every physical observable $\hat{O}$ sandwiched by the variational wavefunction. We give here some order parameter example that we might be interested in:

- The magnetization of a coplanar magnetic order:

$$M = \frac{1}{N} \sum_i \left\| \frac{\langle \psi_{\mathrm{var}} | \mathbf{S}_i | \psi_{\mathrm{var}} \rangle}{\langle \psi_{\mathrm{var}} \mid \psi_{\mathrm{var}} \rangle} \right\| \tag{2.67}$$

- A vectorial spin chirality on nearest neighbor bonds:

$$\chi = \frac{1}{3N} \sum_{i,\alpha} \left| \frac{\langle \psi_{\mathrm{var}} | \left(\mathbf{S}_i \times \mathbf{S}_{i+a_\alpha} \right)^z | \psi_{\mathrm{var}} \rangle}{\langle \psi_{\mathrm{var}} \mid \psi_{\mathrm{var}} \rangle} \right| \tag{2.68}$$

- The amplitude of the singlet superconducting order parameter:

$$\Delta = \sqrt{\frac{1}{4N} \left| \lim_{r \to \infty} \sum_i \frac{\left\langle \psi_{\mathrm{var}} | \Delta^\dagger_{i,\alpha} \Delta_{i+r,\beta} | \psi_{\mathrm{var}} \right\rangle}{\langle \psi_{\mathrm{var}} \mid \psi_{\mathrm{var}} \rangle} \right|}, \tag{2.69}$$

  where

$$\Delta^\dagger_{i,\alpha} = c^\dagger_{i,\uparrow} c^\dagger_{i+a_\alpha,\downarrow} - c^\dagger_{i,\downarrow} c^\dagger_{i+a_\alpha,\uparrow}. \tag{2.70}$$

  The angular dependence of the real-space correlations can be extracted from the correlations.

2.6 Auxiliary-field Quantum Monte Carlo

Although the variational Monte Carlo procedure described above allows to implement in the wavefunction the long-range properties that might be relevant in the low-energy phase diagram, the short range physics cannot be tuned and controlled in the variational wavefunctions. Unfortunately, the short range physics will undoubtly play an important role in the variational energy, since the Hubbard and $t-J$ Hamiltonians are local theories. Therefore, some improvements of the wavefunction might still be prompted for. One further variational technique is the so-called Auxiliary-field Quantum Monte Carlo Method [59, 60, 61, 62, 63, 64, 65, 66, 67], which however suffers in the limit of large system sizes of the well known *quantum sign problem*. Moreover, this method is only valid for Hubbard theories, and cannot be applied to the $t-J$ models. This method will only be considered in Chapter 6, where the three band Hubbard model is considered.

Nevertheless, AFQMC is certainly a powerful technique. The main advantage of the techniques is first that it can deal with both real and complex wavefunctions, and second it can deal with non-collinear magnetism and twisted spin boundary conditions [59]. Finally, there is no special difficulty in AFQMC to measure the physical observables. We discuss here shortly some of the outcomes of this technique. In AFQMC, the following variational wavefunctions are considered:

$$\begin{aligned}
\psi_S^{(1)} &= e^{-\lambda K} e^{-\alpha V} \psi_{MF} && (2.71)\\
\psi_S^{(2)} &= e^{-\lambda' K} e^{-\alpha' V} e^{-\lambda K} e^{-\alpha V} \psi_{MF} && (2.72)\\
\psi_S^{(3)} &= e^{-\lambda'' K} e^{-\alpha'' V} e^{-\lambda' K} e^{-\alpha' V} e^{-\lambda K} e^{-\alpha V} \psi_{MF} && (2.73)\\
\psi_S^{(m)} &= e^{-\lambda_1 K} e^{-\alpha_1 V} ... e^{-\lambda_m K} e^{-\alpha_m V} \psi_{MF} && (2.74)
\end{aligned}$$

$|\psi_{MF}\rangle$ is the non-interacting wavefunction, and it is given by the slater determinant of the matrix ψ_{MF}, its columns being the single particle states. The matrix ψ_{MF} is a square matrix with size $N_e \times N_e$ when $|\psi_{MF}\rangle$ is a tight-binding slater determinant, and the matrix is rectangular with size $2N \times N_e$ when $|\psi_{MF}\rangle$ is a BCS state, where N is the number of sites of the lattice and N_e the number of particles. Moreover, K denotes the kinetic part of the Hamiltonian, and V denotes the on-site Hubbard interaction part. The parameters $\{\lambda_i\}_{i=1,m}$ and $\{\alpha_i\}_{i=1,m}$ are variational parameters. For large m, we recover the Suzuki-Trotter decomposition of the full Hamiltonian, and thus we expect the wavefunction ψ_S^m to converge to the true ground-state when m is sufficiently large. Unfortunately, the quantum sign problem becomes more severe when the number of iterations is increased.

The AFQMC method is based on the decoupling of the interacting V part, that maps the system to a free electronic problem coupled to fluctuating Ising fields. More formally, we apply the Hubbard-Stratanovitch transformation, and the Gutzwiller factor can be written in the possible following forms:

$$\begin{aligned}
e^{-\Delta\tau U n_{i\uparrow} n_{i\downarrow}} &= e^{-\Delta\tau U (n_{i\uparrow}+n_{i\downarrow})/2} \sum_{xi=\pm 1} \frac{1}{2} e^{\gamma x_i \left(n_{i\uparrow}-n_{i\downarrow}\right)} && (2.75)\\
e^{-\Delta\tau U n_{i\uparrow} n_{i\downarrow}} &= e^{-\Delta\tau U (n_{i\uparrow}+n_{i\downarrow}-1)/2} \sum_{xi=\pm 1} \frac{1}{2} e^{\gamma x_i \left(n_{i\uparrow}+n_{i\downarrow}-1\right)} && (2.76)
\end{aligned}$$

The former decoupling is real when $U > 0$ and the latter is real when $U < 0$. Therefore, it is possible to work with real matrices for both the repulsive ($U > 0$) or attractive ($U < 0$) Gutzwiller factor. Indeed, the Gutzwiller factor becomes attractive when a particle-hole transformation is applied for the down spin species. Such a transformation will be used to consider the BCS pairing wavefunction as one-body part in the AFQMC simulations. For clarity we describe below the method when the former decoupling is used. Moreover, γ is defined by : $\cosh(\gamma) = \exp(\Delta\tau\,|U\,|/2)$; s_i is a classical auxiliary Ising field configuration that takes the value $s_i = \pm 1$. These identities come from the more general identity that transforms any quadratic operator to a superposition of linear operators:

$$e^{-\frac{\Delta\tau}{2}\lambda\hat{v}^2} = \int_{-\infty}^{\infty} dx \frac{e^{-x^2/2}}{\sqrt{2\pi}} e^{x\sqrt{-\Delta\tau\lambda}\hat{v}} \tag{2.77}$$

We emphasize that the mapping (2.75) is not unique, as seen in equation (2.75), and the sign problem that can occur in AFQMC depends strongly on the choice of this mapping. The weight of the wavefunction ψ_m is therefore given by:

$$\langle\psi_m|\psi_m\rangle = \sum_{(s_{i_1})..(s_{i_{2m}})} \langle\psi_{MF}|e^{V(s_{i1})}e^{\lambda_1 K}...e^{V(s_{im})}e^{\lambda_m K}e^{\lambda_m K}e^{V(s_{i_{m+1}})}...e^{V(s_{i_{2m}})}|\psi_{MF}\rangle \tag{2.78}$$

where s_{i_1} is an Ising spin configuration on the lattice and the potential $V(u)$ is given by :

$$V_1(u) = \qquad exp\left(2\gamma\sigma\sum_i u_i n_{i\sigma}\right) \tag{2.79}$$

$$V_2(u) = \; exp\left(-\gamma\sum_i u_i\right) exp\left(2\gamma\sum_i u_i n_{i\sigma}\right) \tag{2.80}$$

depending on whether the attractive ($V_1(u)$) or repulsive ($V_2(u)$) Gutzwiller projection is used. In the former case, the Hubbard-Stratanovitch transformation maps the correlated problem on uncorrelated fermions with the spin degrees of freedom coupled to a fluctuating field, and in the latter case the charge degrees of the fermions are coupled to the field. The $V_1(u)$ and $V_2(u)$ operators are diagonal matrices. For instance $V_1(u)$ is given by:

$$V_1\left(u,\gamma\right) = diag\left(2\gamma u_1, \cdots, 2\gamma u_N, -2\gamma u_{N+1}, \cdots, -2\gamma u_{2N}\right) \tag{2.81}$$

Several properties of the Slater determinants are worth mentioning. For any pair of real non-orthogonal Slater determinants, $|\phi\rangle$ and $|\phi'\rangle$, it can be shown that their overlap integral is:

$$\langle\phi|\phi'\rangle = det\left(\Phi^T\Phi'\right) \tag{2.82}$$

The operation on any Slater determinants by any operator $\hat{B}$ of the form:

$$\hat{B} = \exp\left(\sum_{ij} c_i^\dagger U_{ij} c_j\right) \tag{2.83}$$

simply leads to another Slater determinant [68, 69, 70, 71, 64] :

$$\hat{B}|\phi\rangle = \phi_1^{\dagger\prime}\phi_2^{\dagger\prime}...\phi_M^{\dagger\prime}|0\rangle = |\phi'\rangle \tag{2.84}$$

with $\phi_m^\dagger = \sum_j c_{jm}^\dagger$ and $\Phi' = e^U \Phi$, where U is a square matrix whose elements are given by U_{ij} and $B = e^U$ is therefore an $N \times N$ square matrix as well. In conclusion, the operation of $\hat{B}$ on $|\phi\rangle$ simply involves multiplying an $N \times N$ matrix by an $N \times M$ matrix. This allows to apply the exponential of the kinetic term $e^{\lambda K}$ on the Salter determinant $|\psi_{MF}\rangle$. Furthermore, for two states $|L\rangle$ and $|R\rangle$ represented by Slater determinants L and R respectively, the single-particle right and left Green functions are written as :

$$G_{ij}^L \equiv \frac{\left\langle L \left| c_i^\dagger c_j \right| R \right\rangle}{\langle L | R \rangle} = \left[R \left(L^T R \right)^{-1} L^T \right]_{ij} \tag{2.85}$$

$$G_{ij}^R \equiv \frac{\left\langle L \left| c_i c_j^\dagger \right| R \right\rangle}{\langle L | R \rangle} = \delta_{ij} - \left[R \left(L^T R \right)^{-1} L^T \right]_{ij} \tag{2.86}$$

In order to evaluate all the expectation values of the observables, we generate a Monte Carlo sample by using the importance sampling with the following weight function :

$$\omega = det \left(\psi_{MF}^T e^{V(u_1)} e^{\lambda_1 K} e^{V(u_2)} e^{\lambda_2 K} ... e^{\lambda_2 K} e^{V(u_{2m-1})} e^{\lambda 1 K} e^{V(u_{2m})} \psi_{MF} \right) \tag{2.87}$$

where $\{u_i\}$ are the Ising spins of the different species $i = 1, .., 2m$ lying on the lattice. The Monte Carlo algorithm consists to update the Ising variables, from the old s_i to the new one s_i', the and the ratio $r = \omega'/\omega$ is calculated to determine whether to accept or reject the new configuration. In the process updating the spin, the Green function can be used to calculate very fast the ratio of the the weights r:

$$r = det \left(\mathbf{1} + G_L \Delta \right) \tag{2.88}$$

where $\Delta = \left(e^{V' - V} - \mathbf{1} \right)$ and the two states L and R (in the notations of equation (2.85)) that define G_L are :

$$L = \psi_{MF}^T e^{V(u_1)} e^{\lambda_1 K} e^{V(u_2)} e^{\lambda_2 K} ... e^{V(u_i)} \tag{2.89}$$

$$R = e^{\lambda_i K} ... e^{V(u_{2m-1})} e^{\lambda 1 K} e^{V(u_{2m})} \psi_{MF} \tag{2.90}$$

u_i is the spin species that is changed during the move. When a change of the spin of the corresponding species is accepted, the Green function is updated like :

$$G_L' = G_L - \frac{G_L \Delta \left(\mathbf{1} - G_L \right)}{1 + \left(\mathbf{1} - G_L \right) \Delta} \tag{2.91}$$

Moreover, Steve White and collaborators have proposed a very efficient way to carry on the simulations [62] by proposing moves successively for each of the species of spin, that allows for a fast sweep over all the site of the lattice and over all the species of spin. Finally, since the AFQMC is a non-interacting theory, Wick's theorem holds for one spin configuration, and the observables can be extracted from the Green function. Any expectation value of an observable $\hat{O} = \sum\limits_{ijkl} O_{ijkl} c_i^\dagger c_j^\dagger c_k c_l$ taken in a spin state $\mathbf{s} = (\mathbf{s}_1, ..., \mathbf{s}_{2m})$ is given by :

$$\langle\langle \hat{O} \rangle\rangle_s = \sum_{ijkl} O_{ijkl} (G'_{jk} G'_{il} - G'_{ik} G'_{jl}) \tag{2.92}$$

The average is then obtained by sampling the spin configurations :

$$\langle \hat{O} \rangle = \frac{\sum\limits_{\mathbf{s}} \langle\langle \hat{O} \rangle\rangle_s \omega(\mathbf{s})}{\sum\limits_{s} \omega_s} \tag{2.93}$$

The sign problem occurs when ω_s is not positive, or even worse when ω_s is complex. However, the phase of ω_s can be put in the observable:

$$\langle \hat{O} \rangle = \frac{\sum\limits_{\mathbf{s}} \Big(\langle\langle \hat{O} \rangle\rangle_s sign(\omega_s) \Big) |\omega(\mathbf{s})|}{\sum\limits_{s} sign(\omega_s) |\omega_s|} \tag{2.94}$$

The sign problem is nevertheless not entirely solved, since when the lattice becomes large the denominator is strongly fluctuating and $\sum\limits_{s} sign(\omega_s) \approx 0$. In this case the error bars become very large, and the simulation cannot lead to any converged observables.

One further outcome of AFQMC is that the Ising spin configuration generated during one simulation can also play the role of a good variational basis [72]. Therefore, for a given set of Ising configuration $S = \{\sigma_i\}$, and once the corresponding Hamiltonian matrix elements $H_{\lambda,\sigma}$ are known, we can find the variational energy by solving the eigenvalue problem $\sum\limits_{\tau \in S} H_{\sigma\tau} c_\tau = E \sum\limits_{\tau \in S} R_{\sigma\tau} c_\tau$, where c_τ are the eigenvectors, E is the variational energy, and $R_{\sigma\tau}$ is the overlap matrix of the states τ and σ.

2.6.1 Particle-hole transformation

To allow the possibility of a BCS slater determinant for ψ_{MF}, it is more convenient within the AFQMC frame to do a particle-hole transformation of the down spin species:

$$\begin{aligned} d_i &= c_{-i\downarrow}^\dagger \\ d_i^\dagger &= c_{-i\downarrow} \end{aligned}$$

After the transformation, the number of particles is written:

$$N_e = N + \sum_i \left\langle c_i^\dagger c_i - d_i^\dagger d_i \right\rangle \tag{2.95}$$

The Hubbard on-site repulsion also changes sign after the particle-hole transformation, and therefore the Gutzwiller operator applied on ψ_{MF} is written after the particle-hole transformation: $e^{+\sum\limits_i U n_{i\uparrow} n_{i\downarrow}}$. Finally, the particle-hole transformation also changes the hopping K matrix, which is now given by $K_{ij\uparrow\uparrow} = t_{ij}$ when i and j are nearest neighbors, and $K_{ij\downarrow\downarrow} = -t_{ij}$.

Chapter 3

t-J Model on the triangular lattice

3.1 Outline

We investigate the phase diagram of the $t - J$ Model on a triangular lattice using a Variational Monte Carlo approach. We use an extended set of Gutzwiller projected fermionic trial wavefunctions allowing for simultaneous magnetic and superconducting order parameters. We obtain energies at zero doping for the spin-1/2 Heisenberg model in very good agreement with the best estimates. Upon electron doping (with a hopping integral $t < 0$) this phase is surprisingly stable variationally up to $n \approx 1.4$, while the $d_{x^2-y^2} + id_{xy}$ order parameter is rather weak and disappears at $n \approx 1.1$. For hole doping however the coplanar magnetic state is almost immediately destroyed and $d_{x^2-y^2} + id_{xy}$ superconductivity survives down to $n \approx 0.8$. For lower n, between 0.2 and 0.8, we find saturated ferromagnetism. Moreover, there is evidence for a narrow spin-density wave phase around $n \approx 0.8$. Commensurate flux phases were also considered, but these turned out *not* to be competitive at finite doping. This work was published in PRB 73, 014519 (2006).

3.2 Superconductivity in the Cobaltites

After the RVB (Resonating Valence Bond) theory proposed by Anderson in 1987 [13] to explain the superconductivity of high T$_c$ cuprates, the field of frustrated magnetism has seen a number of very exciting developments. Frustrated magnets are systems in which the competition between the exchange integrals leads to a degeneracy for the corresponding classical model [1], and the original expectation was that quantum fluctuations might lead to a spin-liquid behavior, in analogy

---

[1] *Imagine that you are hosting a dinner with an odd number of people in the party.You quickly realize that it is impossible to seat every guest between two members of the opposite sex. This is hardly a calamity, of course.*, Schaak et al. [73]

with the Haldane gap of S=1 chains or S=1/2 two-leg ladders. The theoretical understanding of these properties is at best very primitive, and reliable numerical results are called for.

The recent discovery of superconductivity at low temperatures in the triangular $Na_xCoO_2.yH_2O$ layered compounds [74] is a very interesting event, since it may be the long sought low-temperature resonating valence bond superconductor, on a lattice which was at the basis of Anderson's original ideas on a possible quantum spin liquid state. $Na_xCoO_2.yH_2O$ consists of two dimensional CoO_2 layers separated by thick insulating layers of Na_2^+ ions and H_2O molecules. It is a triangular net of edge sharing oxygen octahedra; Co atoms are at the center of the octahedra forming a $2D$ triangular lattice.

Many interesting behaviors occur in $Na_xCoO_2.yH_2O$. In the high doping limit where charge conduction is present, the magnetic susceptibility shows a strange behavior. In a usual metal, the fraction of spins that can be field-aligned is small and shrinks to zero with decreasing temperature. In contrast, in Na_xCoO_2, the spin population that contributes to the susceptibility just equals the population of holes and stays the same when temperature falls. The susceptibility is therefore like the one of a Mott insulator. This ambivalence between the metallic behavior in the charge conduction and the insulator behavior in the spin susceptibility has led to call the high-doping phase a *spin-density wave metal*.

Equally puzzling at high doping is the fact that Na_xCoO_2 has a large thermo-power. In metals, an electrical (or charge) current involves the flow of electrons and is usually accompanied by an electronic heat current. The thermo-power measures the ratio of the heat to the charge current. In most metals the thermo-power is very small. A clue to understand the large thermo-power is that at low temperature $T = 2K$, the thermo-power is suppressed by a magnetic field. Measurements confirm that the vanishing of the thermo-power coincides with the complete alignment of the spins by the field. Consequently, this implies that the thermo-power is mostly coming from the spin entropy carried by the holes in the *spin-density wave metallic* phase.

Very interestingly, it was also observed that when the compound is cooled below $T = 4K$ [74], it becomes a superconductor when the doping is lying between $1/4 < x < 1/3$. Since then, there has been a tremendous activity in the scientific community to understand the mechanism of superconductivity in this compound, and in particular the role of the water molecules in the superconducting phase. An important point might be the fact that water molecules are screening the strongly fluctuating electrostatic potential of the Na ions from the charge carriers in the CoO_2 layers. Finally, a second question is related to the pairing symmetry in the superconducting phase and is still open. Takada et al. [74] speculated that $Na_xCoO_2.yH_2O$ might be viewed as a doped spin-1/2 Mott insulator. Based on LDA calculations [75], a simplified single band $t{-}J$ picture with negative t and electron doping was put forward [76, 77, 78]. Such systems might thus be the long-sought low-temperature resonating valence bond superconductor, on a

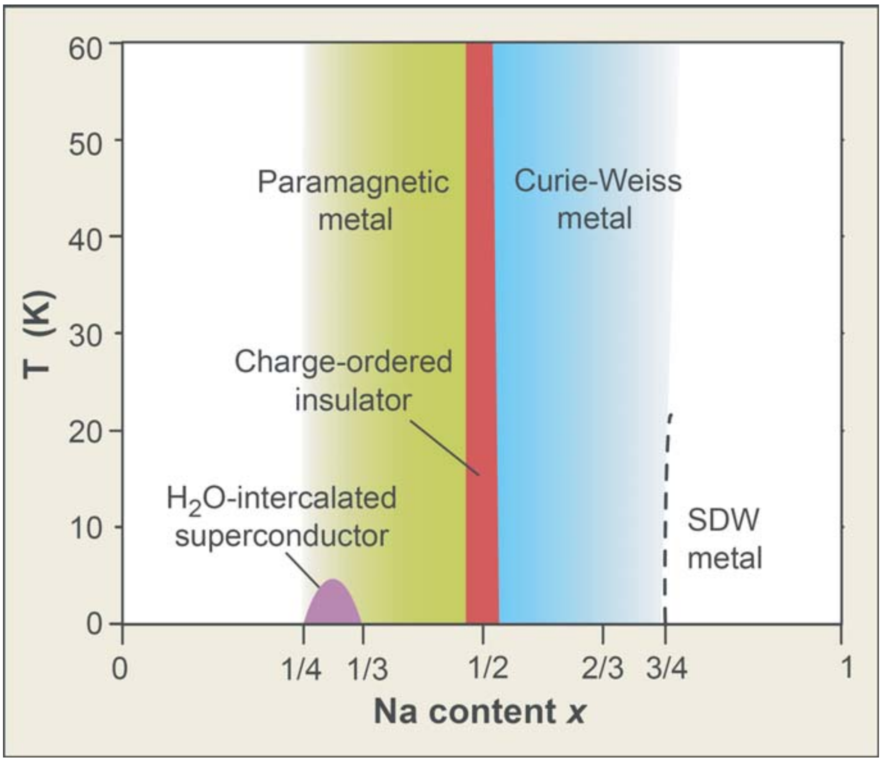

Figure 3.1: The figure was reproduced from Ref. [73]. Phase diagram of $Na_xCoO_2.yH_2O$. The compound is electronically doped. At half-filling ($x = 0$) the compound is unfortunately not stable and could consequently not be studied. The compound becomes superconducting for $x = \frac{1}{4} - \frac{1}{3}$. At high doping, the compound is a spin-density wave metal.

lattice which was at the basis of Anderson's original ideas on a possible quantum spin liquid state [13, 79].

For electrons lying on a triangular lattice, we expect that the interaction between the magnetic frustration and the charge degrees of freedom will be crucial. Indeed, in an insulating material, the on-site repulsion (U term of the Hubbard model) is relieved if each electron can point its spin antiparallel to that of its nearest neighbors. On most lattices (bipartite lattices), this can be done and leads to a state in which spins alternate up and down along each bond direction (the Néel state).

On a triangular lattice, however, the geometric arrangement frustrates such ideal regularity and the question regarding if magnetic order is stabilized at half-filling. Hence, at half-filling the lattice is a frustrated magnet: the competition between the exchange integrals leads to unsatisfied bonds. The resonating valence bond (RVB) scenario proposed by Anderson [14], which was found to be fruitful for describing the cuprates, was argued to be even more relevant in the geometry of the triangular lattice. The original expectation is that quantum fluctuations might lead to a spin-liquid behavior. However, at half-filling, it appears by now that the spin-1/2 triangular lattice has a three sublattice coplanar magnetic order [80,81,82,83]. Quantum fluctuations are nevertheless strong, and the sublattice magnetization is strongly reduced due to these fluctuations. It is therefore expected that the magnetism is fragile and quickly destroyed by doping and that a strong RVB instability is present.

By introducing doping, the problem is even much greater: the electrons/holes are free to hop between nearest neighbor sites and carry an electrical current. Does this itinerancy relieve the geometrical frustration? Does the doped quantum spin state have some particular conductivity? Can these electrons form Cooper pairs to produce superconductivity? These theoretical questions are relevant to understand experiments.

Indeed, RVB mean field theories [76,77,78] were used for the $t-J$ model, and $d_{x^2-y^2} + id_{xy}$ pairing was found over a significant range of doping. The same approach and questions that arise in the framework of the $t-J$ model on the square lattice are thus very relevant in the present frustrated lattice. The success of the variational approach for the square lattice suggests to investigate the same class of variational wavefunctions for the triangular one.

We propose in this chapter to study the $t-J$ model within the framework of the Variational Monte Carlo (VMC) method, which provides a variational upper bounds for the ground state energy. In contrast to mean-field theory, it has the advantage of exactly treating the no double-occupancy constraint. VMC using simple RVB wavefunctions has been used for the triangular lattice [84] and it was found that $d_{x^2-y^2} + id_{xy}$ superconductivity is stable over a large range of doping. However, in the previous study the fact that the $t-J$ is magnetically ordered at half-filling was not taken into account. We expect that the frustration in the triangular lattice may lead to a richer phase diagram and to many different instabilities. We thus propose here to study extended wavefunctions containing at the same time magnetism, flux phase and RVB instabilities, in a similar spirit as for the square lattice [33, 32], in order to study in detail the interplay between frustrated magnetism and superconductivity. Given the non-collinear nature of the magnetic order parameter compared to the case of the square lattice, the task is however much more complicated. We thus present in this work a general mean-field Hamiltonian which takes into account the interplay between magnetic, RVB and flux-phase instabilities. The resulting variational wavefunction is sampled with an extended VMC, which uses *Pfaffian* updates rather than the usual determinant updates. We show that the interplay between the different instabilities leads to a faithful representation of the ground-state at half-filling, and we also find good variational energies upon doping. To benchmark our wavefunction, we carry out exact diagonalizations on a small 12 sites cluster and compare the variational energies and the exact ones. Finally, a commensurate spin-density wave is considered, and is shown to be relevant for the case of hole doping.

The outline of the chapter is as follows: in Sec. 3.3 we present the model and the numerical technique. In Sec. 3.4 we show the variational results both for the case of hole and electron doping. Finally Sec. 3.5 is devoted to the summary and conclusions.

3.3 Variational Monte Carlo

We study in this chapter the $t-J$ model on the triangular lattice defined by the Hamiltonian (1.4). In order to simplify the connection to the Cobaltates we set $t = -1$ in the following and present the results as a function of the electron density $n \in [0, 2]$, half-filling corresponding to $n = 1$. $n > 1$ corresponds to a $t-J$ model at $\tilde{n} = 2 - n$ for $t = 1$, by virtue of a particle-hole transformation.

In the first part of this section, we emphasize on the method to construct a variational wavefunction containing both superconductivity and non-collinear magnetism. The wavefunction allows to consider 3-sublattice magnetism, however, since the latter wavefunction is restricted to a 3 site supercell, we briefly comment on a second simpler variational wavefunction type, which allows to describe commensurate spin order.

In the second part of the section, we define the relevant instabilities and the corresponding order parameters.

3.3.1 Variational wavefunction

In order to study this model we use a variational wavefunction built out of the ground state of the mean-field like Hamiltonian (1.23). H_{MF} contains at the same time BCS pairing ($\mathbf{\Delta}_{i,j} = \{\Delta_{\sigma,\sigma'}\}_{i,j}$), an arbitrary external magnetic field ($\mathbf{h}_i$), and arbitrary hopping phases ($\theta^{\sigma}_{i,j}$), possibly spin dependent. These variational

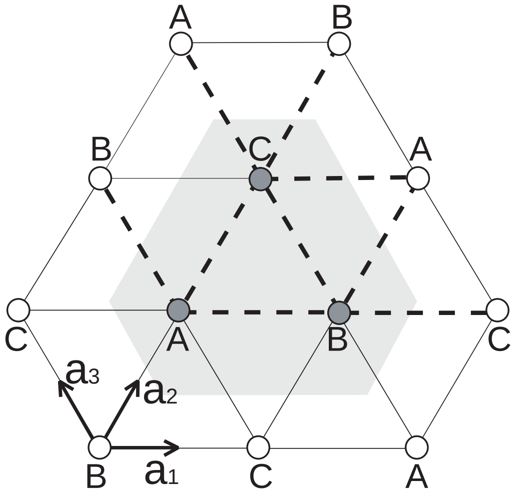

Figure 3.2: 3-site supercell of the triangular lattice. The onsite magnetic variational parameters can vary independently on each of the site A,B and C of the supercell. The BCS pairing as well as the flux vary independently on each of the different dashed bonds.

parameters are unrestricted on the A, B, C sites and the corresponding bonds of a 3-site supercell, as shown in Fig. 3.2. We allow both singlet ($\mathbf{\Delta}_{i,j}^{(S=0)}$) and general triplet ($\mathbf{\Delta}_{i,j}^{(S=1)}$) pairing symmetries to be present. They correspond to choosing:

$$\begin{aligned} \mathbf{\Delta}_{i,j}^{(S=0)} &= \begin{pmatrix} 0 & \psi_{i,j} \\ -\psi_{i,j} & 0 \end{pmatrix} \\ \mathbf{\Delta}_{i,j}^{(S=1)} &= \begin{pmatrix} \psi_{i,j}^2 & \psi_{i,j}^1 \\ \psi_{i,j}^1 & \psi_{i,j}^3 \end{pmatrix} \end{aligned} \tag{3.1}$$

Since H_{MF} is quadratic in fermion operators it can be solved by a Bogoliubov transformation. In the most general case considered here, this gives rise to a 12×12 eigenvalue problem, which we solve numerically. We then find the ground state of H_{MF}

$$|\psi_{MF}\rangle = \exp\left\{ \sum_{i,j,\sigma_i,\sigma_j} a_{(i,j,\sigma_i,\sigma_j)} c_{i\sigma_i}^\dagger c_{j\sigma_j}^\dagger \right\} |0\rangle \tag{3.2}$$

Here $a_{(i,j,\sigma_i,\sigma_j)}$ are numerical coefficients. Note that $|\psi_{MF}\rangle$ has neither a fixed number of particles due to the presence of pairing, nor a fixed total S^z due to the non-collinear magnetic order. Thus in order to use it for the VMC study we apply to it the following projectors: $\mathcal{P}_N$ which projects the wavefunction on a state with fixed number of electrons and $\mathcal{P}_{S^z}$ which projects the wavefunction on the sector with total $S^z = 0$. Finally we discard all configurations with doubly occupied sites by applying the complete Gutzwiller projector $\mathcal{P}_\mathcal{G}$. The wavefunction we use as an Ansatz for our variational study is thus:

$$|\psi_{\text{var}}\rangle = \mathcal{P}_\mathcal{G}\mathcal{P}_{S^z}\mathcal{P}_N\,|\psi_{MF}\rangle = \mathcal{P}_\mathcal{G}\mathcal{P}_{S^z}\left\{\sum_{i,j,\sigma_i,\sigma_j} a_{(i,j,\sigma_i,\sigma_j)}c^\dagger_{i\sigma_i}c^\dagger_{j\sigma_j}\right\}^{N/2}|0\rangle \tag{3.3}$$

Although the wavefunction (5.8) looks formidable, it can be reduced to a form suitable for VMC calculations. Using

$$\langle\alpha| = \langle 0|\, c_{k_1,\sigma_1}...c_{k_N,\sigma_N}, \tag{3.4}$$

we find that

$$\begin{aligned} \langle\alpha \mid \psi_{\text{var}}\rangle &= P_f\left(\mathbf{Q}\right) \\ Q_{i,j} &= a_{(k_i,k_j,\sigma_i,\sigma_j)} - a_{(k_j,k_i,\sigma_j,\sigma_i)} \end{aligned} \tag{3.5}$$

where $P_f(\mathbf{Q})$ denotes the *Pfaffian* of the matrix $\mathbf{Q}$. Using this last relation, the function (5.8) can now be evaluated numerically using a Monte Carlo procedure with Pfaffian updates, as introduced in Ref. [47]. In the particular case where $a_{k,l,\uparrow,\uparrow} = a_{k,l,\downarrow,\downarrow} = 0$ and at $S^z = 0$ (this happens if the BCS pairing is of singlet type *and* the magnetic order is collinear), the Pfaffian reduces to a simple determinant, and the method becomes equivalent to the standard Variational Monte Carlo [42] technique.

The above mean field Hamiltonian and wavefunction contain the main physical ingredients and broken symmetries we want to implement in the wavefunction. In order to further improve the energy and allow for out of plane fluctuations of the magnetic order we also add a nearest-neighbor spin-dependent Jastrow [85] term to the wavefunction:

$$\mathcal{P}_\mathcal{J} = \exp\left(\alpha\sum_{\langle i,j\rangle} S^z_i S^z_j\right), \tag{3.6}$$

where α is an additional variational parameter. Our final wavefunction is thus:

$$|\psi_{\text{var}}\rangle = \mathcal{P}_\mathcal{J}\mathcal{P}_{S^z}\mathcal{P}_N\mathcal{P}_\mathcal{G}\,|\psi_{MF}\rangle \tag{3.7}$$

When $\alpha < 0$ the Jastrow factor favors all configurations which belong to the ground state manifold of a classical Ising antiferromagnet on the triangular lattice. Such a manifold is exponentially large [86], and this Jastrow factor thus provides a complementary source of spin fluctuations.

In what follows we use the wavefunction (3.7) directly for the VMC, but we also examine improved wavefunctions with respect to (3.7) that can be obtained by applying one or more Lanczos steps [57, 45, 58]:

$$|1Ls\rangle = (1 + \lambda H_{t-J})\,|\psi_{\text{var}}\rangle \tag{3.8}$$

with optimized [87] λ. Since the calculation of Lanczos step wave functions beyond the first step is very time consuming, most of the results we will present here were obtained using a single Lanczos step.

In the following, to clearly indicate which wavefunction we use, we will denote them in the following way: MF / J / nLs, where MF denotes the fields present in the mean-field like Hamiltonian H_{MF}, J is present if we use the Jastrow factor, n Ls denotes the presence and the number of Lanczos steps applied on top of the bare wave function.

As usual with the VMC procedure, these general wave functions are now used to minimize the expectation value of the total energy $\langle H_{t-J}\rangle$ by changing the variational parameters. We used a correlated measurement technique [52, 33, 32] combined with parallel processing to smoothen the energy landscape and use a steepest-descent type routine to locate the minimum of energy. We then define the *condensation energy* e_c of the optimal wave function as

$$e_c = e_{\text{var.}} - e_{\text{Gutzwiller}}, \tag{3.9}$$

where $e_{\text{Gutzwiller}}$ is the energy of the Gutzwiller wave function, i.e. the fully projected Fermi sea at zero magnetization. In some cases we had to keep a small BCS pairing field to avoid numerical instabilities. Let us note that the linear size of the $\mathbf{Q}$ matrix is twice as large as in the simpler case of determinantal update VMC. Therefore our largest 108 sites cluster with Pfaffian updates corresponds roughly to a 200 sites cluster using standard updates.

3.3.2 Commensurate order

Since the mean-field Hamiltonian (1.23) is restricted to a 3 site supercell, we investigated also a second class of mean-field Hamiltonians based on collinear commensurate structures, which are not contained in the previous Hamiltonian. For this type of phase, we used a simpler mean-field ansatz along the lines of Ref. [32]. The mean-field Hamiltonian written in k-space is

$$H_{SDW} = \sum_{k,\sigma}\Big(\left(\epsilon_k - \mu\right)c^\dagger_{k\sigma}c_{k\sigma} + f(Q,\sigma)c^\dagger_{k+Q\sigma}c_{k\sigma}\Big) + \sum_k\Big(\Delta_k c^\dagger_{k\uparrow}c^\dagger_{-k\downarrow} + h.c.\Big), \tag{3.10}$$

where k does run over the Brillouin zone of the original triangular lattice, ϵ_k is the dispersion of the free electron Hamiltonian, and Δ_k is the Fourier transform of $\Delta_{i,j}$. Depending on $f(Q,\sigma)$, the ground state of the Hamiltonian is a commensurate charge density wave ($f(Q,\sigma) = f(Q)$) or a spin-density wave ($f(Q,\sigma) = \sigma f(Q)$).

At half-filling, we considered also several commensurate flux phases with $2\pi\times\frac{q}{p}$ flux per plaquette, using the Landau gauge [2] with $p \in \{2,\dots,10\}$ and $q < p$.

---

[2] H_{MF} is gauge invariant, however the gauge plays a non trivial role in the projected wave-

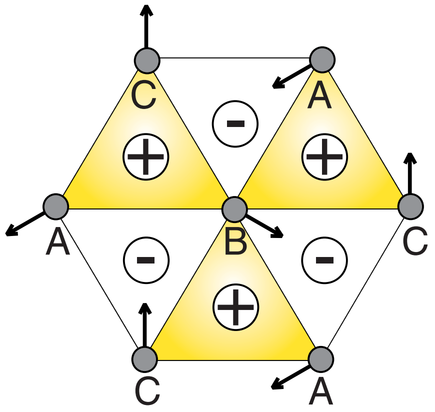

Figure 3.3: The variational parameters $\mathbf{h}_i$ for the coplanar 120° antiferromagnetic order. The spins lie in the $x - y$ plane. The z-component of the vector chirality (± 1) on each triangular plaquette forms a staggered pattern.

The one with the lowest energy was found to be the $q = 1, p = 4$, as predicted theoretically [88], giving an energy close to the simple $d_{x^2-y^2} + id_{xy}$ wavefunction. Upon doping however the energy of such commensurate flux phases are rapidly much worse than the energies of our best wave functions. The main reason for this poor performance upon doping is the rather bad kinetic energy of these wave functions.

3.3.3 Characterization of the encountered instabilities

By minimizing all the variational parameters of the mean-field Hamiltonians (1.23) and (3.10) on a 12 and a 48 site lattice, we find that the relevant instabilities present at the mean field level consists of:

- a 120° coplanar antiferromagnetic order (AF), represented in Fig. 3.3.
- a staggered spin flux phase instability (SFL) with:

$$\begin{aligned} \theta_{i,i+a_1,\sigma} &= \theta\sigma \\ \theta_{i,i+a_2,\sigma} &= -\theta\sigma \\ \theta_{i,i+a_3,\sigma} &= \theta\sigma. \end{aligned}$$

These bond phase factors correspond to a spin current in the z direction which is staggered on elementary triangles of the triangular lattice. This

---

function. Indeed, the kinetic energy of the projected wavefunction depends on the chosen gauge. One cannot exclude that another choice of gauge could lead to a better wavefunction.

instability follows rather naturally, since the 120° antiferromagnetic state itself already displays the same staggered spin currents $(\mathbf{S}_i \times \mathbf{S}_j)^z$ on the nearest neighbor bonds (see Fig. 3.3). The effect of this instability was rather small and visible only at half-filling.

- a translationally invariant superconducting phase with $d_{x^2-y^2} + id_{xy}$ singlet pairing symmetry (d^+), as well as the $d_{x^2-y^2} - id_{xy}$ (d^-). We have also looked extensively for triplet pairing for both electron and hole dopings and low $J/|t| \leq 0.4$ on a 48 site cluster, but with no success. The minimum energy was always found for singlet pairing symmetry.
- a ferromagnetic state with partial or full polarization (F),
- a commensurate collinear spin-density wave [89] (SDW) instability with wavevector $\mathbf{Q}_N = (\pi, -\pi/\sqrt{3})$.

3.3.4 Short-Range RVB wavefunction

Short-range RVB wave-functions were also shown to be good Ansatz for the triangular lattice [90]. Such wave-functions are written in terms of dimers:

$$|\psi_{RVB}\rangle = \prod_{\{C\}} \prod_{k,l=1}^{N} |[k,l]\rangle \tag{3.11}$$

where the product is done over all possible paving C of the lattice with nearest-neighbor dimers $[i,j]$:

$$|[k,l]\rangle = \frac{1}{\sqrt{2}} \left(|\uparrow_k \downarrow_l\rangle - |\downarrow_k \uparrow_l\rangle \right) \tag{3.12}$$

As a matter of fact, such wavefunctions, although they were successful to describe the triangular lattice at half-filling [90], are rather difficult to handle in the present representation and it is not convenient to improve the variational subspace by including long-range valence bonds. Moreover, such wavefunction in the present form cannot be doped easily with additional holes or electrons.

Indeed, when introducing doping, it is more convenient to represent a spin state like the wavefunction (3.11) by a projected BCS wavefunction. As an example, let us consider a nearest-neighbor pairing function that connects nearest neighbor sites in the lattice. It is clear that the more general projected BCS state is written as the sum of all possible partitions of the N-site lattice into singlets $[R_i, R_j]$ and the amplitude of a given partition is provided by the Pfaffian of the matrix $a_{ij} = f_{ij} - f_{ji}$, where f_{ij} was defined in equation (2.22):

$$\begin{aligned} |p - BCS\rangle = \sum_{R_1,\ldots,R_N} \sum_{P(1,..,N)} (-1)^{(P)} \left(f(R_{p(1)}, R_{p(2)}) - f(R_{p(2)}, R_{p(1)}) \right) \\ \ldots \left(f(R_{p(N-1)}, R_{p(N)}) - f(R_{p(N)}, R_{p(N-1)}) \right) c^\dagger_{R_1} \ldots c^\dagger_{R_N} |0\rangle \end{aligned} \tag{3.13}$$

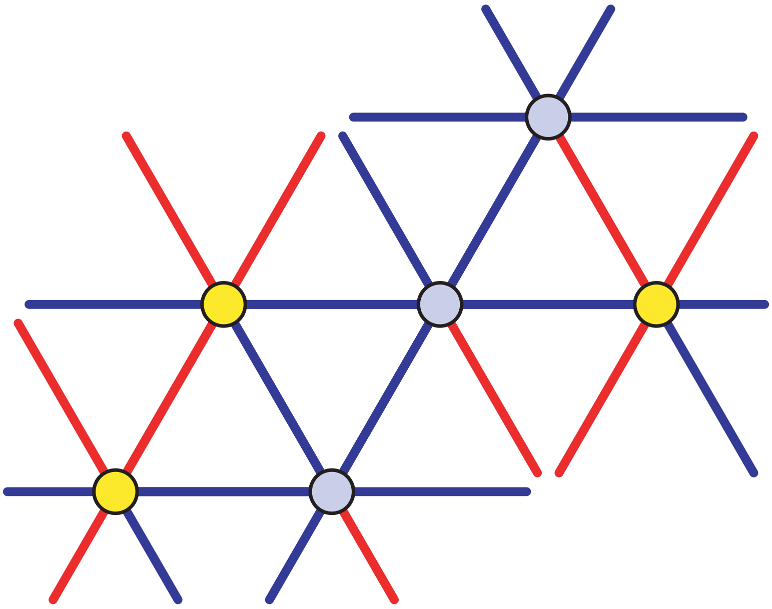

Figure 3.4: The symmetry of the nearest-neighbor gap function Δ_{ij} of the $|p-BCS\rangle$ wavefunction that corresponds to the short-range RVB $|\psi_{RVB}\rangle$. Blue (red) bonds indicate a negative (positive) Δ_{ij}. The unit-cell of the $|p-BCS\rangle$ wavefunction is 2×1, and the white (blue) circles show the A (B) sublattice. When the $|p-BCS\rangle$ wave-function is combined with the Néel magnetic state, the unit-cell contains 6 sites.

.

The sum is running over all the permutation P of the indices $(1...N)$. Remarkably, as proved by Kasteleyn [91], in *planar lattices*, namely the triangular lattice, the square lattice, and the Kagomé lattice, it is possible to choose the phase of the function f_{ij} so that the terms in the sum have all the same sign. In such a case, the projected BCS wavefunction exactly reproduces the short-range RVB state, since the amplitude of each nearest-neighbor singlets is the same.

A recent progress has been made in this direction recently by S.Sorella and collaborators [92], where an explicit mapping of the short-range RVB wavefunction on a simple projected BCS wavefunction $|p-\psi_{BCS}\rangle$ has been done for the limit $-\mu/2 \gg |\Delta_{ij}|$. Indeed, it was shown that the short range RVB state $|\psi_{RVB}\rangle$ is equivalently described by the projected BCS wave function $|p-\psi_{BCS}\rangle$, with a special choice of the variational parameters Δ_{ij} (see Fig. 3.4), for the special case of planar lattices [91]. In the present work, we propose to consider the simple projected BCS wavefunction with the symmetry of Δ_{ij} given in Fig. 3.4. We will denote such a wavefunction by RVB when considered alone, or by RVB/J when the nearest-neighbor Jastrow is also taken into account.

3.3.5 Order parameters

In order to characterize the phases described by the optimal wave functions after projection, we have calculated the the planar magnetism 2.67, the spin chirality operator 2.68 and the long-range pairing correlations 2.69.

3.4 Results and discussion

3.4.1 Half-filling

We consider in this section the Heisenberg model (which is the limit of the $t-J$ model at half-filling, up to a constant). The comparison with the large body of existing results for the Heisenberg model allows us to benchmark the quality of our wavefunction.

Let us first briefly discuss the symmetry of the variational parameters at half-filling. The variational magnetic field minimizes the energy for the two degenerate 120° configurations. We found that the BCS pairing symmetry in the presence of AF order is of d^+ type, whereas the d^-, the $d_{x^2-y^2}$ and the d_{xy} pairings have close but higher energies. Finally, a staggered spin flux variational order improves a little bit the energy. Interestingly, this latter variational order is present in the ground state of the classical Heisenberg model. However, this instability was only relevant at half-filling, and the energy gain when $\delta > 0$ is not significant. Finally, we find that the two-sublattice RVB pairing accommodates very well with the Néel wavefunction and leads to the best variational wavefunction at half-filling. The various energies for these wavefunctions are shown in Fig. 3.5. The $AF{+}RVB/J$ wavefunction is thus the best approximation, within our variational space, of the ground state of the Heisenberg model. We compare its energy with other estimates of the ground state energy in the literature (see Fig. 3.5 and Table 3.1). The mixture of AF and d^+ or RVB instabilities is improving a lot the energy, and our wavefunction has significantly lower energies than the simple d^+ wavefunction, and has energies very close to the best ones available. More precisely, we find in the thermodynamic limit an energy per site of $e = -0.54J$ for our variational wavefunction. A summary of the energies and of the 120° magnetization for the Heisenberg model are given in Table 3.1 and in Fig. 3.5.

Inspection of these results shows that our wavefunction has in the thermodynamic limit an energy only $0.005J$ higher than the estimates of more sophisticated, but restricted to the undoped case, methods [82]. Indeed, these latter methods use pure spin variational wavefunction as a starting point, restoring quantum fluctuations with the so-called fixe node approximation within the Green function's Monte Carlo algorithm.

Since our variational wavefunction already gives an excellent energy it would be interesting to check how the fixe node methods used to improve the energy starting with a much cruder variational starting point would work with our vari-

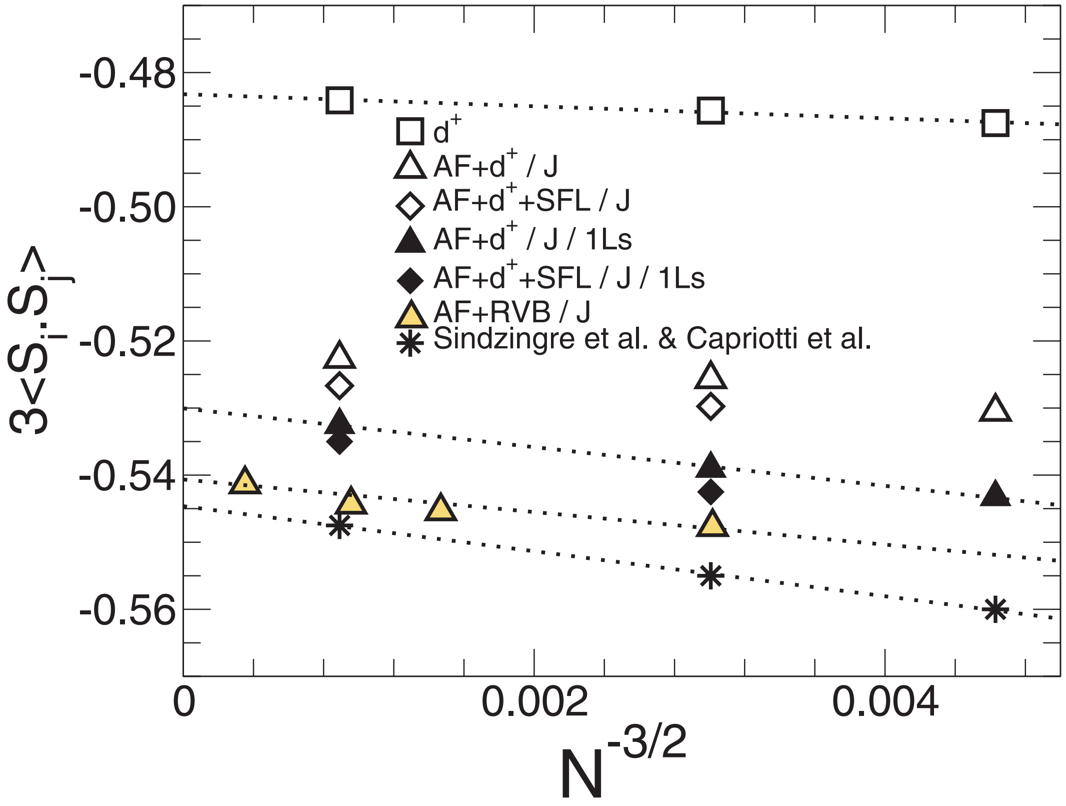

Figure 3.5: Energy per site $e = 3\langle \mathbf{S}_i \cdot \mathbf{S}_j \rangle$ of the different variational wave functions for the Heisenberg model versus the system size $N^{-3/2}$, with $N = 36, 48, 108$ sites. Ordered by increasing condensation energy we find: d^+ (open squares), $AF + d^+/J$ (open triangles), $AF + d^+ + SFL/J$ (open diamonds), $AF + d^+/J/Ls$ (full triangles) and the $AF + d^+ + SFL/J/Ls$ (full diamonds), and finally our best variational Ansatz $AF+RVB/J$ (yellow triangles). The stars are the best estimates of the ground state energy available in the literature [90,82].

Table 3.1: Comparison of the average energy $3\langle S_i \cdot S_j \rangle$ and the average magnetization M_{AF} for the Heisenberg model ($t-J$ model at half-filling) in different recent works for the 36 site cluster and the extrapolation to the thermodynamic limit. The energy and the sublattice magnetization are measured for our wavefunctions at half-filling on a 36 cluster with Periodic/Antiperiodic boundary conditions. Data extrapolated to the thermodynamic limit are also shown.

	$\langle 3S_i \cdot S_j \rangle$	M_{AF}
36 site lattice		
$AF + d^+ + SFL/J/1Ls$	-0.543(1)	0.38
Capriotti et al. [82]	-0.5581	0.406
exact diag [93,81]	-0.5604	0.400
$\infty \times \infty$		
$AF + d^+ + SFL/J$	-0.532(1)	0.36
RVB [92]	$-0.5357(1)$	
RVB/FN [92]	$-0.53989(3)$	0.162(3)
spin-wave results [82]	-0.538(2)	0.2387
$AF + RVB/J$	$-0.540(1)$	0.27(1)
Capriotti et al. [82]	-0.545(2)	0.205(10)

ational wavefunction and which energy it would give. We leave this point for future investigation however [3].

Our wavefunction shows a reduced but finite magnetic order that survives in the triangular Heisenberg antiferromagnet (THA). The 120° magnetization of our wavefunction is reduced by the BCS pairing down to 54% of the classical value (see Fig. 3.11) which is somewhat larger than the spin-wave result. Thus in addition to having an excellent energy, our wavefunction seems to capture the physics of the ground state of the Heisenberg system correctly. Let us note that the BCS order of the wavefunction is destroyed by the full Gutzwiller projector at half-filling. So, despite the presence of a variational superconducting order parameter, the system is of course not superconducting at half filling. Somehow the BCS variational parameter helps to form singlets, which reduces the amplitude of the AF order. This is very similar to what happens for the $t-J$ model on the square lattice: the inclusion of a superconducting gap decreases the energy and decreases also the magnetization from $M \approx 0.9$ down to $M \approx 0.7$, which is slightly larger than the best QMC estimates ($M \approx 0.6$, see Refs. [32,16]). Thus the wavefunction mixing magnetism and a RVB gap seem to be interesting variationally, both in

---

[3] It is worth noting that our wavefunction, which supports Néel magnetism, is a complex function. Since the fixe node approximation deals only with real functions, the so-called fixe phase approximation should be used.

the square and triangular lattice, to restore spin fluctuations that were frozen in the pure classical magnetic wavefunction. For the triangular lattice, the present work is the first attempt to reproduce the magnetic order in the THA in terms of a fermionic representation, which gives results in good agreement with other methods. The great advantage of this approach is of course that the fermionic language allows to directly consider the case of hole and electron doping in the AF background, which is the case we consider in the following sections.

3.4.2 Electron doping: $n \in [1, 2]$

Very few results exist away from half-filling, so in order to have a point of comparison for our variational approach we will compare it with exact diagonalizations on very small clusters. Having ascertained that our wavefunction is indeed in good agreement with the exact results on a small cluster, we can then use it with confidence to describe much larger systems and extract the physics of the thermodynamic limit.

Therefore, we start by comparing on a 12 site cluster different wavefunctions with the exact-diagonalization results for the case of electron doping (see Fig. 3.6), since larger lattices are not readily available. Interestingly, it was found that even with only 2 Lanczos steps on our best wavefunction ($AF + d^+/J$) the energy has almost converged to the exact ground state energy at half-filling. We find that at half-filling, the 2-Lanczos step applied on the $AF + d^+/J/2Ls$ wavefunction for a small 12-site cluster gives an energy per site $e = -0.6051(5)$, which is close to the exact result obtained by Lanczos $e = -0.6103$.

Note that small system size is the worst possible case for a VMC method since the simple variational wavefunction is not expected to reproduce well the short distance correlations, as we fix the long-range magnetic correlations in our variational ansatz by imposing an on-site magnetic field, but we do not introduce short range corrections. Variational Monte Carlo instead focus on the long distance properties, which will become dominant in the energy as the lattice size increases. Nevertheless, the short range correlations contributes significantly to the energy on small lattices. One can thus expect on general grounds the energies to become increasingly good as the system size increases, provided that the correct long range order has been implemented in the wavefunction. The Lanczos iterations allow to correct this local structure of the wavefunction. Here we see that by changing this local structure our wavefunction is converging very fast to the ground state. This is a good indication that even away from half filling our wavefunction is quite efficient in capturing the physics of the system. Actually, the variance of the energy per site σ^2 reaches its maximum value for doping $x = \frac{1}{3}$ ($\sigma^2 = 0.006$), but applying one Lanczos step reduces drastically the variance: $\sigma^2 = 0.0004$. Let us now use our wavefunction to describe large systems away from half filling. We now focus on a 108 site cluster, which is the largest cluster we can treat with a reasonable effort. We have first measured

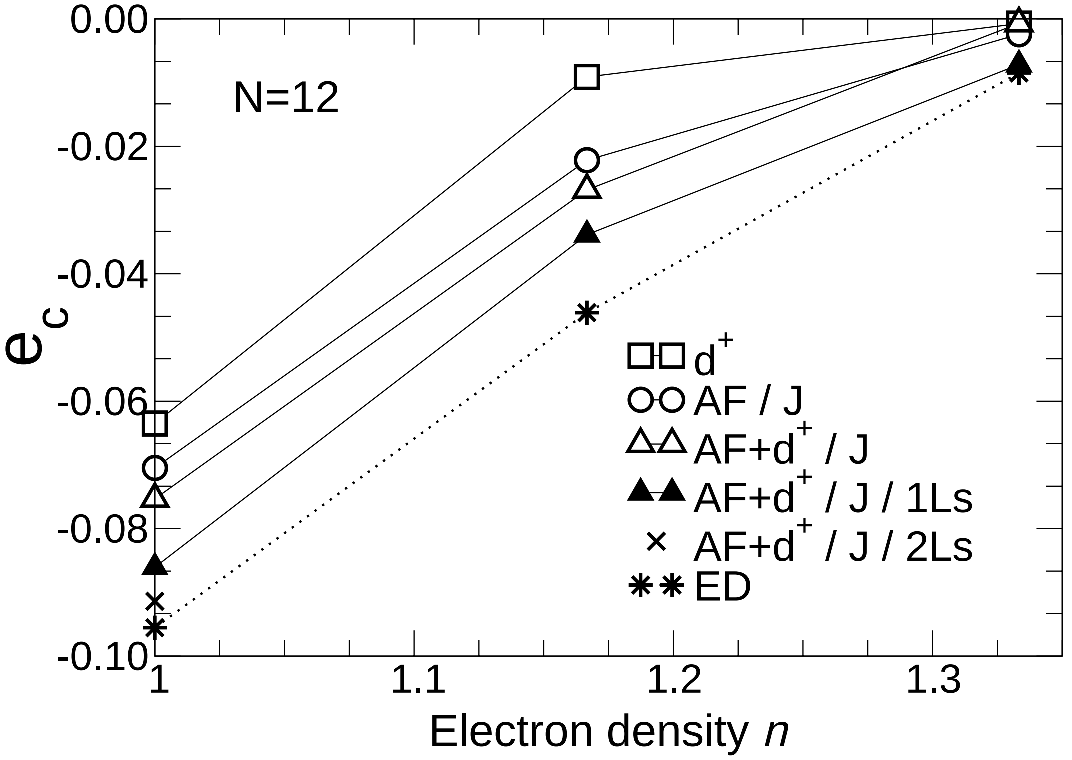

Figure 3.6: Condensation energy per site versus the electron doping for a 12 site cluster for the different variational wavefunctions. We have done exact diagonalization (ED) for a 12 sites cluster with same periodic boundary conditions.

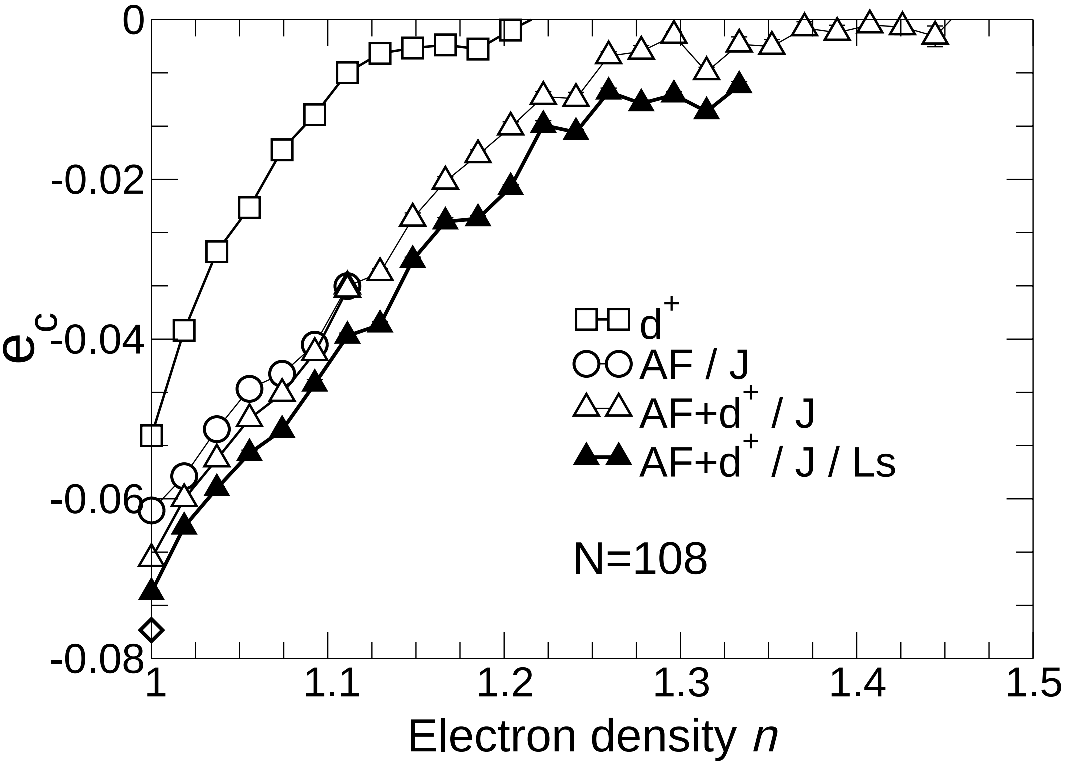

Figure 3.7: Condensation energy per site e_c versus electron doping for the 108 site lattice. We show different wavefunctions and also the best estimate in the literature [82] at half-filling (open diamond).

the condensation energy per site (see Fig. 3.7) for different types of instabilities.

Very interestingly, the AF/J is even better than a simple $d_{x^2-y^2} + id_{xy}$ RVB state. Moreover, the RVB order only weakly increases the condensation energy in presence of the antiferromagnetic background ($AF + d^+/J$). This suggests that superconductivity is only weakly present in the $t-J$ model when $n > 1$ which is also confirmed by the measurement of the superconducting gap (see Fig. 3.9). The RVB/J wavefunction, although it allows to recover a very good variational energy at half-filling, is not stabilized in the electron doping side of the phase diagram (see Fig. 3.8). The superconducting order of our best wavefunction is approximately 4 times smaller in amplitude and in range of stability than the d-wave pairing in a 10×10 *square* lattice with the same boundary conditions. For electron doping $\delta > 0.04$ we find that the d^+ BCS pairing symmetry has the same energies as the d^- one, and also as the wavefunctions with $d_{x^2-y^2}$ and d_{xy} pairings.

Very strikingly, the 120° magnetic order parameter is surviving up to high doping $\delta = 0.4$, see Fig. 3.11. Long-range magnetic order at finite doping is potentially caused by a limitation of the VMC method, since it is not possible in

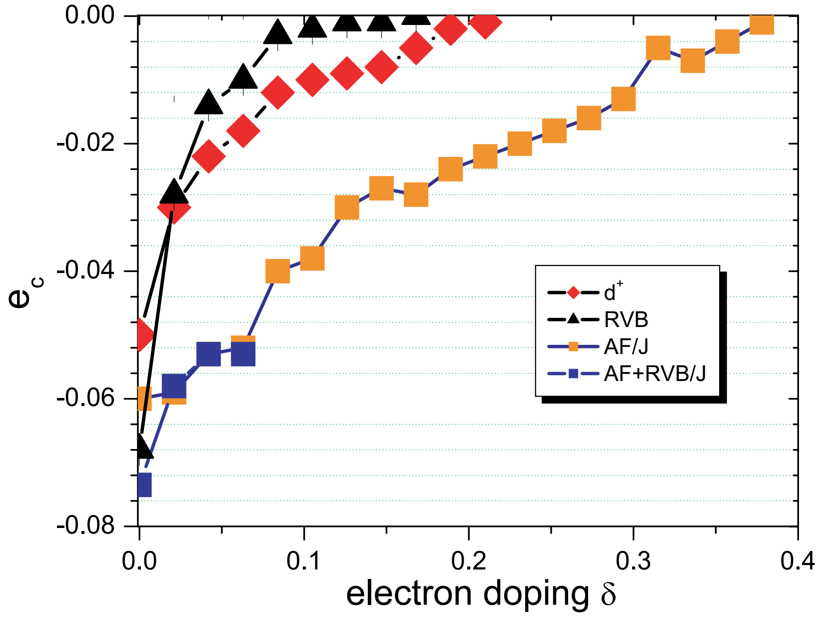

Figure 3.8: Condensation energy per site e_c versus electron doping for the 96 site lattice. We compare the energy of the RVB wavefunction to the energy of the magnetic AF/J wavefunction.

our calculation to model wavefunction with a finite correlation length, i.e. short range 120° magnetic order. In our calculation, we can either totally suppress the long-range 120° and get back to the Gutzwiller wavefunction, or use the long-range 120° magnetic order that is highly stabilized by the potential energy. No intermediate scenario, such as incommensurate structures, is yet available in our calculations, but one can only expect the optimization of the magnetic structure to increase the region of stability for magnetism. We interpret this finding as an indication that the hole motion is not drastically modified by the presence of the non-collinear magnetic structure, so that short range magnetic correlations will survive up to high electron doping. For the $t{-}J^z$ model on the square lattice, it is commonly understood that the Ising Néel order is not surviving high doping because of its costs in kinetic energy: whenever a hole wants to move in an antiferromagnetic spin background, it generates a ferromagnetic cloud. Therefore, good kinetic energies and Néel Ising order are not compatible. In our case, the 3-sublattice order imposes no such constraint on the kinetic energy of the holes, because of the 120° structure. This can be seen in our wavefunction energies: the potential energy is improved when starting from the Gutzwiller wavefunction and adding 120° correlations, but the kinetic energy is unchanged. Our best wavefunction has a better potential energy than the Gutzwiller wavefunction (and also than the different CFP wavefunction), but it

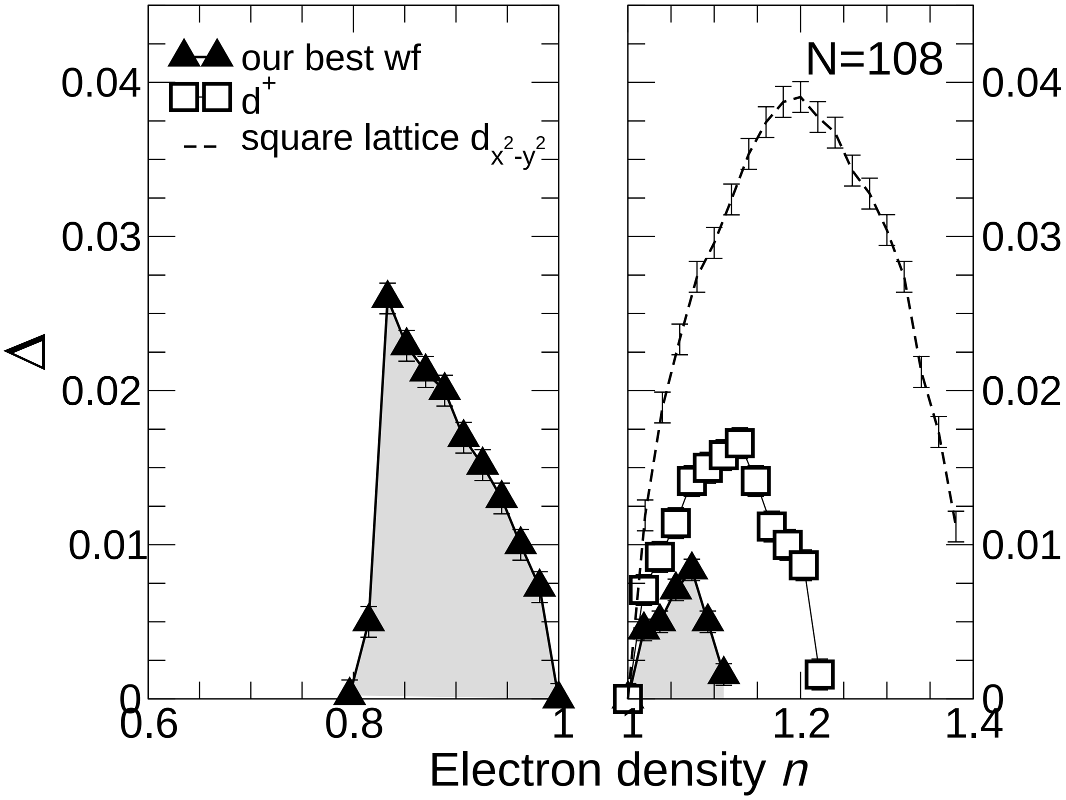

Figure 3.9: Superconducting order parameter Δ, obtained by the long-range correlations of the pairing operator (see equation (2.69)), for a 108 site triangular cluster in our best wavefunction (full triangles), in the d^+ wavefunction (open squares). For comparison we show the amplitude of the d-wave gap in a 10×10 *square* lattice (dashed line).

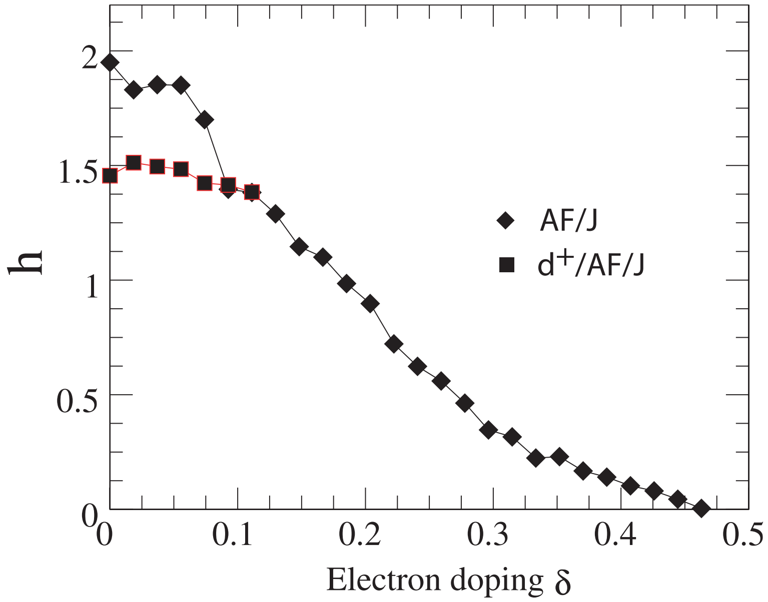

Figure 3.10: Amplitude of the magnetic order parameter versus doping for the $d^+/AF/J$ wavefunction (squares) and AF/J wavefunction (diamonds). The pairing variational parameter allows to reduce the magnetization in the low doping range.

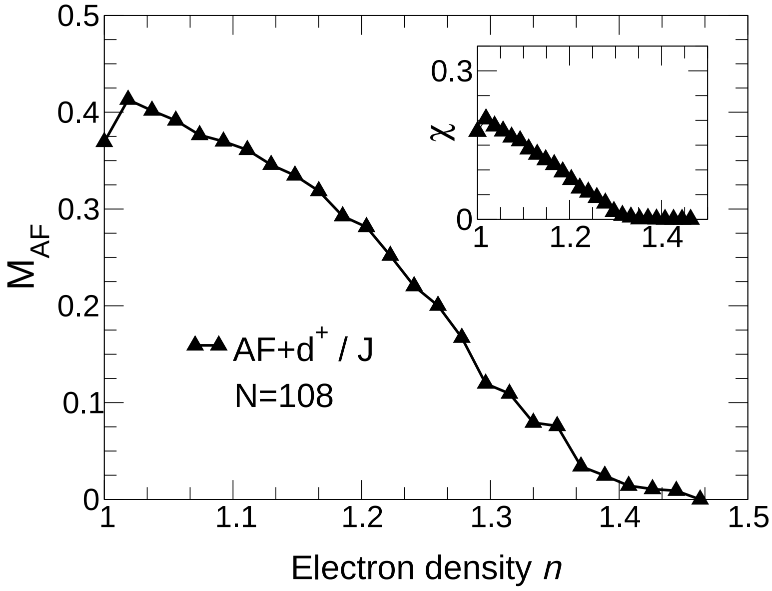

Figure 3.11: Amplitude of the 120° magnetic order M_{AF} measured in the $AF + d^+/J$ for a 108 site cluster. Inset: the amplitude of the staggered spin-current χ in the same wavefunction.

also keeps the same kinetic energy. Therefore, this qualitatively explains why one can stabilize the 3-sublattice magnetic phase for a large set of J values. Finally, we note that the staggered spin-current pattern is also present for doping $\delta = [0, 0.3]$ (see Fig. 3.11).

Interestingly, the Jastrow variational parameter α (5.7) changes sign at $\delta = 0.4$ when $M_{AF} \approx 0$: for $\delta < 0.4$ ($\delta > 0.4$) the Jastrow factor favors classical Ising (ferro-) anti-ferromagnetic states. The VMC results show that the competition between the classical Ising configuration on the triangular lattice and the 120° order improves the energy. We argue that the classical Jastrow simulates with a good approximation quantum fluctuations around the 120° order. Note that the Jastrow does not play the same role as the BCS pairing: the BCS pairing forms configurations of resonating singlets, and the Jastrow factor forms classical Ising configurations. It is also worth noting that at higher doping the Jastrow parameter leads to a small condensation energy of $0.01t$ for a large range of doping ($\delta = [0.4, 0.8]$). It was checked that this gain in energy does not decrease with the size of the lattice and is also present for a square lattice geometry. We found also that for the small clusters (12 and 48 sites) the system was gaining a significant amount of energy when having a weak ferromagnetic polarization. Therefore, this suggests that the Gutzwiller wavefunction is not the best approximation of the ground state of the $t-J$ model in the high doping limit. Nevertheless, the Jastrow factor does not introduce long-range correlation and the variational wavefunction we introduce here is still a Fermi liquid. Note that the variance of the energy per site σ^2 reaches its maximum value for doping $\delta = 0.4$ for the $AF + d^+/J$ with $\sigma^2 = 0.0008$, and applying one Lanczos step leads to $\sigma^2 = 0.0004$.

3.4.3 Hole doping: $n \in [0, 1]$

For hole doping the scenario is strikingly different. The 120° order is weakened in a strong d^+ RVB background and disappears at doping $\delta = 0.08$ (see Fig. 3.13 and Fig. 3.15). Moreover, although the $AF+RVB/J$ wavefunction is stabilized at half-filling, the RVB/J wavefunction is not stabilized for the hole doping part of the phase diagram (see Fig. 3.14). When superconductivity disappears, there is a first order transition to a commensurate spin-density wave. No coexistence between superconductivity and the spin-density wave was found. Then, a ferromagnetic phases emerges with a strong gain of condensation energy. Indeed the polarized states are leading to a strong gain in kinetic energy. This can be understood in the simple picture of the Stoner model, which gives a critical on-site repulsion related to the density of states: $U_{cr}^F = 1/\rho(\epsilon_F)$. Ferromagnetism becomes favorable if ϵ_F is sitting at a sharp peak of $\rho(\epsilon)$. In the triangular lattice the tight binding (TB) density of states is strongly asymmetric and has a sharp peak at the $n = 0.5$ electronic density lying at the Van Hove singularity. Note also that the simple $t-J$ model of a 3 site cluster with 2 electrons shows that in the $t > 0$ the ground state is a singlet, whereas the ground state is a triplet

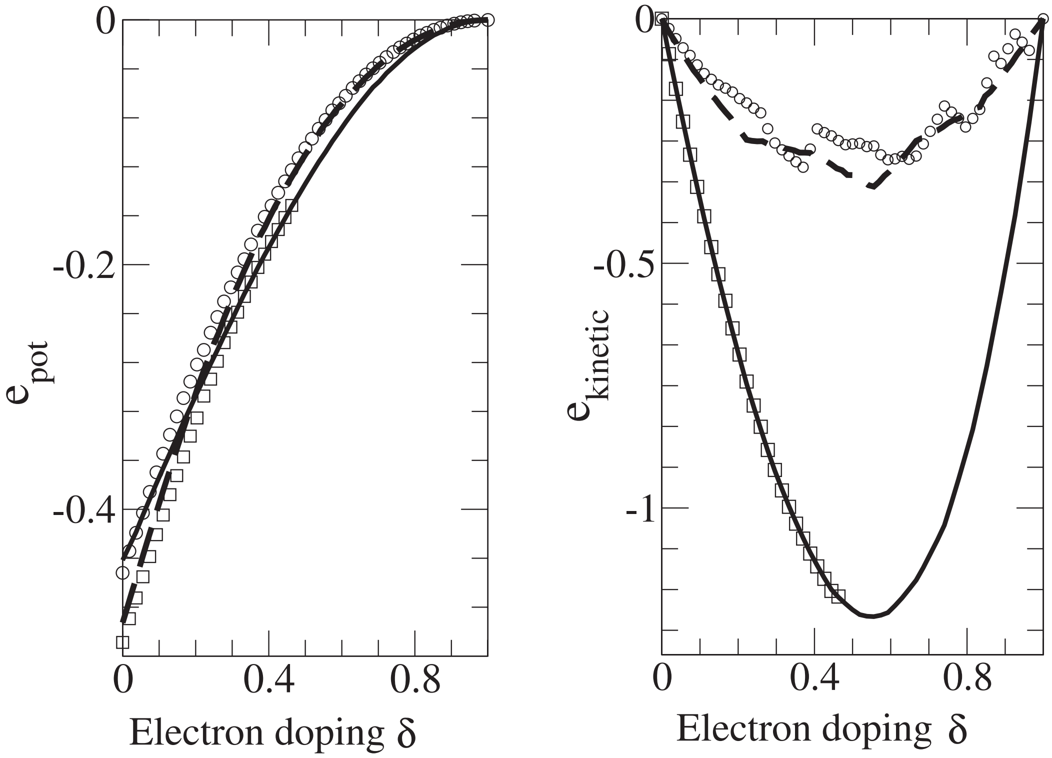

Figure 3.12: Kinetic ($e_{Kinetic}$) and exchange energy ($e_{pot.}$) per site for the Gutzwiller wavefunction (bold line), the commensurate flux phase with $2\pi/3$ flux per plaquette (open circles) and with $\pi/2$ flux per plaquette (dashed line), the $d^{+}/AF/J$ wavefunction (open squares).

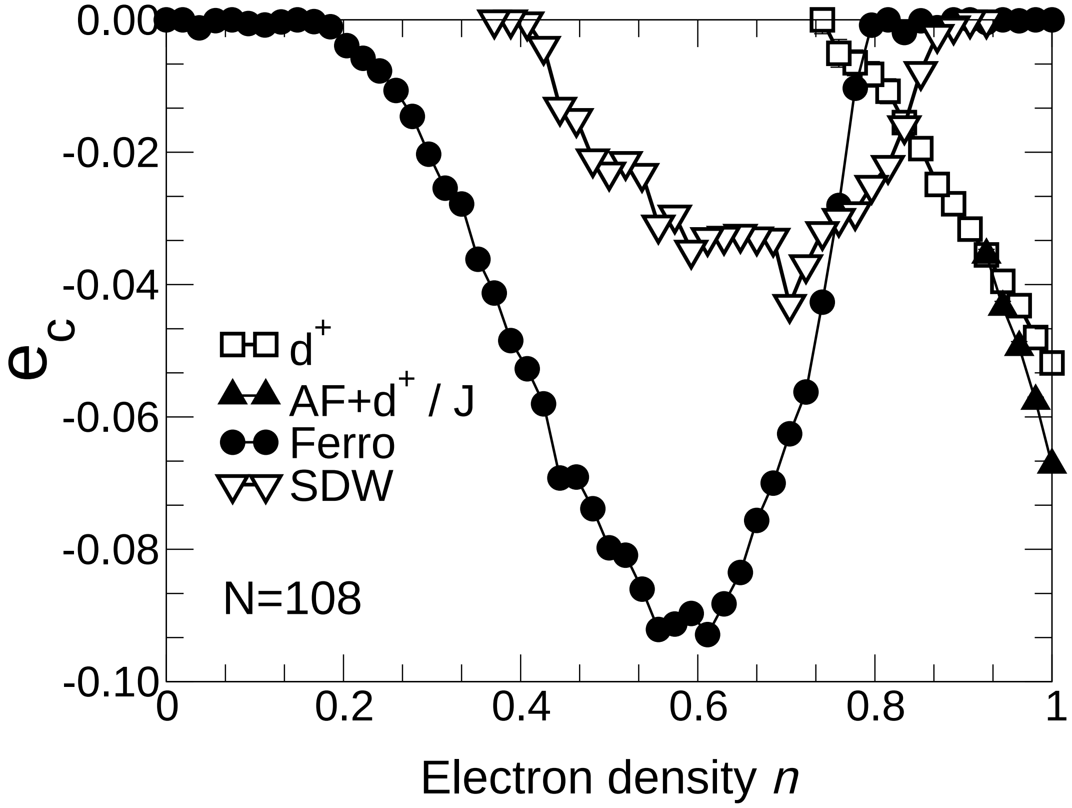

Figure 3.13: Condensation energy per site e_c for different wavefunctions in a 108 site cluster.

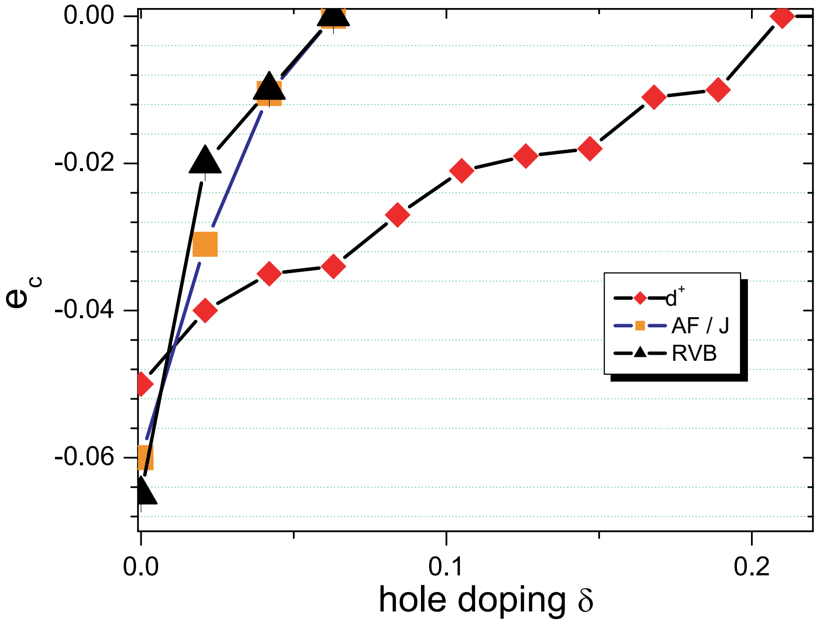

Figure 3.14: Condensation energy per site e_c versus hole doping for the 96 site lattice. We compare the energy of the RVB wavefunction to the energy of the magnetic AF/J wavefunction and to the energy of the BCS d^+ wavefunction.

in the $t < 0$ case. This shows that the negative sign of t with hole doping is inducing ferromagnetic correlations on a very small cluster. We find again trace of these correlations and ferromagnetic tendencies in the range of electronic density $n \in [0.2, 0.8]$ in our 108 site lattice. Such a ferromagnetic instability was also predicted in Ref. [84] by comparing the energy of the RVB wavefunction with an analytical calculation of the energy of the fully polarized state. We see that minimizing the energy by changing the variational onsite magnetic field leads to similar results.

Moreover, at $\delta = 0.5$ doping, there is a nesting of the Fermi surface, with three possible $\mathbf{Q}$ vectors. Thus, it is reasonable to expect that a particle-hole instability of corresponding pitch vector $\mathbf{Q}$ is stabilized close to this doping. We have investigated the following instabilities : a commensurate charge density wave, and a spin-density wave. Interestingly, the commensurate spin-density wave was stabilized. Indeed, we have found that the scattering between the $\mathbf{k}$ and $\mathbf{k}+\mathbf{Q}$ vectors introduced in the Hamiltonian H_{SDW} (particle-hole channel) allows to gain kinetic energy in the range of doping $\delta = [0.15, 0.6]$. For sake of simplicity, we have only considered the mean-field Hamiltonian containing one of the three possible nesting vectors : $\mathbf{Q}_N = (\pi, -\pi/\sqrt{3})$. Finally, the phase is stabilized, when compared to the RVB and ferromagnetic phases, in the window $\delta = [0.16, 0.24]$. Nonetheless, no coexistence between superconduc-

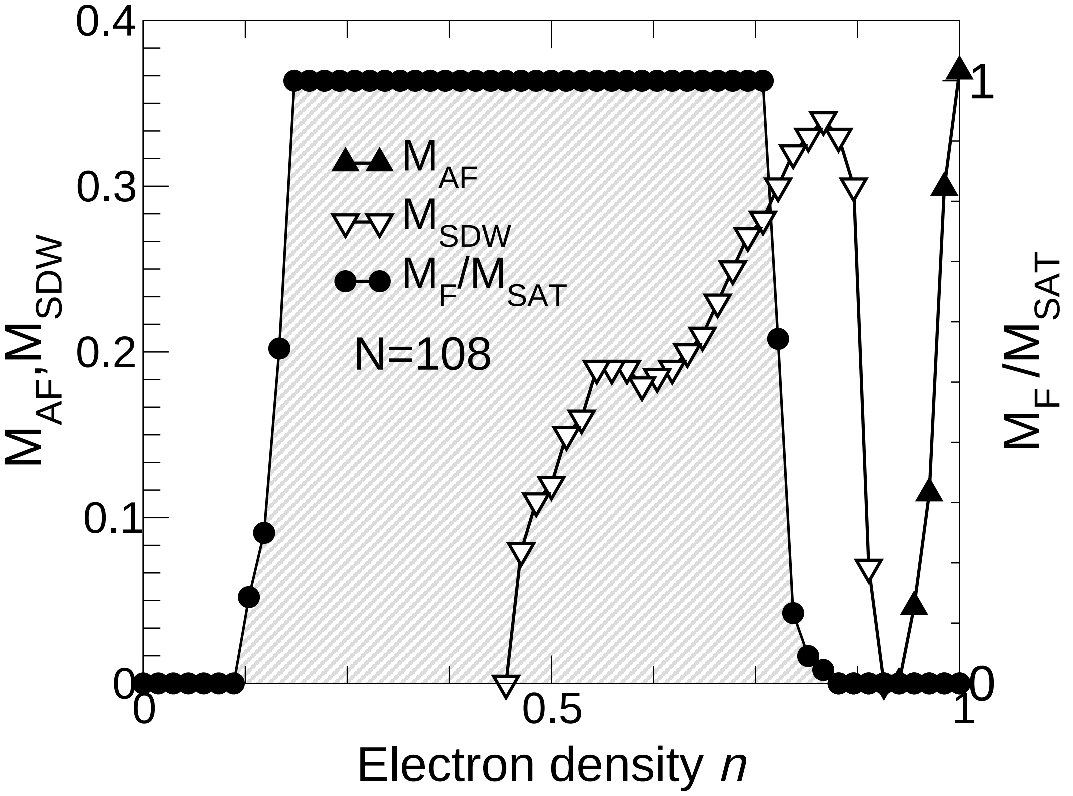

Figure 3.15: Amplitude of the 120° magnetic order measured in our best wavefunction for the 108 site cluster (left scale, full triangles) and the ratio of the polarization M_F on the saturated polarization M_{sat} in our best wavefunction (right scale, full circles). We show also the absolute magnetization M_{SDW} for the spin-density wave wavefunction (left scale, see also Fig. 3.16).

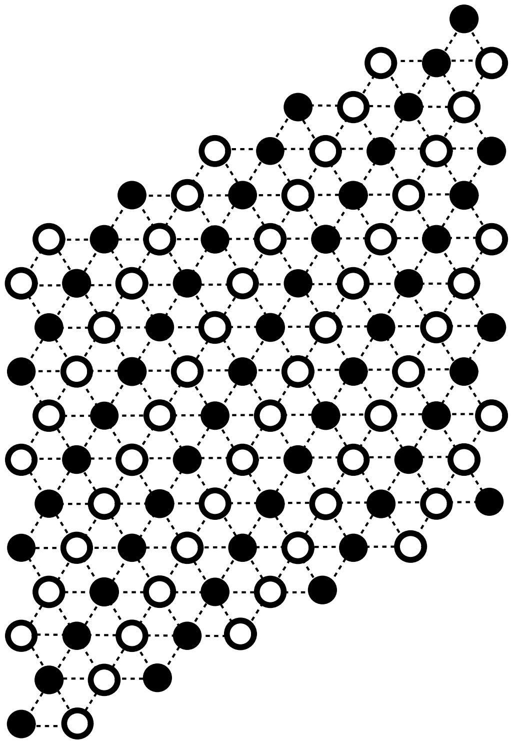

Figure 3.16: On-site magnetization for each site of a 108 site lattice for the spin-density wave wavefunction. Open (filled) circles denotes down (up) spins. The size of each circle is proportional to the respective amplitude of the on-site magnetization. We find that the spins forms a stripe-like pattern, alternating ferromagnetic bonds in the $\mathbf{a_2}$ direction, and antiferromagnetic bond in the two other directions. The average on the lattice sites of the absolute value of the local magnetization is shown in Fig. 3.15.

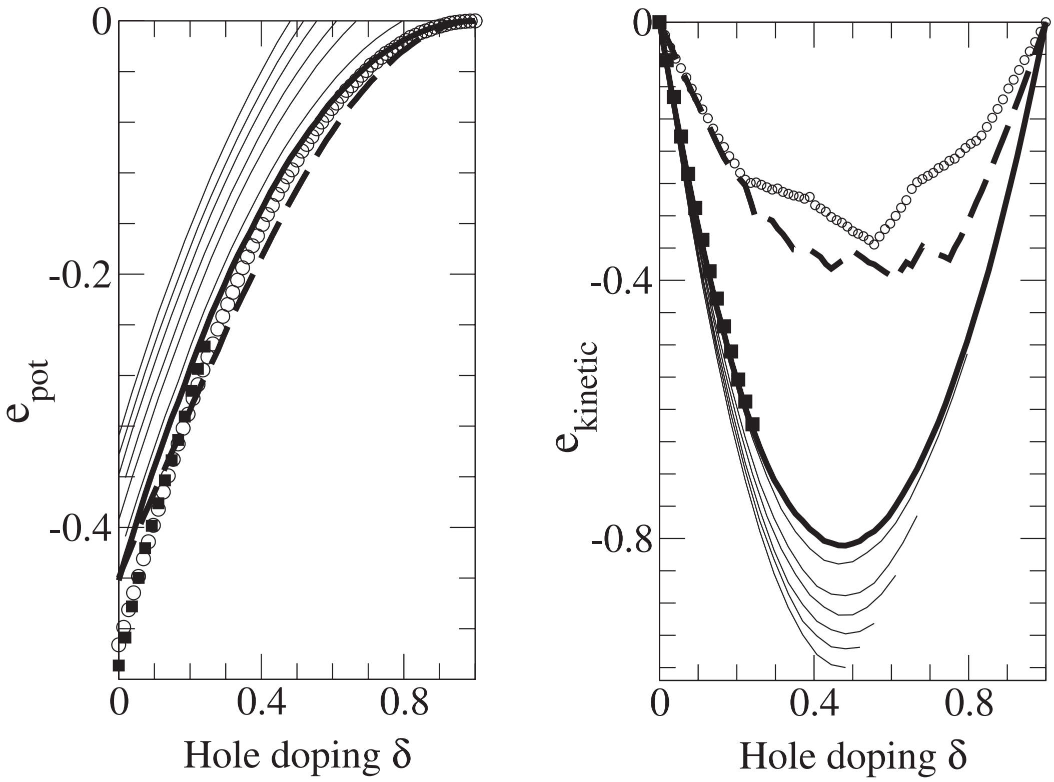

Figure 3.17: Kinetic ($e_{kinetic}$) and exchange energy (e_{pot}) per site for the Gutzwiller (bold line), the commensurate flux phase with $2\pi/3$ flux per plaquette (open circles), with $\pi/2$ flux per plaquette (dashed line), the $d^+/AF/J$ wavefunctions (filled squares), and the polarized wavefunctions (lines) with $S^z = 11, 18, 21, 24, 28$. The polarized wavefunction are shown from top to bottom with increasing (decreasing) polarizations in the left (right) figure. the left figure and decreasing polarization.

tivity and the spin-density wave was found: the energy is minimized either for ($\Delta_k = 0, f(Q) \neq 0$), or ($\Delta_k \neq 0, f(Q) = 0$) depending on the doping, with Δ_k of $d_{x^2-y^2} + id_{xy}$ symmetry type in the latter case. Measuring the on-site magnetization value, we found that the spin-density wave forms a collinear stripe-like pattern in the spin degrees of freedom, whereas the charge is found to be uniformly distributed among the lattice sites, as expected (see Fig. 3.16). The amplitude of the on-site magnetization is shown in Fig. 3.15 as a function of doping.

3.4.4 Phase diagram of the model

Based on our wavefunction we can now give the phase diagram for the doped system on the triangular lattice. The phase diagram, summarizing the various

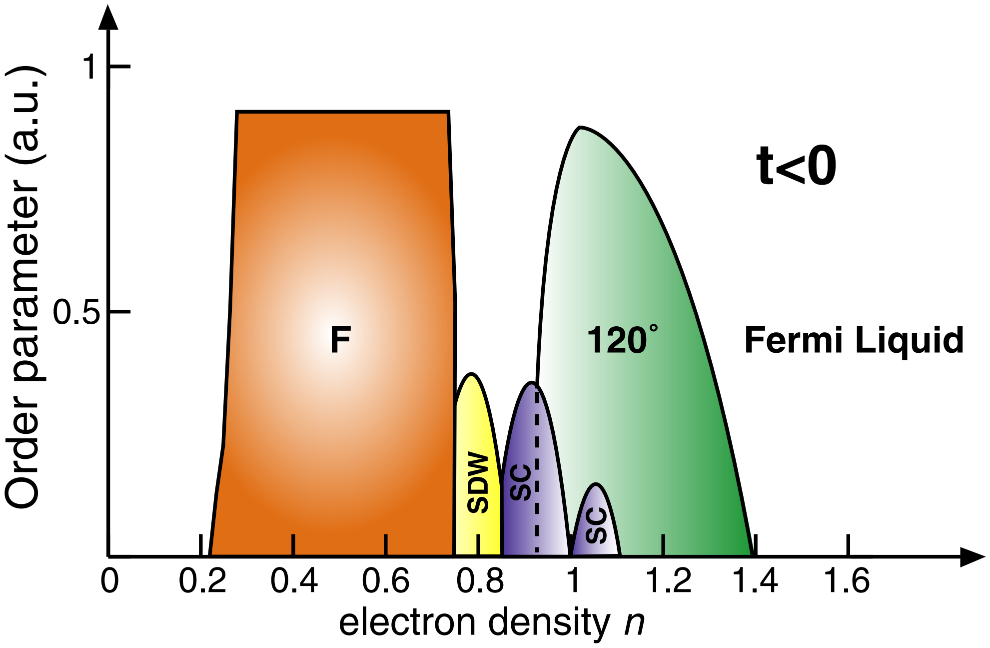

Figure 3.18: Cartoon picture of the phase diagram of the $t{-}J$ model we get with $t < 0$. Here we sketch on an arbitrary scale the order parameter amplitude of the 120° magnetic phase, the ferromagnetic phase (F), the superconducting $d_{x^2-y^2} + id_{xy}$ phase (SC), the commensurate spin-density wave (SDW). Note that for electron density $n > 1.04$ and $n < 0.96$, the energy is degenerated, within the error bars due to the Monte Carlo sampling, with the pairings $d_{x^2-y^2}$, d_{xy} and $d_{x^2-y^2} - id_{xy}$. The pitch vector of the commensurate spin-density wave is $\mathbf{Q}_N = (\pi, -\pi/\sqrt{3})$, and this phase is depicted more in details in Fig. 3.16.

instabilities discussed in the previous sections, is shown in Fig. 3.18. This phase diagram prompts for several comments. First one notices immediately that the competition between magnetism and superconductivity in this model depends crucially on the sign of the hopping integral (see Fig. 3.18).

For both hole and electron doping, the triangular lattice has a very different phase diagram from the square lattice one [4]. In the square lattice, the AF order disappears at $\delta = 0.1$ and the d-wave RVB vanishes at $\delta = 0.4$ for the same value of J. In the triangular lattice, a similar stability of superconductivity exists on the hole side, but the electronically doped side is resolutely dominated by antiferromagnetic instabilities. Our results, based on an improved class of wavefunctions, present marked differences with previous approximate results for

---

[4] In the square lattice the sign of t plays no role because of the particle-hole symmetry of a bipartite lattice.

the doped system. On the electron side, mean-field theories would have suggested that the long-range magnetic order state undergoes a first order phase transition [78] into a uniform d^+ superconducting state at $\delta \approx 3\%$ for values of J similar to those considered here. A rationalization of these results would be that the frustration of the lattice, which was from the start the motivation of RVB as a competing state, disfavors magnetic order. Our results, where the Gutzwiller projection is treated exactly within the residual error bars due to the statistics, are in clear disagreement with this mean-field theory. In contrast with the mean-field result, magnetism is dominant and the superconducting order is not favored on the electronic side. In addition, the $t{-}J$ model on the triangular lattice was expected to have a strong and large RVB instability, since the coordination number is higher than on most of the other lattices, and naively we would expect this to provide an easy way to form singlets. In this chapter we show that it is not the case: for electron doping the system is magnetic, and for hole doping the system is superconducting, but the range of superconductivity is not very large ($\delta < 0.16$), and in any case smaller than on the square lattice.

Previous variational approaches [84] were restricted to pure superconducting wavefunctions $d_{x^2-y^2} + id_{xy}$ on a $t - t'$ square lattice with $t = t'$. In our work it was found that superconductivity is stabilized up to electron doping $\delta \approx 0.24$ and hole doping $\delta \approx 0.2$ for similar albeit slightly different values of J/t ($J/t = 0.3$). In our calculations, for the case of electron doping, which corresponds to the doping in the cobaltite experiments, our phase diagram, using the larger class of wavefunctions, is clearly completely different from this previous result, and the stabilization of the superconductivity in that case was clearly an artefact of the too restricted variational subspace. As shown in Fig. 3.18, superconductivity is strongly weakened by the presence of 3-sublattice magnetization and is present only in the range of electron doping $\delta = [0, 0.12]$. On the contrary, for the case of hole doping, superconductivity had higher energy than ferromagnetic and spin-density wave phases for $\delta > 0.16$. We thus confirm that the previous results are not an artefact of their restricted variational subspace, and find an acceptable agreement for the phase diagram. However we emphasize the presence of the spin-density wave wavefunction that was not considered in the mentioned work and implies a small reduction of the superconductivity range.

Our calculation thus clearly prompts for a reexaminations of the arguments on the nature of superconductivity in a frustrated lattice. Clearly the non-collinear nature of the order parameter helps making the AF order much more stable to electron doping than initially anticipated. Understanding such issues is of course a very crucial and challenging question. Moreover, on the triangular lattice, no significant enhanced cooperative effect between magnetism and superconductivity seems to be observed: the electron doped side has a magnetic signature, and the hole doped side a superconducting one, but the two orders seem to exclude each other as much as they can, in contrast to what happens for the square lattice. Even in the parts of the phase diagram where coexistence is observed, coexistence between magnetism and superconductivity in the electron doped case shows again that superconductivity is decreased in the presence of strong long range magnetic correlations.

3.5 Conclusion

In this chapter we have presented a variational Monte Carlo study of the $t-J$ ($J/t = 0.4$ and $t < 0$) model on the triangular lattice, using extended wavefunctions containing both superconductivity and non-collinear magnetism, as well as flux phase instabilities. The method we used to construct and sample the wavefunction is quite general and applicable to other lattices (honeycomb, kagome, ladders...) as well as other symmetries (e.g. triplet superconductivity). It thus provides a general framework to tackle the competition between antiferromagnetism and superconductivity in frustrated systems. We obtained very good variational energies at half-filling when comparing with other more sophisticated methods, specialized to the half-filled case. The fermionic representation of our wavefunction allows to consider hole and electron doping. The most stable pairing corresponds to singlet pairing. We find that $d_{x^2-y^2}+id_{xy}$ superconductivity is only weakly stabilized for electron doping in a very small window ($\delta = [0, 0.12]$) and is much stronger and also appears in a wider range ($\delta = [0, 0.16]$) in the case of hole doping. A commensurate spin-density wave phase is leading to a gain in kinetic energy and is stabilized in the small window $\delta = [0.16, 0.24]$ hole doping. Finally, ferromagnetism emerges in a wide range for hole doping $\delta = [0.24, 0.8]$. Very surprisingly, the 3-sublattice magnetism which is present at half-filling extends to a very wide range of electron doping $\delta = [0, 0.4]$ and is suppressed very fast in the case of hole doping $\delta = [0, 0.08]$. The large extent of 120° order for electron doping is responsible for the suppression of superconductivity. This feature was neither observed in previous VMC calculations, nor predicted by the mean field theories, and prompts for a reexamination of the question of the stability of magnetic order on a triangular system.

Our results show that, for electron doping, the square and triangular lattices behave in a very different way. For the square lattice, the $t-J$ Hamiltonian finds a domain of stability of superconductivity and a pairing symmetry that is very consistent with other methods. It is thus a natural candidate to investigate superconducting phases in systems like the cuprates. For the case of the triangular lattice, the predicted phase diagram is dominated by antiferromagnetic instabilities, and superconductivity, albeit slightly present, is strongly suppressed. This clearly indicates that, contrarily to what was suggested by mean-field and previous variational calculations, the $t-J$ model itself is not a good starting point to tackle the superconductivity of the cobaltite compounds, where superconductivity is observed in the range of electron density $n = \left[1 + \frac{1}{4}, 1 + \frac{1}{3}\right]$. This model must be completed by additional ingredients to obtain a faithful description of the experimental system. Two missing ingredients in the simple $t-J$ model could solve this discrepancy and perhaps allow to obtain a superconducting instability. On one hand, a strong Coulomb repulsion is expected in this type of compound. Such a long-range interaction is not taken into account in the $t-J$ model. Thus a coulomb V term should be added to get a $t-J-V$ model. On the other hand, in this chapter, we have used a single-band model as a first step to study the Co-based oxides. However, it is quite possible that the multi-band effect plays an essential role for superconductivity [94]. The interaction between the three bands of the compound could play a non trivial role in the physics of the $t-J$ model. Therefore, a study of the 3-band model could also be of interest. Such an analysis can be done by extending the methods exposed in this chapter to these more complicated models.

Chapter 4

Correlated electrons on the honeycomb lattice

4.1 Outline

We investigate the ground state of the t–J model on the honeycomb lattice as a function of doping by variational Monte Carlo calculations. $d_{x^2-y^2} + id_{xy}$ superconductivity is observed in the range of doping $\delta =]0, \frac{1}{8}[$, disappearing at the doping which corresponds to the van Hove singularity of the free electron density of states. Néel order and superconductivity coexist in the range $[0, 0.07]$. The van Hove singularity stabilizes a spin density wave for $\delta = [\frac{1}{8}, 0.22]$. When the spin density wave phase disappears, the system is polarized progressively, reaching full ferromagnetic polarization at $\delta = 0.5$. The work done in this chapter is resulting from a collaboration with Thomas Gloor and Andreas Martin Läuchli. In particular, the mean-field calculations and the Quantum Monte-Carlo calculations in this chapter were done by Thomas Gloor (a former PhD student of Professor Frederic Mila) and by Andreas Martin Läuchli.

4.2 Introduction

The observation of superconductivity in alkali-metal graphite intercalation compounds (GIC's) was reported years ago by Hannay et al. [95]. They are formed by inserting foreign atoms or molecules between the hexagonal two-dimensional sheets of graphite, forming a honeycomb layer geometry, leading to ordered structures. Since graphite is a semi-metal, the electrons accepted or donated by the intercalant (i.e. there is a charge transfer from the intercalate layer to the host carbon layer) modify the electronic properties of graphite, resulting in a metallic behavior in the final material.

Intensive research work in this area was ensued and many GIC's were subsequently found to exhibit superconductivity. An interesting property of the superconducting alkali-metal GIC's is that they are formed from constituents which are not superconducting, yet upon intercalation they undergo normal-to-superconducting transitions. There exists a few materials which have honeycomb lattice geometry and display superconductivity. One of these is the phonon mediated BCS superconductor MgB_2 with the unusually high transition temperature of 39 K [96]. Another example are the intercalated graphite compounds, *e.g.* the recent discovery of superconductivity in C_6Ca with transition temperature 11.5 K [97]. A detailed microscopic understanding of the superconducting mechanism is not known yet for these compounds but interlayer states seem to play an important role suggesting a more 3D behavior [98, 99]. There is also experimental indication for intrinsic superconductivity in ropes of carbon nanotubes [100]. It is worth noting that observation has been made of superconductivity in alkali-metal doped C_{60} [101] and this work has attracted a good deal of attention because of the relatively high T_c in K_3C_{60}.

The honeycomb lattice, like the square lattice, is bipartite and we would expect that it would fit very well with the Néel state (one variety of each of the spin lying respectively on each of the sublattice). However, in the square lattice, the Néel magnetism is also associated with a perfect nesting of the fermi surface (the nesting vector is the $Q = (\pi, \pi)$ vector, which leads to a spin density wave of vector Q). However, what is somewhat different in the honeycomb lattice is that the Fermi surface at half-filling consists only of two points (see Fig.4.1). Moreover, it is worth noting that the free electron density of states vanishes at the Fermi surface. Therefore, the question regarding of the presence of magnetism at half-filling remains an interesting one that we propose to address in this chapter.

This behavior of the free electron density of states is responsible for a Mott metal-insulator transition in the half-filled Hubbard model on the honeycomb lattice at a finite critical on-site repulsion of about $U_{\rm cr} \approx 3.6\,t$ [102, 103, 104, 105]. Therefore the system is a paramagnetic metal below $U_{\rm cr}$, and above $U_{\rm cr}$ an antiferromagnetic insulator. In contrast the square lattice has a van Hove singularity in the density of states at half–filling which leads to an antiferromagnetic insulator already for an infinitesimal on–site repulsion.

As mentioned before, the $t{-}J$ model is the effective model of the Hubbard model in the limit of large on-site repulsion, and at half-filling it coincides with the Heisenberg model. For both the square and the honeycomb lattices, the Heisenberg model has an antiferromagnetic ground state. However the quantum fluctuations are larger in the honeycomb lattice [106] due to the lower connectivity. Upon doping, quite different properties are expected for the honeycomb lattice as compared to the square lattice, since it has a van Hove singularity in the free electron density of states at fillings 3/8 and 5/8. At these fillings the system is expected to undergo spin density wave (SDW) instabilities, whereas in the square lattice d-wave superconductivity can extend without disturbance up to fillings of 1.4.

In that respect, the honeycomb lattice has more similarities with the hole

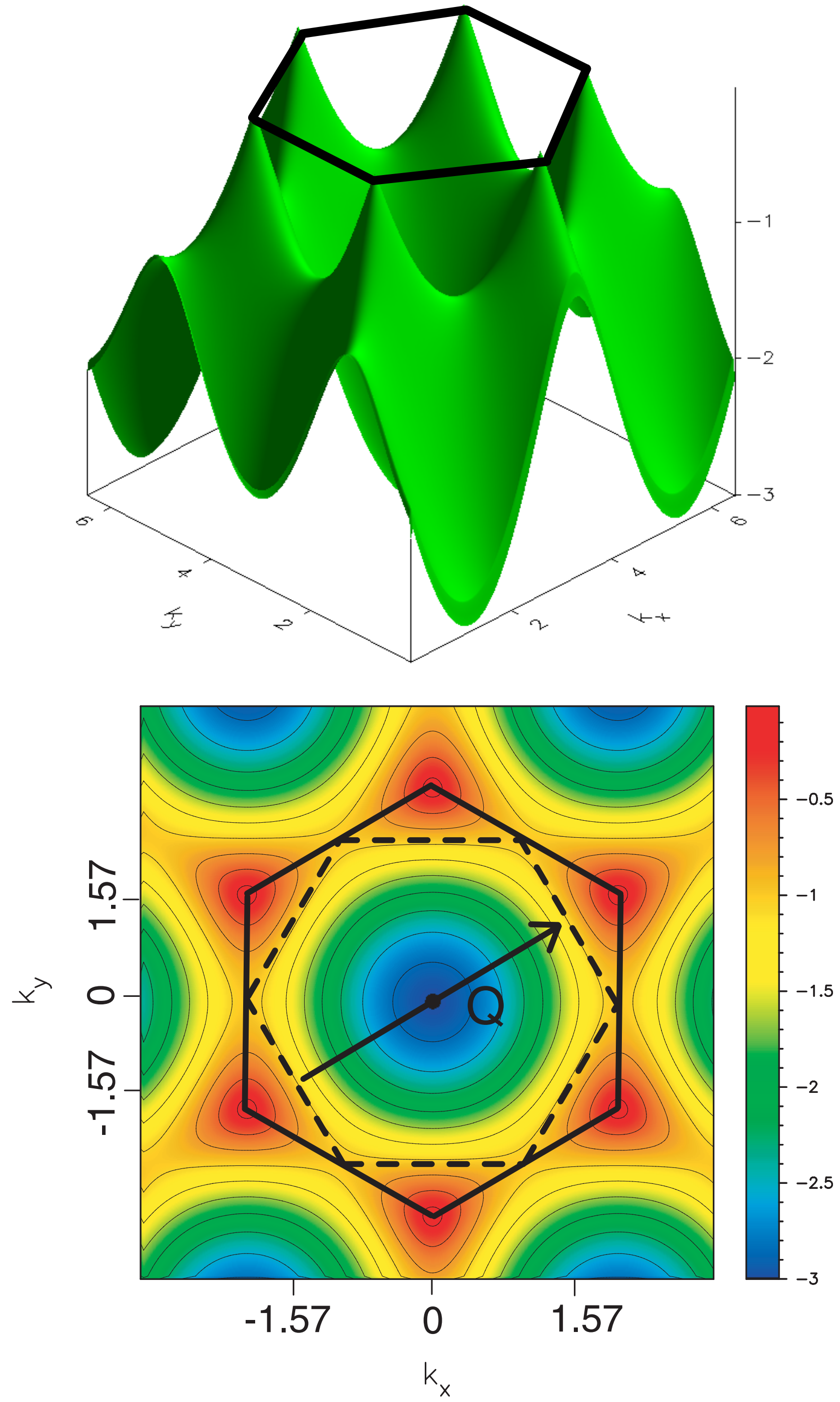

Figure 4.1: Free particle dispersion of the honeycomb lattice. The lower band is shown, and the upper bound is perfectly symmetric. At half-filling, the Fermi-surface is shown by the bold lines. Only six points are filled, and only two of the points are independent, since the other one are identical. zone. The Fermi surface is nevertheless nested, although it consist only of two points. The inner hexagon of the bottom figure (dotted lines) correspond to the Fermi surface at a hole doping of $x = 1/8$. There is an another nesting of the Fermi surface, and of the three nesting vector is $\mathbf{Q}_N = (\pi, -\pi/\sqrt{3})$. In this case the Fermi surface is not reduced to a finite number of points.

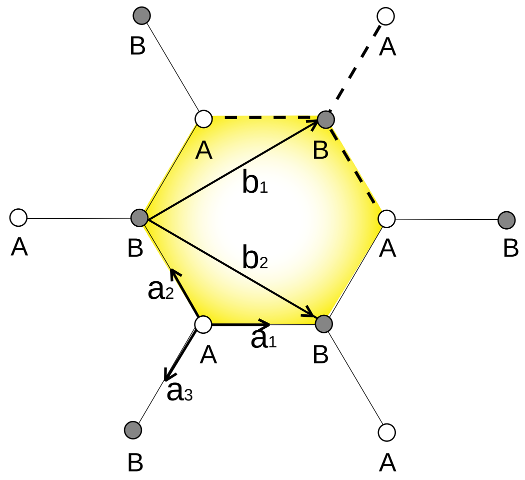

Figure 4.2: The unit-cell of the honeycomb lattice contains two sites. The honeycomb lattice is bipartite and thus it can be separated into two sublattices A and B. For the basis vectors we chose $\mathbf{b_1}$ and $\mathbf{b_2}$, and $\mathbf{a_i}$, i $= 1, 2, 3$, are the unit vectors defining the nearest neighbor directions.

doped ($t < 0$) triangular lattice which has a van Hove singularity at 1/4 filling, a finite U Mott metal–insulator transition [107], and the same lattice symmetry. However the triangular lattice is not bipartite. Therefore the honeycomb lattice can be viewed to be intermediate between the square and the triangular lattice, and a comparison of their magnetic and superconducting properties can give further insight concerning the geometrical influences.

The $t{-}J$ model on the honeycomb lattice has not yet been studied, neither by MF calculation nor VMC simulations. It will be the subject of the present work to investigate the competition between magnetic and superconducting phases in this model at zero temperature. The different phases upon doping are determined by VMC simulations. We present also a MF calculations of the superconducting phase.

4.3 Model and methods

4.3.1 t-J model on the honeycomb lattice

In the following we focus on the ground state properties of the $t - J$ model on the honeycomb lattice 1.4. In the following we set $|t| = 1$ and we adopt a generic value of $J = 0.4|t|$ throughout the chapter. Because of the particle-hole symmetry in the honeycomb lattice the sign of t does not play any role.

In the numerical simulations we have considered finite clusters of the honeycomb lattice with $N = 72$ and $N = 144$ sites. The $N = 72$ cluster is defined by the translation vector $\mathbf{T_1} = n\mathbf{b_1} + n\mathbf{b_2}$ ($\mathbf{b_i}$ are defined in Fig. 5.2) and the vector $\mathbf{T_2} = n\mathbf{b_1} + m\mathbf{b_2}$ orthogonal to $\mathbf{T_1}$. We have used anti-periodic boundary conditions along $\mathbf{T_1}$ and periodic ones along $\mathbf{T_2}$. This allows to reduce the finite size effect. The $N = 144$ cluster uses $2\mathbf{T_1}$ and $2\mathbf{T_2}$.

4.3.2 Variational wavefunctions

Next we introduce the variational subspace that we use to study the ground state of the $t-J$ model. Our variational wavefunctions are built from the ground-states $|\psi_{\mathrm{MF}}\rangle$ of the mean-field like Hamiltonian 1.23. The set of variational parameters is given by χ_{ij} allowing anisotropic nearest neighbor hopping, when $\chi_{ij} = |\chi_{ij}|e^{i\theta_{ij}}$ is complex, it is breaking time-reversal symmetry leading to a so-called flux phase, Δ_{ij} the singlet BCS pairing, and h_i responsible for SDW instabilities. In general $|\psi_{\mathrm{MF}}\rangle$ is not a state of fixed number of particles due to the presence of the BCS pairing. In VMC simulations it is however necessary to work with states of fixed particle number and we therefore apply the projector $\mathcal{P}_N$ which projects on the subspace of N electrons. Further, since the $t-J$ model allows at most one fermion per site, we discard also all configurations with doubly occupied sites by applying the complete Gutzwiller projector $\mathcal{P}_{\mathcal{G}} = \prod_i (1 - n_{i\uparrow}n_{i\downarrow})$. To summarize, our variational wavefunction is written as

$$|\psi_{\mathrm{var}}\rangle = \mathcal{P}_{\mathcal{G}}\mathcal{P}_N \,|\psi_{\mathrm{MF}}\rangle\,. \tag{4.1}$$

Now we give a list of all the variational states which we found to be relevant in the honeycomb lattice.

- FS: The Gutzwiller projected Fermi sea is our reference state, *i.e.* $t_{ij} \equiv 1$, all other parameters equal zero, and thus no minimization is necessary.
- AF: A staggered antiferromagnetic order, *i.e.* $\Delta_{ij} \equiv 0$ and $h_i \equiv (-1)^i h$.
- RVB: A singlet superconducting phase [1], *i.e.* $h_i \equiv 0$, and

  $$\Delta_{ij} \equiv \Delta e^{i\phi_\alpha} \tag{4.2}$$

  where the singlet order parameter has a uniform amplitude but each nearest neighbor bond $\alpha = 1, 2, 3$ is allowed to have its own phase.
- RVB/AF: A state mixing superconductivity and antiferromagnetism.
- F: A ferromagnetic state with partial or full polarization, *i.e.* $\Delta_{ij} \equiv 0$ and $h_i \equiv h$.

---

[1] We have also checked the possibility of triplet pairing, however the minimum of the energy was always found for singlet pairing trial functions.

- SDW: We consider only SDW states of a single wave vector $\mathbf{Q} = 1/2(\mathbf{b_1^*} - \mathbf{b_2^*})$ where $\mathbf{b_1^*}$ and $\mathbf{b_2^*}$ are the two reciprocal basis vectors (*cf* figure 4.1). This vector is chosen because at hole doping of 1/8, one has not only a van Hove singularity but also the Fermi surface is a perfectly nested hexagon with nesting vectors $1/2(\mathbf{b_1^*} - \mathbf{b_2^*})$, $\mathbf{b_1^*} + 1/2\mathbf{b_2^*}$, and $-1/2\mathbf{b_1^*} - \mathbf{b_2^*}$ [2]. In real space these vectors correspond to alternating rows of up and down spins, as shown in figure 4.8.

  The SDW instability is most easily implemented in reciprocal space, where the MF Hamiltonian (1.23) reads (with $\Delta_{ij} \equiv 0$)

$$H_{\mathrm{MF}} = \sum_{\boldsymbol{k},\sigma,n} \epsilon_n(\boldsymbol{k}) \gamma^\dagger_{n,\boldsymbol{k}\sigma} \gamma_{n,\boldsymbol{k}\sigma} + 2\sigma f(\boldsymbol{Q}) \gamma^\dagger_{n,\boldsymbol{k}+\boldsymbol{Q}\sigma} \gamma_{n,\boldsymbol{k}\sigma} \tag{4.3}$$

  and $n = 1, 2$ is the band index of the tight-binding Hamiltonian, $\epsilon_n(\boldsymbol{k})$ and $\gamma_{n,\boldsymbol{k}\sigma}$ are the corresponding dispersions and eigenstates.

4.3.3 Observables

To measure the order parameters and correlations of the optimal wave functions after projection, we have calculated the following observables:

- The staggered magnetization of the antiferromagnetic order:

$$M_{\mathrm{AF}} = \frac{1}{L} \sum_i (-1)^i \frac{\langle \psi_{\mathrm{var}} | S_i^z | \psi_{\mathrm{var}} \rangle}{\langle \psi_{\mathrm{var}} \mid \psi_{\mathrm{var}} \rangle} \tag{4.4}$$

  where L is the total number of lattice sites.

- The amplitude of the singlet superconducting order parameter [108, 21]:

$$S^2_{\alpha,\beta} = \frac{1}{4L} \lim_{r\to\infty} \sum_i \frac{\left\langle \psi_{\mathrm{var}} | B^\dagger_{i,\alpha} B_{i+r,\beta} | \psi_{\mathrm{var}} \right\rangle}{\langle \psi_{\mathrm{var}} \mid \psi_{\mathrm{var}} \rangle}, \tag{4.5}$$

  where

$$B^\dagger_{i,\alpha} = c^\dagger_{i,\uparrow} c^\dagger_{i+\alpha,\downarrow} - c^\dagger_{i,\downarrow} c^\dagger_{i+\alpha,\uparrow}, \tag{4.6}$$

  and α and β are chosen from the three nearest neighbor links. Actually we found that this quantity is always of the form

$$S^2_{\alpha,\beta} = \left| S^2_{\alpha,\beta} \right| e^{i(\phi_\alpha + \phi_\beta)} \tag{4.7}$$

---

[2] We have not considered the more general case of a superposition of the three different possible nesting vectors because of technical difficulties to construct the corresponding wavefunction.

and that $\left|S^2_{\alpha,\beta}\right|$ is independent of the choice of α and β. Therefore it is meaningful to define the following quantity

$$S = \sqrt{\left|S^2_{\alpha,\beta}\right|} \tag{4.8}$$

which we will use for the evaluation of the superconducting order parameter.

4.3.4 RVB mean-field theory of superconductivity

The most systematic approach up to date to formulate an RVB mean field theory is based on the slave boson representation which factorizes the electron operators into charge and spin parts $c^\dagger_{i\sigma} = f^\dagger_{i\sigma} b_i$ called holons and spinons. The charged boson operator b_i destroys an empty site (hole) and $f^\dagger_{i\sigma}$ is a fermionic creation operator which carries the spin of the physical electron. The constraint of no doubly occupied site can now be implemented by requiring $\sum_\sigma f^\dagger_{i\sigma} f_{i\sigma} + b^\dagger_i b_i = 1$ at each site. In the slave boson formalism the t–J model becomes [20]

$$\begin{aligned} H = -t \sum_{\langle i,j\rangle\sigma} \left(f^\dagger_{i\sigma} f_{j\sigma} b^\dagger_j b_i + \text{h.c.}\right) + J \sum_{\langle i,j\rangle} \left(\boldsymbol{S}_i \cdot \boldsymbol{S}_j - \frac{n_i n_j}{4}\right) \\ - \mu_0 \sum_i n_i + \sum_i \lambda_i \left(\sum_\sigma f^\dagger_{i\sigma} f_{i\sigma} + b^\dagger_i b_i - 1\right) \end{aligned} \tag{4.9}$$

where $\boldsymbol{S}_i = 1/2 \sum_{\sigma\sigma'} f^\dagger_{i\sigma} \boldsymbol{\sigma}_{\sigma\sigma'} f_{i\sigma'}$ and $n_i = \sum_\sigma f^\dagger_{i\sigma} f_{j\sigma}$. This Hamiltonian is gauge invariant by simultaneous local transformation of the holon and spinon operators $f_{i\sigma} \to f_{i\sigma} e^{i\varphi_i}$ and $b_{i\sigma} \to b_{i\sigma} e^{i\varphi_i}$. Now one can make a mean field approximation by a decoupling in a series of expectation values $\chi_{ij} = \sum_\sigma \left\langle f^\dagger_{i\sigma} f_{j\sigma} \right\rangle$, $\Delta_{ij} = \sum_\sigma \langle f_{i\uparrow} f_{j\downarrow} - f_{i\downarrow} f_{j\uparrow} \rangle$ and $B_i = \left\langle b^\dagger_i \right\rangle$. To have a superconducting state in the slave boson representation it is not sufficient that the fermions form Cooper pairs but also the bosons need to be in a coherent state of a Bose condensate. On the square lattice one finds [20] that the particle–particle expectation values have d–wave symmetry, *i.e.* $\Delta_x = -\Delta_y$. The mean field phase diagram suggests some phase transitions, however χ_{ij}, Δ_{ij}, and B_i cannot be true order parameters since they are not gauge invariant. In fact Ubbens and Lee [109] have shown that gauge fluctuations destroy completely these phases and only a d–wave superconducting dome is left over. Moreover these fluctuations diminish also the tendency for superconductivity and seem to destroy it completely near half–filling where they believe that it is unstable towards more complicated phases such as a staggered flux phase.

In this section we will use a simplified version of the previously mentioned RVB theory. Despite of its simplicity this theory should nevertheless predict the correct symmetry of the superconducting order parameter and be able to make some predictions about the spinon excitations. In fact this simplified RVB theory predicts d–wave superconductivity on the square lattice [20] and was also applied to the Shastry–Sutherland [110] and triangular lattice [77]. It is based on a decoupling of the superexchange term in singlet operators. Given the identity

$$\boldsymbol{S}_i \cdot \boldsymbol{S}_{i+\alpha} - \frac{n_i n_{i+\alpha}}{4} = -\frac{1}{2} B^\dagger_{i,\alpha} B_{i,\alpha} \tag{4.10}$$

a decoupling in $\Delta_{ij} \equiv \langle B_{i,\alpha} \rangle$ is a natural choice. To handle the bosons one assumes that all the Lagrange multipliers λ_i are equal to a single value λ which plays the role of the boson chemical potential. We replace the boson operators by a static value which is chosen such that $\left\langle b^\dagger_i b_j \right\rangle = \delta$ for all i, j [109, 20, 110, 77]. Thus in this approximation the effect of the slave bosons (or equivalently of the Gutzwiller projection) is included in a very simplified way which effectively multiplies the kinetic energy of the spinons by the hole concentration δ and redefines their chemical potential $\mu \rightarrow \mu_0 + \lambda$:

$$\begin{aligned} H^{\mathrm{MF}}_{tJ} = -t\delta \sum_{\langle i,j \rangle \sigma} \left(f^\dagger_{i\sigma} f_{j\sigma} + \mathrm{h.c.} \right) - \mu \sum_i n_i \\ - \frac{J}{2} \sum_{\langle i,j \rangle} \Big(\left\langle B^\dagger_{i,\alpha} \right\rangle B_{i,\alpha} + B^\dagger_{i,\alpha} \langle B_{i,\alpha} \rangle \\ - \left\langle B^\dagger_{i,\alpha} \right\rangle \langle B_{i,\alpha} \rangle \Big) \end{aligned} \tag{4.11}$$

In addition we use the simple ansatz of equation (4.2) for the RVB order parameter Δ_{ij}. The mean field solution is obtained by minimizing the corresponding free energy density

$$\phi = -\mu + \frac{3}{4} J \Delta^2 - \frac{1}{L} \sum_{\boldsymbol{k} j} \left(\varepsilon_j(\boldsymbol{k}) + \frac{2}{\beta} \ln\left[1 + \exp(-\beta \varepsilon_j(\boldsymbol{k}))\right] \right)$$

with respect to Δ, ϕ_{ij} and under the conservation of particle number constraint

$$\frac{\partial \phi}{\partial \mu} = -\frac{N}{L} \qquad \Rightarrow \qquad \delta = -\frac{1}{L} \sum_{\boldsymbol{k} j} \frac{\partial \varepsilon_j(\boldsymbol{k})}{\partial \mu} \tanh\left(\frac{\beta \varepsilon_j(\boldsymbol{k})}{2} \right).$$

$\varepsilon_{j=\pm}(\boldsymbol{k})$ are the dispersions of the single particle spinon excitations above the ground-state. They are given by

$$\begin{aligned} \varepsilon_\pm(\boldsymbol{k}) = \Big(\mu^2 + J^2 |B(\boldsymbol{k})|^2 + \delta^2 |\xi(\boldsymbol{k})|^2 \\ \pm 2\delta \sqrt{J^2 |B(\boldsymbol{k})|^2 \left(\mathrm{Im}\, \xi(\boldsymbol{k})\right)^2 + \mu^2 |\xi(\boldsymbol{k})|^2} \Big)^{1/2} \end{aligned} \tag{4.12}$$

where

$$\begin{aligned}\xi(\boldsymbol{k}) &= t\left(e^{i(\alpha_2-\alpha_1)} + e^{i\alpha_2} + 1\right),\\ B(\boldsymbol{k}) &= \Delta/2\left(e^{-i\phi_3}\cos(\alpha_2-\alpha_1) + e^{-i\phi_2}\cos\alpha_2 + e^{-i\phi_1}\right).\end{aligned}$$

α_1 and α_2 are the projections on the reciprocal vectors: $\boldsymbol{k} = \alpha_1/2\pi\,\mathbf{b_1} + \alpha_2/2\pi\,\mathbf{b_2}$.

We emphasize that Δ is not the superconducting order parameter which is actually given in our approximation by $\left\langle c^\dagger_{i\uparrow}c^\dagger_{j\downarrow}\right\rangle = \left\langle b_i f^\dagger_{i\uparrow} b_j f^\dagger_{j\downarrow}\right\rangle \simeq \langle b_i b_j\rangle \left\langle f^\dagger_{i\uparrow} f^\dagger_{j\downarrow}\right\rangle$. At zero temperature we have $\left\langle c^\dagger_{i\uparrow}c^\dagger_{j\downarrow}\right\rangle \simeq \delta\Delta$.

4.4 Results and discussion

4.4.1 VMC approach

The VMC approach allows the exact evaluation (up to statistical error bars) of the energy expectation value of the Gutzwiller projected trial functions defined previously. The goal is now to find the lowest energy state at each doping level. To compare the energy expectation values of the different states we define the *condensation energy* e_c

$$e_c = e_{\text{var}} - e_{\text{FS}}, \tag{4.13}$$

which is the energy gain per site with respect to the FS state, the Gutzwiller projected Fermi sea. The results for the 72 and the 144 sites cluster are shown in figures 4.3 and 4.4. We have checked that our variational subspace is large enough by minimizing the trial function (4.1) on the 72 sites cluster with respect to all parameters of the Hamiltonian (1.23) simultaneously, not allowing however the breaking of translational symmetry. By comparing the results for the two clusters we see that our results are rebust with respect to size effects.

For all filling factors we have found that the isotropic hopping term $t_{ij} \equiv 1$ and $\theta_{ij} \equiv 0$ always give the minimal energy. Moreover for the symmetry of the RVB state we found $d_{x^2-y^2}+id_{xy}$ symmetry in the minimal energy configuration at all dopings, *i.e.* the phases in equation (4.2) are given by $\phi_1 = 2\pi/3$, $\phi_2 = 4\pi/3$, and $\phi_3 = 0$. Of course one can interchange these phases and also add or subtract 2π to each of them and still the same energy.

In the reminder of this section we will describe in detail the different phases appearing in the honeycomb lattice from our VMC simulations.

4.4.2 Half-filling

At half-filling we found that the optimal energy wavefunction is the RVB/AF mixed state. This state has a considerable fraction (66%) of the classical Néel magnetism. However, our variational ansatz seems to overestimate the tendency

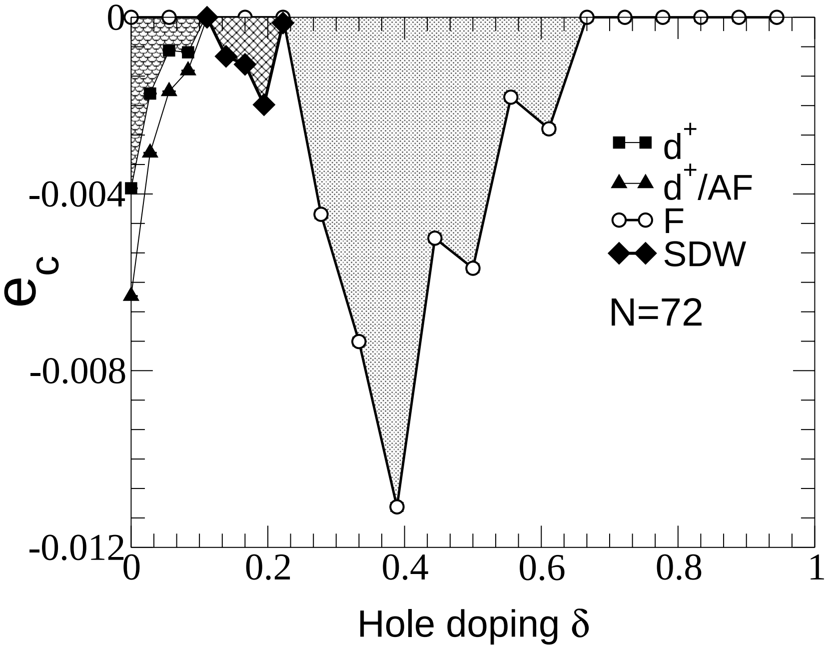

Figure 4.3: Condensation energy versus doping for the 72 site lattice of the various proposed wavefunctions.

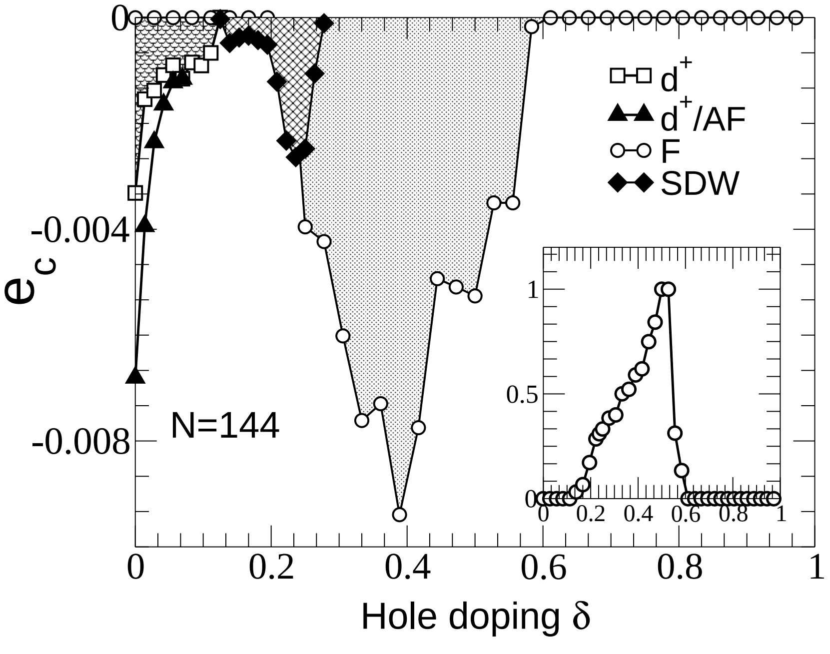

Figure 4.4: Condensation energy versus doping for the 144 site lattice of the various proposed wavefunctions. Inset: polarization of the ferromagnetic wavefunction divided by the saturation value.

lattice	FS	best VMC	QMC
triangular	$-0.3547(2)$	$-0.5330(5)$ [112]	$-0.5450(1)$ [82]
square	$-0.4270(2)$	$-0.6640(1)$ [32]	$-0.6692(1)$ [113]
honeycomb	$-0.5275(2)$	$-0.5430(2)$	$-0.5440(10)$ [114]

Table 4.1: We compare the Heisenberg energy per site in the thermodynamic limit (in units of J) from VMC (Gutzwiller projected FS, the best available trial state) and from exact quantum Monte Carlo simulations.

towards antiferromagnetism: QMC calculations give a lower value for the magnetic order (53% of the classical value [106]). The magnetic order is slightly more renormalized in the honeycomb lattice than in the square lattice, where QMC gives a magnetic order of 60% of the classical value [111]). This is expected as the fluctuations should be larger in the honeycomb lattice due to a lower coordinance number. The over estimation of magnetism at half-filling seems to be a general feature of this type of wavefunction, since the same discrepancy occurs also for the triangular and square lattice [32, 112].

As can be seen from table 4.1, the Gutzwiller projected Fermi sea state gives a value surprisingly close to the exact value in the honeycomb lattice. This is not the case for the square and the triangular lattices. However from figure 4.5 it becomes clear that there is no fundamental difference in the projected FS state on different lattices. The spin-spin correlations decrease with distance very rapidly to zero for all lattices with the only difference that the nearest neighbor correlations are substantially larger on the honeycomb lattice.

4.4.3 Magnetism and Superconductivity

We find that superconductivity is observed in the small range of doping $\delta =]0, \frac{1}{8}[$. The BCS pairing is suppressed at the doping which corresponds to the van Hove singularity in the free electron density of states. We note also that a coexistence of a Néel phase and superconductivity is present in the range $[0, 0.07]$ (see figure 4.6). The VMC simulations and the self-consistent MF calculations predict $d_{x^2-y^2}+id_{xy}$ symmetry for the superconducting order parameter. Also the amplitude of the mean-field pairing order parameter is in good agreement with the variational calculations in the relevant range of doping $]0, 1/8[$. There is a strong reduction of the order parameter close to 1/8 doping, and the MF solutions show a long tail falling down at $\delta = 0.4$. The long MF tail for dopings larger than 1/8 has no relevance since we have shown in our VMC calculations that superconductivity is completely suppressed by SDW and ferromagnetic instabilities in this region.

Interestingly, the excitations of the quasi-particles in the MF scheme are gapless at half-filling, but the excitation gap rises up to a maximum value of approx-

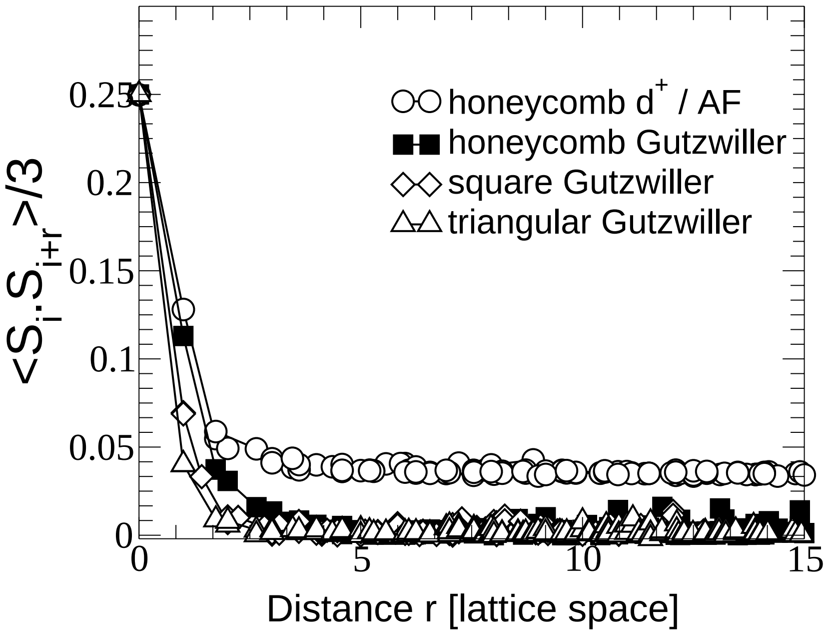

Figure 4.5: Spin-spin correlations of the Gutzwiller projected Fermi sea as a function of distance for different lattices.

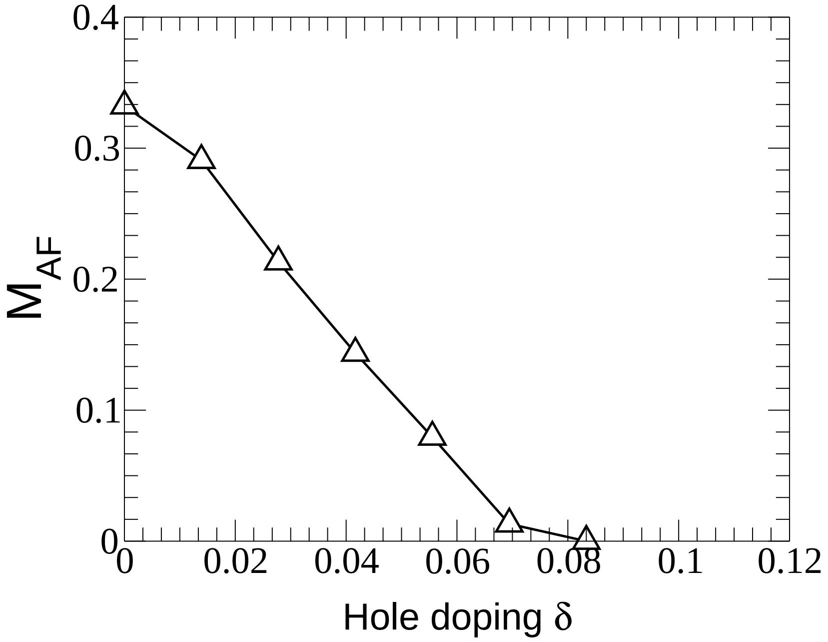

Figure 4.6: The staggered magnetization of our best wavefunction versus doping for the 144 site cluster.

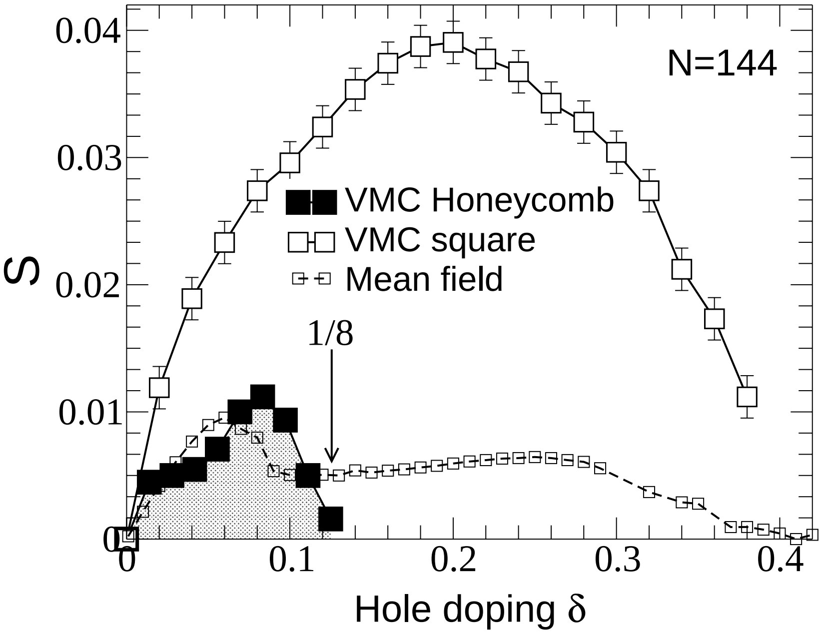

Figure 4.7: Superconducting order parameter of our best wavefunction versus doping in the 144 site cluster (filled squares). For the same value of J, we show the slave-boson mean-field results (small open squares) the d-wave superconducting order parameter (open squares) with periodic boundary conditions along e_x and anti-periodic conditions along e_y in a 100 site cluster.

imatively 0.15 t (this rise and the maximal value seem to be independent of the J value) and decreases to zero again. For comparison, the gap is always zero in the square lattice, and in the triangular lattice it is finite at any doping except at half-filling.

The range and amplitude of the superconducting phase suggests that only weak superconductivity is observed in the honeycomb lattice (see figure 4.7): the maximal amplitude and the range of existence are four times smaller than the ones of the d–wave pairing in the square lattice. The amplitudes in the triangular lattice are twice as large in the hole doped ($t < 0$) case and similar in the electron doped case [112]. This is argued to be an effect of the van Hove singularity at hole doping 1/8 which lies relatively close to half-filling.

4.4.4 Spin Density Wave and Ferromagnetism

At the van Hove singularity a spin density wave is emerging which is stable in the range $\delta = [\frac{1}{8}, 0.22]$. The wavevector of this phase corresponds to one of the Fermi surface nesting vectors at 1/8 doping (see figure 4.1). To characterize this state after Gutzwiller projection we measured the on-site magnetization for every

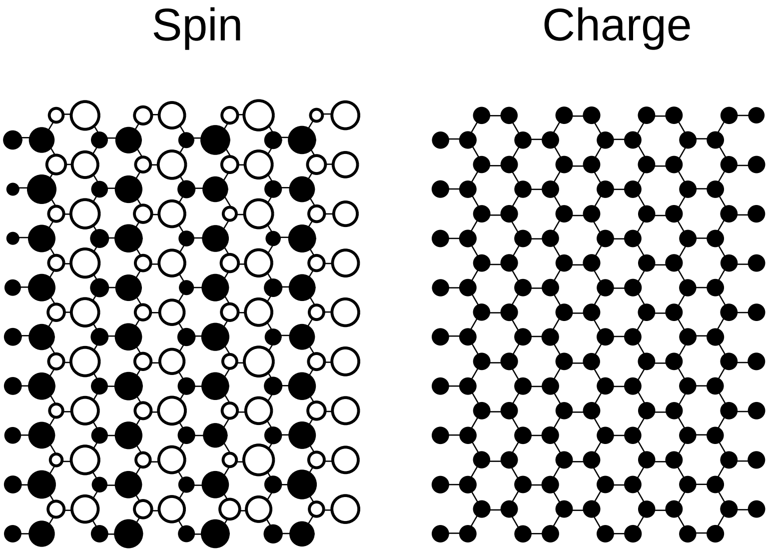

Figure 4.8: On the left: mean on-site magnetization for the spin density wave wavefunction at doping $\delta = 0.18$ on the 144 sites cluster. Size of the symbols are the absolute value of the on-site spin, black filled circles are denoting down spin, and open circles are for up spins. The absolute value for the big (small) circles is $S_i^z = 0.20(1)$ ($S_i^z = 0.10(1)$). On the right: mean value of the on-site charge. We find that the charge is uniformly distributed among the lattice.

site of the lattice at doping $\delta = 0.18$ (see figure 4.8). We found that the charge is uniformly distributed among the lattice, but the spins are forming stripe like patterns. Incommensurate phases were not investigated in the present work, but could be variationally stabilized as well.

An optimization of the kinetic energy can be obtained for doping $\delta > 0.22$ by a small polarization of the system. Indeed, the spin density wave phase is replaced by a weakly polarized ferromagnetic phase at doping $\delta = 0.22$. Then the system is polarized progressively, reaching a 100% polarization at $\delta = 0.5$, and zero polarization occurs again at $\delta = 0.6$ (see inset of figure 4.4). This ferromagnetic phase is still very different from the Nagakoa ferromagnetism observed in the triangular lattice. In the triangular lattice the system reaches a 100% polarization very quickly, and the range of existence is centered around the van Hove singularity, leading to the strongest energy gain exactly at this singularity; here the polarization is done progressively when going away from the van Hove singularity.

This result is in agreement with reference [115] where it was shown that a fully polarized state is unstable in the intervalls $\delta =]0.379, 0.481[$ and above $\delta = 0.643$.

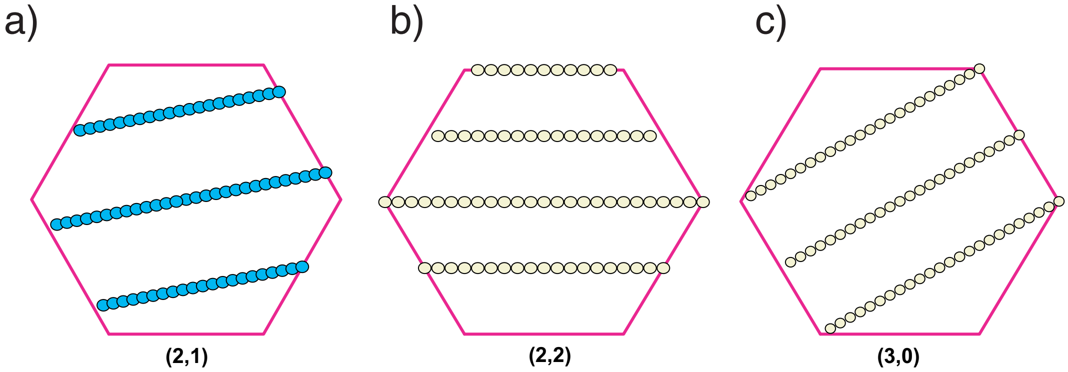

Figure 4.9: Reciprocal space of a) the (2,1) tube , b) the armchair (2,2) tube, and c) the zig-zag (3,0) tube. The armchair and zig-zag tubes have a metallic dispersion.

4.5 Variational Monte-Carlo applied to the Carbon nanotubes

The study of carbon nanotubes is also an interesting event, since their discovery by Iijima in 1991 [116], has become a full research field with significant contributions from all areas of research in solid-state. Single-walled carbon nanotube (SWCNT) are constituted by a single graphene plane wrapped into a cylinder. The Fermi surface of graphene is very particular: it is reduced to six discrete points at the corners of the $2D$ lattice Brillouin zone [117] as shown in Fig.4.1. As a result, depending on their diameter and their chirality which determine the boundary conditions of the electronic wave functions around the tube, the nanotube can be either semiconducting or metallic, depending on the lines of k points in the Brillouin Zone crosses the 6 points of the Fermi surface (see Fig. 4.9). It has been shown that only the zero-chirality armchair nanotubes have zero electronic band gap, the others having a small charge gap and being therefore semi-conductors or insulators depending on their radius and chirality. Let us note that the special zig-zag geometry has also a zero charge gap in the free electronic band theory.

While superconductivity is well established in graphene, this phenomenon was only recently investigated for the nanotubes : intrinsic superconductivity was experimentally observed in ropes of nanotubes [118]. Data show the existence of intrinsic superconductivity in ropes of carbon nanotubes in which the number of tubes varies between 30 and 400. The question of the existence of superconducting correlations in the limit of the individual tube cannot however be answered yet.

Whereas graphene is doped with alkali-dopants, there are no chemical dopants in the ropes of carbon nanotubes. As shown in previous works there is some possibility of hole doping of the tubes by the gold metallic contacts [119].

Very interestingly, the nanotubes allow the investigation of superconductivity in the $1D$ limit which was never explored before. We propose in this section to study the $t-J$ model on wrapped honeycomb sheet in order to investigate how our variational wavefunction behaves in this limit. The variational wavefunction supports, as in the previous section, both antiferromagnetism and superconductivity order parameters.

Nevertheless, in $1D$ systems it is known that no continuous symmetry can be broken and therefore we do not expect to stabilize real long-range order in the true quantum ground state. The continuous symmetry breaking is indeed necessary for superconductivity (broken $U(1)$ symmetry) and also for antiferromagnetism (broken $SU(2)$ symmetry). Although these phases cannot form the true ground-state of the $t-J$ model, the fluctuations around them can still be important for determining its physics. For example, one could imagine that such fluctuations stabilize a superconducting state in ropes of nanotubes. In view of this argument, we believe that it is pertinent to study the tendency toward superconductivity in nanotubes with our wavefunctions.

We therefore use the variational approximation for different chiralities $\mathbf{T_1} = (l_1, l_2)$ (the notation was introduced in section 4.3). The vector $\mathbf{T_1}$ fixes the chirality of the nanotube, and $\mathbf{T_2}$ is chosen to be orthogonal to $\mathbf{T_1}$. We have considered one armchair nanotube of chirality $(2,2)$, zig-zag nanotubes $(3,0)$ and $(4,0)$, and the other tubes $(2,1)$, $(3,1)$ and $(3,2)$. We used periodic boundary along $\mathbf{T_1}$, such that the tube is wrapped. The geometry of a carbon nanotube imposes that the tube is open along $\mathbf{T_2}$. However, to minimize the finite size effect, we have also used periodic boundary conditions in this direction. The tube was studied in the limit when $\|\mathbf{T_2}\| \gg \|\mathbf{T_1}\|$. Let us emphasize that in experiments the nanotubes have bigger diameter than the one considered here: the size in experiments would rather correspond to $(10,10)$ wrapping for the armchair nanotube. Besides, the size of the nanotubes in experiments is not the same for all of the tubes, and a distribution of sizes is expected.

Eventually, the $t-J$ model describes the physics of a doped Mott insulator. When we consider this model for nanotubes, the question whether the undoped compounds are still close to the Mott-insulating phase is relevant. However, the spin-gap obtained by QMC calculation for the different nanotubes is finite, although its value decreases when the diameter of the tube is larger. Therefore, it is expected that close to half-filling the ground state of the nanotubes is not a Fermi liquid. Superconductivity, if present in nanotube, might therefore be driven by strong correlation in these compounds, as opposed to a BCS phonon-mediated mechanism.

4.5.1 Néel-like fluctuations in carbon nanotubes at half-filling

When minimizing the energy of our wavefunction on different nanotubes, we find that antiferromagnetism is still stabilized. The stabilization of finite long-range AF order in our quasi-$1D$ system is obviously an artefact of our calculations, since the Mermin-Wagner theorem [120] implies that no continuous symmetry of the hamiltonian can be broken at $T = 0K$ in a $1D$ system. Nevertheless, we expect that our results give a qualitative answer on the strength of the Néel correlations. For instance, we expect that when the variational magnetic order is strong, then the true ground will certainly have strong Néel like fluctuations as well. Furthermore, our variational results might hold for experiments done on a finite set of neighboring nanotubes, where the inter-tube coupling might restore the possibility for true long-range magnetic order.

We show a benchmark the variational calculations at half-filling in Table 4.2. We have first carried on calculations at half-filling, to be able to compare with the exact results obtained with the Quantum Monte-Carlo method.

Because the carbon nanotubes break the 120° symmetry which was present in the $2D$ honeycomb lattice, we expect that the exchange energy is also anisotropic. In Table 4.2 we depict the nearest-neighbor exchange energy in the three different directions of the lattice $\mathbf{a_i}$.

Interestingly, the variational approximation reproduces remarkably well the Quantum Monte-Carlo results. The comparison of the different wavefunction shows, on one hand, that the Gutzwiller wavefunction catches already approximatively the good symmetry in some of the nanotubes, on another hand, in addition the introduction of the AF variational parameter allows to correct slightly the exchange energy so that we get similar results to the QMC. The anisotropy of the exchange energy which is already present in the Gutzwiller wavefunction sheds light on the fact that the projection of the $t-J$ model plays a subtle role, that allows to already catch some of the features of the true ground state.

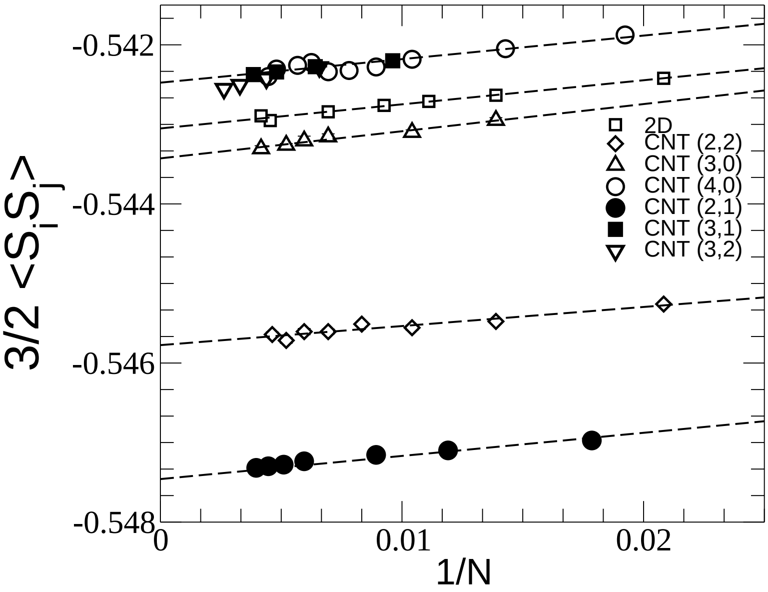

Figure 4.10: Scaling of the Heisenberg energy per site ($t - J$ model at half-filling) for our best variational wavefunction.

In order to compare further with the QMC, we have calculated the energy per site and staggered magnetization per site for different nanotube lengths, such that we could extrapolate the result in the thermodynamic limit (see Fig. 4.10, 4.11, and Table 4.3). Unexpectedly, we find that the AF/RVB wavefunction is still a good Ansatz for the nanotubes at half-filling.

Nanotube	$\langle S_i \cdot S_{i+a_1}\rangle$	$\langle S_i \cdot S_{i+a_2}\rangle$	$\langle S_i \cdot S_{i+a_3}\rangle$
$(2,2)$			
QMC	$-0.376(1)$	$-0.360(1)$	$-0.360(1)$
VMC Δ/AF	$-0.372(1)$	$-0.360(1)$	$-0.356(1)$
VMC Δ	$-0.379(1)$	$-0.350(1)$	$-0.349(1)$
VMC Gutzwiller	$-0.316(1)$	$-0.360(1)$	$-0.368(1)$
$(3,0)$			
QMC	$-0.374(1)$	$-0.354(1)$	$-0.374(1)$
VMC Δ/AF	$-0.369(1)$	$-0.348(1)$	$-0.373(1)$
VMC Δ	$-0.374(1)$	$-0.336(1)$	$-0.377(1)$
VMC Gutzwiller	$-0.360(1)$	$-0.330(1)$	$-0.362(1)$
$(4,0)$			
QMC	$-0.367(1)$	$-0.356(1)$	$-0.369(1)$
VMC Δ/AF	$-0.364(1)$	$-0.351(1)$	$-0.370(1)$
VMC Δ	$-0.372(1)$	$-0.313(1)$	$-0.386(1)$
VMC Gutzwiller	$-0.370(1)$	$-0.310(1)$	$-0.376(1)$
$(2,1)$			
QMC	$-0.392(1)$	$-0.339(1)$	$-0.373(1)$
VMC Δ/AF	$-0.410(1)$	$-0.330(1)$	$-0.363(1)$
VMC Δ	$-0.430(1)$	$-0.308(1)$	$-0.353(1)$
VMC Gutzwiller	$-0.434(1)$	$-0.264(1)$	$-0.355(1)$
$(3,1)$			
QMC	$-0.366(1)$	$-0.359(1)$	$-0.371(1)$
VMC Δ/AF	$-0.363(1)$	$-0.352(1)$	$-0.371(1)$
VMC Δ	$-0.354(1)$	$-0.312(1)$	$-0.407(1)$
VMC Gutzwiller	$-0.351(1)$	$-0.380(1)$	$-0.322(1)$
$(3,2)$			
QMC	$-0.369(1)$	$-0.362(1)$	$-0.360(1)$
VMC Δ/AF	$-0.373(1)$	$-0.355(1)$	$-0.362(1)$
VMC Δ	$-0.390(1)$	$-0.319(1)$	$-0.360(1)$
VMC Gutzwiller	$-0.380(1)$	$-0.313(1)$	$-0.361(1)$

Table 4.2: Nearest-neighbor exchange energy in the three directions for a 144 site clusters for various wavefunctions are depicted. Data obtained with the Quantum Monte-Carlo method are also shown.

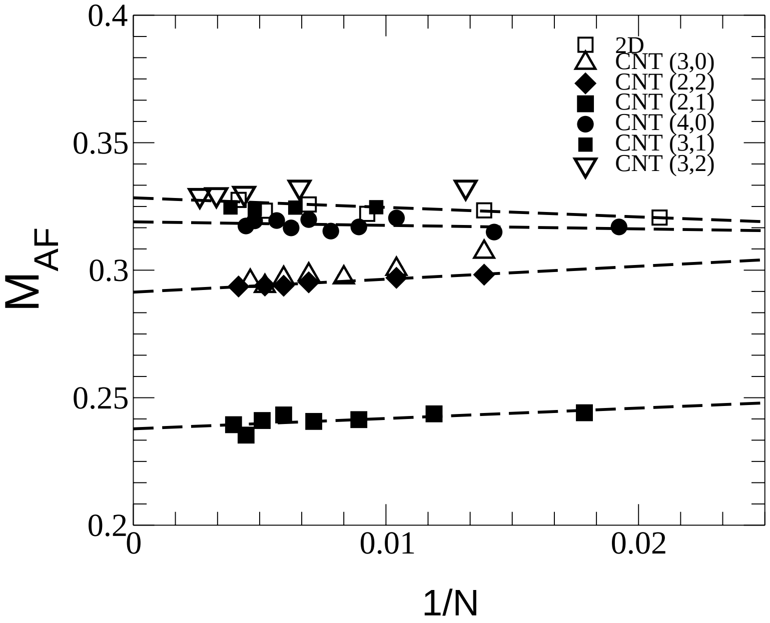

Figure 4.11: Scaling of the staggered magnetization per site in the Heisenberg model ($t - J$ model at half-filling) for our best variational wavefunction.

The antiferromagnetic order depends also on the wrapping of the tube. The amplitude of the spin-spin correlations versus the diameter of the tube is shown in Fig.4.12. We find that it decreases very fast when the diameter reaches the diameter of the 2-leg ladder case. In this limit, the variational magnetism is totally suppressed.

4.5.2 Doping Carbon nanotubes

Our variational wavefunction has the advantage to allow hole doping. Therefore, since it reproduces well the Quantum Monte-Carlo results at half-filling, we have studied the effect of hole doping.

We observe that not only the amplitude of superconductivity, but the phase of the pairing on each nearest neighbors link depends on the wrapping of the tube (see Fig.4.13). We have measured the phase after projection of the BCS pairing in the different tubes (see also Table 4.3). We observe that the phases of the pairing observable is moving from the $d_{x^2-y^2} + id_{xy}$ symmetry in the case of the 2 dimensional lattice towards intermediate value and converge to the d-wave symmetry in the case of the 2-leg ladder, which is also the smallest nanotube that can be wrapped with a 2-site unit-cell. In conclusion, we find both the suppression of the magnetism when the diameter is small (see Fig. 4.12) and reaches the limit of the 2-leg ladder, and we find an enhancement of the pairing

Tube	E_{var}/N	E_{QMC}/N	M_{AF}	ϕ_{a_1}	ϕ_{a_2}	ϕ_{a_3}	$\lvert\Delta_{a_1}^{max}\rvert$	$\lvert\Delta_{a_2}^{max}\rvert$	$\lvert\Delta_{a_3}^{max}\rvert$	Δ_S
$2D$	−0.5430(1)	−0.5450(10)	0.330(2)	0	0.66(1)	1.33(1)	0.0100(1)	0.0100(1)	0.0100(1)	0
(3,0)	−0.5458(1)	−0.5498(5)	0.290(2)	1.50(1)	1.00(1)	0.0140(1)	0.0069(1)	0.0140(1)	0.110(10)	0.110(10)
(2,2)	−0.5435(1)	−0.5482(5)	0.290(2)	1.25(1)	1.00(1)	0.0140(1)	0.0110(1)	0.0140(1)	0.094(5)	0.094(5)
(4,0	−0.5425(1)	−0.5468(10)	0.320(2)	0	1.25(1)	0.25(1)	0.0070(1)	0.0080(1)	0.0070(1)	0.04(1)
(2,1)	−0.5475(1)	−0.5529(1)	0.240(2)	0	1.25(1)	0.75(1)	0.0100(1)	0.0080(1)	0.0080(1)	0.14(1)
(3,1)	−0.5426(1)	−0.5472(1)	0.330(2)	0	1.50(1)	0.90(1)	0.011(1)	0.013(1)	0.011(1)	0.028(2)
(3,2)	−0.5427(1)	−0.5462(1)	0.328(2)	0	1.31(1)	0.82(1)	0.005(1)	0.007(1)	0.007(1)	0.026(1)

Table 4.3: Heisenberg energies per site E/N obtained in the variational wavefunction (E_{var}) and by QMC (E_{QMC}) are shown. Both the energy and the staggered magnetization per site M_{AF} were extrapolated to the thermodynamic limit. Also the amplitude ($|\Delta_{a_i}^{max}|$) and the phase (ϕ_{a_i}) of the pairing observable obtained at optimal doping are shown. The phases are in units of π. Finally, the spin-gap Δ_S obtained by QMC is depicted.

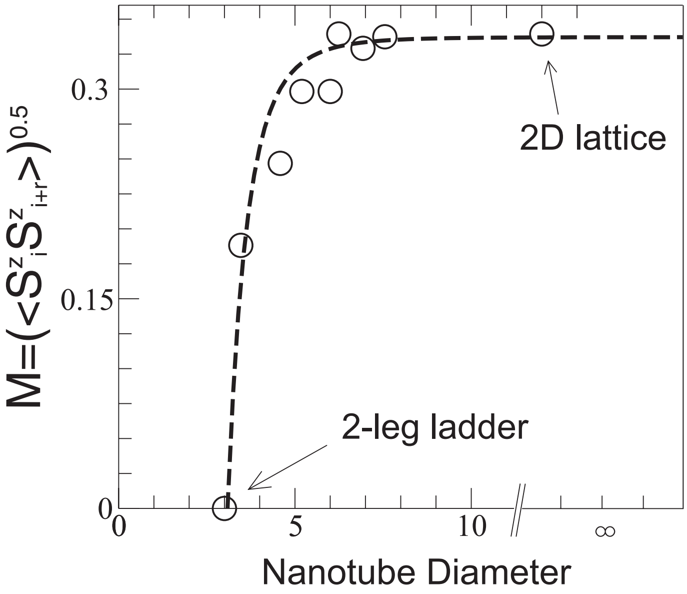

Figure 4.12: Spin-spin correlations at half-filling obtained by VMC in our best variational wavefunction. The values were extrapolated to the thermodynamic limit of the nanotubes. The value obtained for the 2D honeycomb lattice is also shown.

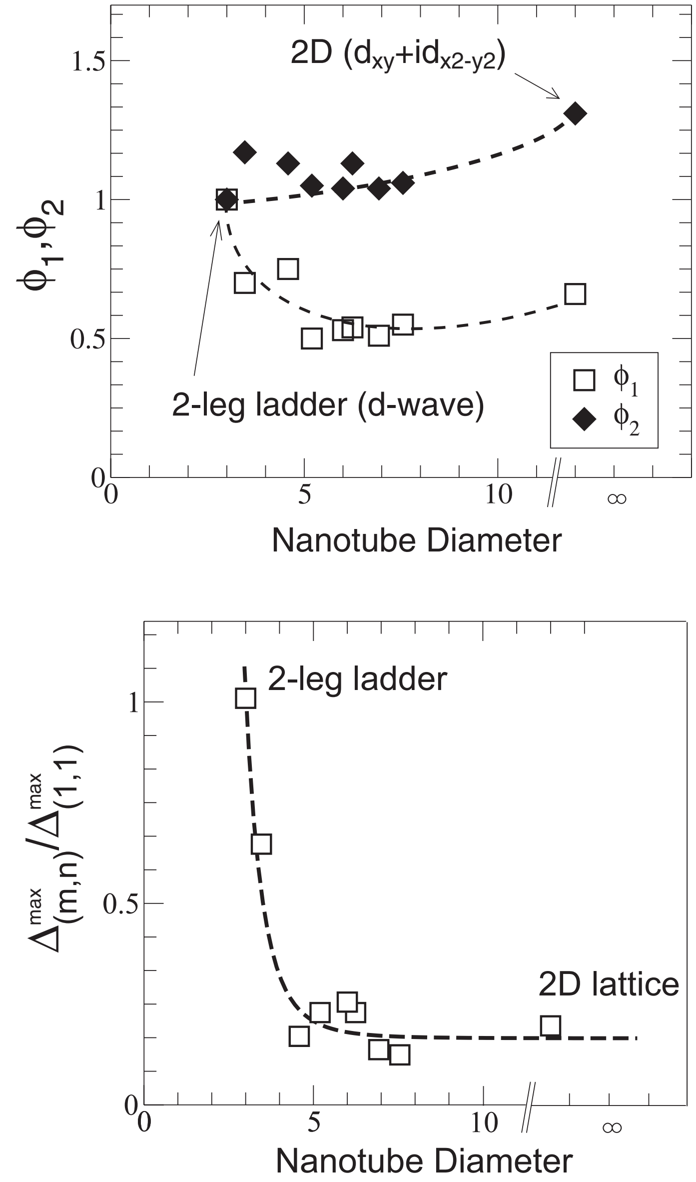

Figure 4.13: Maximum pairing amplitude (bottom figure) obtained in the projected variational wavefunction and phases of the pairing ϕ_1,ϕ_2 for the different nanotubes (top figure). The symmetry of the pairing is $d_{x^2-y^2} + id_{xy}$ like in the two dimension limit and d-wave like in the limit of the 2-leg ladder. The dashed lines are guide to the eyes.

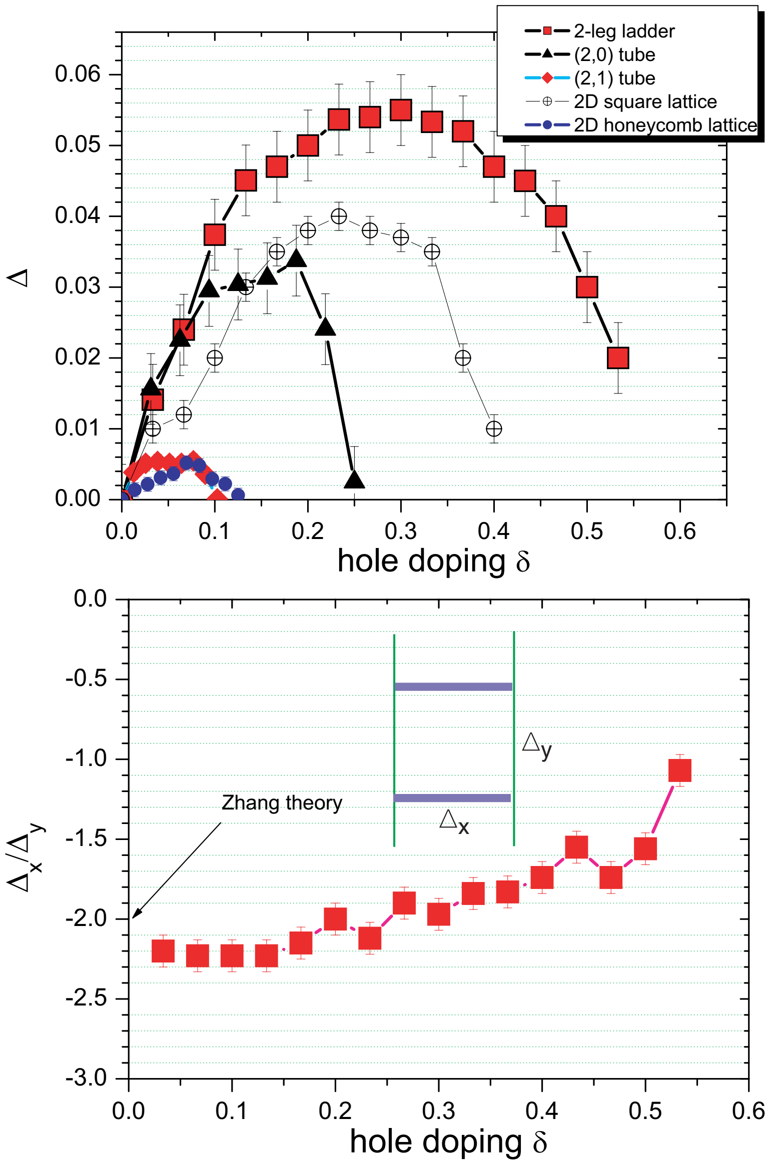

Figure 4.14: Top: Pairing amplitude obtained from the pairing operator correlations in the projected variational wavefunction. When the pairing amplitude is anisotropic, the maximum value of the pairing along the different directions is shown. Inset: the symmetry of the pairing in the 2-leg ladder is shown. The pairing is stronger along the arms of the ladder, and is with opposite sign and weaker amplitude in the vertical direction. The pairing amplitude obtained in the two dimensional square lattice (open circles) and honeycomb lattice (blue circles) are shown for comparison. Bottom: the ratio Δ_x/Δ_y is shown for the 2-leg ladder. S.C. Zhang predict that $\Delta_x = -2\Delta_y$ in the limit of zero doping [121]. We find within the variational results a ratio ≈ 2.2, which is not very far from the theory.

order parameter in the same limit (see Fig.4.13). This can be interpreted as the signature that quantum fluctuations become much larger when the tube reaches the one dimensional limit, and our variational (but non-physical) magnetic parameter is no longer stabilized when these fluctuations become too strong. At the same time, it is interesting to note that the pairing survives very well in the 1D limit, though we do not expect any real pairing in a quasi-1D model. Indeed, in this limit the ground state will be a Luttinger liquid. The fact that the pairing is large in our variational approach might be a signature that the true Luttinger liquid ground state is not a Fermi liquid and does not have magnetic order.

4.6 Conclusion

We have determined the ground state phase diagram of the $t-J$ model (with a generic value of $J = 0.4$) on the $2D$ honeycomb lattice using VMC calculations. Our results are summarized in Fig. 4.15. At half-filling, we have found antiferromagnetism and superconducting variational parameters that coexist in the variational wavefunction. The alternating magnetization is 66% of the classical value, which is slightly higher than the 50% obtained with exact quantum Monte Carlo. However, the energy obtained is very close to the exact value: we find an Heisenberg energy per site with VMC of 0.5430(1) which is only 0.3% higher than the QMC value. A phase of coexistence of the two order parameters is found in the range $\delta = [0, 0.07]$, and superconductivity is suppressed at the van Hove singularity. Therefore the range of superconducting order is $\delta =]0, \frac{1}{8}[$. The amplitude and range of existence of the superconducting parameter are four times smaller than in the square lattice. We found good agreement between the VMC calculations and an the RVB MF theory in the superconducting phase, namely the same $d_{x^2-y^2} + id_{xy}$ symmetry and a similar amplitude of the pairing order parameter. Moreover the spinon excitation spectrum is gapped for $0 < \delta \lesssim 1/8$.

For hole dopings larger than 1/8, we find that a spin density wave (SDW) of wavevector $\boldsymbol{Q} = 1/2(\mathbf{b_1^*} - \mathbf{b_2^*})$ is stabilized in the range $\delta = [\frac{1}{8}, 0.22]$. The SDW phase leads to an optimization of the kinetic energy. However, a stronger gain in kinetic energy, and also a lower variational energy, is obtained at $\delta = 0.22$ with a weak ferromagnetic polarized phase, which is polarized linearly and reaches full polarization at doping $\delta = 0.5$. Ferromagnetism disappears again at $\delta = 0.6$.

The variational results discussed in this work might be relevant for the symmetry of the pairing measured in the superconducting phase in graphene. Moreover, it was found in the present work that the nanotubes have a finite spin-gap, and therefore the nanotubes close to half-filling can be argued to be close to the Mott-insulating phase. The VMC calculations show that the phase of the complex pairing is different in the nanotubes than in the 2D honeycomb lattice, provided the superconducting phase is not an artefact of the calculations. This observation is relevant for the experiments, where superconductivity is found in

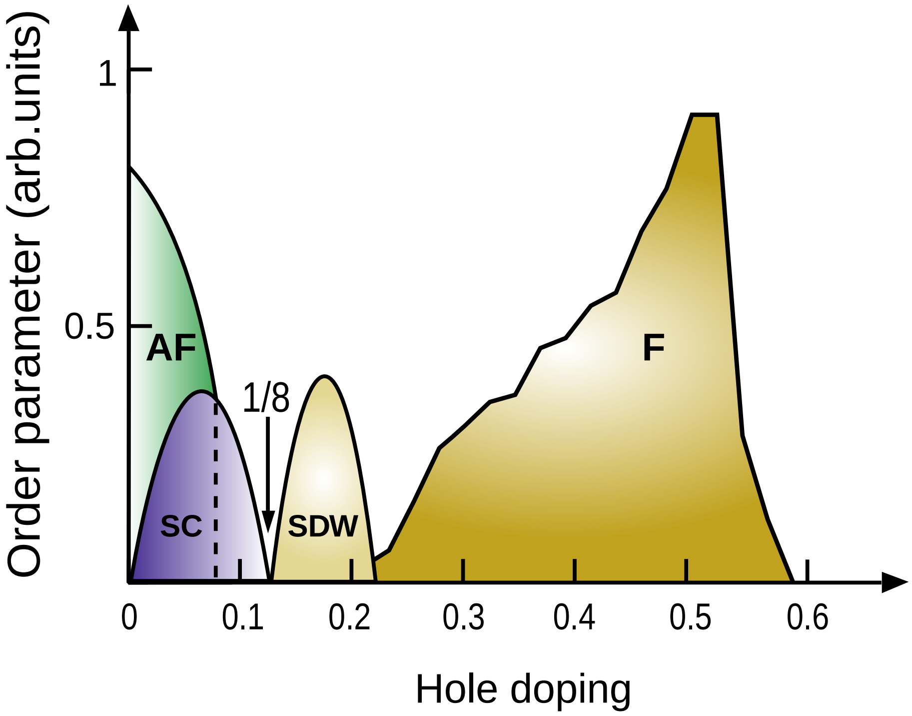

Figure 4.15: Cartoon picture of the phase diagram: the superconducting phase (SC), the Néel phase (AF), the spin density wave phase with pitch vector $\mathbf{Q}_N = (\pi, -\pi/\sqrt{3})$ (SDW), and the partially polarized ferromagnetic phase (F).

ropes of nanotubes.

Chapter 5

Bond-order-wave staggered flux phase for the $t\!-\!J$ model on the square lattice

5.1 Outline

Motivated by the observation of inhomogeneous patterns in some high-T$_c$ cuprate compounds, several variational Gutzwiller-projected wave-functions with built-in charge and bond order parameters are proposed for the extended $t-J-V$ model on the square lattice at low doping. First, following a recent Gutzwiller-projected mean-field approach (Phys. Rev. B. **72**, 060508(R) (2005)), we investigate, as a function of doping and Coulomb repulsion, the stability of the staggered flux phase with respect to small spontaneous modulations of squared unit cells ranging from 2×2 to $\sqrt{32} \times \sqrt{32}$. It is found that a 4×4 bond-order (BO) modulation appears spontaneously on top of the staggered flux pattern for hole doping around 1/8. A related wave-function is then constructed and optimized accurately and its properties studied extensively using an approximation-free variational Monte Carlo scheme. Finally, the competition of the BO-modulated staggered flux wave-function with respect to the d-wave RVB wave-function or the commensurate flux state is investigated. It is found that a short range Coulomb repulsion penalizes the d-wave superconductor and that a moderate Coulomb repulsion brings them very close in energy. Our results are discussed in connection to the STM observations in the under-doped regime of some cuprates. This work was done in collaboration with the group of Didier Poilblanc (IRSAMC, Toulouse, France). The very nice work related to the renormalized mean-field calculations within this chapter were done by Sylvain Capponi and Didier Poilblanc. The work was published in PRB 74, 104506 (2006).

5.2 Checkerboard Pattern in the cuprates

The phase diagram of the hole-doped cuprates shows mainly four different electronic phases existing at low temperature. Among them are the Mott insulator phase, the superconducting phase, and the more usual Landau Fermi liquid phase (or metallic phase). A fourth phase, of controversial nature, occurs at light doping, located above the superconducting phase and was named the *pseudogap* regime. This later regime shows peculiar electronic phenomena, prompting for proposals that it might contain a hidden charge or spin order.

With an increasing number of materials and novel experimental techniques of constantly improving resolution, novel features in the global phase diagram of high-T_c cuprate superconductors have emerged. One of the most striking is the observation, in some systems, of a form of local electronic ordering, especially around 1/8 hole doping.

The recent scanning tunneling microscopy/spectroscopy (STM/STS) experiments of underdoped $Bi_2Sr_2CaCu_2O_{8+\delta}$ (BSCO) in the pseudogap state have shown evidence of *energy-independent* real-space modulations of the low-energy density of states (DOS) [122,123,124] with a spatial period close to four lattice spacings. A similar spatial variation of the electronic states has also been observed in the pseudogap phase of $Ca_{2-x}Na_xCuO_2Cl_2$ single crystals ($x = 0.08 \sim 0.12$) by similar STM/STS techniques [125].

Low-temperature ($T = 100mK$) electronic structure imaging studies of a lightly hole-doped copper oxide $Ca_{2-x}Na_xCuO_2Cl_2$ using Tunneling spectroscopy were carried on (see Fig.5.1). The doping was fixed in these studies by using samples with Na concentrations $x = 0.08, 0.10, 0.12$, which leads to superconducting $T_c = 0, 15, 20K$ respectively.

Indeed, for the considered samples, the spectrum exhibits a V shaped energy gap centered at the Fermi energy. It was mainly found that the states within this gap undergo spatial modulations with a checkerboard structure, and has 4 × 4 CuO_2 in the unit-cell. The structure changes only weakly inside the V-shaped energy gap [1] [2].

Although it is not clear yet whether such phenomena are either generic features or really happening in the bulk of the system, they nevertheless raise important theoretical questions about the stability of such structures in the framework of microscopic strongly correlated models.

Moreover, intricate atomic-scale electronic structure variations also exist within the checkerboard larger structure. Therefore, the experimental results would be in

---

[1] Note that the first observation was made around a vortex core in J.E. Hoffman, E.W. Hudson, K.M. Lang, V. Madhavan, H. Eisaki, S. Uchida, and J.C. Davis, Science **295**, 466 (2002).

[2] Note that the *energy-dependent* spatial modulations of the tunneling conductance of optimally doped BSCO can be understood in terms of elastic scattering of quasiparticles. See J.E. Hoffman, K. McElroy, D.H. Lee, K.M. Lang, H. Eisaki, S. Uchida, and J.C. Davis Science **297** 1148 (2002).

agreement with an unanticipated electronic state order, possibly the hidden electronic order existing in the low-temperature pseudo-gap regime of $Ca_{2-x}Na_xCuO_2Cl_2$. Since the cuprates were argued to be well described by strongly correlated models, like the $t-J$ and Hubbard model, and since these theories were successful to explain many of the experimental data, we propose in this chapter to study the $t-J$ Hamiltonian (1.4) on a square lattice, in order to study the possibility for checkerboard like modulations. In this chapter, we consider the model without the $\hat{n}_i\hat{n}_j$ term of the original model:

$$H_{t-J} = -t \sum_{\langle i,j\rangle,\sigma} \left(c^\dagger_{i,\sigma} c_{j,\sigma} + h.c. \right) + J \sum_{\langle i,j\rangle} \mathbf{S}_i \cdot \mathbf{S}_j$$

H_{t-J} operates only in the subspace where there are no doubly occupied sites, which can be formally implemented by a Gutzwiller projector (see later). In the following we set $|t| = 1$ (unless specified otherwise) and we adopt a generic value of $t/J = 3$ throughout the chapter. Because of the particle-hole symmetry in the square lattice the sign of t does not play any role.

In this chapter, we analyze the stability and the properties of new inhomogeneous phases (which may compete in certain conditions with the d-wave superconducting RVB state) by extending the previous mean-field and variational treatments of the RVB theory. In addition, we shall also consider an extension of the simple $t-J$ model, the $t - J - V$ model, containing a Coulomb repulsion term written as,

$$V = \frac{1}{2} \sum_{i \neq j} V(|i-j|) \, (n_i - n) \, (n_j - n) \ , \tag{5.1}$$

where n is the electron density (N_e/N, N_e electrons on a N-site cluster). Generically, we assume a screened Coulomb potential :

$$V(r) = V_0 \frac{\exp^{-r/l_0}}{r} \ , \tag{5.2}$$

where we will consider two typical values $l_0 = 2, 4$ and $V_0 \in [0, 5]$ and where the distance r is defined (to minimize finite size effects) as the *periodized* distance on the torus [3]. The influence of this extra repulsive term in the competition between the d-wave RVB state and some inhomogeneous phases is quite subtle and will be discussed in the following.

One route to deal with the Gutzwiller projection is to use a *renormalized mean-field (MF) theory* [127] in which the kinetic and superexchange energies are renormalized by different doping-dependent factors g_t and g_J respectively. Further mean-field treatments of the interaction term can then be accomplished in the particle-particle (superconducting) channel. Crucial, now well established,

---

[3] The Manhattan distance of Ref. [126] is used.

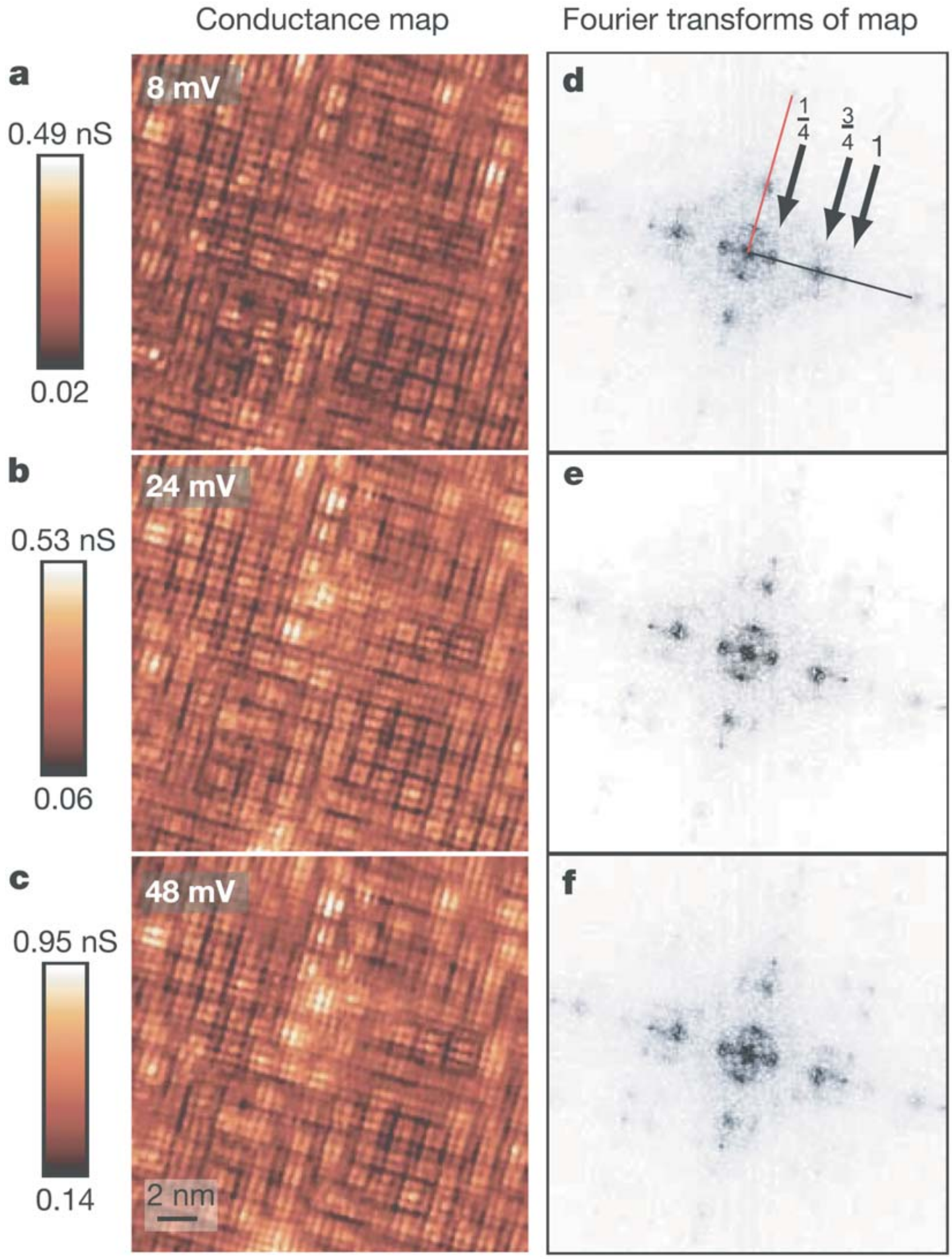

Figure 5.1: The figure was reproduced from Ref. [125]. Left column : conductance map at fixed energies, lying within the V-shape gap (see text) of the energy spectrum, $E_F + 8meV$, $E_F + 24meV$, $E_F + 48meV$ from top to bottom. The local density of state is showing real space modulations consistent with a 4×4 CuO_2 checkerboard structure. Right: the Fourier transform map of the real space modulations. The modulations in the conductance map contains mainly three reciprocal q-vector $q = (1, 0) \times 2\pi/a_0$, $q = (1/4, 0) \times 2\pi/a_0$, $q = (3/4, 0) \times 2\pi/a_0$. The fourier transform of the conductance map does not break the 90° rotational symmetry. The temperature was fixed to $T = 100mK$ and the doping is $x = 0.10$; the bulk critical tempature T_c is for these condition $T_c = 150mK$.

experimental observations such as the existence of a pseudo-gap and nodal quasiparticles and the large renormalization of the Drude weight are remarkably well explained by this early MF RVB theory [22].

An extension of this approach [128,126] will be followed in Section 5.3 to investigate inhomogeneous structures with checkerboard patterns involving a decoupling in the particle-hole channel. As (re-) emphasized recently by Anderson and coworkers [22], this general procedure, via the effective MF Hamiltonian, leads to a Slater determinant $|\Psi_{\rm MF}\rangle$ from which a correlated wave-function $\mathcal{P}_{\mathcal{G}}\,|\Psi_{\rm MF}\rangle$ can be constructed and investigated by VMC.

Since the MF approach offers a reliable *guide* to construct translational symmetry-breaking projected variational wave-functions, we will present first the MF approach in section 5.3 before the more involved VMC calculations in Section 5.4. Novel results using a VMC technique associated to inhomogeneous wave-functions will be presented in Section 5.4.

5.3 Gutzwiller-projected mean-field theory

5.3.1 Gutzwiller approximation and mean-field equations

We start first with the simplest approach where the action of the Gutzwiller projector $\mathcal{P}_{\mathcal{G}}$ is approximately taken care of using a Gutzwiller approximation scheme [31]. We generalize the MF approach of Ref. [128, 129], to allow for non-uniform site and bond densities. Recently, such a procedure was followed in Ref. [126] to determine under which conditions a 4×4 superstructure might be stable for hole doping close to 1/8. We extend this investigation to arbitrary small doping and other kinds of supercells. In particular, we shall also consider 45-degree tilted supercells such as $\sqrt{2} \times \sqrt{2}$, $\sqrt{8} \times \sqrt{8}$ and $\sqrt{32} \times \sqrt{32}$.

The weakly doped antiferromagnet is described here by the renormalized $t-J$ model Hamiltonian,

$$H^{\rm ren}_{t-J} = -tg_t \sum_{\langle ij\rangle\sigma} (c^\dagger_{i,\sigma} c_{j,\sigma} + h.c.) + Jg_J \sum_{\langle ij\rangle} \mathbf{S}_i \cdot \mathbf{S}_j \tag{5.3}$$

where the local constraints of no doubly occupied sites are replaced by statistical Gutzwiller weights $g_t = 2x/(1+x)$ and $g_J = 4/(1+x)^2$, where x is the hole doping. A typical value of $t/J = 3$ is assumed hereafter.

Decoupling in both particle-hole and (singlet) particle-particle channels can be considered simultaneously leading to the following MF hamiltonian,

$$
\begin{aligned}
H_{\mathrm{MF}} = -t \sum_{\langle ij\rangle\sigma} g^t_{ij}(c^\dagger_{i,\sigma}c_{j,\sigma} + h.c.) + \sum_{i\sigma} \epsilon_i n_{i,\sigma} \\
-\frac{3}{4}J \sum_{\langle ij\rangle\sigma} g^J_{i,j}(\chi_{ji}c^\dagger_{i,\sigma}c_{j,\sigma} + h.c. - |\chi_{ij}|^2) \\
-\frac{3}{4}J \sum_{\langle ij\rangle\sigma} g^J_{i,j}(\Delta_{ji}c^\dagger_{i,\sigma}c^\dagger_{j,-\sigma} + h.c. - |\Delta_{ij}|^2),
\end{aligned}
\tag{5.4}
$$

where the previous Gutzwiller weights have been expressed in terms of local fugacities $z_i = 2x_i/(1+x_i)$ (x_i is the local hole density $1-\langle n_i\rangle$), $g^t_{i,j} = \sqrt{z_i z_j}$ and $g^J_{i,j} = (2-z_i)(2-z_j)$, to allow for small non-uniform charge modulations [130]. The Bogoliubov-de Gennes self-consistency conditions are implemented as $\chi_{ji} = \langle c^\dagger_{j,\sigma}c_{i,\sigma}\rangle$ and $\Delta_{ji} = \langle c_{j,-\sigma}c_{i,\sigma}\rangle = \langle c_{i,-\sigma}c_{j,\sigma}\rangle$.

In principle, this MF treatment allows for a description of modulated phases with *coexisting* superconducting order, namely supersolid phases. Previous investigations [126] failed to stabilize such phases in the case of the *pure* 2D square lattice (i.e. defect-free). Moreover, in this Section, we will restrict ourselves to $\Delta_{ij} = 0$. The case where both Δ_{ij} and χ_{ij} are non-zero is left for a future work, where the effect of a defect, such as for instance a vortex, will be studied.

In the case of finite V_0 , the on-site terms ϵ_i may vary spatially as $-\mu+e_i$, where μ is the chemical potential and e_i are on-site energies which are self-consistently given by,

$$
e_i = \sum_{j\neq i} V_{i,j}\langle n_j\rangle\,. \tag{5.5}
$$

In that case, a constant $\sum_{i\neq j} V_{i,j}(\langle n_i\rangle\langle n_j\rangle + n^2)$ has to be added to the MF energy. Note that we assume here a *fixed* chemical potential μ. In a recent work [131], additional degrees of freedom where assumed (for $V_0 = 0$) implementing an unconstrained minimization with respect to the on-site fugacities. However, we believe that the energy gain is too small to be really conclusive (certainly below the accuracy one can expect from such a simple MF approach). We argue that we can safely neglect the spatial variation of μ in first approximation, and this will be confirmed by the more accurate VMC calculations in Section 5.4. Incidently, Ref. [131] emphasizes a deep connection between the stability of checkerboard structures [126] and the instability of the SFP due to nesting properties[4] of some parts of its Fermi surface [132].

---

[4] Note that the Fermi surface of the SFP is made of four small elliptic-like *pockets* centered around ($\pm\pi/2, \pm\pi/2$)

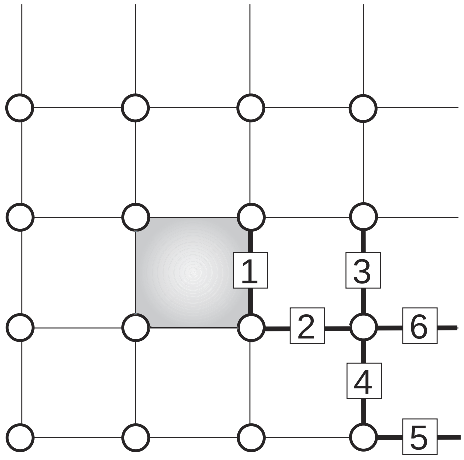

Figure 5.2: 4×4 unit-cell used in both the MF approach and the variational wave-function. Note the existence of 6 independent bonds (bold bonds), that for convenience are labelled from $1-6$, and of 3 *a priori* non-equivalent sites. The center of the dashed plaquette is the center of the (assumed) C_{4V} symmetry. Other sizes of the same type of structure are considered in the MF case, respectively : 2×2, $\sqrt{8} \times \sqrt{8}$, and $\sqrt{32} \times \sqrt{32}$ unit cells.

5.3.2 Mean-field phase diagrams

In principle, the mean-field equations could be solved in real space on large clusters allowing for arbitrary modulations of the self-consistent parameters. In practice, such a procedure is not feasible since the number of degrees of freedom involved is too large. We therefore follow a different strategy. First, we assume fixed (square shaped) supercells and a given symmetry within the super-cell (typically invariance under 90-degrees rotations) to reduce substantially the number of parameters to optimize. Incidently, the assumed periodicity allows us to conveniently rewrite the meanfield equations in Fourier space using a reduced Brillouin zone with a very small mesh. In this way, we can converge to either an absolute or a local minimum. Therefore, in a second step, the MF energies of the various solutions are compared in order to draw an overall phase diagram.

In previous MF calculations [126], stability of an inhomogeneous solution with the 4×4 unit-cell shown in Fig. 5.2 was found around $x = 1/8$. Here, we investigate its stability for arbitrary doping and extend the calculation to another possible competing solution with a twice-larger (square) unit-cell containing 32 sites. The general solutions with different phases and/or amplitudes on the independent links will be referred to as bond-order (BO) phases. Motivated by experiments [122, 125], a C_{4V} symmetry of the inhomogeneous patterns around a central plaquette will again be assumed for both cases. Note that such a feature greatly reduces the number of variational parameters and hence speeds up the convergence of the MF equations. Starting from a central plaquette, like in Fig. 5.2, a larger $\sqrt{32} \times \sqrt{32}$ unit-cell (not shown) can easily be constructed with 10 non-equivalent bonds (with both independent real and imaginary parts) and *a priori* 6 non-equivalent sites. Note that this new unit-cell is now tilted by 45 degrees.

At this point, it is important to realize that patterns with a smaller number of non-equivalent bonds or sites are in fact subsets of the more general modulated structures described above. For example, the SFP is obviously a special case of such patterns, where all the $\chi_{i,j}$ are equal in magnitude with a phase oriented to form staggered currents, and where all the sites are equivalent. This example clearly indicates that the actual structure obtained after full convergence of the MF equations could have *higher* symmetry than the one postulated in the initial configuration which assumes a random choice for all independent parameters. In particular, the equilibrium unit-cell could be smaller than the original one and contain a fraction (1/2 or 1/4) of it. This fact is illustrated in Fig. 5.3 showing two phase diagrams produced by using different initial conditions, namely 4×4 (top) and $\sqrt{32} \times \sqrt{32}$ (bottom) unit-cells. Both diagrams show consistently the emergence of the SFP at dopings around 6% and a *plaquette* phase (2×2 unit-cell with two types of bonds) at very small doping [5] [6]. In addition, a phase with a $\sqrt{8} \times \sqrt{8}$ super-cell is obtained for a specific range of doping and V_0 (see Fig. 5.3 on the top). Interestingly enough, all these BO phases can be seen as *bond-modulated SFP* with 2, 4, 8 and up to 16 non-equivalent (staggered) plaquettes of slightly different amplitudes. This would be consistent with the SFP instability scenario [132] which suggests that the wavevector of the modulation should vary continuously with the doping. Although this picture might hold when $V_0 = 0$, our results show that the system prefers some peculiar spatial periodicities (like the ones investigated here) that definitely take place at moderate V_0.

Let us now compare the two phase diagrams. We find that, except in some doping regions, the various solutions obtained with the 4×4 unit-cell are recovered starting from a twice larger unit-cell. Note that, due to the larger number of parameters, the minimization procedure starting from a larger unit-cell explores a larger phase space and it is expected to be more likely to converge to the absolute minimum. This is particularly clear (although not always realized) at large doping $x = 0.14$, where we expect an homogeneous Fermi Liquid (FL) phase (all bonds are real and equal), as indeed seen in Fig. 5.3 on the bottom. On the contrary, Fig. 5.3 on the top reveals, for $V_0/J \in [1.5, 3]$, a modulated $\sqrt{8} \times \sqrt{8}$ structure, which is an artefact due to the presence of a local minimum (see next).

Since the MF procedure could accidentally give rise to local minima, it is of

---

[5] Note that, in this regime, antiferromagnetism is expected. Such a competition is not considered here.

[6] Also found in $SU(2N)$ mean-field theory; see M. Vojta, Y. Zhang and S. Sachdev, Phys. Rev. B. **62**, 6721 (2000) and references therein.

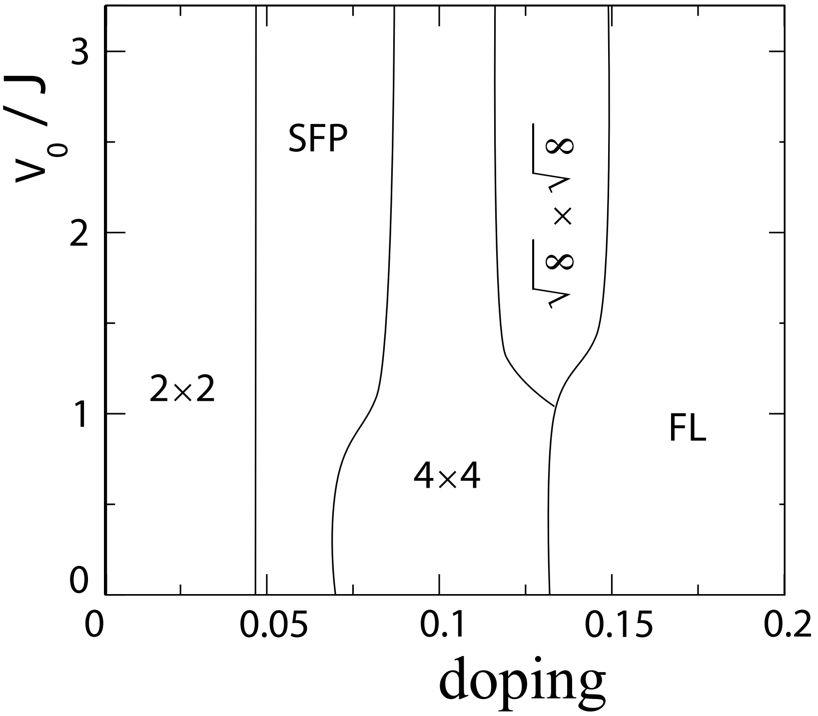

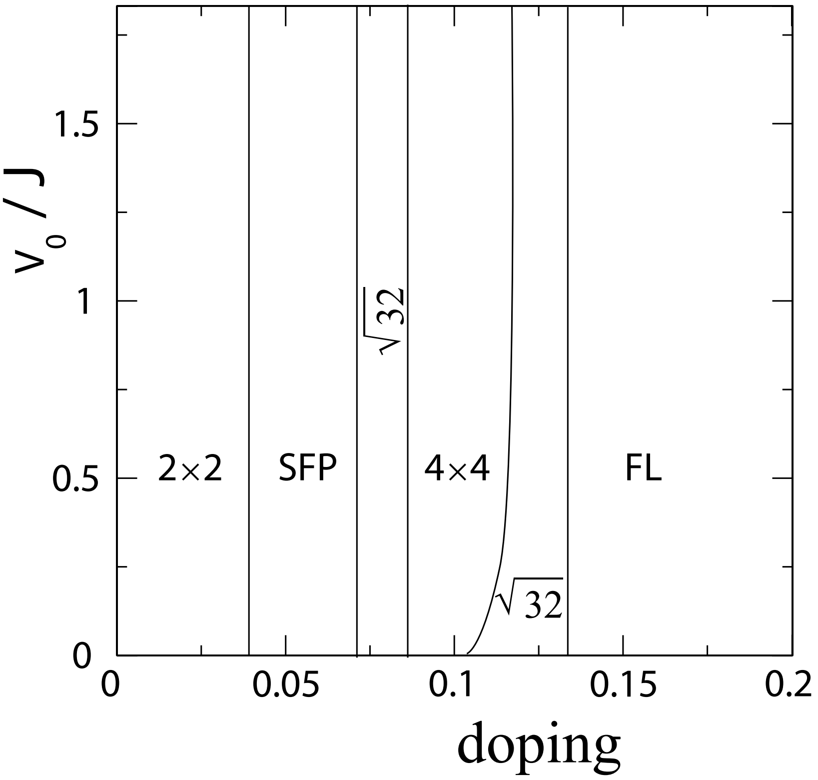

Figure 5.3: Mean-field phase diagrams obtained by solving self-consistently the mean-field equations on a 128×128 lattice (for $l_0 = 4$) vs hole doping x and repulsion V_0 (in units of J). Top: results obtained assuming a 4×4 unit cell; Bottom: same with a $\sqrt{32} \times \sqrt{32}$ tilted unit cell. In both cases, a C_{4v} symmetry is assumed (see text).

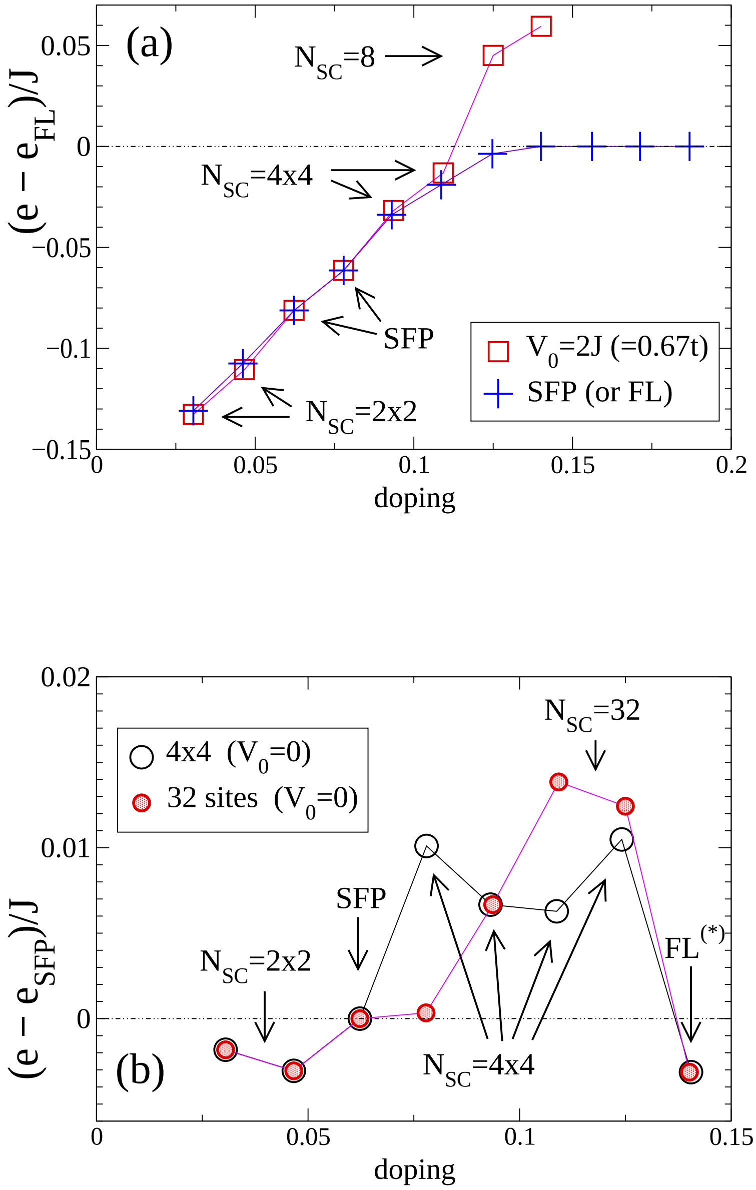

Figure 5.4: (a) Energy per site (in units of J and for $t = 3J$) obtained by solving the mean-field equations using the *initial* 4×4 unit-cell (see text) for a moderate value of V_0. The SFP energy is also shown for comparison. The FL energy has been substracted from all data for clarity. (b) Comparison of the energies (for $V_0 = 0$) using different initial conditions (see text), a 4×4 or a $\sqrt{32} \times \sqrt{32}$ unit-cell; due to very small energy differences, the SFP energy is used as a reference for an easier comparison. The different phases specified by arrows and characterized by the number of sites N_{SC} of their actual supercells refer to the ones in Fig. 5.3. For doping $x = 0.14$, the minimization leads to a solution with small imaginary parts (of order 10^{-4}) very similar to a FL phase, which we call FL*.

interest to compare the MF energies obtained by starting with *random* values of all independent parameters within the two previously discussed unit-cells. For convenience, we have substracted from all data either the FL (in Fig. 5.4(a)) or the SFP (in Fig. 5.4(b)) *reference* energy. From Figs. 5.4(a,b) we see that we can converge towards a local energy minimum, often modulated in space, which is not the absolute minimum. Indeed, over a large doping range, the lowest energy of the all solutions we have found is obtained for homogeneous densities and bond magnitudes. Nevertheless, we see that the 4×4 modulated phase is (i) locally stable and (ii) is very close in energy to the homogeneous (SFP) phase which, often, has a slightly lower energy. Note that, around $x \simeq 1/8$, the states with $\sqrt{8} \times \sqrt{8}$ and $\sqrt{32} \times \sqrt{32}$ supercells are clearly metastable solutions (and using a larger initial unit-cell is not favorable in the latter case). In contrast, in this range of doping, the 4×4 checkerboard state is very competitive w.r.t. the SFP. Therefore, it makes it a strong candidate to be realized either in the true ground state of the model, or present as very low excited state[7]. In fact, considering such small energy differences, it is clear that an accurate comparison is beyond the accuracy of the MF approach. We therefore move to the *approximation-free* way of implementing the Gutzwiller projection with the VMC technique, that allows a detailed comparison between these variational homogeneous and inhomogeneous states.

5.4 Variational Monte Carlo simulations of 4×4 superstructures

Motivated by the previous mean-field results we have carried out extensive Variational Monte Carlo simulations. In this approach, the action of the Gutzwiller projection operator is taken care of exactly, although one has to deal with finite clusters. In order to get rid of discontinuities in the d-wave RVB wave-function, we consider (anti-)periodic boundary conditions along e_y (e_x). As a matter of fact, it is also found that the energy is lower for twisted boundary conditions, hence confirming the relevance of this choice of boundaries. We have considered a 16×16 square cluster of $N = 256$ sites. We also focus on the 1/8 doping case which corresponds here to $N_e = 224$ electrons on the 256 site cluster. Following the previous MF approach, we consider the same generic mean-field hamiltonian,

$$H_{\mathrm{MF}} = \sum_{\langle i,j\rangle,\sigma} \Big(- \tilde{t}_{i,j} c^{\dagger}_{i\sigma} c_{j\sigma} + h.c. \Big) + \sum_{i\sigma} \epsilon_i c^{\dagger}_{i\sigma} c_{i\sigma} \, , \tag{5.6}$$

where the complex bond amplitudes $\tilde{t}_{i,j}$ can be written as $\left|\tilde{t}_{i,j}\right| e^{i\theta_{i,j}}$, and $\theta_{i,j}$ is a phase oriented on the bond $i \rightarrow j$. The on-site terms ϵ_i allow to control the

---

[7] Our 4×4 solution bears some similarities with those obtained within $SU(2N)/Sp(2N)$ mean field theories; see M. Vojta, Phys. Rev. B. **66**, 104505 (2002). Note however that the large-N Sp(2N) scheme implies a superconducting state.

magnitude of the charge density wave. However, the energy was found to be minimized for all the ϵ_i equal to the same value in the range $V_0 = [0, 5]$ and for the two parameters $l_0 = 2, 4$. In fact, we find that strong charge ordered wave-functions are not stabilized in this model [8].

In this Section, we shall restrict ourselves to the 4×4 unit-cell where all independent variational parameters are to be determined from an energy minimization. This is motivated both by experiments [122, 125] and by the previous MF results showing the particular stability of such a structure (see also Ref. [126]). As mentioned in the previous Section, we also impose that the phases and amplitudes respect the C_{4V} symmetry within the unit-cell (with respect to the center of the middle plaquette, see Fig. 5.2), reducing the numbers of independent links to 6. To avoid spurious degeneracies of the MF wave-functions related to multiple choices of the filling of the discrete k-vectors in the Brillouin Zone (at the Fermi surface), we add very small random phases and amplitudes (10^{-6}) on all the links in the 4×4 unit cell.

Let us note that commensurate flux phase (CFP) are also candidate for this special 1/8 doping. In a previous study, a subtle choice of the phases $\theta_{i,j}$ (corresponding to a gauge choice in the corresponding Hofstadter problem [28]) was proposed [30], which allows to write the $\phi = p/16$ ($p < 16$) flux per plaquette wave-function within the same proposed unit-cell [30] and is also expected to lead to a better kinetic energy than the Landau gauge (in the Landau gauge the unit-cell would be a line of 16 sites). However, we have found that the CFP wave-functions turned out *not* to be competitive for our set of parameters V_0, due to their quite poor kinetic energy, although they have very good Coulomb and exchange energies. We argue that such CFP wave-functions would become relevant in the large Coulomb and/or J regimes (see table 5.1).

In order to further improve the energy, we also add a nearest-neighbor spin-independent Jastrow [50] term to the wave-function,

$$\mathcal{P}_{\mathcal{J}} = \exp\left(\alpha \sum_{\langle i,j \rangle} n_i n_j\right), \tag{5.7}$$

where α is an additional variational parameter. Finally, since the $t - J$ model allows at most one fermion per site, we discard all configurations with doubly occupied sites by applying the complete Gutzwiller projector $\mathcal{P}_{\mathcal{G}}$. The wave-function we use as an input to our variational study is therefore given by,

$$|\psi_{\text{var}}\rangle = \mathcal{P}_{\mathcal{G}} \mathcal{P}_{\mathcal{J}} |\psi_{\text{MF}}\rangle \tag{5.8}$$

In the following, we shall introduce simple notations for denoting the various variational wave-functions, BO for the bond-order wave function, SFP for the

---

[8] Note that the bond modulation itself leads to non-equivalent sites which, strictly speaking, should have slightly different electron densities (although the ϵ_i might be constant).

Table 5.1: Set of energies per lattice site for $V_0 = 1$ and $l_0 = 4$ for different wave-functions. The best commensurate flux phase in the Landau gauge with flux per plaquette $p/16$ was found for $p = 7$. We also show the energy of the CFP with flux 7/16 written with another choice of gauge. We show the total energy per site (E_{tot}), the kinetic energy per site (E_{T}), the exchange energy per site (E_{J}) and the Coulomb energy per site (E_{V}).

wave-function	E_{tot}	E_{T}	E_{J}	E_{V}
FS	-0.4486(1)	-0.3193(1)	-0.1149(1)	-0.0144(1)
CFP 7/16[1]	-0.3500(1)	-0.1856(1)	-0.1429(1)	-0.0216(1)
CFP 7/16[2]	-0.4007(1)	-0.2369(1)	-0.1430(1)	-0.0208(1)
SFP	-0.4581(1)	-0.3106(1)	-0.1320(1)	-0.0155(1)
BO	-0.4490(1)	-0.3047(1)	-0.1302(1)	-0.0141(1)
RVB	-0.4564(1)	-0.3080(1)	-0.1439(1)	-0.0043(1)
$SFP/\mathcal{J}$	-0.4601(1)	-0.3116(1)	-0.1315(1)	-0.0169(1)
$BO/\mathcal{J}$	-0.4608(1)	-0.3096(1)	-0.1334(1)	-0.0177(1)
$RVB/\mathcal{J}$	-0.4644(1)	-0.3107(1)	-0.1440(1)	-0.0086(1)

[1] Landau gauge

[2] Gauge of Ref. [30]

staggered flux phase, RVB for the d-wave RVB superconducting phase, FS for the simple projected Fermi sea, and we will use the notation $MF/\mathcal{J}$ ($MF = BO, SFP, RVB, FS$) when the Jastrow factor is applied on the mean-field wave-function. Finally, it is also convenient to compare the energy of the different wave-functions with respect to the energy of the simple projected Fermi sea (i.e. the correlated wave-function corresponding to the previous FL mean-field phase), therefore we define a *condensation energy* as $e_c = e_{var} - e_{FS}$.

In Fig. 5.5 we present the energies of the three wave-functions $BO/\mathcal{J}$, $SFP/\mathcal{J}$ and $RVB/\mathcal{J}$ for Coulomb potential $V_0 \in [0, 5]$. We find that for both $l_0 = 2$ and $l_0 = 4$ the RVB phase is not the best variational wave-function when the Coulomb repulsion is strong. The bond-order wave-function has a lower energy for $V_0 > 2$ and $l_0 = 2$ ($V_0 > 1.5$ and $l_0 = 4$). Note that the (short range) Coulomb repulsion in the cuprates is expected to be comparable to the Hubbard U, and therefore $V_0 \approx 5$ or 10 seems realistic. Independently of the relative stability of both wave-functions, the superconducting d-wave wave-function itself is strongly destabilized by the Coulomb repulsion as indicated by the decrease of the variational gap parameter for increasing V_0 and the suppression of superconductivity at $V_0 \simeq 7$ (see Fig. 5.6).

Nevertheless, we observe that the difference in energy between the bond-order wave-function and the staggered flux phase remains very small. We show in table 5.2 the order parameters measured after the projection for the $RVB/\mathcal{J}$,

Table 5.2: Order parameters for the different wave-functions for $V_0 = 1.5$ and $l_0 = 4$. We depict the following order parameters: $t_{i,j} \times e^{i\phi_{i,j}}$, where $t_{i,j}$ ($\phi_{i,j}$) is the amplitude (phase) of $\langle c_i^{+} c_j \rangle$, and the exchange energy $\langle S_i.S_j \rangle$, for the 6 independent bonds labelled for convenience according to Fig. 5.2. The sign of $\phi_{i,j}$ is according to the staggered flux pattern (see arrows in Fig. 5.10). We note that the $RVB/\mathcal{J}$ is uniform by construction. The variational superconducting order parameter is $\Delta_{RVB} = 0.3$ for the $RVB/\mathcal{J}$ wave-function and $\Delta_{RVB} = 0$ for the $SFP/\mathcal{J}$ and $BO/\mathcal{J}$ wave-functions.

	bond 1	bond 2	bond 3	bond 4	bond 5	bond 6
$t_{i,j}$						
$RVB/\mathcal{J}$	0.077(1)	0.077(1)	0.077(1)	0.077(1)	0.077(1)	0.077(1)
$SFP/\mathcal{J}$	0.085(1)	0.085(1)	0.085(1)	0.085(1)	0.085(1)	0.085(1)
$BO/\mathcal{J}$	0.082(1)	0.083(1)	0.093(1)	0.088(1)	0.086(1)	0.084(1)
$\|\phi_{i,j}\|$						
$RVB/\mathcal{J}$	0	0	0	0	0	0
$SFP/\mathcal{J}$	0.438(1)	0.438(1)	0.438(1)	0.438(1)	0.438(1)	0.438(1)
$BO/\mathcal{J}$	0.527(1)	0.502(1)	0.473(1)	0.390(1)	0.338(1)	0.384(1)
$-\langle S_i.S_j \rangle$						
$RVB/\mathcal{J}$	0.215(1)	0.215(1)	0.215(1)	0.215(1)	0.215(1)	0.215(1)
$SFP/\mathcal{J}$	0.197(1)	0.197(1)	0.197(1)	0.197(1)	0.197(1)	0.197(1)
$BO/\mathcal{J}$	0.215(1)	0.207(1)	0.215(1)	0.187(1)	0.186(1)	0.170(1)

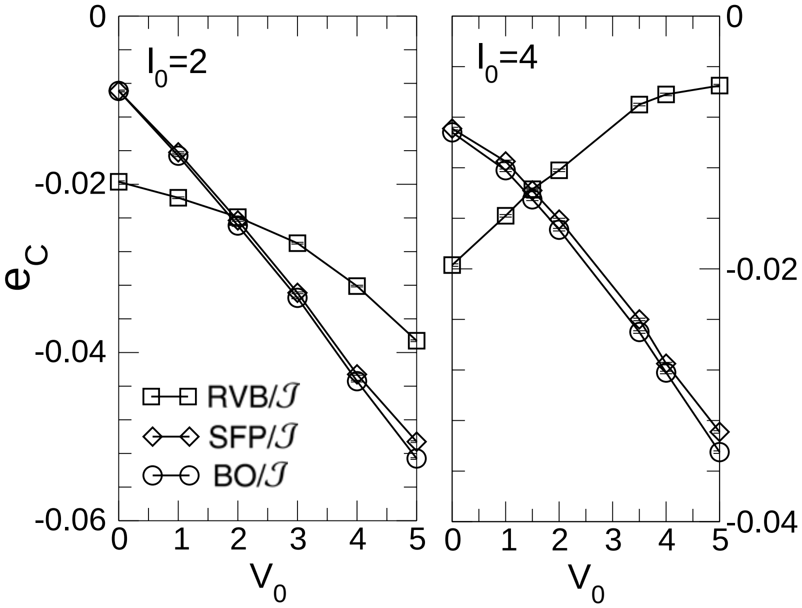

Figure 5.5: Energy per lattice site of the $RVB/\mathcal{J}$, $SFP/\mathcal{J}$ and $BO/\mathcal{J}$ wave-functions minus the energy of the projected Fermi sea wave-function.

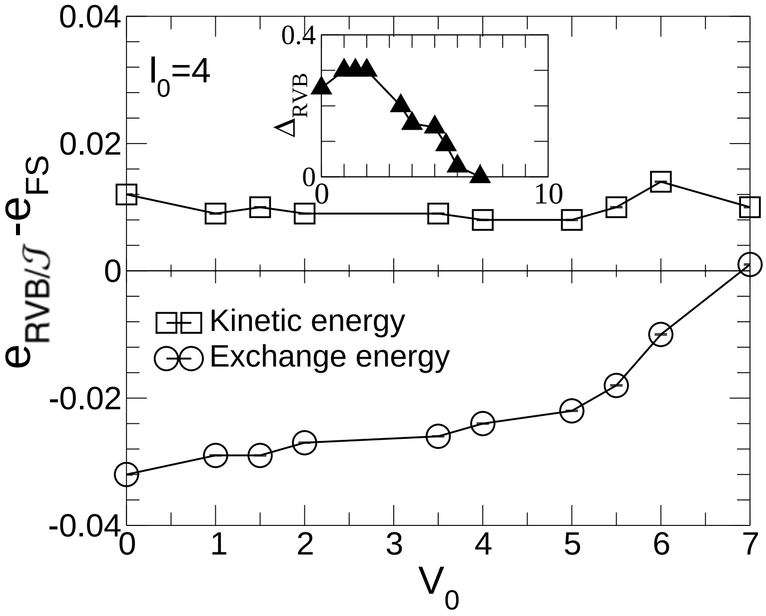

Figure 5.6: Kinetic and exchange energy per site of the $RVB/\mathcal{J}$ wave-function minus the respective exchange and kinetic energy of the simple projected Fermi sea. Inset: value of the variational d-wave gap.

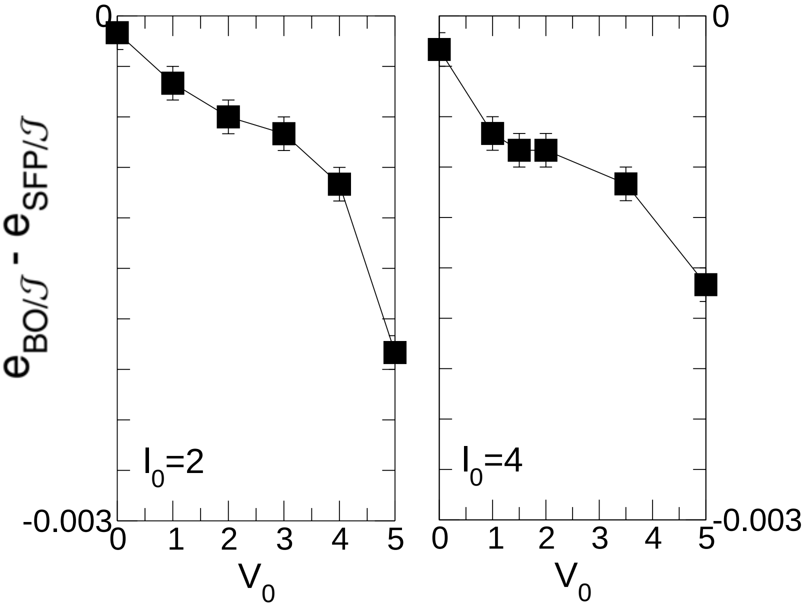

Figure 5.7: Total energy per site of the $BO/\mathcal{J}$ minus the energy of the $SFP/\mathcal{J}$ wave-functions.

$SFP/\mathcal{J}$ and $BO/\mathcal{J}$ wave-functions. As expected the $RVB/\mathcal{J}$ and the $SFP/\mathcal{J}$ wave-functions are homogenous within the unit-cell. In contrast, the $BO/\mathcal{J}$ wave-function shows significant modulations (expected to be measurable experimentally) of the various bond variables w.r.t their values in the homogeneous SFP. In Fig. 5.7 we show the small energy difference (see scale) between the two wave-functions. Interestingly, the difference is increasing with the strength of the potential. We notice that the two wave-functions correspond to two nearby local minima of the energy functional at zero Coulomb potential (see Fig. 5.8), which are very close in energy (the $BO/\mathcal{J}$ wave-function is slightly lower in energy than the $SFP/\mathcal{J}$) and are separated by a quite small energy barrier. Note that in Fig. 5.8 we consider the variational bond order parameters and not the projected quantities.

When the repulsion is switched on, the height of the energy barrier increases and the $SFP/\mathcal{J}$ wave-function does not correspond anymore to the second local minima. Indeed, when $V_0 > 0$ the second local energy minima *shifts* continuously from the point corresponding to the simple $SFP/\mathcal{J}$ wave-function. The metastable wave-function lying at this second local minima is a weak bond-order (SFP-like) wave-function that preserves better the large kinetic energy while still being able to optimize better the Coulomb energy than the homogeneous SFP. Moreover, to understand better the stabilization of the BO-modulated staggered flux wave-functions w.r.t the homogeneous one, we have plotted in Fig. 5.9 the difference in the respective kinetic energy, the exchange energy and the Coulomb

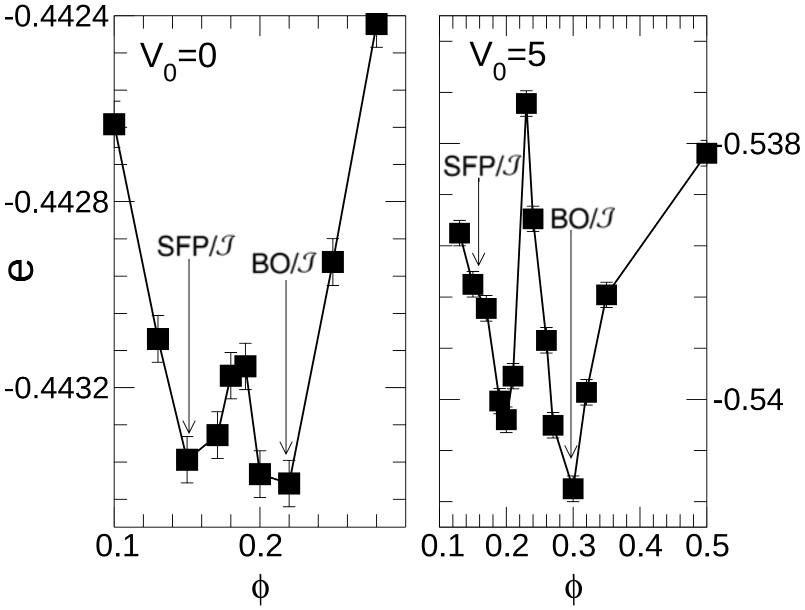

Figure 5.8: Total energy per site of the $BO/\mathcal{J}$ variational wave-function with variational parameters $Im\left(\tilde{t}_{i,j}\right) = \pm\phi$ on the bonds $1, 2, 3$, and $Im\left(\tilde{t}_{i,j}\right) = \pm 0.149$ on the bonds $4, 5, 6$. The sign of $Im\left(\tilde{t}_{i,j}\right)$ is oriented according to the staggered flux pattern. We have chosen for all the links $Re\left(\ \tilde{t}_{i,j}\right) = 0.988$. Results for $V_0 = 0$ and $V_0 = 5$ with $l_0 = 4$ are shown.

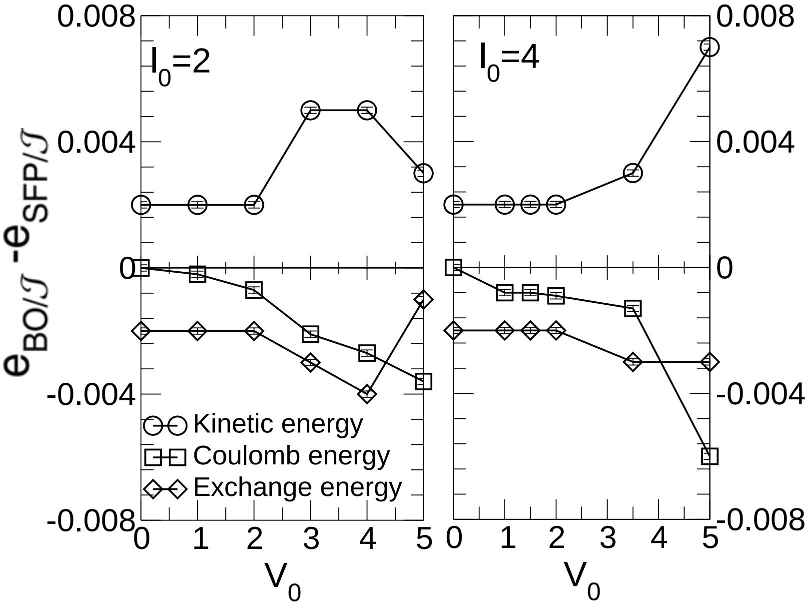

Figure 5.9: Kinetic, exchange and Coulomb energy per site of the $BO/\mathcal{J}$ wave-function minus the respective associated energy of the $SFP/\mathcal{J}$ wave-function.

energy of the $SFP/\mathcal{J}$ and $BO/\mathcal{J}$ wave-functions. We conclude that the two wave-functions, although qualitatively similar (they both exhibit an underlying staggered flux pattern), bear quantitative differences: the staggered flux phase (slightly) better optimizes the kinetic energy whereas the bond-order wave-function (slightly) better optimizes the Coulomb and exchange energies so that a small overall energy gain is in favor of the modulated phase. Therefore, we unambiguously conclude that, generically, bond-order modulations should spontaneously appear *on top* of the staggered flux pattern for moderate doping.

Finally, we emphasize that the bond-order wave-function is not stabilized by the Coulomb repulsion alone (like for a usual electronic Wigner cristal) exhibiting coexisting bond order and (small) charge density wave. Moreover, the variational parameters ϵ_i in Eq. (5.6) are found after minimizing the projected energy to be set to equal values on every site of the unit-cell. Let us also emphasize that the bond-order wave-function is not superconducting as proposed in some scenarios [130]. In the actual variational framework, we do not consider bond-order wave-function embedded in a sea of d-wave spin singlet pairs.

In fact, we do not expect a bulk d-wave RVB state to be stable at large Coulomb repulsion (because of its very poor Coulomb energy) nor a bulk *static* checkerboard SFP at too small Coulomb energy. However, for moderate Coulomb repulsion for which the d-wave RVB remains globally stable, sizeable regions of checkerboard SFP could be easily nucleated e.g. by defects. This issue will be

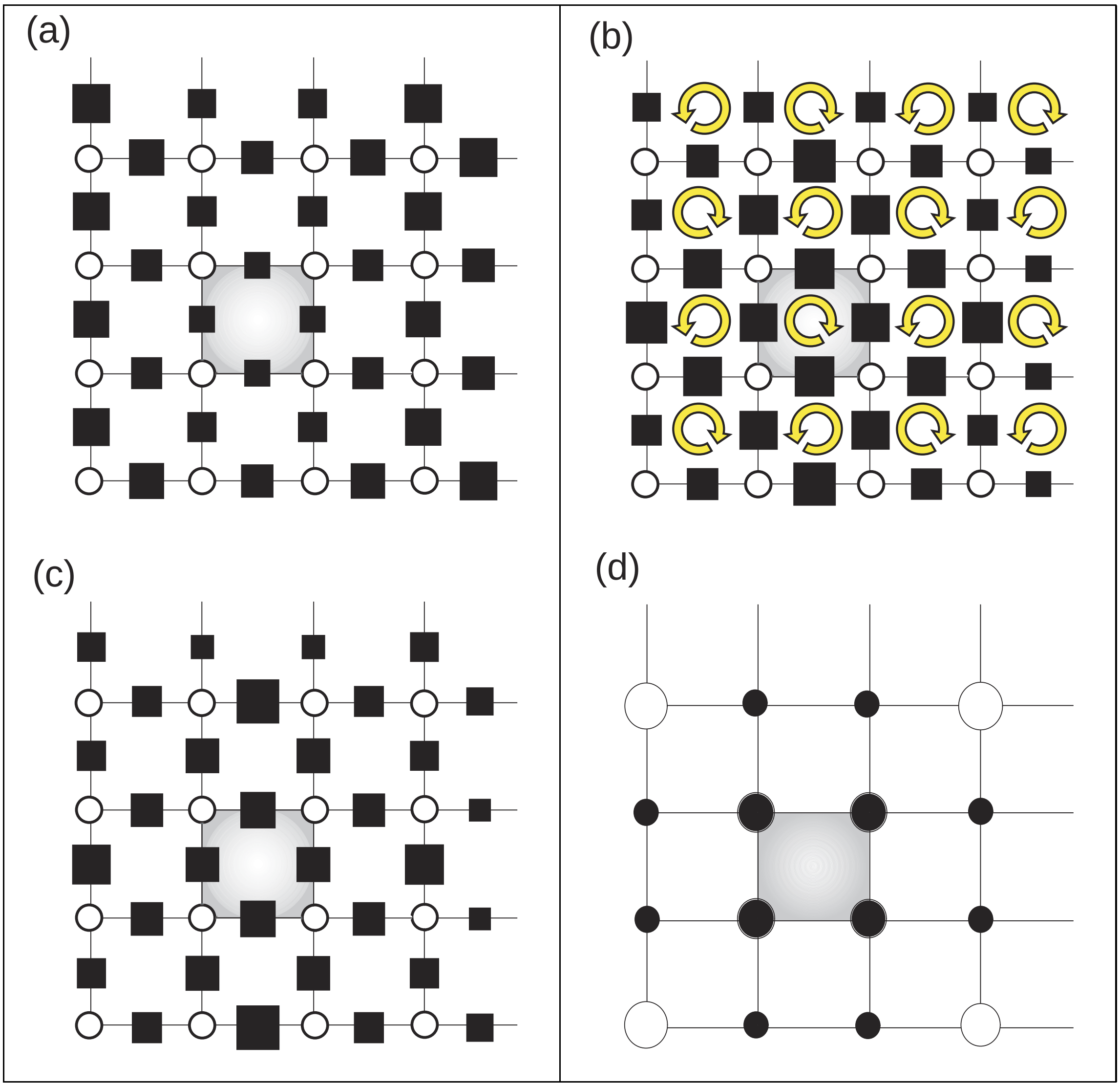

Figure 5.10: Local expectation values (a,b,c) of the kinetic and exchange energies of the projected $BO/\mathcal{J}$ wave-functions on each of the bonds within the unit-cell. Width of filled square symbols is proportional to the (a) real and (b) imaginary part of $\langle c_i^+ c_j \rangle$, and (c) to the local exchange energy $\langle \mathbf{S}_i \cdot \mathbf{S}_j \rangle$. The sign of the imaginary part of the hopping bonds is according to the staggered flux pattern (arrows). The wave-function has small charge density variations (d), therefore we subtract the mean value n to the local density: size of circles are proportional to $\langle n_i - n \rangle$, and circles are open (filled) for negative (positive) sign. The biggest circle corresponds to an on-site charge deviation of 2%. All the above results are for $l_0 = 4$ and $V_0 = 5$.

addressed using renormalized MF theory in a future work. An extension of our VMC study with simultaneous inhomogeneous bond-order and singlet pair order parameters (as required to treat such a problem) is difficult and also left for a future work. Note also that low-energy *dynamic fluctuations* of checkerboard (and SFP) characters could also exist within the d-wave RVB state but this is beyond the scope of our present work.

The properties of the $BO/\mathcal{J}$ staggered flux wave-function are summarized in Fig. 5.10 showing the real and imaginary parts of the measured hopping term $\langle c_i^+ c_j \rangle$ between every nearest neighbor sites of our candidate $BO/\mathcal{J}$ wave-function. We also present the exchange term on each bonds of the lattice, and the local on-site charge density. We find that the bond-order wave-function has both (spin-spin) bond density wave and (small) charge density wave components. Nonetheless, the charge modulations are very small (the maximum charge deviation from the mean on-site charge is of the order of 2%) , and the charge density is a little bit larger in the center of the unit-cell. As expected, the $SFP/\mathcal{J}$ has homogeneous hopping and exchange bonds within the unit-cell. Therefore, we conclude that after projection the modulated variational wave-function differs quantitatively from the uniform one: the $BO/\mathcal{J}$ staggered flux wave-function is quite inhomogeneous (although with a very small charge modulation) leading to an increased magnetic energy gain while still preserving a competitive kinetic energy, a characteristic of the homogeneous $SFP/\mathcal{J}$ wave-function.

5.5 Conclusion

In conclusion, in this chapter we have investigated the $t{-}J{-}V$ model using both mean-field calculations as well as more involved variational Monte-Carlo calculations. Both approaches have provided strong evidence that bond-order wave-functions (of underlying staggered flux character) are stabilized at zero and finite Coulomb repulsion for doping close to 1/8. In particular, variational Monte-Carlo calculations show that a bond modulation appears spontaneously on top of the staggered flux phase. This is in agreement with the work of Wang et al. [132] predicting an instability of staggered flux type. We have also shown that the modulated and homogeneous SFP, although nearby in parameter space, are nevertheless separated from each other by a small energy barrier. While both staggered flux wave-functions provide an optimal kinetic energy, the bond-modulated one exhibits a small extra gain of the exchange energy. On the other hand, a short range Coulomb repulsion favors both staggered flux wave-function w.r.t the d-wave RVB superconductors and brings them close in energy.

Finally, it would be interesting to study if the checkerboard pattern could spontaneously appear in the vicinity of a vortex in the mixed phase of the cuprates. Such an issue could be addressed by studying the $t{-}J{-}V$ model on a square lattice extending our variational scheme to include *simultaneously* nearest neighbor pairing and bond modulated staggered currents. It is expected that, while the pairing is suppressed in the vicinity of the vortex, the checkerboard pattern might be variationally stabilized in this region.

Chapter 6

Spontaneous time reversal symmetry breaking in the cuprates

6.1 Outline

The three-band Hubbard model on the square lattice is believed to be relevant for the copper oxide high-T$_c$ compounds. We used the projected wavefunction variational approach for this model. It has been repeatedly suggested that orbital currents might appear in this model, and we propose to use an extended variational scheme to look at such an instability. In this chapter we perform variational Monte Carlo calculations for an orbital current wavefunction. It is found that local Gutzwiller projection is not efficient enough for this Hamiltonian, and a long-range Jastrow projector helps to treat correctly the doubly occupied site in the three-band Hubbard model. The orbital currents wavefunction is found to be variationally stable for realistic Hamiltonian parameters in the hole doping range $x = 0. - 0.15\%$. Energies and correlations are compared to exact results obtained on a small cluster.

6.2 Experimental evidence of spontaneous circulating currents in YBCO

Since the discovery of the high temperature superconductors, one of the leading issues is the origin of the pseudo-gap phase which exists in the the low hole doping part (underdoped region) of the copper oxide superconductor phase diagram.

A strong activity has emerged on the circulating current phases in correlated electron systems. One example is provided by the so-called staggered flux (SF) phases [133,134,135]. Many of their properties were discussed, but not considered

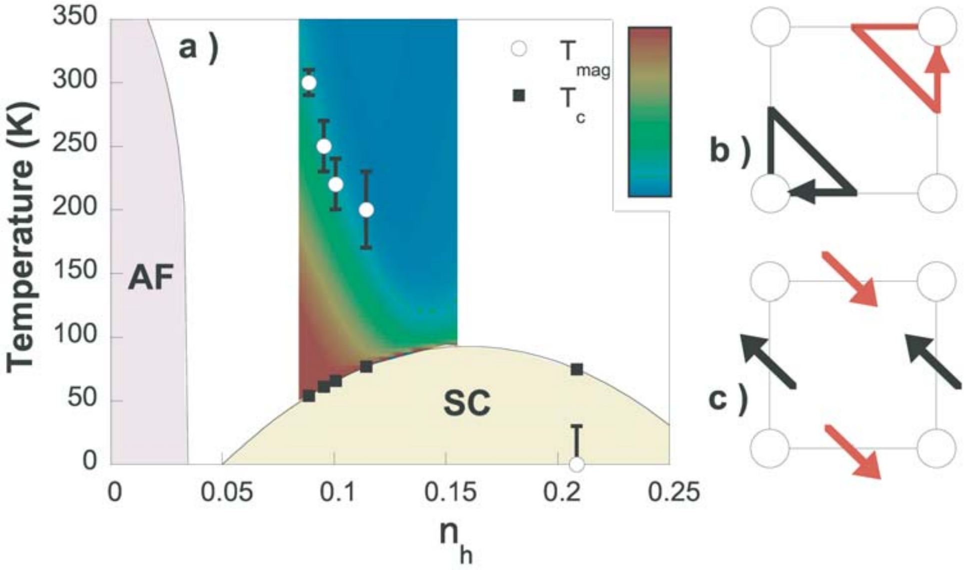

Figure 6.1: Reproduced from Ref. [136]. a) The colors indicate the magnetic moments intensity versus the hole doping concentration n_h. The white dots indicates the pseudo-gap critical temperature T* obtained from resistivity measurements. b) the θ_2 phase proposed by Chandra Varma that characterize the pseudo-gap phase of the cuprates, c) on-site spins lying on the oxygen atoms.

further in the absence of experimental evidence. The discovery of an unusual and robust regime called the pseudo-gap in superconductors has changed the picture once more. The pseudo-gap has a density of states looking like a superconducting gap, but the state itself is not superconducting. This phase is remarkable as physical properties show anomalies with respect to the behavior expected for a standard metal and at the same time there is no evidence of broken symmetry so far. One of the accepted scenarii is that the pseudo-gap state represents a precursor of the superconducting state. Another scenario would be that an order parameter associated with the pseudo-gap phase is competing with the superconducting one. In this context a proposal has been made recently that a true broken symmetry is the origin of the pseudo-gap [137]. This state would lead to a breakdown of time reversal symmetry in which the circulating currents obey translational symmetry.

One of the recent proposal is that the anomalous properties of the cuprates may be due to quantum critical fluctuations of current patterns formed spontaneously in the CuO_2 planes. Related to this assumption, a break-through was realized recently by Bourges et al. [136]: by using polarized elastic neutron diffraction, they report the signature of an unusual magnetic order in the underdoped phase of YBa2Cu3O6 $+ x$ (YBCO). They argue that this hidden order param-

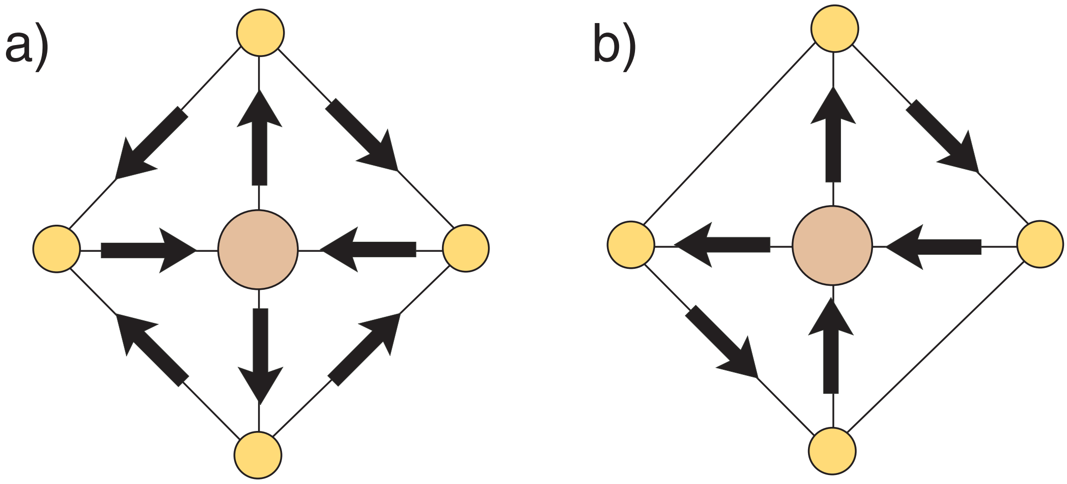

Figure 6.2: The phase θ_1 (a) and θ_2 (b) proposed by Chandra Varma as candidates for the pseudo-gap phase of the cuprates. The arrows indicate the currents orientation.

eter defines the pseudo-gap phase of cuprates. They found that the magnetic intensity occurs on top of nuclear Bragg peaks with no additional Bragg peaks: this indicates that no translational symmetry breaking of the lattice is associated with this order parameter.

Moreover, the pattern of the observed magnetic scattering corresponds to the one expected in the circulating current theory of the pseudo-gap state with current loops inside the CuO_2 unit-cell developed by Chandra Varma [138], especially with the θ_2 phase proposed recently by Chandra Varma, which has two current loops per copper unit-cell. Nevertheless, an alternative scenario considering a decoration of the unit cell with staggered moments on the oxygen sites could also account for the measurements. Combining all measurements done in different samples, it was found that the magnetic moments had also an in-plane component: the mean angle between the direction of the moments with the axis perpendicular to the planes was estimated to be $\phi = 45°$. The intensity of the observed moments, which develops well above T_c (close to room temperature), is reported to be about $M = 0.05 - 0.1\mu_B$.

Finally, this phenomenology suggests a quantum critical point close to optimal doping. Critical fluctuations around this point would then be responsible for the anomalous properties of the pseudo-gap phase.

6.3 three-band Hubbard model

In order to investigate the mechanism of circulating currents (CC), superconductivity (SC) and antiferromagnetism (AF) in cuprate high-Tc superconductors, we examine the ground state of the two-dimensional three-band Hubbard model for CuO_2 planes. Indeed, we cannot use the simpler one-band Hubbard or t-J model since we want to include the possibility for circulating currents around the CuO_2 plaquettes. We neglect, in the first part of this work, the out-of-plane oxygens (apical oxygens), since it is commonly believed that the CuO_2 plane contains the essential features of high-Tc cuprates. It is not an easy task to clarify the ground state properties of the $2D$ three-band Hubbard model because of the strong correlations among d and p electrons. We must treat the strong correlations properly to understand the phase diagram of the high-Tc cuprates. The quantum variational Monte Carlo (VMC) method is a tool to investigate the overall structure of the phase diagram from weak to strong correlation regions. A purpose of this work is to investigate the property of the orbital current phase, the antiferromagnetic state and the competition between antiferromagnetism and superconductivity for finite U_d, following the ansatz of Gutzwiller-projected wave functions.

In this work, we propose to study the physics of correlated electrons in the following 3-band Hamiltonian 1.1. The compound has one hole per Cu site at half-filling, and we find it more convenient to work in hole notations: we consider therefore that $p^\dagger$ ($d_d^\dagger$) creates one hole on a oxygen (copper) site. The matrix $S_{i,j}$ contains the phase factor that comes from the hybridization of the p-d orbitals. In hole notation, it is possible to perform a gauge transformation that transforms the matrix S_{ij} so that all the final hopping integrals are negative (see Fig. 6.3). In what follows, we use the gauge transformation only for the exact diagonalization calculations, since it allows to keep the rotational symmetries, which would be broken by the usual sign convention. Nevertheless, all the physical observables are gauge invariant and the results will not depend on the gauge choice. Furthermore, the doping is defined as the number of additional holes per copper unit cell. At half-filling (0 doping) the system has one hole per copper. We can therefore dope in holes by adding additional particles, or dope in electrons by removing particles. It is important to notice that, even when $t_{pp} = 0$, the model has no particle/hole symmetry. Since we propose to study the stability of orbital flux current, we do not use anti-periodic boundary conditions which would generate an artificial additional flux through the lattice. We consider throughout this paper realistic values for the Hamiltonian parameters [9, 10, 8]:

- $U_d = 10.5eV$ and $U_p = 4eV$
- $t_{dp} = 1.3eV$ and $t_{pp} = 0.65eV$
- $\Delta_p = 3.5eV$
- $V_{dp} = 1.2eV$

This model was investigated by means of variational Monte Carlo [139, 140], however the authors were not looking for the orbital current instability. On the

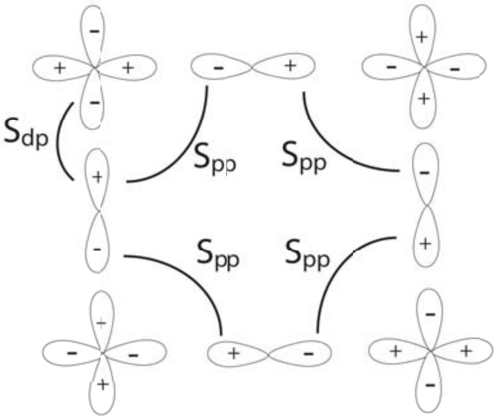

Figure 6.3: The gauge choice in the Lanczos calculations. the d_{x2-y2} and p_σ orbitals are shown. The phases due to the hybridization in this gauge are $S_{dp} = -1$ for the copper-oxygen links, and $S_{pp} = -1$ for the oxygen-oxygen links. In this gauge choice, the signs of the transfer integrals do not anymore break the 90° rotational symmetry. This latter symmetry is used in the Lanczos calculations as an additional quantum number, that allows to diagonalize the Hamiltonian matrix in smaller blocks of the Hilbert space.

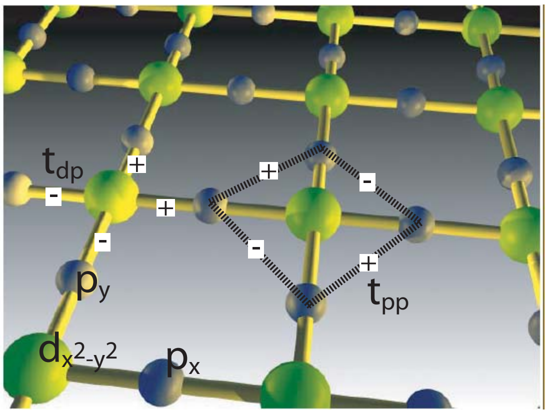

Figure 6.4: A single CuO_2 layer, the copper are indicated as large sphere, and the oxygens as small one. The system has one hole per copper site at half-filling. Both the transfer integral t_{dp} between the $d_{x^2-y^2}$ and the $p_{x,y}$ orbitals and the transfer integral t_{pp} between the p_x and the p_y orbitals are considered. In hole notations the bonding orbitals enter the Hamiltonian with a positive transfer integral sign, and the anti-bonding orbitals with a negative sign. The signs of the t_{pp} and t_{dp} transfer integrals are shown.

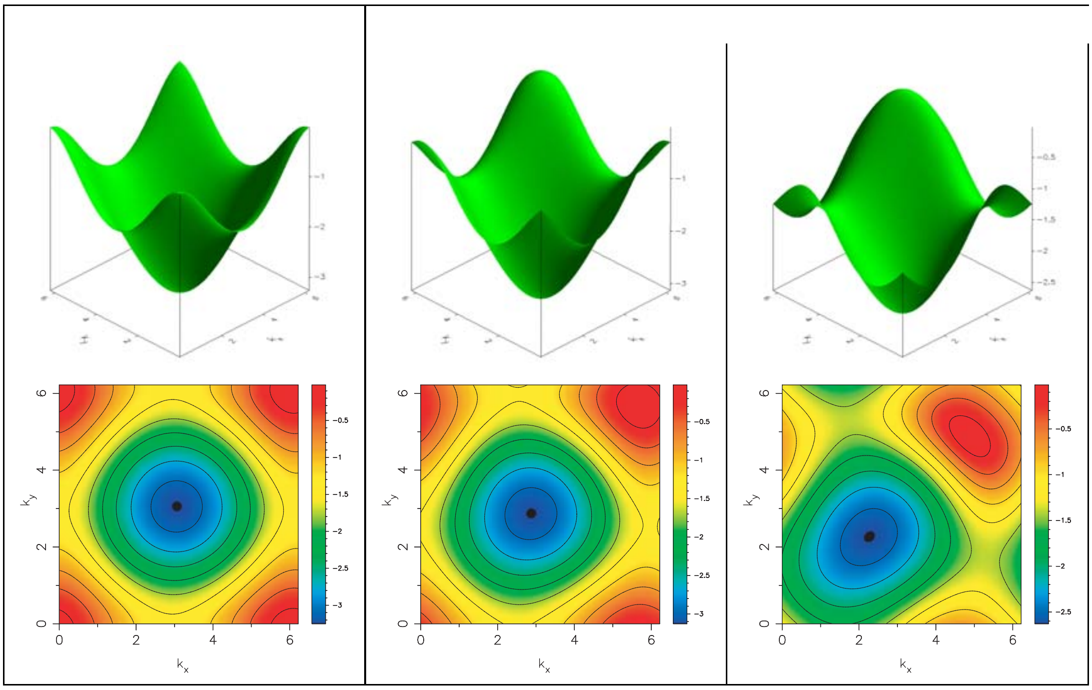

Figure 6.5: Free particle dispersion in hole notation of the Fermi sea (left) and of the θ_2 orbital current phase with mean-field flux flowing though one of the circulating plaquette $\phi^{mf} = 0.9$ (middle) and $\phi^{mf} = 2.1$ (right). The minimum of the dispersion is shifted along the diagonal of the Brillouin Zone.

other hand, a recent exact diagonalization was carried out by M. Greiter and collaborators [141]. They found no evidence for spontaneous orbital currents in finite-size studies of an effective $t-J$ model for the three-band model of the CuO$_2$ planes. The mapping of the three-band Hubbard model on this $t-J$ model is however expected to be valid only in the limit $\epsilon_p/t_{pd} \gg 1$, that is however not satisfied for realistic parameters obtained for the cuprates [9]. Therefore, additional exact diagonalization calculations of the three-band Hubbard model are still called for. Moreover, they used exact diagonalizations on a small 8 copper site lattice, which leads to large finite-size effect, although the size of the Hilbert space is already very large. Finally, in the calculations of M. Greiter and collaborators, the Hilbert space was truncated by keeping the lowest energy levels, which though it was argued to be under control, is not giving exact results which can directly be compared to variational results. Therefore, further variational Monte Carlo calculations are certainly needed to study larger systems.

6.4 A pair of particles in a three-site ring

Let us first consider a simple model describing a pair of up and down spin particles on a simple three-site ring. The sites are connected by a hopping integral t, and we consider an on-site repulsion $U > 0$ and a nearest neighbor Coulomb repulsion V :

$$H_3 = t \sum_{\langle i,j\rangle\sigma} c^+_{i\sigma} c_{j\sigma} + U \sum_i n_{i\uparrow} n_{i\downarrow} + V \sum_{\langle i,j\rangle} n_i n_j \tag{6.1}$$

The Hilbert space contains 9 states, and when we consider translational symmetries, it is reduced to 3 states :

$$\begin{aligned} P_1 &= \left|\uparrow\downarrow \circ\right\rangle + e^{ik}\left|\circ \uparrow\downarrow\right\rangle - e^{-ik}\left|\downarrow \circ \uparrow\right\rangle \\ P_2 &= \left|\downarrow\uparrow \circ\right\rangle + e^{ik}\left|\circ \downarrow\uparrow\right\rangle - e^{-ik}\left|\uparrow \circ \downarrow\right\rangle \\ P_3 &= \left|d \circ \circ\right\rangle + e^{ik}\left|\circ d \circ\right\rangle + e^{-ik}\left|\circ \circ d\right\rangle \end{aligned}$$

where d is a doubly occupied site, and k takes the value $k = 0, 2\pi/3, 4\pi/3$. The ground state of free particles ($U = V = 0$) $|\psi_0\rangle$ is in the sector $k = 0$ for $t < 0$, and the state is degenerate in the sectors $k = 0, \pm 2\pi/3$ for $t > 0$. The ground-state energy for $t < 0$ is given by $E = -4|t|$ and is non-degenerate, while we get a four-fold degeneracy for $t > 0$ with energy $E = -2|t|$. In the latter case, two of the eigenvectors lie in the sector $k = 0$ and the two other eigenvectors lie respectively in the sectors $k = 2\pi/3$ and $k = -2\pi/3$. This is a trivial result understood in terms of the free dispersion of a one dimensional chain with periodic boundary conditions. However, it is worth noting that the circulation of the current around the ring is finite for the ground state component lying in the $k = \pm 2\pi/3$ sectors when $t > 0$. In the latter case we get, in each of the $k = \pm 2\pi/3$ sectors of the Hilbert space, the circulation of the current: $F = 1.1547|t|$, where :

$$F = \langle J_{12}\rangle + \langle J_{23}\rangle + \langle J_{32}\rangle \tag{6.2}$$

and the definition of the current is obtained by the conservation of the density:

$$\frac{\delta n_i}{\delta t} = 0 = \frac{\hbar e}{c}\left[H, n_i\right] = \sum_{\langle i,j\rangle} J_{i,j} \tag{6.3}$$

which leads to the definition of the current operator on a link [1]:

$$J_{ij} = \sum_\sigma \left(i t_{ij} c^\dagger_{i\sigma} c_{j\sigma} + c.c. \right) \tag{6.4}$$

We emphasize that this definition of the current-operator is gauge invariant. When $U, V > 0$, the states $k = \pm 2\pi/3$ have higher energies, but the degeneracy

---

[1] This leads to the same definition as the derivative of the Hamiltonian with respect to the gauge field $\mathcal{A}_{ij}$: $\frac{\delta H}{\delta \mathcal{A}_{ij}} = J_{ij}$.

is restored when $U = V$. Following this simple argument, we could expect that circulating currents will occur in the plaquettes of the lattice that have the sign $t > 0$ [2], provided they are stabilized by the electronic correlations.

This trivial argument can be tested by looking at the correlations of the current operator of the three-band Hubbard model in a small 12 site lattice in the free-electron case ($U_d = U_p = V_{dp} = 0$). Therefore, we consider two choices of the hopping signs, none of them being the one of the cuprates compound, but which have respectively two and four circulating triangles around each copper atom, i.e. the former having two triangle plaquette with $t > 0$ and the latter having four triangle plaquettes with $t > 0$ (see Fig. 6.6). The current-current correlations on a very short-range scale are consistent with the above argument: we get a strong circulation of the current around the triangle plaquette that have positive hopping integrals or gauge equivalent hopping integrals. The correlations of the current operator are defined as follows:

$$C_{kl} = \langle \hat{J}_{12} \hat{J}_{kl} \rangle \tag{6.5}$$

where $(1, 2)$ denotes a fixed reference link. If the distance between $(1, 2)$ and (k, l) is large enough, the quantity will decorrelate and therefore we can estimate the current value $j_{kl} = \sqrt{C_{kl}}$.

Actually we find that for the sign of the hoppings that have respectively two and four circulating plaquette around each copper, short range current patterns are present in the Fermi sea, that have the symmetry of the phases θ_2 and θ_1 (see Fig. 6.6), that were proposed as candidates for the underlying order in the pseudo-gap phase of the cuprates by Chandra Varma. However, for the physical Hamiltonian which correspond to the cuprates, the choice of the sign is equivalent to negative hopping integrals on all the bonds. Therefore, following the above simple argument, only a weak circulation of the current along the triangle plaquette is expected at first sight. Nevertheless, this is only a trivial argument based on the physics of a three-site ring, and to have further insights in the physics of the three-band Hubbard model, we propose as a first step to perform mean-field calculations on a large lattice.

6.5 Bogoliubov-De Gennes mean-field theory

Our starting point is the non-local Hubbard model, which is described by the following Hamiltonian :

$$H = -\sum_{ij\sigma} t_{ij} c^\dagger_{i\sigma} c_{j\sigma} + \sum_{i\sigma} \epsilon_i c^\dagger_{i\sigma} c_{i\sigma} - \mu \sum_{i\sigma} c^\dagger_{i\sigma} c_{i\sigma} + \frac{1}{2} \sum_{ij\sigma\sigma'} U_{ij} c^\dagger_{i\sigma} c_{i\sigma} c^\dagger_{j\sigma'} c_{j\sigma'} \tag{6.6}$$

---

[2] We note that the system with hopping integrals $t_{12} > 0$, $t_{23} < 0$ and $t_{31} < 0$ is equivalent to the system with $t_{12} > 0$, $t_{23} > 0$ and $t_{31} > 0$ by a simple gauge transformation.

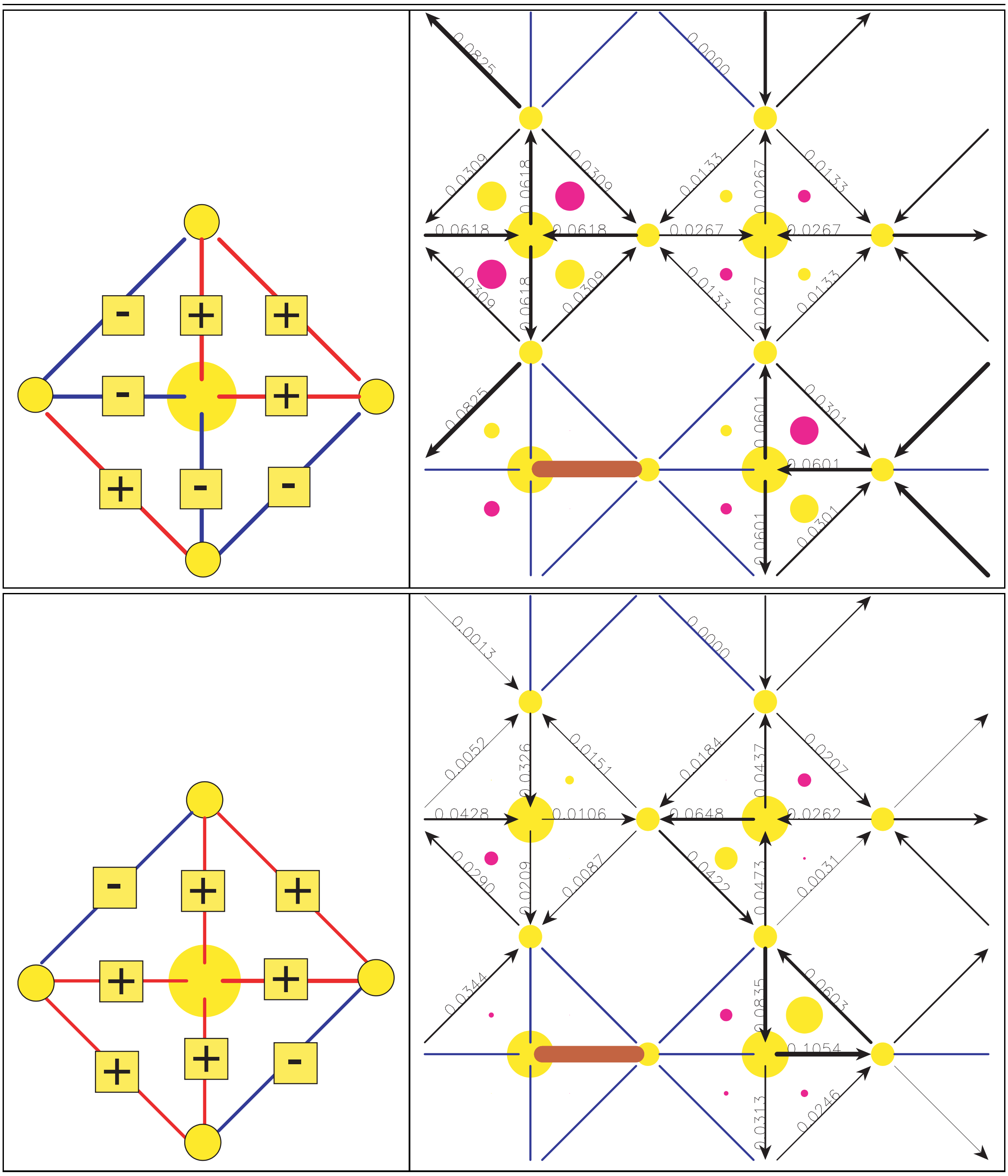

Figure 6.6: Free particle calculations. Top left : sign of the hopping integrals that are considered in the calculations. In this CuO_4 cell all the hopping sign can be transformed by a gauge transformation to a positive hopping sign. Therefore, according to the simple three-site ring argument, the current is expected to circulate in the 4 triangles around the copper atom. Top right : current-current correlations in the corresponding free (U_d=U_p=V_{dp}=0) Hubbard electron model that have the sign defined in the top-left picture. The lattice is filled with 6 holes (50% doping) and the current pattern is θ_1 like. Bottom left : choice of the hopping sign where the unit-cell has 2 circulating plaquette. Bottom right : current-current correlations that show a θ_2 like current pattern.

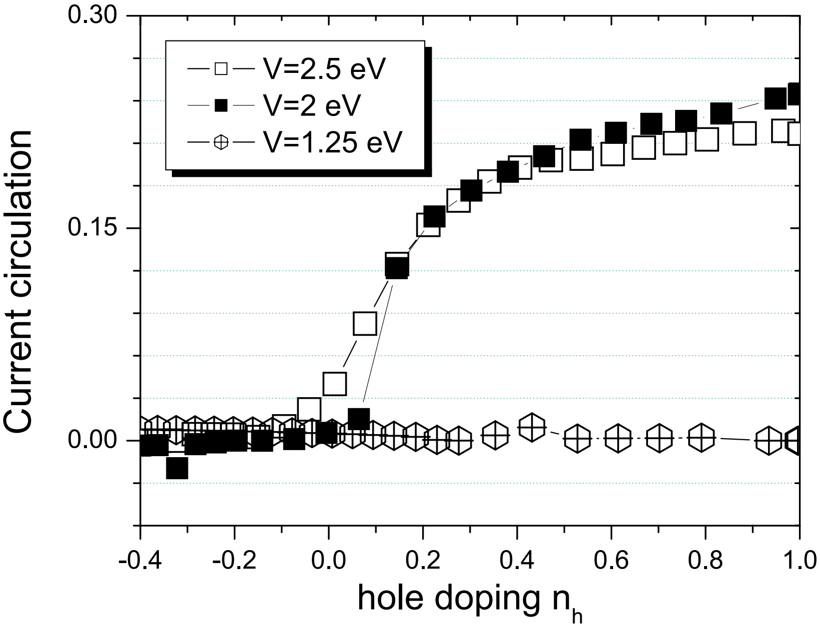

Figure 6.7: Circulation of the orbitals current around one triangle plaquette within the mean-field calculations. We show the circulation for different values of the Coulomb repulsion. The current has same amplitude on the oxygen-oxygen links and on copper-oxygen links. The symmetry of the circulating phases at $V = 2.$ and $V = 2.5$ is θ_2 like.

Where the creation and annihilation operators $c_i^\dagger$ and c_i create and annihilate holes with spin σ in the orbital centered at the lattice point labeled by i, t_{ij} is the amplitude for hopping from site j to site i, ϵ_i is the energy level of the orbital at site i, μ is the chemical potential and U_{ij} is the interaction energy of two holes with opposite spin on the same site $i = j$, and of two holes on neighboring sites $i \neq j$. To obtain the generalized, non-local, Bogoliubov De Gennes equations we first make a mean field approximation for the pairing field [142]:

$$\Delta_{ij} = -U_{ij} \left\langle c_{i\sigma} c_{j-\sigma} \right\rangle \tag{6.7}$$

The tight-binding lattice has nearest neighbor hopping interactions (t_{ij}), as well as a coupling between particle and hole space, via a superconducting order parameter (Δ_{ij}). If the interactions are purely on-site (U_{ii}) repulsions then the pairing potential will be purely local (Δ_{ii}). On the other hand when the interaction is non-local ($U_{ij}, i \neq j$) the pairing potential Δ_{ij} will also be non-local. Another mean field decoupling that takes into account the effect of the U interactions by having a hopping renormalization is also considered (decoupling in the particle-hole channel) :

$$\chi_{ij} = U_{ij} \left\langle c_{i\sigma}^\dagger c_{j\sigma} \right\rangle \tag{6.8}$$

Assuming that the fluctuations about the mean values are small we can write the self-consistent mean-field equations :

$$H_{ij} = \left(\begin{array}{cc} H_{ij} & \Delta_{ij} \\ \Delta^*_{ij} & -H^*_{ij} \end{array} \right) \tag{6.9}$$

In the fully self-consistent Bogoliubov De Gennes equation the normal state Hamiltonian H_{ij} is given by :

$$H_{ij} = (t_{ij} + \frac{1}{2} U_{ji} \chi_{ji}) + (\epsilon_i - \mu)\, \delta_{ij} \tag{6.10}$$

And :

$$\sum_j H_{ij} \left(\begin{array}{c} u^n_j \\ v^n_j \end{array} \right) = E_n \left(\begin{array}{c} u^n_i \\ v^n_i \end{array} \right) \tag{6.11}$$

We then perform the Bogoliubov canononical transformation enabling us to obtain u_{ni} and v_{ni}, the particle and hole amplitudes at site i, associated with an eigen-energy E_n and where Δ_{ij} is the possibly non-local pairing potential or gap function. This allows us to find the self-consistent equations to be satisfied [35, 36, 37, 38, 39, 40]:

$$\Delta_{ij} = -U_{ij} F_{ij} \tag{6.12}$$

with :

$$F_{ij} = \langle c_{i\sigma} c_{j-\sigma} \rangle = \sum_n \left(u^n_i \left(v^n_j \right)^* \left(1 - f\left(E_n \right) \right) - \left(v^n_i \right)^* \left(u^n_j \right) f\left(E_n \right) \tag{6.13}$$

and:

$$\chi_{ij} = \sum_\sigma \left\langle c^\dagger_{i\sigma} c_{j\sigma} \right\rangle = 2 \sum_n \left(\left(u^n_i \right)^* u^n_j f\left(E_n \right) + v^n_i \left(v^n_j \right)^* \left(1 - f\left(E_n \right) \right) \right) \tag{6.14}$$

$f(E_n)$ is the usual Fermi-Dirac distribution. A solution to the above system of equations will be fully self-consistent provided that both the χ_{ij} and Δ_{ij} potentials are determined consistently. We turn now to the results for the three-band Hubbard model. We have carried out mean-field calculations by solving the self-consistent Bogololiubov equations. It was argued that this mean-field consistent frame [142] insures current conservation. We assume a 2-copper unit-cell (6 sites) and solve the equations on a 12×12 copper lattice (496 sites). We have iterated the equations until the observables were converged up to 10^{-4}, which is basically achieved in a few hundred of steps. We checked that minimizing all the parameters on smaller lattices was leading to the same result. We did not consider a further spin decoupling that would lead to antiferromagnetism, since we are mostly interested in time-reversal symmetry breaking.

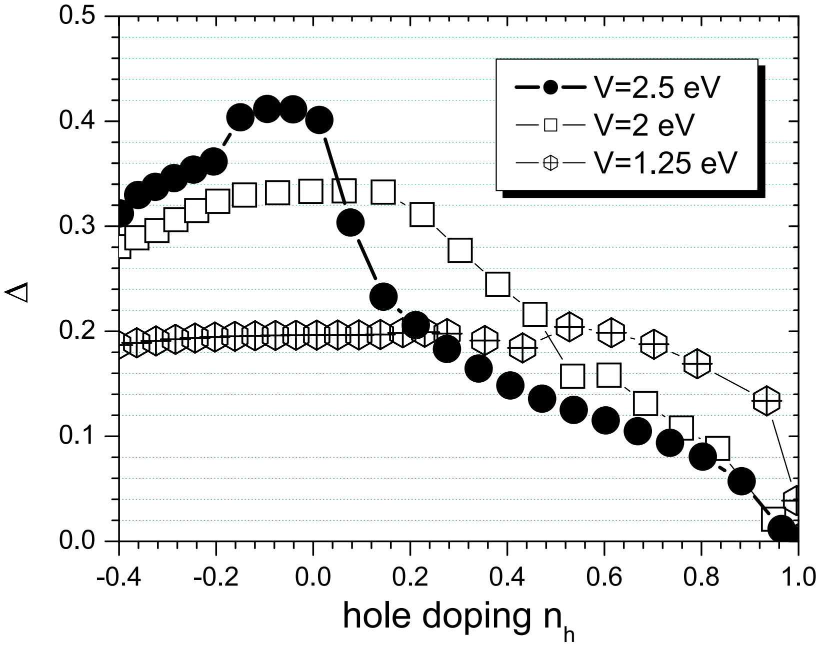

Figure 6.8: Amplitude of the mean-field RVB parameter Δ_{ij}, where (i, j) are copper-oxygen links. The symmetry of the mean-field order parameter consist of real phases $+1$ for the d_{x2-y2} -p_x and d_{x2-y2} -p_y copper-oxygen links, and -1 for the d_{x2-y2} -p_{-x} and for the d_{x2-y2} -p_{-y} links.

Once the self-consistency is achieved, we measure the order parameter $\langle c^\dagger_{k\sigma} c_{l\sigma}\rangle = |\langle c^\dagger_{k\sigma} c_{l\sigma}\rangle| e^{i\theta_{kl}}$ in the mean-field wavefunction. The current operator is then defined by:

$$\langle j^{MF}_{kl}\rangle = \sum_\sigma i t^{MF}_{kl} \langle c^\dagger_{k\sigma} c_{l\sigma}\rangle + c.c. \tag{6.15}$$

When the self-consistency condition is satisfied, t^{MF}_{kl} is given by:

$$t^{MF}_{kl} = t_{kl} - V_{dp}\langle c^\dagger_{l\sigma} c_k\rangle \tag{6.16}$$

In terms of the phase θ_{kl}, this finally gives:

$$\langle j^{MF}_{kl}\rangle = \sum_\sigma i \left(t_{kl} |\langle c^\dagger_{k\sigma} c_{l\sigma}\rangle| e^{i\theta_{kl}} - V_{dp} |\langle c^\dagger_{k\sigma} c_{l\sigma}\rangle| |\langle c^\dagger_{l\sigma} c_{k\sigma}\rangle| \right) \tag{6.17}$$

and we get:

$$\langle j^{MF}_{kl}\rangle = 2\sum_\sigma t_{kl} |\langle c^\dagger_{k\sigma} c_{l\sigma}\rangle| \sin i\theta_{kl} \tag{6.18}$$

Eventually we find that the expectation value of the mean-field current operator j^{MF}_{kl}, when measured in the mean-field ground-state, is also equal to the expectation value of the true current operator defined for the Hubbard model :

$$j_{kl} = \sum_\sigma i t_{kl} \langle c^\dagger_{k\sigma} c_{l\sigma}\rangle + c.c. \tag{6.19}$$

We emphasize that the relation $\langle j^{MF}_{kl}\rangle = \langle j_{kl}\rangle$ breaks down when the calculations are not self-consistent.

We find that for large nearest-neighbors Coulomb repulsion $V_{dp} \approx 2$ (see Fig. 6.7) the orbital currents start to develop for the hole doping part of the phase diagram. The orbital current phase is however stable for unrealistic large hole doping range. A more sophisticated treatment of the Coulomb repulsion terms is certainly called for to avoid the artefact of the mean-field calculations.

6.6 Variational wavefunction

The wavefunction that we consider throughout this chapter is defined by the usual BCS like mean-field hamiltonian (1.23):

$$\begin{aligned} H_{MF} = \sum_{\langle i,j\rangle} \chi_{ij} c^\dagger_{i\sigma} c_{j,\sigma} + \Delta^{var}_p \sum_{p,\sigma} \hat{n}_{p\sigma} + \mu \sum_i \hat{n}_i \\ + \sum_{\langle i,j\rangle} \left(\Delta_{i,j} c^\dagger_{i,\uparrow} c^\dagger_{j,\downarrow} + c.c.\right) + \sum_i \mathbf{h_i}.\mathbf{S_i} \end{aligned} \tag{6.20}$$

Where χ_{ij} , Δ^{var}_p and Δ_{ij} are complex variational parameters. The order parameter $\mathbf{h}_i$ allow to consider Néel magnetism. Finally, μ is the chemical potential and $\Delta_p^v ar$ is the renormalized energy difference between the d and p atomic levels in the variational wavefunction. The parameters χ_{ij} are independent within one copper unit-cell (this represents 8 complex parameters) with both an amplitude and a phase. When χ_{ij} is complex, the order parameter is associated with an external flux which leads to the circulation of the holes. The operator $c_{i\sigma}^{\dagger}$ creates a hole in the orbitals d_{x2-y2} , p_x and p_y.

Moreover, we consider pairing parameters between nearest oxygen neighbors but also a pairing between oxygen sites with $|i-j|<3$ (this gives 106 complex parameters). This allows to have a first approximation of the pairing between Zhang-Rice singlets, which is expected to lead to the d-wave superconducting instability in the $t-J$ model [12].

The chemical potential in the mean-field Hamiltonian is fixed such that the non-projected wavefunction has a mean-number of holes that is consistent with the hole doping which is considered. To simplify the calculation, we will consider independently each of the instabilities, and denote by FLUX/SDW/RVB the part of the wavefunction that was considered.

Furthermore, we introduce a correlated part with a spin and charge Jastrow factor:

$$\mathcal{J}=\exp\left(\sum_{i,j=1,N} v_{ij}^c n_i n_j\right)\exp\left(\sum_{i,j=1,N} v_{ij}^S S_i^z S_j^z\right) \tag{6.21}$$

where all v_{ij}^c and v_{ij}^S are considered as free variational parameters. We impose however the symmetry of the lattice $\mathcal{T}\times\mathcal{P}$, where $\mathcal{P}$ is the point-group symmetry of the lattice, and $\mathcal{T}$ are the translations which are consistent which the unit-cell of the wavefunction (we assume in our case a 2-copper unit-cell to allow Néel magnetism). In what follows, we will denote by Ja/{Flux/RVB/SDW} a wavefunction that contains the Jastrow.

6.6.1 Jastrow factor obtained after optimization

Interestingly enough, we find after calculations that the charge Jastrow factor is slowly decreasing with the distance (see Fig. 6.9), and the nearest-neighbor charge repulsion is not negligible. We find this result even when the true nearest neighbor repulsion is zero : $V_{dp}=0$. This certainly means that the on-site repulsion U_d generates via second-order process a first neighbor repulsion that is captured by the Jastrow factor. This is in agreement with the fact that our results are generally only weakly dependent on V_{dp}.

6.7 Minimization of the Energy

The minimization of the variational parameters for a three-band model is not a simple task, and a difficult problem to overcome is the fact that the minimization

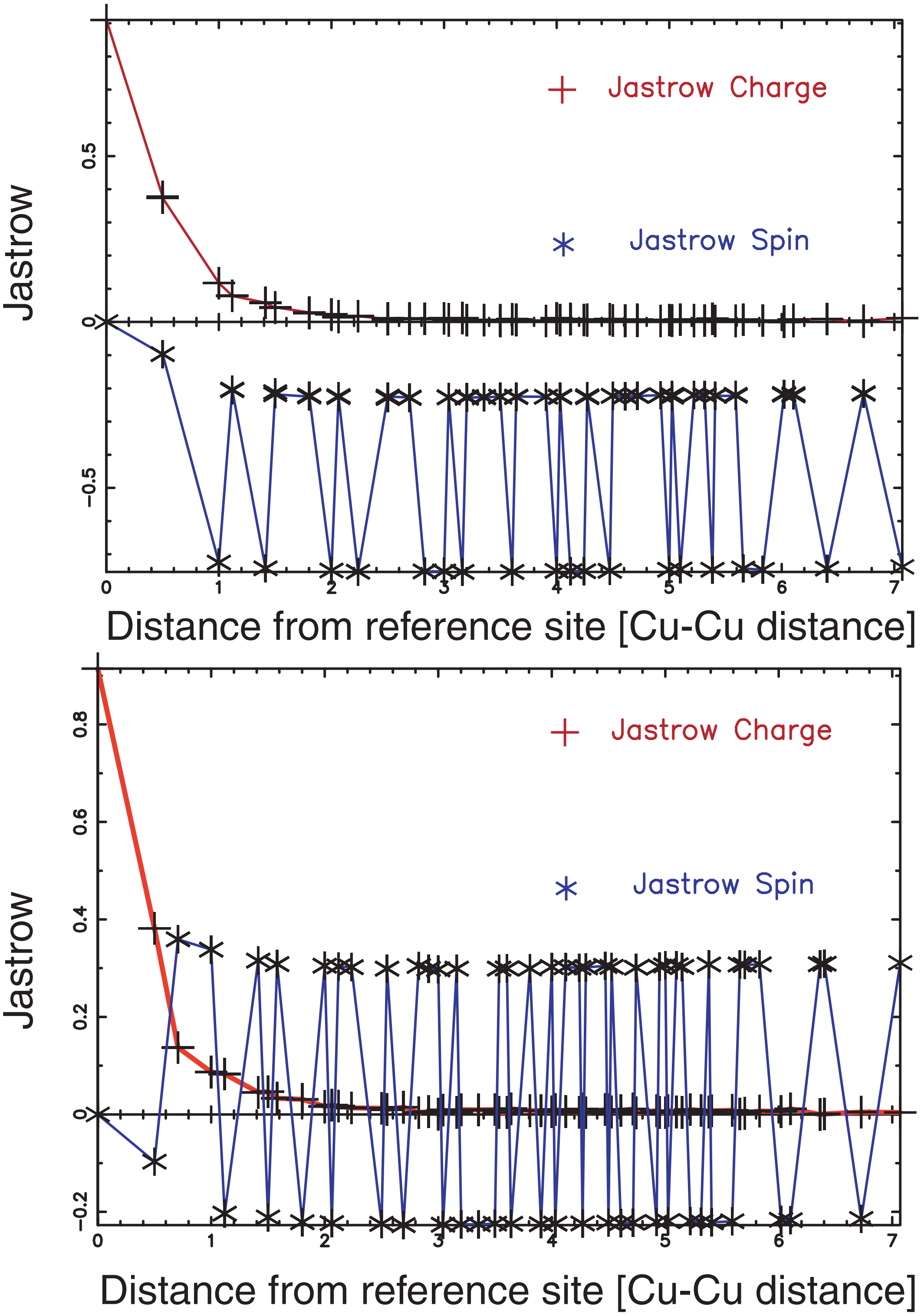

Figure 6.9: Jastrow factor versus distance for the charge parameters (red) and the spin (blue) parameters versus the distance. Top : the reference site is a copper site, bottom : the reference site is an oxygen site.

process falls most of the time in local minima. For example, using the simple Fermi sea projected with a local Gutzwiller factor, we find mainly two local minima by minimizing the variational parameters : (i) a minimum where the gutzwiller projection is very strong, which will lead to a very bad kinetic energy, and once the kinetic energy is very poor, the system will finally minimize the charge transfer energy by using a larger Δ_p^{var}, (ii) a local minimum where the wavefunction optimizes its kinetic energy by using a small Δ_p^{var}, and a weak Gutzwiller projection. These local minima are likely to be found if the long-range Jastrow factor is not used.

Moreover, we use in this chapter a stochastic minimization procedure [52, 51] to minimize both the parameters of the uncorrelated part of the wavefunction and the Jastrow parameters at the same time. This method allows one to deal with a large number of parameters, since the gradients are calculated all at the same time during a simulation. The new parameters are then calculated using the obtained gradients, and the procedure is iterated until the parameters are converged.

Once the final wavefunction is optimized, we can apply finally one further Lanczos step on the wavefunction. If the energy changes qualitatively, this means that the parameters are either not converged, or more generally that the wavefunction is not good enough to catch the low energy physics of the ground state. Moreover, the wavefunction can be used as a guiding function for the Green function Monte Carlo (GFMC) procedure which allow to correct the correlations of the observable, or it can also be used as an input for further Auxiliary-Field Quantum Monte Carlo (AFQMC) calculations. Starting the simulation by assuming random variational parameters, we find after usually a hundred iterations a convergence of both the variational energy and the variance. However, since the calculation is variational, we cannot rule out the possibility that this minimum is only local. A typical Variance/Energy profile is shown in Fig. 6.10. Once our wavefunction is minimized, we measure every observable, and we normalize every quantity by the number of copper atoms in the lattice.

6.8 Current-current correlations in a small cluster : Lanczos

Before doing the variational calculation, we have first considered the current-current correlations in small 8 copper lattice (24 sites) with respectively 9 and 10 holes (the corresponding doping are $x = 0.125\%$ and $x = 0.25\%$). We considered periodic boundary conditions. Such small clusters can be studied by exact diagonalization (Lanczos). We found that the ground state is in the sector of the Hilbert space $S^z = 0$. By considering rotational (3 rotations), translational (7 translations) and the mirror symmetries, we can reduce the Hilbert space of 10

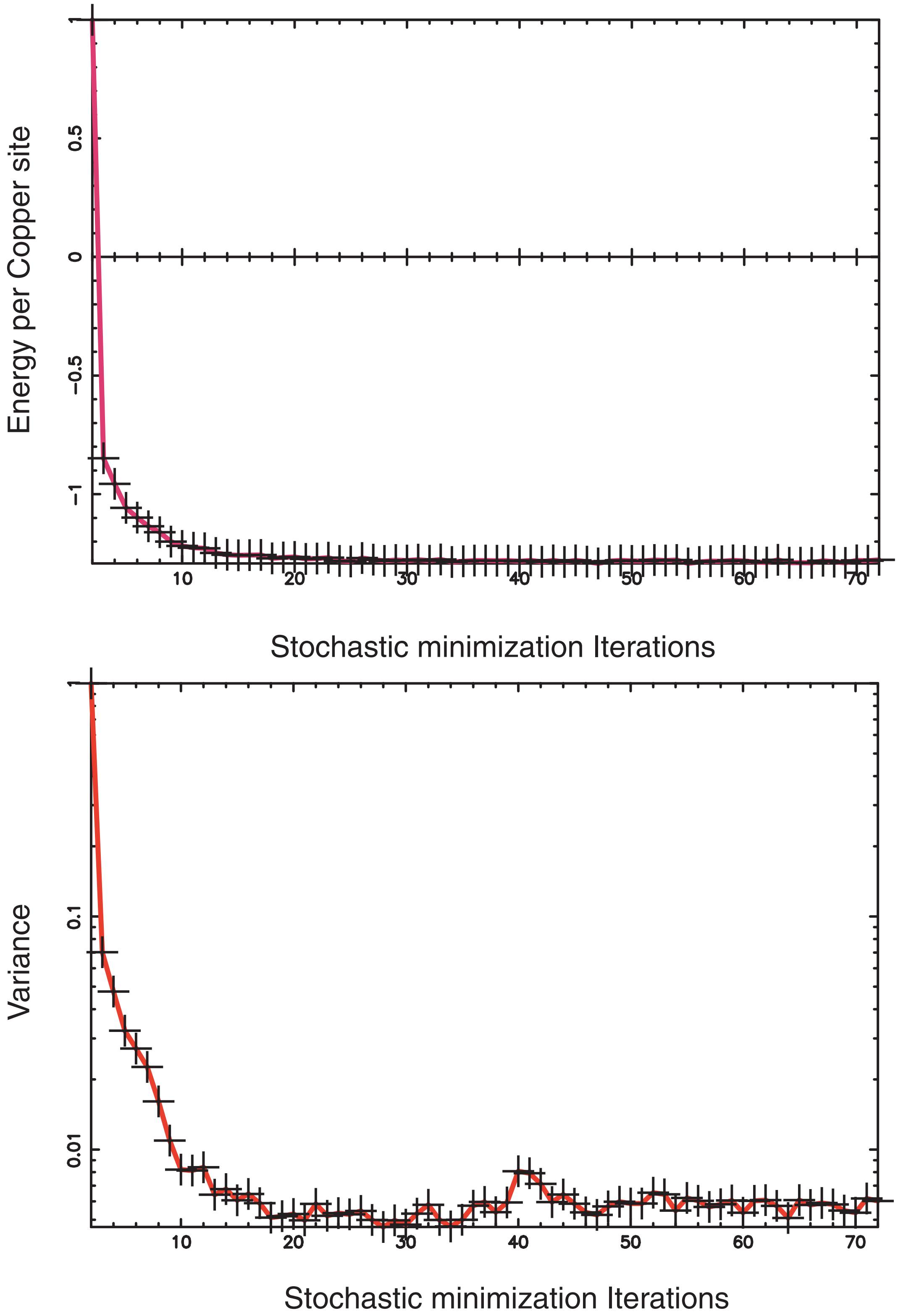

Figure 6.10: Energy and Variance versus the number of minimization iterations.

holes in the 24-site cluster down to the reasonable size of $28'231'558$ states. For both 9 and 10 holes, the ground state was found in the sectors $\chi_M = 1$ (mirror) and $\chi_R = -1$ (rotation) sector. We find that the ground state is lying in the $k_x = k_y = \pi$ sector for doping 0.125% and in the $k_x = k_y = 0$ sector for doping 0.25%. Regarding the 9-holes calculations, the results must be taken with care. On one hand, we have for this particular case a polarized ground state ($S^z = 1/2$) which is clearly not representative of the thermodynamic limit. Equally puzzling, the ground state has a finite impulsion, which is a certainly a strong finite-size effect as well. The latter two facts could lead to strange behavior in the correlation functions. Moreover, the free fermi shell is degenerate for the case of 9 holes, and not degenerate for the case of 10 holes.

Regarding the doping of 25% obtained with 10 holes, we are lying at much larger doping than the experimental range where the circulating current phase was observed by Bourges and collaborators. We can still however learn about the symmetry of the current pattern if present. We find indeed that the current correlations are rather small for the largest distance in the lattice (see Fig. 6.12, the reference link is indicated by the bold link, the most distant plaquette is indicated by the dotted box, the current correlations are about ≈ 0.006 and we find current circulation with a symmetry close to the θ_2 phase).

For finite-size clusters, time reversal symmetry cannot be broken in finite-size clusters, but we can approximate the value of the current by considering the square root of the current-current correlations, which would lead to a current amplitude of approximately $\approx 0.07eV$. Interestingly, we find that the pattern of the correlations is the same for the three distant plaquette from the reference link, and the obtained symmetry is close to the θ_2 symmetry, although one of the $p-p$ current orientation is flipped when compared with the θ_2 current pattern. Furthermore, the sum of the three oriented currents around one triangle is finite and opposite in two of the opposite triangle around one copper, suggesting that if true currents are present, the symmetry would be θ_2 like.

Surprisingly, we found that the current-current correlations depend only weakly on the Coulomb repulsion V_{dp}: for $V_{dp} = 3$ we found small variations of amplitude $< 3\%$ and the orientations of the current-current correlation pattern does not change.

Since we want to deal with broken symmetry theories, and look at the possibility of currents in the ground state of the Hubbard model , or at least in the low energy states of the Hubbard Hamiltonian, we turn back to Variational Monte Carlo simulations on larger lattices. Variational Monte Carlo is certainly a powerful tool to deal with possible symmetry breaking at zero temperature. Though it cannot give the true ground state properties, it allows for looking at the tendency towards long-range order instabilities.

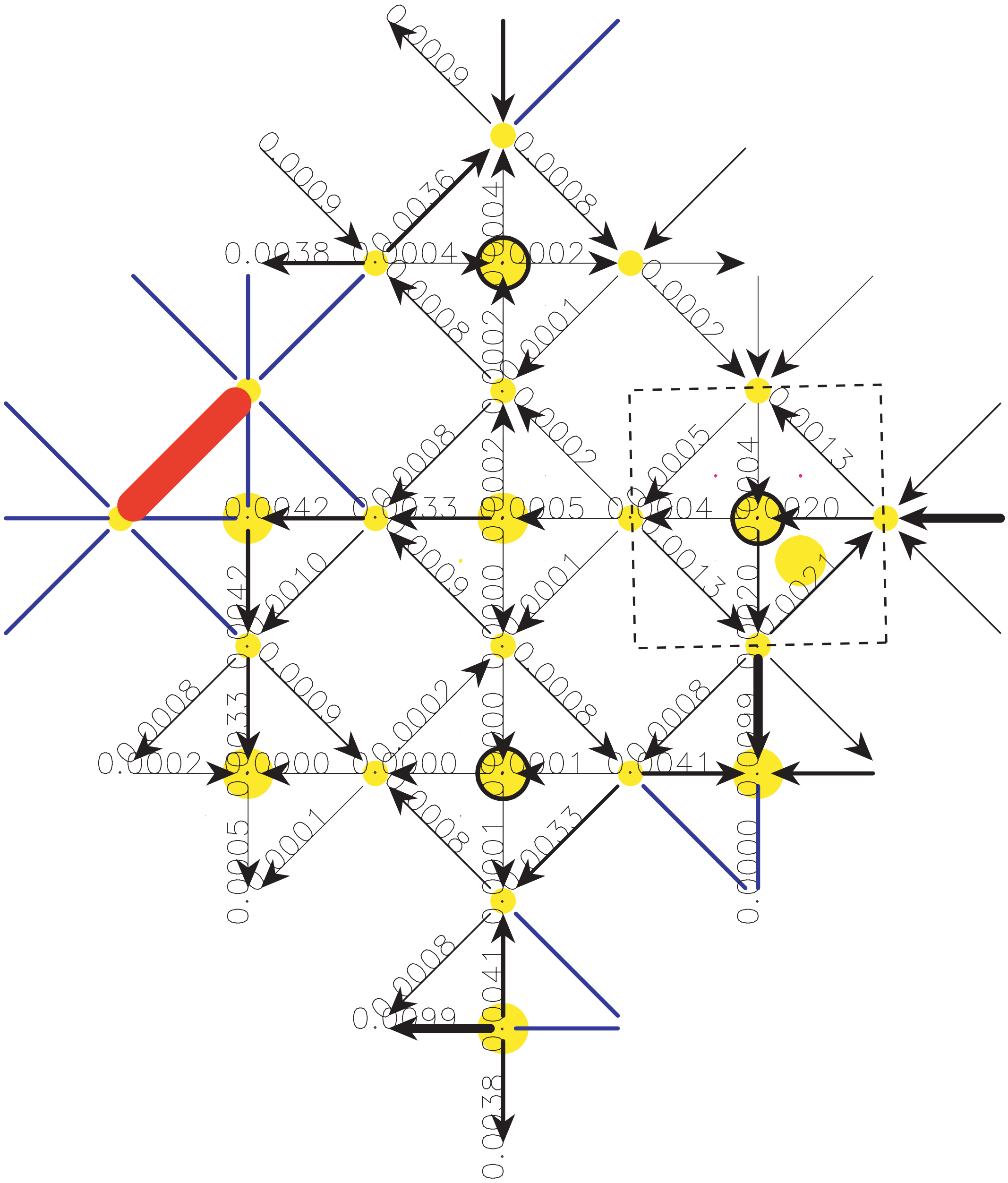

Figure 6.11: Current-current correlations for 9 holes ($S^z = 1/2$) on a 8 copper lattice (24 sites) obtained by Lanczos. The reference link is indicated by the bold link, the most distant plaquette is indicated by the dotted box. The blue (green) circles are indicating circulation inside a triangle with clockwise (anti-clockwise) direction, the radius of the circles is proportional to the circulation of the current around the corresponding triangle.

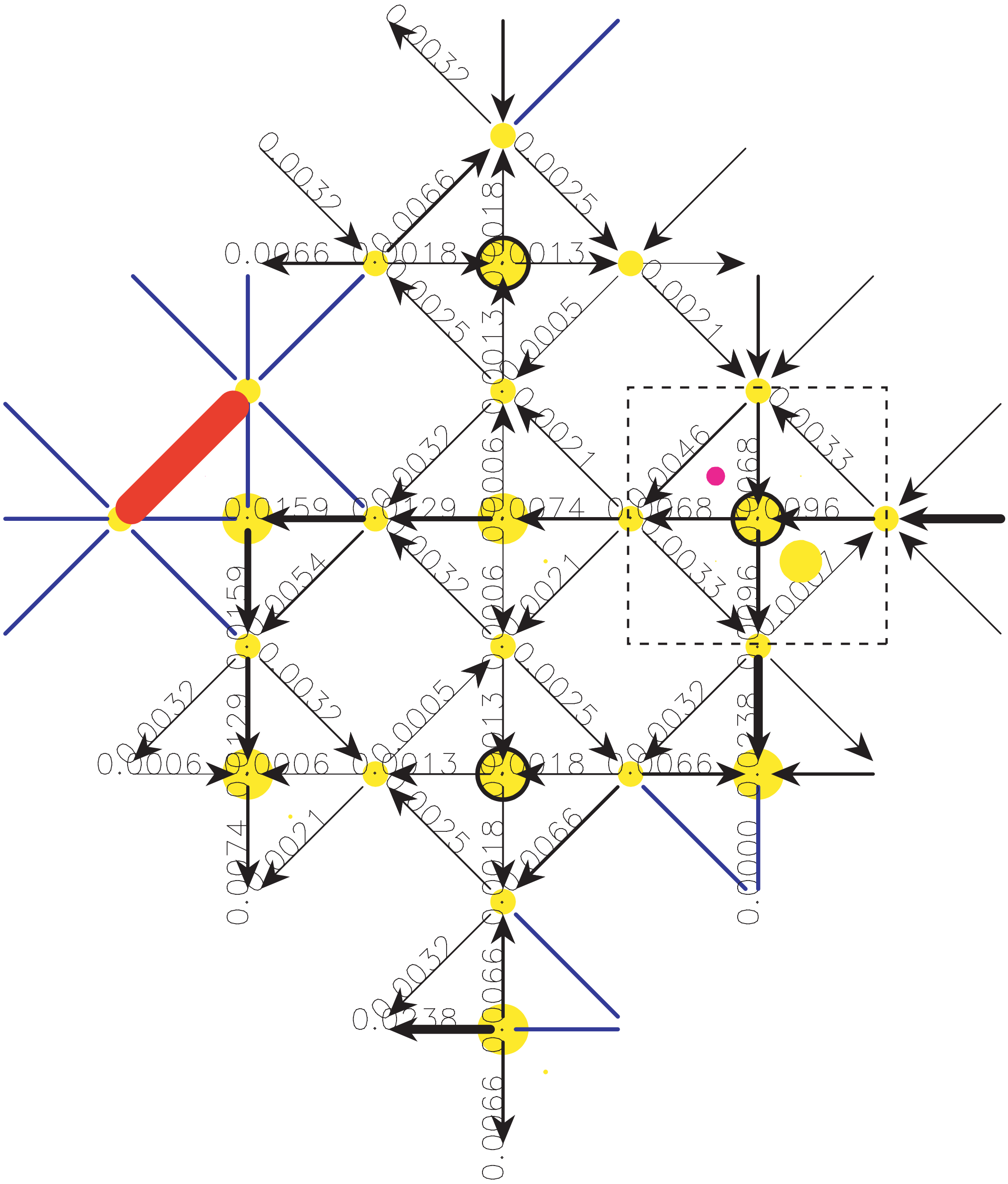

Figure 6.12: Current-current correlations for 10 holes ($S^z = 0$) on a 8 copper lattice (24 sites) obtained by Lanczos. The reference link is indicated by the bold link, the most distant plaquette is indicated by the dotted box, the current correlations are about ≈ 0.006 and we find current circulation with a symmetry close to the θ_2 phase. The blue (green) circles are indicating circulation inside a triangle with clockwise (anti-clockwise) direction, the radius of the circles is proportional to the circulation of the current around the corresponding triangle.

6.9 Comparison VMC/AFQMC/Lanczos

Exact-diagonalization calculations are interesting for comparison with non-exact techniques, like variational Monte Carlo, though they are restricted to very small clusters and can only give limited information on the long-range properties. Consequently, we propose in this section a benchmark of the quality of the wavefunction (6.20). We first compare energies for a small 8 copper cluster (24 sites) with 10 holes (see Table 6.1). Interestingly, we find that our variational wavefunction is very close in energy to the true ground state when the full Jastrow and the RVB parameters are considered (wavefunction RVB/JA) . The energy of the best variational wavefunction can be systematically improved by minimizing the new wavefunction $|\psi'\rangle = \left(1+\alpha\hat{H}\right)|\psi\rangle$, where α is a variational parameter (this procedure is called *Lanczos Step*). We obtain an improved energy (wavefunction 1LS/RVB/JA, see Table 6.1), which has an energy similar to what can be obtained with the Green function Monte Carlo method (GFMC). The latter method suffers from the minus sign problem, and we have to use the fixed node (FN) approximation to overcome this problem, using the long-range Jastrow wavefunction as a guiding function. This latter procedure gives improved variational energies. The GFMC, though it improves drastically the energy, can only be used in our implementation for real wavefunction [3], and therefore is not suited to improve the circulating current wavefunction. Another problem of the GFMC is that the calculations of non-diagonal observables needs a very large amount of computer time. The auxiliary-field quantum Monte Carlo (AFQMC) technique allows also to improve the wavefunction. AFQMC considers the improved wavefunction $|\psi'\rangle = e^{\lambda_1\hat{K}}e^{\mu_1\hat{U}} \times ... \times e^{\lambda_m\hat{K}}e^{\mu_m\hat{U}}|\psi\rangle$, where $\lambda_1...\lambda_m$ and $\mu_1...\mu_m$ are variational parameters, $m = 1,..,5$ is the number of iterations. In AFQMC $|\psi\rangle$ is allowed to be complex, and $\hat{K}$ and $\hat{U}$ are respectively the operators of the kinetic and on-site repulsion parts of the Hubbard Hamiltonian (we apply the AFQMC method on the orbital current instability). The limitation of AFQMC is that it cannot deal with the long-range Jastrow factor that optimizes our variational wavefunction. The reason for this is related to the well known *sign* problem which occurs in Quantum Monte Carlo simulations, though it is related in AFQMC to the choice of the Hubbard-Stratanovitch transformation that maps the correlated problem to uncorrelated fermions coupled to an external fluctuating field. Hence, in the framework of AFQMC calculations, we drop out the full Jastrow factor and keep only the local Gutzwiller projection. The energy for different iterations of the AFQMC method are shown in Fig. 6.13 and Table 6.10.1, and convergence is apparently obtained for $m = 5$.

In conclusion, each quantum method has some advantages and some restrictions, but our best simple variational wavefunction leads to energies that are

---

[3] The so-called fixed phase approximation should be used to use the GFMC with complex wavefunctions.

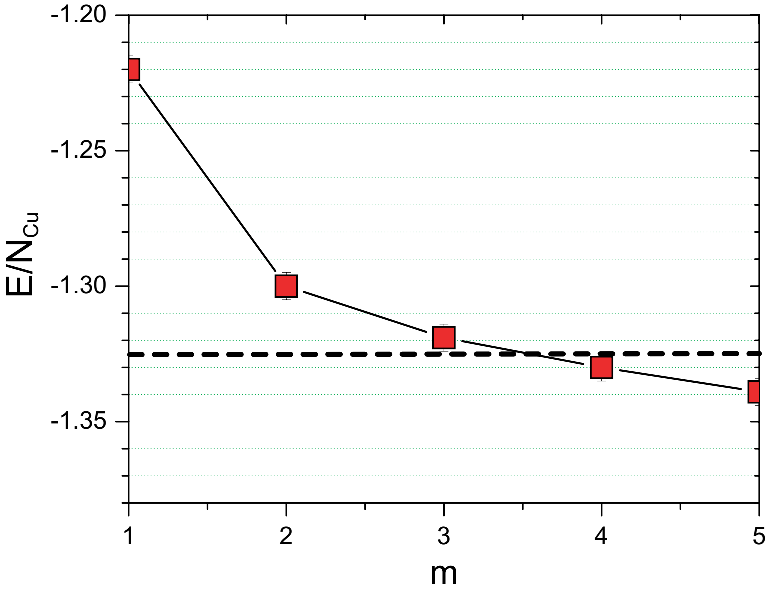

Figure 6.13: Energy of the AFQMC/FLUX wavefunction for different iterations m. The horizontal dotted line show the energy of our best variational Jastrow wavefunction JA/FLUX/1LS

similar to those obtained with the different improved Quantum Monte Carlo methods. Furthermore, we find that improving the wavefunction with Quantum Monte Carlo technique (GFMC,AFQMC) converges almost to the true ground state for the small 8-copper lattice.

6.10 Variational Monte Carlo calculations on large lattices

6.10.1 Orbital currents

In the previous section we showed that our best variational Ansatz describes qualitatively the low energy physics on small clusters. By moving towards larger lattices, we found after minimization that finite orbital currents are stabilized for both hole and electron doping close to $x = 0.08 - 0.15$ (see Fig. 6.15). The current pattern consists of lines of current along the $x, y, x + y$ direction, like in the θ_2 phase, but the current along the $x + y$ diagonal is reversed (see inset of Fig. 6.15).

The amplitude of the circulation of the charge current around one triangle plaquette is shown in Fig. 6.15. We find a current circulation of about $0.1eV$, which is smaller than what is obtained within the mean-field theory $\approx 0.30eV$ (Fig. 6.7), but which is close to the approximate current value extracted from the Lanczos calculations $\approx 0.07eV$. A small but finite energy gain is obtained by considering the orbital current instability (see Fig. 6.14).

Nevertheless, though the projected current pattern has current flowing around the opposite direction along the diagonal, the symmetry of the non-projected variational parameters is θ_2 like. The current operator defined at the mean-field level $\hat{J}_{MF} = \left(t_{ij}^{var} c_i^\dagger c_j + c.c. \right)$ is also in agreement with the θ_2 pattern. This latter operator is valid in the broken symmetry mean-field theory, and t_{ij}^{var} are complex hoppings entering the mean-field Hamiltonian H_{MF}. The Janus-like duality between the mean-field operator $\hat{J}_{MF}$ and the true gauge invariant operator $\hat{J}$ leads to non-trivial difficulties in the understanding of the variational results. On one hand, at the mean-field level, we find a true θ_2 orbital current phase that minimizes the energy of the true Hubbard Hamiltonian. On the other hand, on a pure mathematical point of view, the physical current once measured in our variational Ansatz has not the same pattern. The main reason that explains the duality lies in equation (6.3). Indeed, the information on the current is not contained entirely in the wavefunction, but depends on the Hamiltonian that is considered (the current operator is given by equation (6.3)). From another point of view, we could expect that a good enough mean-field decoupling of the Hubbard Hamiltonian would lead to mean-field operators that are consistent with the low-energy physics. The relation between $\hat{J}$ and $\hat{J}_{MF}$ is investigated further in Appendix B. Therefore, we find a current pattern that does not have the current conservation in each of the $p_x - d_{x2-y2} - p_y$ plaquette. We note that the conservation of the current is satisfied by considering the periodic conditions of the full lattice. Furthermore, we get a finite current flowing through the boundary of the lattice, which is clearly forbidden in the thermodynamic limit. We could expect that the energy of our variational Ansatz is minimized due to the current flowing

w.f.	E_{tot}	T_{dp}	T_{pp}	U_d	U_p	Δ_p	V_{dp}	variance
Lanczos	-1.13821	-3.10036	-0.79666	0.26737	0.08398	1.77545	0.63201	0
Gutzwiller	$-0.8987(1)$	-3.04326	-0.88752	0.27849	0.11712	1.88523	0.75122	0.190
JA/FLUX	$-1.0505(1)$	-3.03928	-0.82504	0.27835	0.07725	1.82681	0.63139	0.051
1LS/JA/FLUX	$-1.0877(1)$	-3.06206	-0.84549	0.25164	0.08835	1.84430	0.63553	0.018
JA/RVB	$-1.0775(1)$	-3.06068	-0.83073	0.26176	0.08197	1.83466	0.64076	0.018
AFQMC/FLUX	$-1.0814(1)$	-2.73965	-0.59317	0.39413	0.04142	1.20917	0.60668	0.001
1LS/JA/RVB	$-1.1153(1)$	-3.14070	-0.83715	0.26559	0.08736	1.86495	0.64469	0.018
GFMC/JA	$-1.1112(5)$			0.26966	0.08708	1.77314	0.63177	0.001

Table 6.1: Variational energies of the different variational wavefunctions compared with the exact diagonalization calculations (Lanczos) done on a 8 copper lattice with 10 holes and $S^z = 0$. We show the total energy (E_{tot}), the kinetic energy of the copper-oxygen links (T_{dp}) and of the oxygen-oxygen links (T_{pp}), the on-site repulsion energy of the d (U_d) and p (U_p) orbitals, the expectation value of the charge gap operator (Δ_p), and the expectation value of the Coulomb repulsion between the d and p orbitals (V_{dp}). The Lanczos step applied on the RVB wavefunction is the best variational Ansatz (1LS/JA/RVB) The auxiliary field Quantum Monte Carlo applied on the orbital current wavefunction (AFQMC/FLUX) and the fixe node approximation applied on a simple Jastrow wavefunction (GFMC/JA) are also shown.

w.f.	E_{tot}	variance	$M = \sqrt{\langle S_i^z S_{i+r}^z \rangle}$
JA/SDW	$-1.5742(5)$	0.00148(5)	0.3200(5)
1LS/JA/SDW	$-1.5756(5)$	0.00125(5)	0.3366(5)
GFMC/JA/SDW	$-1.575(2)$	0.0010(5)	0.3441(5)

Table 6.2: Projected antiferromagnetic order parameter $M = lim_{r\rightarrow\infty}\sqrt{\langle S_i^z S_{i+r}^z \rangle}$ at half-filling on a 6 × 6 copper lattice (108 sites) for the magnetic variational wavefunction JA/SDW, for the same wavefunction improved by one lanczos step 1LS/JA/SDW, and for the fixe node method using the JA/SDW as a guiding wavefunction.

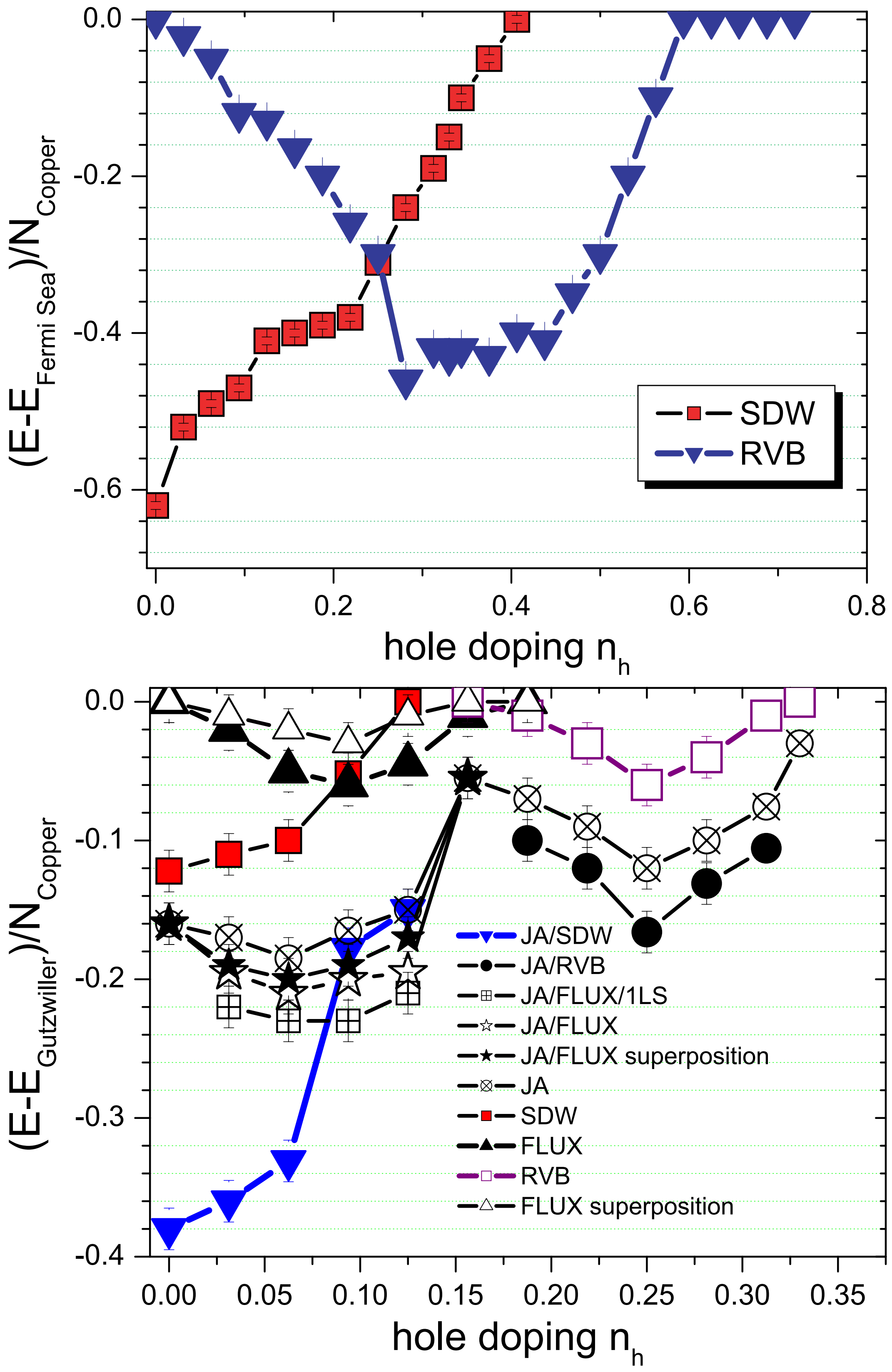

Figure 6.14: Top : Energy of the SDW and RVB wavefunctions when compared to the free Fermi sea. No Gutzwiller projection was considered for these calculations. Bottom : Hierarchy of the variational energies of the different variational wavefunctions when compared to the Gutzwiller projected wavefunction. Calculations were done on a 192 site lattice.

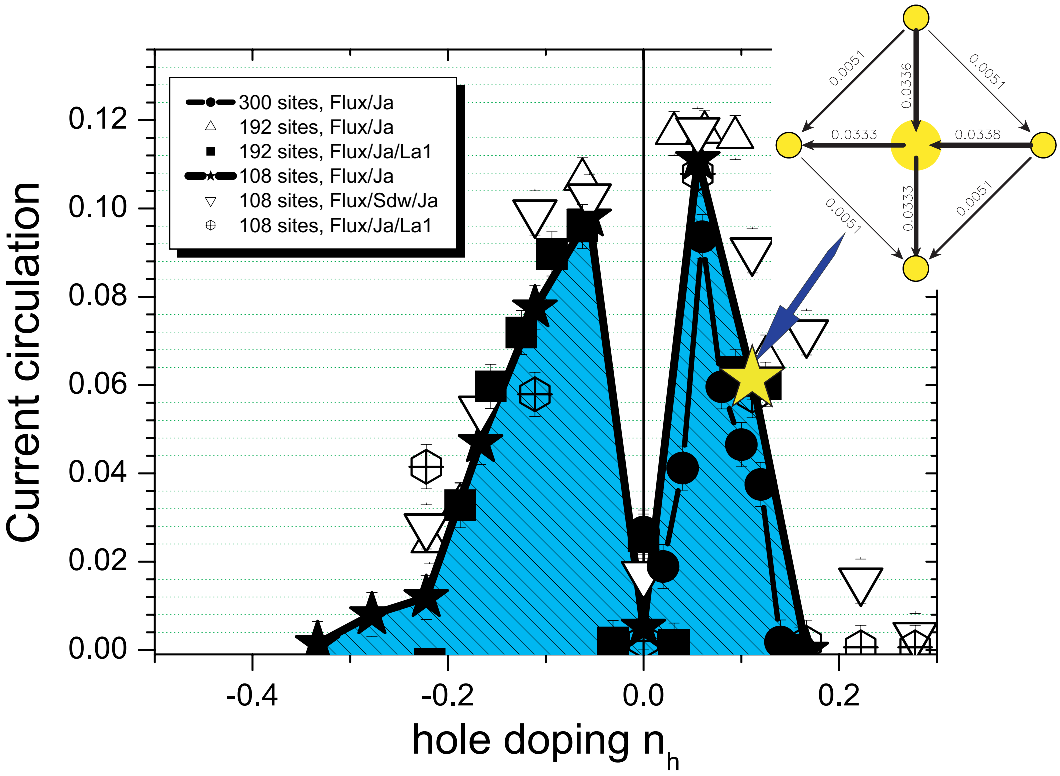

Figure 6.15: Circulation of the current around one plaquette in the three-band Hubbard model obtained by VMC for different lattice sizes. The current pattern is close to the θ_2 symmetry: however, the obtained pattern has current running in the reversed direction on the oxygen-oxygen links. The resulting circulation of the current is finite for two opposite triangle plaquettes around the copper site, and vanishes for the two other plaquettes. This leads to un-physical macroscopic currents running through the boundary conditions.

through the torus on which the lattice is defined [143]. Moreover, by imposing the current conservation inside each $p_x - d_{x2-y2} - p_y$ triangle, we find that the sign of the variational $d-p$ kinetic part is changed and such a wavefunction with local conserved current has a worse kinetic energy. At present stage we cannot reach a definitive conclusion.

It is also interesting to carry out further variational calculations on lattices with open boundary conditions. This will at least remove the flux at the boundary. However, we expect very large finite size effect for such geometries. These calculations are done in section 6.10.2. Since the circulation of the current found by variational Monte Carlo is rather small, we would like to check if this small circulation persists upon other improvements of the wavefunction. To assess such an issue, we first compare the energy and the current circulation value when we

w.f.	E_{tot}	Current circulation
JA/FS	$-1.2445(4)$	
GFMC/JA/FS	$-1.3257(4)$	
JA/FLUX	$-1.2722(5)$	0.102(2)
JA/FLUX/1LS	$-1.3258(1)$	0.113(5)
FLUX/AFQMC m=1	$-1.220(1)$	0.091(5)
FLUX/AFQMC m=2	$-1.300(1)$	0.094(5)
FLUX/AFQMC m=3	$-1.319(1)$	0.096(5)
FLUX/AFQMC m=4	$-1.330(5)$	0.112(1)
FLUX/AFQMC m=5	$-1.339(4)$	0.104(1)

Table 6.3: Variational energies and the circulation of the current around one plaquette for different AFQMC iterations $m = 1, ..., 5$. Results were obtained on a 96 site lattice.

apply successively AFQMC optimizations (see table 6.10.1). Auxiliary-field quantum Monte Carlo is a very powerful tool to improve further our wavefunction. The method is purely variational, but it might suffer from the so-called *quantum sign* problem. However, we find that the sign problem is not severe for lattice with 32 copper sites (96 sites). Therefore, we checked on a 32-copper site lattice the quality of our wavefunction at hole doping $x = 0.125\%$. In Table 6.10.1 we show the energies of the different AFQMC iterations, and convergence is almost reached for 5 iterations. Interestingly enough, the current amplitude does not change significantly when the energy converges to the ground state energy. This supports the presence of current along lines in the lattice in the ground state of the Hubbard model when periodic boundary conditions are present.

6.10.2 Open boundary conditions

The previously discussed θ_2 flux wavefunction consists mainly of horizontal and vertical lines and has only currents on the diagonal lines. Therefore, there is a finite current flowing across the boundary conditions of the lattice, which is not allowed in the thermodynamic limit. Noteworthy, considering anti-periodic conditions for the Hubbard model [4] would also lead to a flux through the lattice, and the energy of this model would be slightly lower than the Hubbard model with periodic conditions. The energy corrections due to the boundary conditions is a finite-size-effect decreasing with the size of the lattice like $1/L$, where L is the linear size of the lattice. Similarly, the ground state of a copper-Oxide model on

---

[4] A cluster with so-called anti-periodic conditions in one of the e_x (e_y) direction has a change in the sign in the hopping integrals that connect sites across the vertical (horizontal) boundary of the lattice.

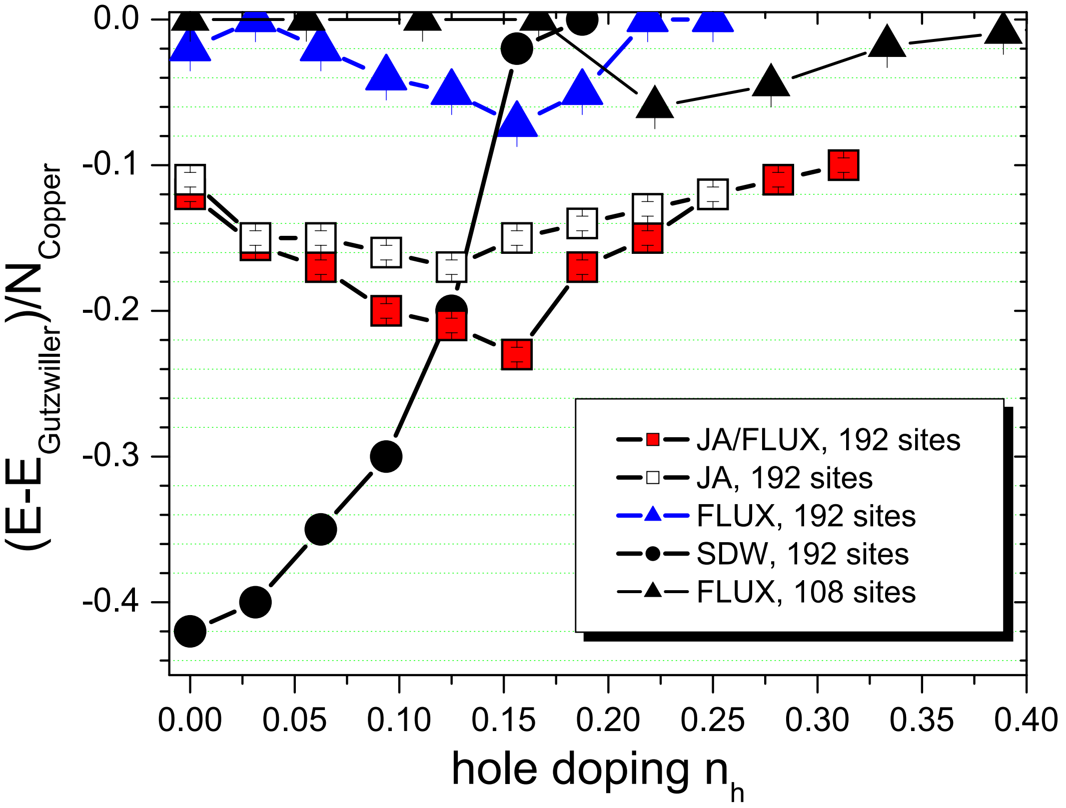

Figure 6.16: Energy difference between the different variational Ansatz and the Gutzwiller wavefunction. Open boundary conditions are assumed in these calculations.

a ring coupled to an external flux [143] is minimized in finite-size rings at integer values of the flux quanta. The ring can be seen as a one dimensional chain with periodic boundary conditions and therefore it has also in this case a net current running through the boundary conditions. In conclusion, models with artificial flux through the boundary conditions are known to introduce corrections to the energy for finite-size clusters. Therefore, the small energy optimization of the JA/FLUX wavefunction could well be due to a finite-size effect. However, there is a subtle but crucial difference between comparing the energy of the groundstates of Hamiltonians with different periodic/anti-periodic conditions, or having different flux imposed, and comparing for a given model the energy of different variational wavefunction. In the former case, the parameters of the model are changed, and a finite flux through the boundary conditions is stabilized in the ground state. But this flux is already introduced in the original Hamiltonian, and it is natural to observe it in the ground state. In the latter case, the Hubbard Hamiltonian does not contain any flux originally, but the variational Ansatz opti-

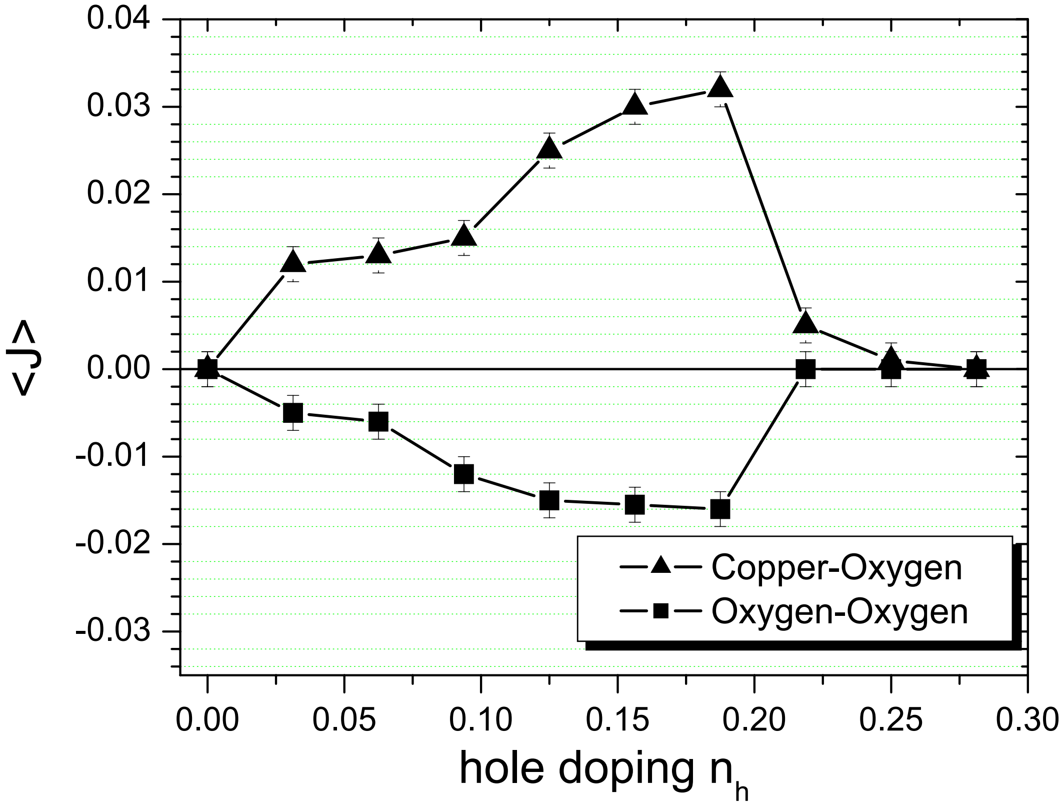

Figure 6.17: Amplitude of the current obtained in the JA/FLUX wavefunction for a 192 site lattice with open boundary conditions. The current operator measured on a copper-oxygen and on a oxygen-oxygen link is shown. The sign is positive when the current is oriented according to the θ_2 current pattern, and negative when its direction is opposite.

mizes the energy by spontaneously generating a finite flux. This occurs due to the presence of strong interactions, and it is not connected to the geometry of the lattice. In order to prevent the JA/FLUX wavefunction to have a net current across the boundary, we have done further calculations for clusters with open boundary conditions. In this particular case, the usual reciprocal space construction of the variational wavefunction is no longer valid, and the real-space diagonalization of the mean-field Hamiltonian must be used (see Chapter 2). The θ_2 flux wavefunction is still stabilized, though the range of stabilization is for slightly higher doping range on the small 36 copper lattice, and moves towards smaller doping range for a 64 copper lattice (see Fig.6.16). The current pattern measured in the projected wavefunction is identical to the pattern obtained with periodic boundary conditions. However, the current is not conserved at the vertices where the line of currents meet the boundary conditions, though the current is conserved in the simulations with periodic boundary conditions. We emphasize that no condition is present at the variational level that would ensure the current conservations in the variational wavefunction which is proposed as Ansatz for the three-band Hubbard model.

Finally, we conclude that the JA/FLUX wavefunction is stabilized also in the case when it cannot have a non-physical flux through the boundary. Nevertheless, the open boundary conditions are also expected to introduce severe finite-size effects, that could also stabilize non-physical phases.

6.10.3 Magnetism and superconductivity

According to previous VMC evaluations for the $U_d = \infty$ three-band Hubbard model [140], the antiferromagnetic region extends up to 50% hole doping and the d-wave superconducting phase exists only in the infinitesimally small region near the boundary of the antiferromagnetic phase. Thus, previous VMC results concluded that the chance for d-wave superconductivity is small in the three-band Hubbard model. It was concluded that the parameters of the Hubbard Hamiltonian should be tuned such that the anfiferromagnetic phase shrinks to a smaller range of doping. We propose to study in this section the stabilization of the RVB and magnetic phase with our Jastrow wavefunction, which is expected to treat correctly the correlations.

Therefore, besides the orbital current instabilities, we considered also the possibility for Néel magnetic long-range order and superconductivity. We considered as a first approximation only the $Q = (\pi, \pi)$ pitch vector for the spin density wave. We would although expect that the pitch vector is doping dependent. This issue was addressed for the three-band Hubbard model in Ref. [59]. The possibility for stripes was also considered by variational calculations [139]. In our work, we expect that the long-range correlations contained in the Jastrow factor will allow a correct treatment of the spin correlations. We find indeed that the magnetic order parameter $M = \lim_{r\to\infty} \sqrt{\langle S_i^z S_{i+}^z \rangle})$ is for our best variational wavefunction 66% of the classical value (see Table 6.2). Using this wavefunction as a guiding function for the fixed node calculations, we find a slightly higher magnetic order with 69%. This value can be compared with the 60% obtained by quantum Monte Carlo in the one-band Heisenberg model. However, in the three-band Hubbard model, the magnetic instability is strongly dependent on the oxygen-oxygen hopping integral t_{pp}. Since this hopping frustrates the geometry, we find that the magnetic order is destroyed when $t_{pp} \approx 2eV$.

Nevertheless, the magnetic instability is overestimated when compared to the cuprates phase diagram where it vanishes for a small hole doping of approximately $x = 2\%$. The spin density wave is however very likely to be stabilized in variational calculations, since the alternating magnetization allow to avoid double occupancy in the uncorrelated part of the wavefunction. The presence of magnetic order obviously costs kinetic energy, but it it does a better job than a

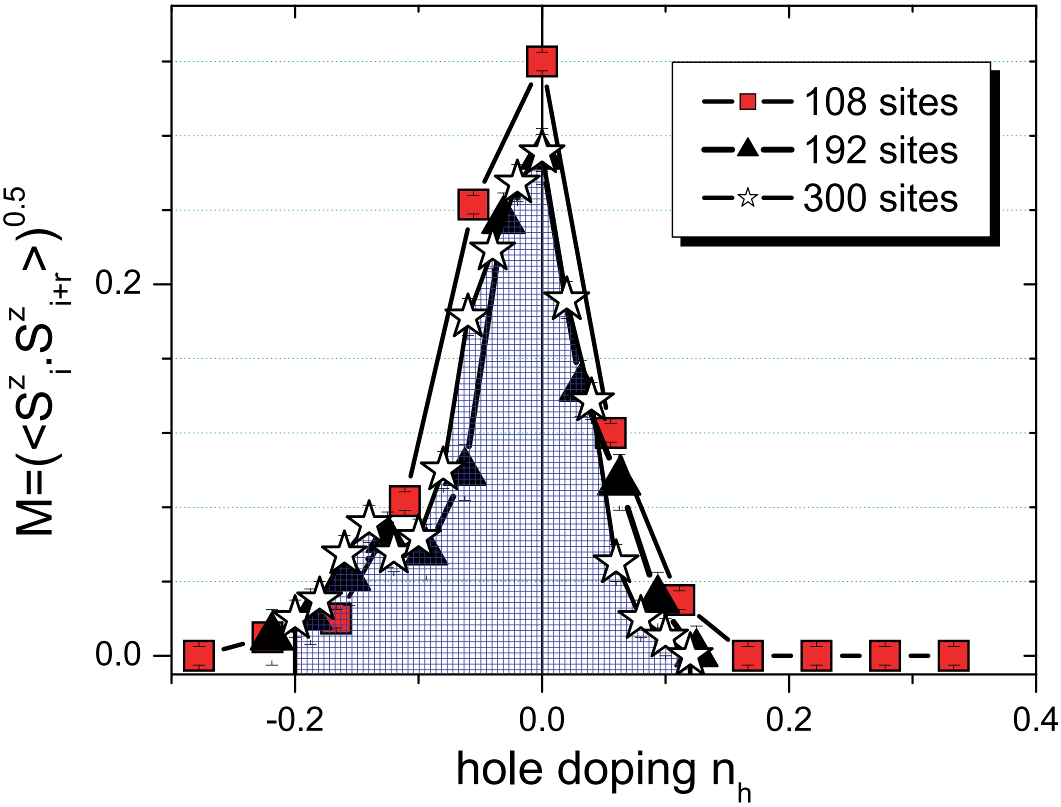

Figure 6.18: Magnetic order parameter $M = \lim_{r\to\infty} \sqrt{\langle S_i^z S_{i+}^z \rangle})$ versus the hole doping. The saturated value for the magnetic order parameter is $M = 0.5$.

pure local gutzwiller projection, which kills very strongly the kinetic energy. Another way to reduce the double occupancy is done by the resonating valence bond instability, which optimizes both the double occupancy and the kinetic energy. We show in Fig. 6.14 the energy gains of the SDW and RVB instabilities when no projection are present. The two instabilities cross at around $x \approx 20\%$ doping. However, the correlated part of the wavefunction plays a drastic role and clearly needs to be considered. Very interestingly, we find that the symmetry of the pairing Δ_{ij} is, in the real space representation of the three-band Hubbard model, not restricted to nearest neighbor copper and oxygen sites. Indeed, no energy optimization can be obtained when the pairing is restricted to oxygen-oxygen and copper-oxygen bonds. This can be understood in terms of the Zhang-Rice mapping of the three-band Hubbard model to the one band $t{-}J$ model. In the frame of this theory, the particles of the $t{-}J$ model are equivalent to a local copper-oxygen $d_\uparrow\,(p_{x\downarrow} - p_{-x\downarrow} + p_{y\downarrow} - p_{-y\downarrow})$ singlet in the three-band language. It was very strongly established that a d-wave RVB instability is present in the $t{-}J$ model [19, 144, 24, 129], but it is not intuitive to get a picture of this superconducting instability in terms of the holes in the three-band Hubbard model. The symmetry that was found in our calculations, by the energy minimization of the RVB wavefunction, is shown in Fig. 6.19. We note that for a reference site i, Δ_{ij} consists of four strong plaquettes (bold square in Fig. 6.19) around the reference site. The sign of the pairing has a d-wave symmetry for these latter plaquettes, and additionally, inside each of the plaquette the sign is alternating identically to the Zhang-Rice singlet $d_{\uparrow}\left(p_{x\downarrow} - p_{-x\downarrow} + p_{y\downarrow} - p_{-y\downarrow}\right)$ symmetry.

6.11 Role of the Apical oxygens

The theoretical challenge is to find the simplest model of the copper-oxygen plane which would contain all the essential physical aspects. The electronic structure calculations suggest that a good starting point is provided by the previously discussed three-band model, including coper 3d$_{x2-y2}$ orbitals and oxygen 2p$_{\sigma}$ orbitals. It has been repeatedly argued that the two dimensional plane contains the essential of the low energy physics. Zhang and Rice pointed out that a hole in a copper d_{x2-y2} orbital and a hole in the oxygen orbital form a local singlet for the realistic parameters of the three-band Hamiltonian, and the three-band model does reduce to an effective single-band t-J model.

However, one of the issues related to a breakdown of such a mapping is related to the presence of additional apical oxygens. It was proposed for example that a triplet states could be favored, instead of the singlet state, and stabilized by the occupancy of apical oxygens and copper $d_{3z^2-r^2}$ orbitals. Indeed, since the early days of high-temperature superconductivity, the question of a possible role of apical sites in cuprates superconductors has been controversially discussed. A part of the measurements were consistent with the conjecture that there is a significant influence of the apical site on high-Tc superconductivity.

Moreover, further theoretical investigations using a six-band Hubbard model interaction scheme showed that some holes with Cu3d$_{3z2-r2}$ orbital character do exist (experimental evidence for this can be found in Ref. [145]), and that a fraction of them is hybridized with the apical oxygen [146]. This can easily be understood, since there is a strong Coulomb repulsion between the holes at Cu sites, the extra holes introduced by doping residing primarily on oxygen sites.

Furthermore, it has been pointed out that for a realistic description of the principal features of the cuprates superconductors, like for example the insulating gap in the undoped parent compounds, one has to include also the orbitals of apical oxygens.

Several experiments indicate that the out-of-plane apical oxygen orbitals are also involved in accommodating some of the holes doped into the CuO_2 planes. One of the most exciting ones is that there might exist a correlation between the maximal critical temperature T$_c$ reached in different cuprates and the copper-to-apex bonding, as well as the Madelung potential at the apical oxygen measured

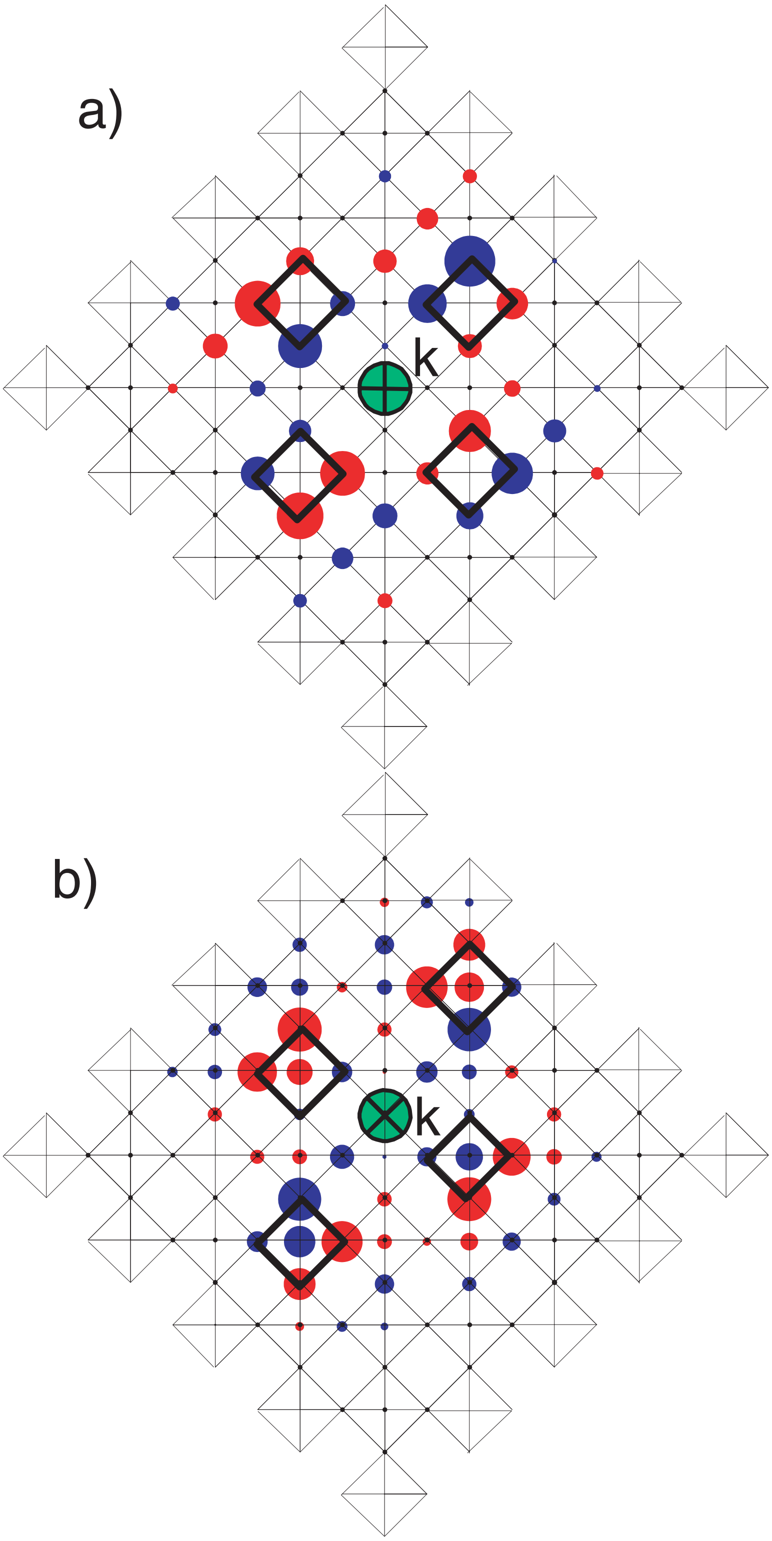

Figure 6.19: RVB variational parameters Δ_{ij}, where a reference site i is located at the site located at the center of the cluster, and j is running through all the site of the lattice. Red (blue) circles denotes positive (negative) Δ_{ij}, and the radius of the circle is proportional to $|\Delta_{ij}|$. Top: the reference site i is located on a copper site. Bottom : the reference site i is located on an oxygen site.

with respect to that at the oxygens in the planes [147]. Equally interesting, X-ray absorption spectroscopy on single crystals of infinite-layer compounds of Ca doped YBCO compounds have shown that superconductivity might appear in this compound only when holes are present at the apical oxygen sites [148].

Going also in this direction, it was argued recently that upon hole doping, the static charge attraction between the apical oxygens and the d orbitals could lead to a reduction of this distance [149]. Theoretically, it was shown by the first-principles variational calculations of the spin-density-functional approach that the optimized distance between apical O and Cu in $\mathrm{La}_{2-x}\mathrm{Sr}_x\mathrm{CuO}_4$ which minimizes the total energy decreases upon Sr doping. As a result, the elongated CuO_6 octahedrons by the Jahn-Teller interactions, shrink by doping holes. This shrinking effect was called *anti-Jahn-Teller effect*.

We propose to address the issue of the presence of apical oxygen, in the context of circulating orbital currents, and we use the same variational frame-work as developed in the previous section. We consider the extended 6-band Hubbard model including the two additional apical oxygens surrounding a copper atom and also the additional d_{3z2-r2} orbitals:

$$\begin{aligned}
H = &\sum_{m,\alpha\sigma} \epsilon_\alpha n_{m,\alpha\sigma} + \epsilon_p + \sum_{k,\sigma} n_{k,a\sigma} + \sum_{\langle m,i\rangle,\alpha\sigma} t_{\alpha p} \left(d^\dagger_{m,\alpha\sigma} p_{i\sigma} + c.c.\right) + \\
&t_{za} \sum_{\langle m,k\rangle,\sigma} \left(d^\dagger_{m,z\sigma} a_{k\sigma} + c.c\right) + t_{pp} \sum_{\langle i,j\rangle,\sigma} \left(p^\dagger_{i\sigma} p_{j\sigma} + c.c.\right) + t_{pa} \sum_{\langle i,k\rangle,\sigma} \left(p^\dagger_{i\sigma} a_{k\sigma} + c.c.\right) + \\
&U_d \sum_{m\alpha} n_{m,\alpha\uparrow} n_{m,\alpha\downarrow} + U_p \sum_i n_{i,p\uparrow} n_{i,p\downarrow} + U_a \sum_k n_{k,a\uparrow} n_{k,a\downarrow} + \left(U_{xz} - \tfrac{1}{2} J_{xz}\right) \sum_m n_{mx} n_{mz} + \\
&J_{xz} \sum_m \left(d^\dagger_{m,x\uparrow} d^\dagger_{m,x\downarrow} d_{m,z\downarrow} d_{m,z\uparrow} + c.c.\right) - 2J_{xz} \sum_m s_{mx} \cdot s_{mz} + \sum_{\langle m,i\rangle} U_{\alpha p} n_{m\alpha} n_{ip} + \\
&\sum_{\langle m,k\rangle,\alpha} U_{\alpha a} n_{m\alpha} n_{ka}
\end{aligned} \tag{6.22}$$

Here the $d^\dagger_{mx\sigma}$ and $d^\dagger_{mz\sigma}$ creates a hole respectively in the d_{x2-y2} and d_{3z2-r2} orbitals; $p_{i\sigma}$ refer to the orbitals lying inside the plane, and $a_{i\sigma}$ refer to the apical oxygen orbitals. Furthermore, S_{mx} and S_{mz} are spin operators for the d_{x2-y2} and d_{3z2-r2} orbitals. The Hamiltonian contains inter-orbitals Hund's coupling J_{xz} which reduces the on-site Coulomb repulsion U_{xz}. The first three terms specify the reference hole atomic energies. The hopping elements $t_{\alpha p}$ ($\alpha = x, z$), t_{za}, t_{pp}, t_{pa} stand for the copper-oxygen-in-plane, copper-Apical-oxygen, oxygen-oxygen-in-plane, oxygen-in-plane-Apical-oxygen hoppings respectively. The on-site intra-orbitals Coulomb repulsion are U_d, U_p and U_a respectively, while the inter-orbital Coulomb and exchange energies at copper sites are U_{xz} and J_{xz}. Only the most important nearest neighbor Coulomb repulsions U_{dp} and U_{da} were considered. Moreover, we consider a set of realistic parameters [145, 147, 150, 151]:

$\epsilon\,(d_{x^2-y^2})$	0	$\epsilon\,(d_{3z^2-r^2})$	0.64
$\epsilon\,(p_\sigma)$	3.51	$\epsilon\,(a_z)$	2.05
$t\,(d_{x^2-y^2}, p_\sigma)$	1.30	$t\,(d_{3z^2-r^2}, p_\sigma)$	0.95
$t\,(d_{3z^2-r^2}, a_z)$	0.82	$t\,(p_\sigma, p_\sigma)$	0.61
$t\,(p_\sigma, a_z)$	0.33		
$J_{xz}\,(d_{x^2-y^2}, d_{3z^2-r^2})$	1.19		
$U\,(p_\sigma)$	4.19	$U\,(a_z)$	3.67
$U\,(a, d)$	0.18	$U\,(p, d)$	0.60
$U\,(d_{x^2-y^2}) = U\,(d_{3z^2-r^2})$	8.96	$U\,(d_{x^2-y^2}, d_{3z^2-r^2})$	6.58

In what follows, we add an additional phenomenological parameter D_1 that describes the distance between the copper atom and the apical oxygens. If the distance is reduced, we expect that the transfer integrals t_{za}, t_{pa} will be increased. We consider therefore $D_1 t_{za}$ and $D_1 t_{pa}$ as hopping integrals and we propose to tune D_1.

After the minimization process in a 32 copper lattice (192 sites), we find that the current circulation in the $p_x - d_{x2-y2} - p_y$ plaquette when $D_1 < 1.5$, with a current pattern close to θ_2 symmetry of the three-band Hubbard model (see Fig. 6.21). We get indeed the same orbital current pattern as the one discussed in the previous section for the range $D_1 \in [0, 1.5]$. We can raise the same critics to this orbital current instability, i.e. there is a finite flux running through the periodic boundaries and there is no current conservation inside all the triangle plaquettes.

It is worth noting that, when $D_1 > 1.5$, the current circulates mainly in the $p_x - p_z - p_y$ plaquettes and in the $p_x - d_z - p_y$ plaquettes, with a pattern corresponding to θ_1 symmetry (see Fig. 6.21). However, the current is a true rotational flow in these latter plaquettes and the conservation of the current is almost achieved in all the plaquettes. Let us note that the latter plaquettes have the hopping signs that correspond to the circulating plaquettes discussed in section 6.6. In this limit, the current flowing across the boundary is small, and the current pattern has a finite out-of-plane component.

Interestingly, it was also found in neutron experiments that the magnetic moments have an in-plane component, which would be consistent with our present result, though we had to introduce an additional parameter D_1 to tune the transfer integral parameter to obtain a stronger t_{za} and t_{pa} transfer integrals. Noteworthy, this would be consistent with the assumption that the apical oxygen are getting closer to the copper sites when the system is doped with additional holes. As discussed in Ref. [149], this could happen if the electrostatic force between the copper and apical oxygen becomes strong. Eventually, when $D_1 = 1.5$, the two types of patterns are close in energy and consequently, we could expect a 2-fold degenerate ground state in the intermediate regime. If the θ_1 and θ_2 instabilities stabilized variationally in the six-band model are taken seriously, than a 2-fold discrete order parameter could be built in the regime $D_1 \approx 1.5$, and we might expect a finite temperature transition associated with this order parameter [5].

6.12 Bond-Charge repulsion

In the calculations, presented so far, the strong correlations between the electrons were mainly contained in the Coulomb repulsion term of the three- and six-band Hubbard Hamiltonians. However, only a very rough approximation of the two-body Coulomb observables was considered, by assuming a diagonal form $\hat{V} = U_{ij}\hat{n}_i\hat{n}_j$. The purpose of this section is to consider a more realistic description of the two-body Coulomb observable. Indeed, in this section we want to include the renormalization of the single-hole hopping t_{ij} due to the Coulomb repulsion in the three-band Hubbard Hamiltonian. In particular, for the case of the three-band Hubbard model, since the distance between the copper and the $p-p$ bond is small, we propose in this section to include the repulsion between the $p-p$ bonds and a charge localized at a d_{x2-y2} orbital [152, 153]. We start with the Coulomb observable in second quantization:

$$\hat{V} = \sum_{ijkl,\sigma\sigma'} c^{\dagger}_{i\sigma} c^{\dagger}_{j\sigma'} c_{k,\sigma'} c_{l,\sigma} \phi_{ijkl} \tag{6.23}$$

and ϕ_{ijkl} is defined in terms of the Wannier orbitals $\phi_i\left(r-R_i\right)$:

$$\phi_{ijkl} = \int d^3r^3 d^3r' \phi^{\dagger}_i\left(r-R_i\right)\phi^{\dagger}_j\left(r'-R_j\right)V_{ee}\left(r-r'\right)\phi_k\left(r'-R_k\right)\phi_l\left(r-R_l\right) \tag{6.24}$$

Therefore, to take into account a more realistic description of the Coulomb interactions, we consider the additional interacting term in the *electron notations*:

$$H_3 = V_2\left(\sum_{\langle i,j\rangle,\sigma} t_{ij} c^{+}_{i,\sigma} c_{j,\sigma}\left(n_{i-\sigma}+n_{j,-\sigma}\right) + \sum_{\langle i,j,k\rangle\sigma}\left(t_{ij} n_k c^{+}_{i,\sigma} c_{j,\sigma} + c.c.\right)\right) \tag{6.25}$$

This term is nothing else but a correlated hopping process. It was suggested in the context of the one band Hubbard model that non-diagonal Coulomb interactions might be important for superconductivity, namely, the so-called bond-charge repulsion, i.e. the Coulomb interaction between a bond charge and an atomic charge [153]. In general, the contribution of these interactions in real materials are very different; for instance, for 3d electrons in transition metals U,V,V_2 have typically the proportions 20 : 3 : 0.5.

---

[5] The Mermin-Wagner theorem prevents any continuous symmetry breaking at a finite temperature in two dimensions, but a it does not rule out the possibility for a discrete symmetry breaking.

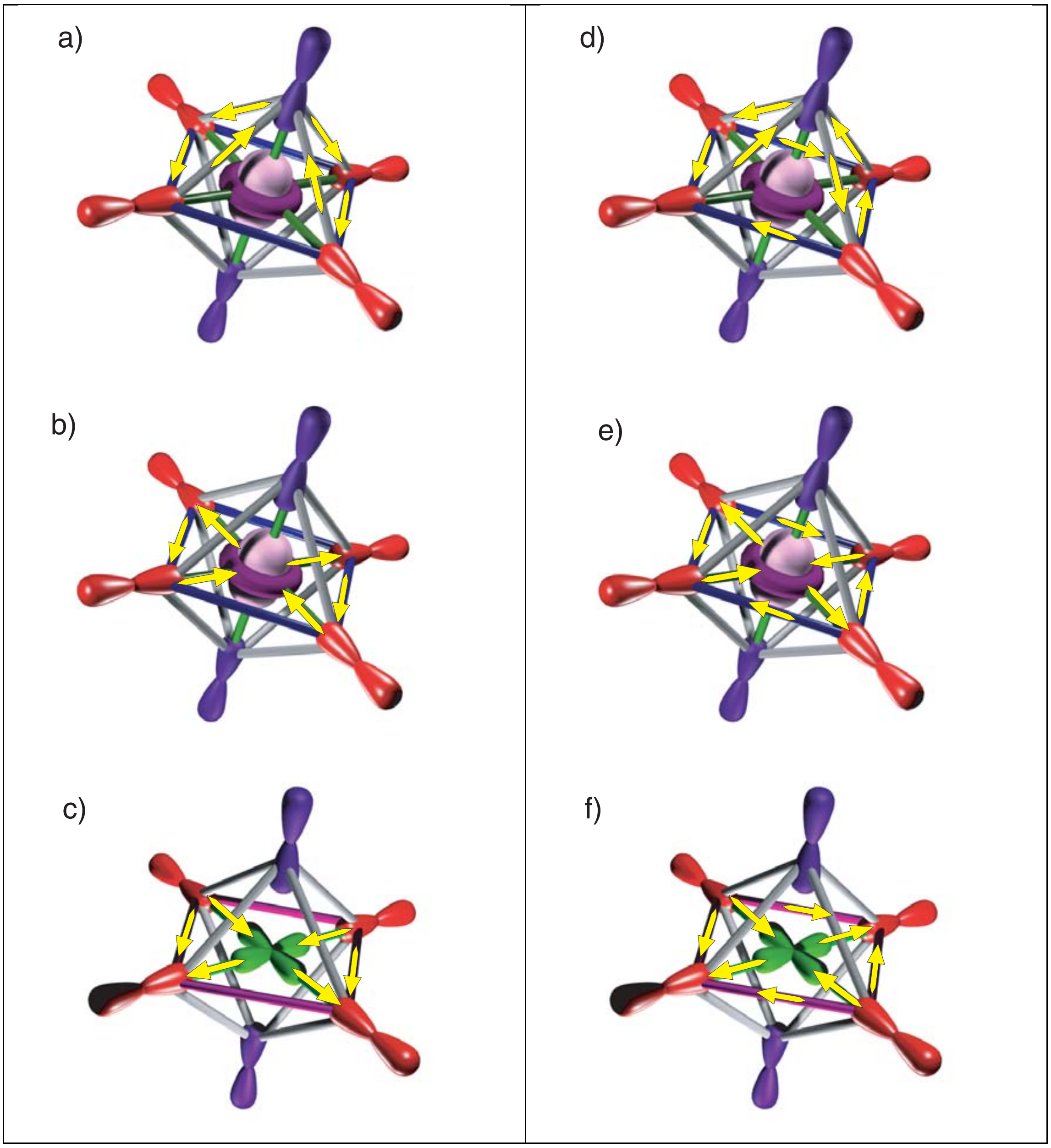

Figure 6.20: Flux pattern obtained in the six-band Hubbard model. The current is circulating with a θ_2 like pattern a),b),c) or with a θ_1 like pattern d),e),f). The current is circulating in the $p_x - p_z - p_y$ plaquettes a),d), in the $p_x - d_z - p_y$ plaquettes b),e), and in the $p_x - d_x - p_y$ plaquettes c),f).

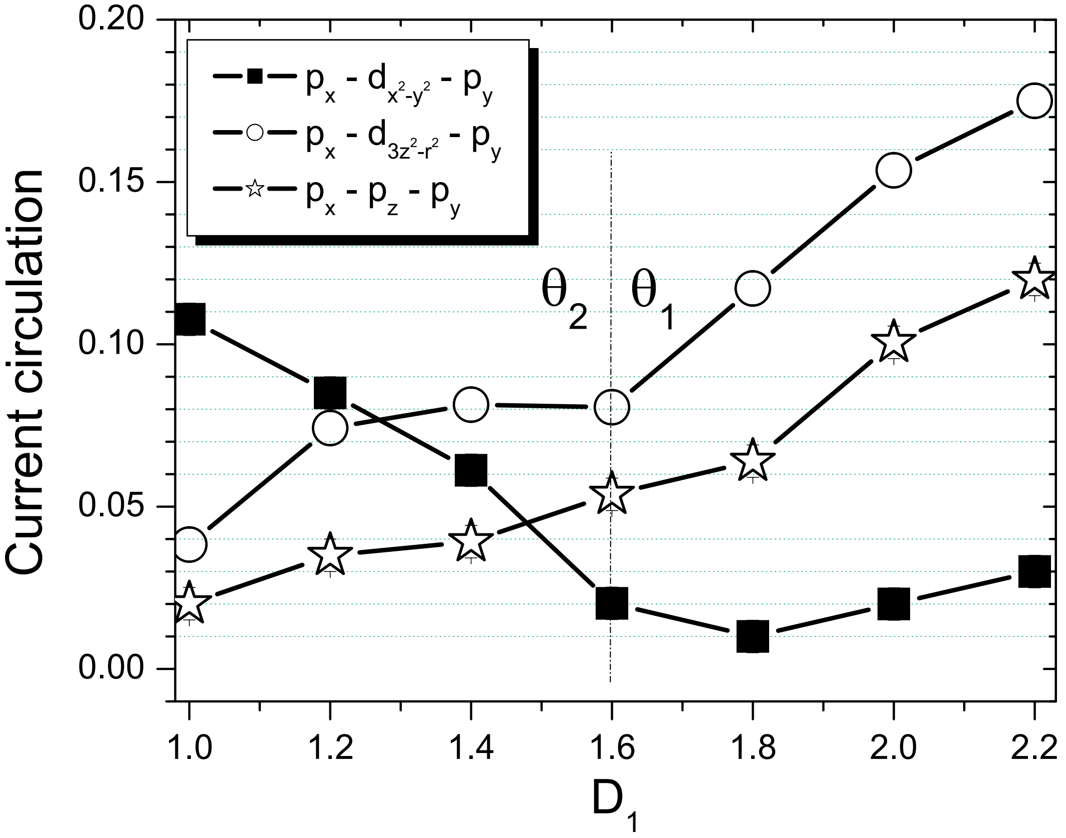

Figure 6.21: Circulation of current around a $p_x - p_z - p_y$ plaquette (triangles), around a $p_x - d_z - p_y$ plaquette (squares), and around a $p_x - d_x - p_y$ plaquette (circles) when the apical oxygen-copper distance D_1 is reduced. The symmetry of the orbital current pattern is θ_2 like when $D_1 < 1.5$ and the current is circulating inside the horizontal plane. When $D_1 > 1.5$ the symmetry changes towards the θ_1 pattern and the current has a finite out-of-plane component. The calculations were done on a 192 site lattice.

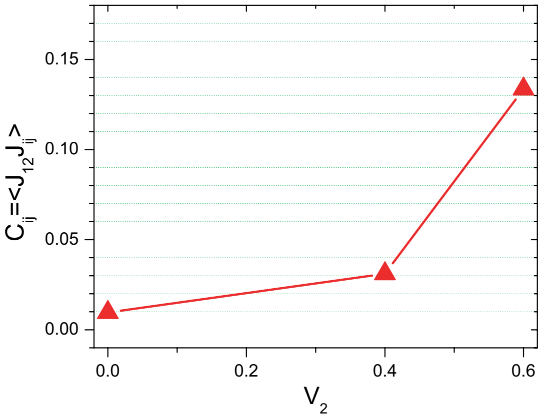

Figure 6.22: Lanczos calculations of the current-current correlations for the two most distant links in a 8 copper lattice with 10 holes ($S_i^z = 0$). The correlations of the current operator increase strongly with V_2.

By applying the variational Monte Carlo procedure to the extended Hamiltonian containing both the parameters of the usual three-band Hubbard Hamiltonian and the correlated hopping term V_2, we find a clear enhancement of the orbital currents when $V_2 > 0.4$. The currents become large when the doping is close to $x \approx 0.12$. In the VMC frame, we find that the symmetry of the charge currents is still θ_2 like (Fig. 6.24). The current-current correlations in a small 8 copper cluster were also calculated, and we find very strong correlations, though the symmetry in the small cluster is θ_1 like (see Fig. 6.22 and Fig. 6.24). The change of the orbital current pattern between the small 8 copper lattice and larger lattice suggests that the finite-size effects are too strong on cluster as small as 8 coppers. Although it is difficult to extract a well defined current value in the Lanczos calculations, we show in Fig. 6.22 how the current correlations evolve when the correlated hopping term increases.

6.13 Conclusion

In this work we have considered several scenarii that are shedding light on the possibility for spontaneous time reversal symmetry breaking in Hubbard-like models. As a first step, we have considered a simple three-site ring with a pair of holes: this small model already shows that when the hopping integral t is positive, there is a natural trivial charge circulation. Indeed, further variational Monte Carlo and mean-field calculations show that for some particular choices of the sign of the hopping transfer integral within the three-band Hubbard model, orbital currents are strongly stabilized. When the choice of the hopping sign leads to 2 triangles with positive hopping sign around each copper site, the resulting sym-

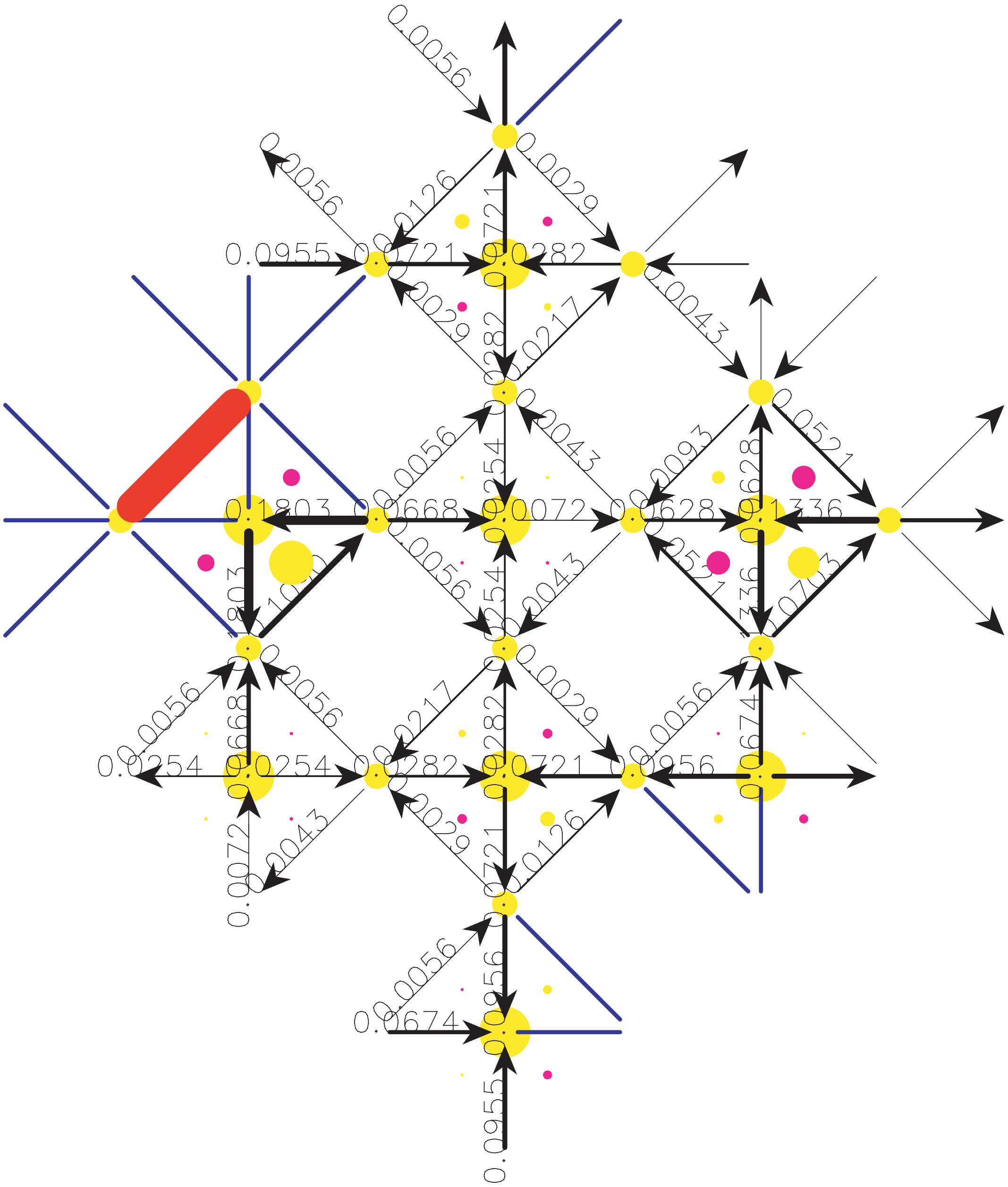

Figure 6.23: Current-current correlations obtained by Lanczos for 10 holes ($S^z = 0$) on a 8 copper lattice (24 sites) with $V_2 = 0.6$.

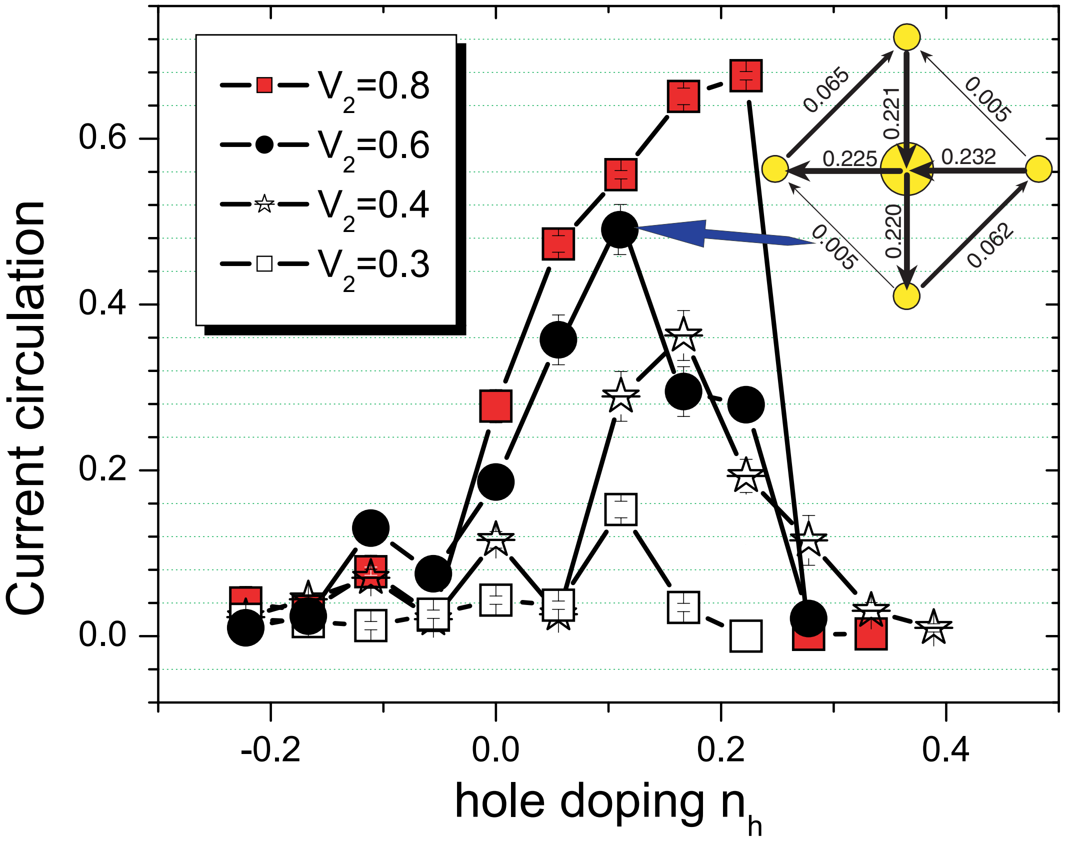

Figure 6.24: Circulation of the current for different doping obtained by VMC with the JA/FLUX wavefunction in a 192 site lattice. We show result for $V_2 = 0.4, 0.6, 0.8$. The pattern of the circulating currents is θ_2 like.

metry is θ_2 like, and when the hopping signs lead to 4 triangles with positive hopping transfer, the orbital current symmetry is θ_1 like. Current-current correlations measured in the corresponding free Fermi sea wavefunction show that short-range correlations with the respective symmetry are present with corresponding $\theta_{1,2}$ for these two particular choices of the hopping signs. Nevertheless, these choices of the transfer integrals are arbitrary and do no correspond to the real physical model, which is expected to describe the cuprates. Applying the Variational Monte Carlo method, we found in our best variational Ansatz the presence of small currents for doping close to $x = 0.08$. The symmetry of the currents measured in the projected wavefunction consists of lines of currents, as in the θ_2 phase, but with reversed diagonal currents. We get a net macroscopic current running through the periodic boundary of the lattice, which is clearly forbidden in the thermodynamic limit and suggests that the presence of currents at the variational level might be an artefact. On the other hand, the variational parameters of the variational function are exactly those of the θ_2 phase. The other competing instabilities are the spin-density wave and the resonating valence bond wavefunctions. Antiferromagnetism is found to be stable for $x = [0., 0.11]$, and the Néel magnetism is reduced at half-filling down to 68% of the classical value by the quantum fluctuations. When the doping is close to 0.25%, we find superconductivity with a d-wave like symmetry, although the energy gain of the superconducting wavefunction is small, and it is difficult to get a definitive conclusion on the exact nature of the RVB phase. We proposed additionally two other models that might shed light on the presence of orbital currents: (1) We extended first the three-band Hubbard model by considering the additional out-of-plane apical oxygens and the copper d_{3z2-r2} orbitals, (2) We considered an additional correlated hopping term in the three-band Hubbard model. In the former model we found interestingly that when the transfer integral connected to the apical oxygen are slightly enhanced, then strong orbital currents start to develop with an in-plane magnetic moment, in agreements with neutron experimental results. In the latter model, we found that the orbital currents are strongly stabilized when the correlated hopping $V_2 \approx 0.4$. The symmetry of the current pattern in this case is θ_2-like. As an outlook, we would suggest to study further the orbital current present in the three-band Hubbard model when open boundaries are considered. In this particular case, the flux running through the boundary would at least be removed, and the stability of the charge current phase could be better studied. Finally, it has also been argued that holes doped in the antiferromagnetically correlated spin systems induce incommensurate spin correlations in the ground state for the one- and three-band Hubbard models within mean-field approximations. Therefore, it would be interesting to compare the energies of these phases with our Jastrow projected wavefunction, and see if these latter phases are still present.

Chapter 7

Conclusion

For the square lattice, both the variational Monte Carlo method (VMC) [32, 18, 19, 21] and mean-field (MF) theories [20] were successful to find a d-wave superconducting phase that is in good agreement with experimental data. Nevertheless, not so many variational Monte Carlo data exist for other geometries, that might be able to describe well the magnetic and superconducting instabilities in other compounds, like in the cobaltites or in the graphene. Moreover, since the discovery of the high temperature superconductors, one of the leading issue is the origin of the pseudo gap phase which exists in the the low hole doping side (underdoped region) of the phase diagram. No present theory was yet able to catch all the features of the pseudo-gap phase of the cuprates. In the present dissertation, progress has been achieved in these directions.

Recent data obtained in the cobaltite compound $\mathrm{Na}_x\mathrm{CoO}_2.\mathrm{yH}_2\mathrm{O}$ showed that superconductivity is obtained by cooling the compound below $T = 4K$ [74] and for electron doping between $1/4 < x < 1/3$. In chapter 3 we have presented a variational Monte Carlo study of the $t-J$ ($J/t = 0.4$ and $t < 0$) model on the triangular lattice, using extended wavefunctions containing both superconductivity and non-collinear magnetism, as well as flux phase instabilities. The method provided a general framework to tackle the competition between antiferromagnetism and superconductivity and we obtained very good variational energies at half-filling when compared to other more sophisticated methods. The fermionic representation of our wavefunction allowed to consider hole and electron doping. The most stable pairing corresponds to singlet pairing. We found that $d_{x^2-y^2} + id_{xy}$ superconductivity is only weakly stabilized for electron doping in a very small window ($\delta = [0, 0.12]$) and is much stronger and also appears in a wider range ($\delta = [0, 0.16]$) in the case of hole doping. Since the results are not in agreement with the experimental results, it is suggesting that the $t-J$ model might be not sufficient to account for superconductivity in the electron doped side of the phase diagram. In particular, we expect that the oxygen atoms might play an important role for superconductivity. Another missing ingredient in the simple $t-J$ model that could restore the agreement with the experimental data, is the strong Coulomb repulsion V between nearest-neighbors.

In order to analyze how the magnetism and the superconductivity depend on the geometry of the compound, we have extended further in chapter 4 the variational study to correlated electrons on the honeycomb lattice, which could give a good description of graphene single sheets. At half-filling, we have found a ground state mixing at the same time antiferromagnetism and superconducting pairing. The staggered magnetization is 66% of the classical value, which is slightly higher than the 50% obtained with exact Quantum Monte Carlo. However, the energy obtained is very close to the exact value: we find a variational Heisenberg energy per site, extrapolated to the thermodynamic limit, that is only 0.3% higher than the quantum Monte Carlo result. A coexistence phase between the two order parameters is found in the range $x = [0, 0.07]$, and superconductivity is suppressed at the van Hove singularity $x = 1/8$. Therefore the range of the superconducting order is $\delta =]0, \frac{1}{8}[$. The amplitude and the range of existence of the superconducting parameter is four times smaller than in the square lattice. We find good agreement between the VMC calculations and an RVB MF theory in the superconducting phase, namely the same $d_{x^2-y^2} + id_{xy}$ symmetry and a similar amplitude of the pairing order parameter. For hole doping larger than 1/8, we find that a spin density wave (SDW), with pitch vector equal to one of the three possible nesting vectors, is stabilized in the range $\delta = [\frac{1}{8}, 0.22]$. The SDW phase leads to an optimization of the kinetic energy. However, a stronger gain in kinetic energy, and also a lower variational energy, is obtained at $\delta = 0.22$ with a weak ferromagnetic polarized phase, which is polarized linearly and reaches full polarization at doping $\delta = 0.5$. Ferromagnetism disappears again at $\delta = 0.6$.

We performed also measurements on a number of single sheet wrapped nanotubes, in order to investigate the limit of the quasi-1D system with variational Monte Carlo. We observe that not only the amplitude of the superconductivity, but the phase of the pairing on each nearest-neighbor link depend on the wrapping of the tube. We have measured the phase after projection of the BCS pairing in the different tubes, and we observe that the phases of the pairing observable moves from the $d_{x^2-y^2} + id_{xy}$ symmetry in the case of the 2 dimensional lattice towards intermediate value, and converge to the d-wave symmetry in the case of the 2-leg ladder, which is also the smallest nanotube that can be wrapped with a 2-site unit-cell. We found a suppression of the magnetism when the diameter is small and reaches the limit of the 2-leg ladder, and an enhancement of the pairing order parameter in the same limit. This might be interpreted as the signature that quantum fluctuations become much larger when the tube reaches the one dimensional limit, and our variational magnetic order parameter is no longer stabilized when these fluctuations become too strong. At the same time, it is interesting to note that the pairing survives very well in the 1D limit, though we do not expect any real pairing in a quasi-1D model. Indeed, in this limit the ground state will be a Luttinger liquid.

Finally, we considered the square lattice geometry, and extended the previous VMC approaches to allow for bond-order modulations in the variational wavefunction. This is motivated by the observation of inhomogeneous checkerboard patterns in some high-T_c cuprate compounds. Using several variational Gutzwiller-projected wavefunctions with built-in charge and bond order parameters, we studied the extended $t-J-V$ model on the square lattice at low doping. It was found with both VMC and mean-field theory that the model stabilizes a 4×4 bond-order modulation spontaneously on top of the staggered flux pattern for hole doping around 1/8. The competition of the BO-modulated staggered flux wavefunction with respect to the d-wave RVB wavefunction or the commensurate flux state was investigated, and it was found that a short range Coulomb repulsion penalizes the d-wave superconductor for $V \approx 1 - 2eV$, and that the Coulomb repulsion brings them very close in energy.

One of the further recent proposals for the pseudo-gap phase of the cuprates is that the anomalous properties of the cuprates may be due to quantum critical fluctuations of current patterns formed spontaneously in the CuO_2 planes. Related to this assumption, a break-through was realized recently by Bourges et al. [136], by using polarized elastic neutron diffraction, who reported the signature of an unusual magnetic order in the underdoped phase of $YBa2Cu3O6 + x$ (YBCO). They argue that this hidden order parameter defines the pseudo-gap phase of cuprates. They found that no translational symmetry breaking of the lattice is associated with this order parameter. Moreover, the pattern of the observed magnetic scattering corresponds to the one expected in the circulating current theory of the pseudo-gap state with current loops inside the CuO_2 unit-cell developed by Chandra Varma [138], especially with a current pattern that has two current loops per copper unit-cell. In this dissertation, we have considered several theoretical scenarii that might shed light on the possibility for spontaneous time reversal symmetry breaking in Hubbard-like models. As a first step, we have measured the current-current correlations in a small 8 copper cluster, where exact diagonalization calculations can still be done. No clear signature of a current pattern is found for hole doping $x = 25\%$. However, the small size of this cluster does not allow for lower doping studies, and we applied the Variational Monte Carlo method on larger system sizes. We found in our best variational Ansatz the presence of small currents for doping close to $x = 0.12\%$. However, the symmetry of the currents measured in the projected wavefunction consists of line of currents, identically to the θ_2 phase, but with reversed diagonal line of currents on the oxygen-oxygen bonds. This leads to a finite flux flowing through the periodic boundary of the lattice, which is clearly forbidden in the thermodynamic limit, suggesting that the presence of current at the variational level might be an artefact. The other competing instabilities are the spin density wave and the resonating valence bond wavefunctions. Anti-ferromagnetism is found to be stable for $x = 0 - 11\%$, and Néel magnetism is reduced at half-filling down to 68% of the classical value by the quantum fluctuations. When the doping is close to 0.25% we find the presence of superconductivity with a d-wave like symmetry, although the energy gain of the superconducting wavefunction is small, and it is difficult to get a definitive conclusion on the exact nature of the RVB phase. We proposed additionally two other models that might shed light on the presence of orbital currents: (1) We extended first the three-band Hubbard model by considering the additional out-of-plane apical oxygens and the copper d_{3z2-r2} orbitals, (2) We considered an additional correlated hopping term in the three-band Hubbard model. In the former model we found interestingly that when the transfer integrals connected to the apical oxygen are slightly enhanced, then strong orbital currents start to develop with an in-plane magnetic moment, in agreement with neutron experimental results. In the latter model, we found that the orbital currents are strongly stabilized when the correlated hopping $V_2 \approx 0.4$. The symmetry of the current pattern in this case is θ_2 like. Additionally, we have studied further the orbital current present in the three-band Hubbard model when open boundaries are considered. In this particular case, the flux flowing through the boundary is removed, and the charge current phase is still stabilized. Finally, it has also been argued that holes doped in the antiferromagnetically correlated spin systems induce incommensurate spin correlations in the ground state for the one-band hubbard model and three-band model within the mean-field approximation. Therefore, it would be interesting to compare the energies of these phases with our Jastrow projected wavefunction, and see if these phases are still present.

Bibliography

[1] J. G. Bednorz and K. A. Mller. *Z. Physik B*, 1986.

[2] L. Gao, Y. Y. Xue, F. Chen, Q. Xiong, R. L. Meng, D. Ramirez, C. W. Chu, J. H. Eggert, and H. K. Mao. *Phys. Rev. B*, 1994.

[3] N. D. Mermin. *Phys. Rev.*, 176:250, 1968.

[4] mark S. Hybertsen and Michael Schlter. *Phys. Rev. B*, 39(13):9028, 1989.

[5] D. S. Dessau, Z.-X. Shen, D. M. King, D. S. Marshall, L. W. Lombardo, P. H. Dickinson, A. G. Loeser, J. DiCarlo, C.-H Park, A. Kapitulnik, and W. E. Spicer. *Phys. Rev. Lett.*, 71(17):2781–2784, Oct 1993.

[6] J. G. Tobin, C. G. Olson, C. Gu, J. Z. Liu, F. R. Solal, M. J. Fluss, R. H. Howell, J. C. O'Brien, H. B. Radousky, and P. A. Sterne. *Phys. Rev. B*, 45(10):5563–5576, Mar 1992.

[7] C. M. Varma, S. Schmitt-Rink, and E. Abrahams. *Solid State Commun.*, 62:681, 1987.

[8] V. J. Emery. *Phys. Rev. Lett.*, 58:2794, 1987.

[9] Mark S. Hybertsen, E. B. Stechel, M. Schluter, and D. R. Jennison. *Phys. Rev. B*, 41(16):11068, 1990.

[10] F. Mila. *Phys. Rev. B*, 38(16):11358, 1988.

[11] J. Zaanen and A. Oleś. *Phys. Rev. B*, 37:9423, 1988.

[12] F. C. Zhang and T. M. Rice. 37:3759, 1988.

[13] P. W. Anderson. *Mater. Res. Bull.*, 8:153, 1973.

[14] P. W. Anderson. *Science*, 235:1196, 1987.

[15] P. W. Anderson. *Science*, 235:1196, 1987.

[16] Anders W. Sandvik. *Physical Review B (Condensed Matter)*, 56(18):11678–11690, 1997.

[17] E. Dagotto. *Rev. Of Mod. Phys.*, 66:763, 1994.

[18] H. Yokoyama and H. Shiba. *J. Phys. Soc. Jpn.*, 57:2482, 1988.

[19] C. Gros. *Phys. Rev. B*, 38:931, 1989.

[20] G. Kotliar. *Phys. Rev. B*, 37:3664, 1988.

[21] Arun Paramekanti, Mohit Randeria, and Nandini Trivedi. *Phys. Rev. B*, 70(5):054504, 2004.

[22] P.W. Anderson, P.A. Lee, M. Randeria, T.M. Rice, N. Trivedi, and F.C. Zhang. *J. Phys. Condens. Matter*, 16:R755–R769, 2004.

[23] I. Affleck and J.B. Marston. *Phys. Rev. B.*, 37:R3774, 1989.

[24] D. A. Ivanov. *Phys. Rev. B*, 70:104503, 2004.

[25] P.A. Lee, N. Nagaosa, T.K. Ng, and X.G. Wen. *Phys. Rev. B*, 57:6003, 1998.

[26] X.G. Wen and P.A. Lee. *Phys. Rev. Lett.*, 76:503, 1996.

[27] M.U. Ubbens and P.A. Lee. *Phys. Rev. B*, 46(46):8434, 1992.

[28] D. Hofstadter. *Phys. Rev. B*, 14:2239, 1976.

[29] P.W. Anderson, B.S. Shastry, and D. Hristopulos. *Phys. Rev. B.*, 40:8939, 1989.

[30] D. Poilblanc, Y. Hasegawa, and T. M. Rice. *Phys. Rev. B.*, 41:1949, 1990.

[31] M.C. Gutzwiller. *Phys. Rev. Lett.*, 10:159, 1963.

[32] T. Giamarchi and C. Lhuillier. *Phys. Rev. B*, 43:12943, 1991.

[33] T. Giamarchi and C. Lhuillier. In V. Aguilera-Navarro, editor, *Condensed Matter Theories, Vol. 5.* Plenum, 1989.

[34] P W Anderson, P A Lee, M Randeria, T M Rice, N Trivedi, and F C Zhang. *J PHYS.CONDENS.MATTER*, 16:R755, 2004.

[35] K. Tanaka and F. Marsiglio. *cond-mat/0002260*, 2000.

[36] Amit Ghosal, Catherine Kallin, and A. John Berlinsky. *Phys. Rev. B*, 66(21):214502, Dec 2002.

[37] Daniel Knapp, Catherine Kallin, Amit Ghosal, and Sarah Mansour. *Physical Review B (Condensed Matter and Materials Physics)*, 71(6):064504, 2005.

[38] S.N. Coppersmith. *Phys. Rev. B*, 42(4):2259–2267, 1990.

[39] J. E. Hirsch. *Physica C*, 194:119–125, 1991.

[40] M. Miezejewski and M. M. Maska. *Phase Transitions*, 78(1-3):285–293, 2005.

[41] Takashi Yanagisawa. *J. Phys. A : Math. Gen.*, 36:9337–9349, 2003.

[42] D. Ceperley, G. V. Chester, and M. H Kalos. *Phys. Rev. B*, 16(7):3081, 1977.

[43] C. Gros, R. Joynt, and T. M. Rice. *Phys. Rev. B*, 36(1):381, 1987.

[44] Claudius Gros. *Phys. Rev. B*, 38(1):931, 1988.

[45] E. Heeb. PhD thesis, ETHZ, Zürich (Switzerland), 2001.

[46] Andreas W.M. Dress. *Advances in Mathematics*, 112:120–134, 1995.

[47] J. P. Bouchaud, A. Georges, and C. Lhuillier. *J. Phys. (Paris)*, 49:553, 1988.

[48] Arthur Cayley. *Journal fuer die reine angewandte Mathematik*, (38):93, 1849.

[49] M. C. Gutzwiller. *Phys. Rev.*, 137:A1726, 1965.

[50] Robert Jastrow. *Physical Review*, 98(5):1479, 1955.

[51] Sandro Sorella. *Phys. Rev. B*, 71:241103, 2005.

[52] C. J. Umrigar, K. G. Wilson, and J. W. Wilkins. *Phys. Rev. Lett.*, 60:1719, 1988.

[53] Michael I. Friswell and Sondipon Adhikari. *AIAA Journal*, 38(12):2355, 2000.

[54] Eric Blanc and Wtodzimierz Paciorek. *Journal of Applied Crystallography*, 34:480–483, 2001.

[55] Richard B. Nelson. *AIAA Journal*, 14(9):1201, 1976.

[56] Li Shu, Wang Bo, and Hu Ju-Zhong. *Applied Mathematics and Mechanics (English Edition)*, 24(1):92, 2003.

[57] E. Heeb and T. M. Rice. *Europhys. Lett.*, 27:673, 1993.

[58] F. Becca. PhD thesis, SISSA, Trieste (Italy), 2001.

[59] F. F. Assad. *Phys. Rev. B*, 47(13):7910–7918, 1993.

[60] Shiwei Zhang, J. Carlson, and J. E. Gubernatis. *Phys. Rev. B*, 55(12):7464–7477, 1997.

[61] Yukitoshi Motome and Masatoshi Imada. *Journal of the Physical Society of Japan*, 67(9):3199–3215, 1998.

[62] S. R. White, D. J. Scalapino, and R. L. Sugar. *Phys. Rev. B*, 40(1):506–516, 1989.

[63] Yukitoshi Motome and masatoshi Imada. *Journal of the Physical Society of Japan*, 67(9):3199–3215, 1998.

[64] Wirawan Purwanto and Shiwei Zhang. *Physics/0403146*, 2006.

[65] R. Blankenbeeler, D. J. Scalapino, and R. L. Sugar. *Phys. Rev. D*, 24(8):2278, 1981.

[66] FeiLin, Jurij Smakov, Erik S. Sorensen, Catherine kallin, and A. John Berlinsky. *cond-mat/0411422*, 2004.

[67] S. Sorella, E. Tossatti, S. Baroni, R. Car, and M. Parrinello. *International Journal of Modern Physics B*, 1(5):993–1003, 1988.

[68] R. M. Fye. *Phys. Rev. B*, 33(9):6271, 1986.

[69] J. E. Hirsch. *Phys. Rev. B*, 31(7):4403, 1985.

[70] J. E. Hirsch. *Phys. Rev. B*, 28(7):4059, 1983.

[71] Shiwei Zhang and Henry Krakauer. *Phys. Rev. Lett.*, 90(13):136401, 2003.

[72] M. Frick and H.De. Raedt. *Z.Phys.B - Condensed matter*, 88:173–179.

[73] R. E. Schaak, T. Klimczuk, M.L. Foo, and R. J. Cava. *Nature*, 424:527, 2003.

[74] K. Takada, H. Sakurai, E. Takayama-Muromachi, F. Izumi, R. A. Dilanian, and T. Sasaki. *Nature*, 53:422, 2003.

[75] D. J. Singh. *Phys. Rev. B*, 61(20):13397–13402, 2000.

[76] G. Baskaran. *Phys. Rev. Lett.*, 91(9):097003, 2003.

[77] B. Kumar and B. S. Shastry. *Phys. Rev. B*, 68:104508, 2003.

[78] Qiang-Hua Wang, Dung-Hai Lee, and Patrick A. Lee. *Phys. Rev. B*, 69(9):092504, 2004.

[79] P. Fazekas and P. W. Anderson. *Phil. Mag.*, 30:423–440, 1974.

[80] D. Huse and V. Elser. *Phys. Rev. Lett.*, 60:2531, 1988.

[81] B. Bernu, C. Lhuillier, and L. Pierre. *Phys. Rev. Lett.*, 69(17):2590–2593, 1992.

[82] Luca Capriotti, Adolfo E. Trumper, and Sandro Sorella. *Phys. Rev. Lett.*, 82(19):3899–3902, 1999.

[83] Th. Jolicoeur, E. Dagotto, E. Gagliano, and S. Bacci. *Phys. Rev. B*, 42(7):4800, 1990.

[84] T. Watanabe, H. Yokoyama, Y. Tanaka, J. Inoue, and M. Ogata. *J. Phys. Soc. Jpn.*, 73:3404, 2004.

[85] R. Jastrow. *Phys. Rev.*, 98:1479, 1955.

[86] G. H. Wannier. *Physical Review*, 79(2):357–364, 1950.

[87] Sandro Sorella. *Phys. Rev. B*, 64(2):024512, 2001.

[88] D. S. Rokhsar. *Phys. Rev. Lett.*, 65:1506, 1990.

[89] Carsten Honerkamp. *Phys. Rev. B*, 68(10):104510, 2003.

[90] P. Sindzingre, P. Lecheminant, and C. Lhuillier. *Phys. Rev. B*, 50(5):3108–3113, 1994.

[91] P. W. Kasteleyn. *J. Math. Phys.*, 4:287, 1963.

[92] Seiji Yunoki and Sandro Sorella. *Physical Review B (Condensed Matter and Materials Physics)*, 74(1):014408, 2006.

[93] B. Bernu, P. Lecheminant, C. Lhuillier, and L. Pierre. *Phys. Rev. B*, 50(14):10048–10062, 1994.

[94] W. Koshibae and S. Maekawa. *Phys. Rev. Lett.*, 91(25):257003, 2003.

[95] N. B. Hannay, T. H. Geballe, B. T. Matthias, K. Andres, P. Schmidt, and D. MacNair. *Physical Review Letters*, 14(7):225–226, 1965.

[96] J. Nagamatsu, N. Nakagawa, T. Muranaka, Y. Zenitani, and J. Akimitsu. *Nature*, 410:63, 2001.

[97] T. E. Weller, M. Ellerby, S. S. Saxena, R. P. Smith, and N. T. Skipper. *Nature Phys.*, 1:39, 2005.

[98] M. Posternak, A. Baldereschi, A. J. Freeman, E. Wimmer, and M. Weinert. *Phys. Rev. Lett.*, 50:761, 1983.

[99] G. Csányi, P. B. Littlewood, A. H. Nevidomskyy, C. J. Pickard, and B. D. Simons. *Nature Phys.*, 1:42, 2005.

[100] A. Kasumov, M. Kociak, M. Ferrier, R. Deblock, S. Guéron, B Reulet, I. Khodos, O. Stéphan, and H. Bouchiat. *Phys. Rev. B*, 68:214521, 2003.

[101] R. A. Jishi and M. S. Dresselhaus. *Physical Review B (Condensed Matter)*, 45(21):12465–12469, 1992.

[102] S. Sorella and E. Tosatti. *Europhys. Lett.*, 19:699, 1992.

[103] L. M. Martelo, M. Dzierzawa, L. Siffert, and D. Baeriswyl. *Z. Phys. B*, 103:335, 1997.

[104] N. Furukawa. *J. Phys. Soc. Jpn.*, 70:1483, 2001.

[105] T. Paiva, R.T. Scalettar, W. Zheng, R.R.P. Singh, and J. Oitmaa. *Phys. Rev. B*, 72:085123, 2005.

[106] E. V. Castro, N. M. R. Peres, K. S. D. Beach, and A. W. Sandvik. 2005. cond-mat/0508204.

[107] H. R. Krishnamurthy, C. Jayaprakash, S. Sarker, and W. Wenzel. *Phys. Rev. Lett.*, 64:950, 1991.

[108] S. Sorella, G. B. Martins, F. Becca, C. Gazza, L. Capriotti, A. Parola, and E. Dagotto. *Phys. Rev. Lett.*, 88:117002, 2002.

[109] M. U. Ubbens and P. A. Lee. *Phys. Rev. B*, 49:6853, 1994.

[110] B. Sriram Shastry and Brijesh Kumar. *Prog. Theor. Phys. Suppl.*, 145:1, 2002.

[111] A. W. Sandvik. *Phys. Rev. B*, 56:11678, 1997.

[112] Cédric Weber, Andreas Läuchli, Frédéric Mila, and Thierry Giamarchi. *Physical Review B (Condensed Matter and Materials Physics)*, 73(1):014519, 2006.

[113] D. M. Ceperley. *Rev. Mod. Phys.*, 67:279, 1995.

[114] J. D. Reger, J. A. Riera, and A. P. Young. *J. Phys.: Condens. Matter*, 1:1855, 1989.

[115] T. Hanisch, G. S. Uhrig, and E. Müller-Hartmann. *Phys. Rev. B*, 56:13960, 1997.

[116] Sumio Iijima, P. M. Ajayan, and T. Ichihashi. *Physical Review Letters*, 69(21):3100–3103, 1992.

[117] P. R. Wallace. *Physical Review*, 71(9):622–634, 1947.

[118] A. Kasumov, M. Kociak, M. Ferrier, R. Deblock, S. Gueron, B. Reulet, I. Khodos, O. Stephan, and H. Bouchiat. *Physical Review B (Condensed Matter and Materials Physics)*, 68(21):214521, 2003.

[119] Arkadi A. Odintsov. *Physical Review Letters*, 85(1):150–153, 2000.

[120] N. D. Mermin and H. Wagner. *Phys. Rev. Lett.*, 17:1133, 1967.

[121] Shoucheng Zhang. *Phys. Rev. B*, 42(1):1012–1014, Jul 1990.

[122] M. Vershinin, S. Misra, S. Ono, Y. Abe, Y. Ando, and A. Yazdani. *Science*, 303:1995, 2004.

[123] G. Levy, O. Fischer M. Kugler, A.A. Manuel, and M. Li. *Phys. Rev. Lett.*, 95:257005, 2005.

[124] A. Hashimoto, N. Momono, M. Oda, and M. Ido. *Physical Review B (Condensed Matter and Materials Physics)*, 74(6):064508, 2006.

[125] T. Hanaguri, C. Lupien, Y. Kohsaka, D.H. Lee, M. Azuma, M. Takano, H. Takagi, and J.C. Davis. *Nature*, 430:1001, 2004.

[126] D. Poilblanc. *Phys. Rev. B*, (R0605508), 2005.

[127] F.C. Zhang, C. Gros, T.M. Rice, and H. Shiba. *Supercond. Sci. Technol.*, 1:36, 1988.

[128] D. Poilblanc. *Phys. Rev. B*, 41:R4827, 1990.

[129] T. Giamarchi and C. Lhuillier. *Phys. Rev. B*, 42(16):10641, 1990.

[130] P.W. Anderson. *cond-mat/0406038.*

[131] Chunhua Li, Sen Zhou, and Ziqiang Wang. *Physical Review B (Condensed Matter and Materials Physics)*, 73(6):060501, 2006.

[132] Z. Wang, G. Kotliar, and X.F. Wang. *Phys. Rev. B*, 42:R8690, 1990.

[133] Fu Chun Zhang. *Phys. Rev. Lett.*, 64(8):974, 1990.

[134] T. K. Lee and L. N. Chang. *Phys. Rev. B*, 42(13):8720, 1990.

[135] Shoudan Liang and Nandini Trivedi. *Phys. Rev. Lett.*, 64(2):232, 1990.

[136] B. Fauqué, Y. Sidis, V. Hinkov, S. Pailhès, C. T. Lin, X. Chaud, and P. Bourges. *Physical Review Letters*, 96(19):197001, 2006.

[137] C. M. Varma, Z. Nussinov, and W. van Saarloos. *Phys. Rep.*, 361:267, 2002.

[138] C. M. Varma. *Physical Review B (Condensed Matter and Materials Physics)*, 73(15):155113, 2006.

[139] Takashi Yanagisawa, Soh Koike, and Kunihiko Yamaji. *Phys. Rev. B*, 64:184509, 2001.

[140] A. Oguri, T. Asahata, and S. Mackawa. *Physica B*, 186-188:953–955, 1993.

[141] Martin Greiter and Ronny Thomale. *Phys. Rev. Lett.*, 99:027005, 2007.

[142] A. M. Martin and James F. Annett. *Phys. Rev. B*, 57(14):8709, 1998.

[143] A. Sudbø, C. M. Varma, T. Giamarchi, E. B. Stechel, and R. T. Scalettar. *Phys. Rev. Lett.*, 70(7):978–981, Feb 1993.

[144] Hisatoshi Yokoyama and Masao Ogata. *Phys. Rev. B*, 53(9):5758, 1996.

[145] A. K. MacMahan, James f. Annette, and Richard M. Martin. *Phys. Rev. B*, 42(10):6268, 1990.

[146] E. Pellegrin, N. Nücker, J. Fink, S. L. Molodtsov, A. Gutiérrez, E. Navas, O. Strebel, Z. Hu, M. Domke, G. Kaindl, S. Uchida, Y. Nakamura, J. Markl, M. Klauda, G. Saemann-Ischenko, A. Krol, J. L. Peng, Z. Y. Li, and R. L. Greene. *Phys. Rev. B*, 47(6):3354–3367, Feb 1993.

[147] Carmine Lubritto, Krzysztof Rosciszewski, and A.M. Oles. *J. Phys.: Condens. Matter*, 8:11053–11068, 1996.

[148] N. Nucker, M. Merz, P. Schweiss, E. Pellegrin, S. Schuppler, Th. Wolf, V. Chakarian, J. Freeland, Y. U. Idzerda, M. kaser, G. Muller-Vogt, E. E rand S. Kikkawa, and G. Liu. *Journal of Superconductivity*, 22(1):143, 1999.

[149] H. Kamimura, H. Ushio, and S. Matsuno. *Springer-Verlag Berlin Heidelberg*, page 157165.

[150] Seva Nimkar, D.D. Sarma, H.R. Krishnamurthy, and S. Ramasesha. *Phys. Rev. B*, 48(10):7355–7362, 1993.

[151] Kizashi Yamaguchi. *Internation Journal of Quantum Chemistry*, 37:167–196, 1990.

[152] J. Appel, M. Grodzicki, and F. Paulsen. *Phys. Rev. B*, 47(5):2812–2820, 1993.

[153] Luis A. Perez and Chumin Wang. *Journal of Superconductivity : Incorporating Novel Magnetism*, 13(6):925–928, 2000.

Appendix A

The projected wave-function written with Determinants and Pfaffians

During a variational Monte-Carlo simulation, we need to project the variational wave-function ϕ in the basis of real-space fermion configurations. We define a real-space configuration of a fixed number of fermions, and we consider first the case of a $S^z = 0$ fermionic configuration :

$$|\alpha\rangle = \left(c^\dagger_{R_1\uparrow} ... c^\dagger_{R_N\uparrow} c^\dagger_{R'_1\downarrow} ..... c^\dagger_{R'_N\downarrow} \right) |0\rangle \tag{A.1}$$

The wave-function ϕ is given by:

$$|\phi\rangle = \sum_{\{i_1...i_N\};\{j_1...j_N\}} \{a(i_1, j_1)...a(i_N, j_N)\}\, c^\dagger_{i_1\uparrow} ... c^\dagger_{i_N\uparrow} c^\dagger_{j_1\downarrow} ..... c^\dagger_{j_N\downarrow} |0\rangle \tag{A.2}$$

where $2N$ is the number of particles contained in the wave-function, and $a(i, j)$ are numerical coefficients found by the diagonalization of the mean-field hamiltonian. Only permutations $\mathcal{P}$ of the fermions indices in (A.1) will be kept by the projection of $|\phi\rangle$ onto the state $\langle\alpha|$:

$$I = \{i_1, ..., i_N\} = \mathcal{P}\{R_1, ..., R_N\} \tag{A.3}$$

$$J = \{j_1, ..., j_N\} = \mathcal{P}'\{R'_1, ..., R'_N\} \tag{A.4}$$

By ordering the up and the down fermions respectively we get:

$$|\phi\rangle = \sum_{I,J} \{a(i_1, j_1)...a(i_N, j_N)\} (-1)^{sign(\mathcal{P})} (-1)^{sign(\mathcal{P}')} c^\dagger_{R_1\uparrow} ... c^\dagger_{R_N\uparrow} c^\dagger_{R'_1\downarrow} ... c^\dagger_{R'_N\downarrow} |0\rangle \tag{A.5}$$

Moreover, we can further order the $a_{i,j}$ terms with respect to the index i :

$$|\phi\rangle = \sum_J \left(\sum_I a(R_1, P(j_1))...a(R_N, P(j'_N))(-1)^{sign(\mathcal{P})}(-1)^{sign(\mathcal{P}')} \right) c^\dagger_{R_1\uparrow}...c^\dagger_{R_N\uparrow} c^\dagger_{R'_1\downarrow}.....c^\dagger_{R'_N\downarrow} |0\rangle \quad (A.6)$$

Using that $j_k = P'(R'_k)$, we get:

$$|\phi\rangle = \sum_J \left(\sum_I a(R_1, P(P'(R'_1)))...a(R_N, P(P'(R'_N)))(-1)^{sign(\mathcal{P})}(-1)^{sign(\mathcal{P}')} \right) c^\dagger_{R_1\uparrow}...c^\dagger_{R_N\uparrow} c^\dagger_{R'_1\downarrow}.....c^\dagger_{R'_N\downarrow} |0\rangle \quad (A.7)$$

This leads to the final result that the projection of the state $|\phi\rangle$ on the configuration $\langle\alpha|$ is a determinant:

$$\begin{aligned} \langle\alpha|\phi\rangle = & \sum_{\mathcal{P}} a(R_1, \mathcal{P}(R'_1))...a(R_N, \mathcal{P}(R'_N))(-1)^{sign(\mathcal{P})} \\ = & \qquad det\left(\{a(R_i, R'_j)\}\right) \end{aligned}$$

This calculation can be extended to the case of a polarized fermionic configuration:

$$|\alpha\rangle = c^\dagger_{R_1\sigma_{R1}}...c^\dagger_{R_{2N}\sigma_{R_{2N}}} |0\rangle \quad (A.8)$$

And the terms in the wave-function $|\phi\rangle$ that are not killed by the projection are given by:

$$\begin{aligned} |\phi\rangle &= \sum_{\{i_1...i_{2N}\}} \{a(i_1, i_2)...a(i_{2N-1}, i_{2N})\} c^\dagger_{i_1\sigma_{i1}}..c^\dagger_{i_{2N}\sigma_{i_{2N}}} |0\rangle \\ &= \sum_{\{\{i_1<i_2\}..\{i_{2N-1}<i_{2N}\}\}} \{(a(i_1, i_2) - a(i_2, i_1)) \ldots (a(i_{2N-1}i_{2N}) - a(i_{2N}, i_{2N-1}))\} c^\dagger_{i_1\sigma_{i1}}..c^\dagger_{i_{2N}\sigma_{i_{2N}}} |0\rangle \\ &= \sum_{\mathcal{P}} \left\{D_{(\mathcal{P}(R_1),\mathcal{P}(R_2))}...D_{(\mathcal{P}(R_{2N-1}),\mathcal{P}(R_{2N}))}(-1)^{sign(\mathcal{P})}\right\} c^\dagger_{R_1\sigma_{R_1}}..c^\dagger_{R_{2N}\sigma_{R_{2N}}} |0\rangle \\ &= Pf\left(\{D(R_i, R_j)\}\right) c^\dagger_{R_1\sigma_{R_1}}..c^\dagger_{R_{2N}\sigma_{R_{2N}}} |0\rangle \quad (A.9) \end{aligned}$$

where $D_{ij} = (a_{ij} - a_{ji})$ and the sum in (A.9) is taken over all partitions of $(R_1...R_{2N})$ into pairs (i_1, i_2). We get therefore that the projection of the state $|\phi\rangle$ onto the basis element $\langle\alpha|$ is a Pfaffian. However, the equation (A.9) cannot be reduced to a determinant like in equation (A.7), since the $a(i1, i2)$ terms cannot be ordered separately with respect to the index i_1 and i_2.

Appendix B

A Simple variational wavefunction for a pair of particles

We consider in this Appendix a simple variational wavefunction for the three-band Hubbard model on a simple CuO_4 cluster. We study the more general variational wavefunction for a $S^z = 0$ pair of holes, that is :

$$|\psi\rangle = \left(\alpha d_\uparrow^\dagger d_\downarrow^\dagger + \left(\sum_j \beta_j d_\uparrow^\dagger p_{j\downarrow}^\dagger - \gamma_j d_\downarrow^\dagger p_{j\uparrow}^\dagger\right) + \lambda_{ij} p_{i\uparrow}^\dagger p_{j\downarrow}^\dagger\right)|0\rangle \tag{B.1}$$

where d stands for the d_{x2-y2} orbital and p for the p_σ orbitals. The current operator measured in this wavefunction is given for a $d-p$ link by:

$$\langle j_{d-p_x}\rangle = it_{d-p_x}\left(\alpha^\dagger\left(\gamma_x + \beta_x\right) + \sum_j\left(\beta_j^\dagger\lambda_{xj} + \gamma_j^\dagger\lambda_{jx}\right)\right) + c.c. \tag{B.2}$$

and the current operator measured along a $p_x - p_y$ link by:

$$\langle j_{p_x-p_y}\rangle = it_{p_x-p_y}\left(\beta_x^\dagger\beta_y + \gamma_x^\dagger\gamma_y + \sum_j\left(\lambda_{xj}^\dagger\lambda_{yj} + \lambda_{jx}^\dagger\lambda_{jy}\right)\right) + c.c. \tag{B.3}$$

Similar equations hold for bonds obtained by 90° rotations. The current will therefore be finite when α, β, γ and λ_{ij} are complex numbers: $\alpha = R_a e^{ia}$, $\beta_{x,y} = Re^{ib_{x,y}}$, $\gamma_{x,y} = Re^{ic_{x,y}}$ and $\lambda_{ij} = L_{ij}e^{il_{ij}}$.

$$\begin{aligned}\langle j_{d-p_x}\rangle = 2t_{d-p_x}\Big(&R_a R\sin(c_x - a) + R_a R\sin(b_x - a)\\ &+ \sum_j\left(RL_{xj}\sin(l_{xj} - b_j) + RL_{jx}\sin(l_{jx} - c_j)\right)\Big)\end{aligned} \tag{B.4}$$

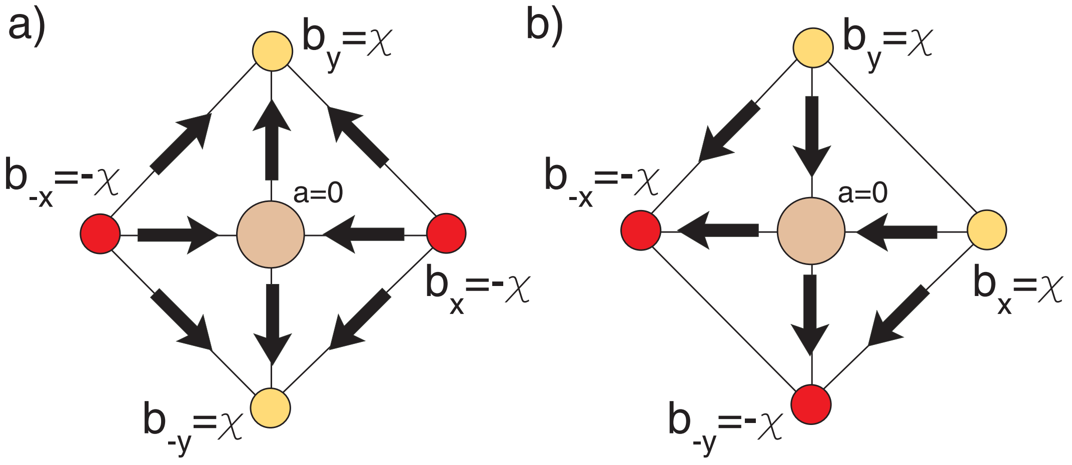

Figure B.1: The two patterns of current that can be obtained when $a = 0$ is imposed, and $t_{dp} = -1$, $t_{pp} < 0$. The arrows indicate the current orientations. Additional complex parameters λ_{ij} and α must be used to obtain the conservation of the current inside one triangle plaquette. For example, when $a = \pi$ the current arrows on the horizontal and vertical links are reversed, and the current is then circulating around the triangle plaquettes. However, when $a = \pi$ the hopping energy on these bonds is also changing sign, and therefore the energetic cost for having circulating currents is of the order of t_{d-p_x}.

And:

$$\langle j_{p_x-p_y} \rangle = 2t_{p_x-p_y} \Big(R^2 \sin(b_y - b_x) + R^2 \sin(c_y - c_x) + \sum_j \left(L_{xj} L_{yj} \sin(l_{yj} - l_{xj}) \right) \Big) \quad \text{(B.5)}$$

Moreover, the kinetic energy on these links is obtained by replacing the *sin* by *cos* in the expressions (B.4) and (B.5). Besides, we assume for simplicity that $t_{d-p_x} = -1$, and we consider that all the oxygen-oxygen bonds have also negative transfer integrals ($t_{p_x-p_y} < 0$). This choice of the sign is equivalent to the hybridization obtained in the physical three-band Hubbard model for the cuprates. In Fig. B.1 we show two simple examples of current patterns that are obtained for two choices of the parameters b. Noteworthy is the fact that the currents cannot be oriented as a rotational flow around a triangle plaquette when $t_{d-p_x} < 0$ and $t_{p_x-p_y} < 0$. When $t_{p_x-p_y} > 0$ the current is a true rotational flow and the conservation of the current is easily obtained inside each triangle plaquette. By imposing the conservation of the current in all the triangle plaquettes, we get when the phases $b = \pm\chi$ are chosen according to the pattern (a) of Fig. B.1:

$$\frac{\sin(\chi - a)}{\sin(-2\chi)} = 2\frac{t_{pp}}{t_{dp}} \frac{R}{R_a} \quad \text{(B.6)}$$

Since the energy difference between the oxygen and the copper atomic levels is of the order of $\sim 3.5eV$, the component of the wavefunction $p^{\dagger}_{\uparrow}p^{\dagger}_{\downarrow}$ is expected to be negligible, and we can assume to simplify the calculations that $L_{ij} \sim 0$. Finally, we get the current conservation inside the triangle plaquette, for the alternative pattern (b) of Fig. B.1, when this equation is satisfied:

$$\frac{\sin(\chi - a)}{\sin(-2\chi)} = \frac{t_{pp}}{t_{dp}}\frac{R}{R_a} \tag{B.7}$$

The right hand term of the two equations above is positive for the choice of the transfer integrals that corresponds to the physical compounds. However, the left handed term is negative when $a < \chi$, and moreover, the conservation of the current at the copper vertex imposes $a = \{0, \pi\}$. We emphasize that for the unphysical choice of the hopping integral $t_{pp} > 0$, the equations can be satisfied. In conclusion, for the physical choice of the hopping hybridizations, the current will be rotationally circulating with the two types of patterns proposed by C.Varma [138] only when the simple wavefunction has a negative term $-|\alpha|d^{\dagger}_{\uparrow}d^{\dagger}_{\downarrow}$, but the sign of the t_{dp} kinetic energy is reversed at the same time. The above simple variational theory is however valid only for a pair of electrons in a small cluster. A more general variational wavefunction for many electrons, in the three-band Hubbard model on a large lattice, is given by the ground-state of the following mean-field Hamiltonian :

$$H_{MF} = \sum_{\langle i,j \rangle} t_{ij} e^{i\theta_{ij}} c^{\dagger}_{i\sigma} c_{j\sigma} + c.c. \tag{B.8}$$

This hamiltonian describes free electrons coupled to an external magnetic field, that enters the equations through the θ_{ij} variables. We assume now that θ_{ij} is oriented like the current pattern θ_2 proposed by Chandra Varma. In particular, θ_{ij} takes two different amplitudes on the copper-oxygen links ($|\theta_{Cu-O}| = \alpha_1$) and on the links oxygen-oxygen ($|\theta_{O-O}| = \alpha_2$). We define the current operator $\hat{\jmath}$ and the kinetic energy $\hat{K}$ associated with the same bond :

$$\hat{\jmath}_{kl} = \sum_{\sigma} i t_{kl} c^{\dagger}_{i\sigma} c_{j\sigma} + c.c. \tag{B.9}$$

$$\hat{K}_{kl} = \sum_{\sigma} t_{kl} c^{\dagger}_{i\sigma} c_{j\sigma} + c.c. \tag{B.10}$$

$\hat{\jmath}$ and $\hat{K}$ are shown in Fig.B.2 for the parameters (α_1, α_2). The wavefunction is defined for a 64 copper lattice doped with holes at $x = 0.125$. $\hat{\jmath}$ is orientated such that when $j_{Cu-O}, j_{O-O} > 0$ the pattern is orientated similarly to the θ_2 pattern of C. Varma. We see in Fig.B.2 that the zone where $j_{Cu-O} > 0$ and $j_{O-O} > 0$ (short dashed rectangular box) corresponds to a maximum of the kinetic energy and therefore is not expected to be stabilized by other interactions, since the cost in energy for such a phase is of the order of $1.3eV$ in the cuprates.

Nevertheless, we found in the three-band Hubbard model that the wavefunction with (α_1, α_2) lying in the long-dashed rectangular box of Fig.B.2 was optimal. This later wavefunction has a current pattern which is similar to the θ_2 phase of C.Varma, but has reversed current lines on the oxygen-oxygen bonds, and the amplitude of these lines is small. On the other hand, we measured the corresponding mean-field operator that are defined by :

$$\hat{j}_{kl}^{MF} = \sum_{\sigma} i t_{kl} e^{i\theta_{kl}} c_{i\sigma}^{\dagger} c_{j\sigma} + c.c. \tag{B.11}$$

$$\hat{K}_{kl}^{MF} = \sum_{\sigma} t_{kl} e^{i\theta_{kl}} c_{i\sigma}^{\dagger} c_{j\sigma} + c.c. \tag{B.12}$$

We show in Fig.B.3 the range of parameters (α_1, α_2) that are stabilized in variational Monte-Carlo calculations (short-dashed rectangular box). For the corresponding range of parameters the mean-field current operator is identical to the θ_2 phase of C. Varma, with strong currents on the oxygen-oxygen bonds. In conclusion, the variational calculations stabilize a wavefunction that has a flux through the periodic boundaries and a weak current on the oxygen-oxygen links when the physical current observable $\hat{j}$ is considered, but the same wavefunction would have a true current circulation inside the triangle plaquettes when the mean-field current operator j^{MF} is measured in this same wavefunction.

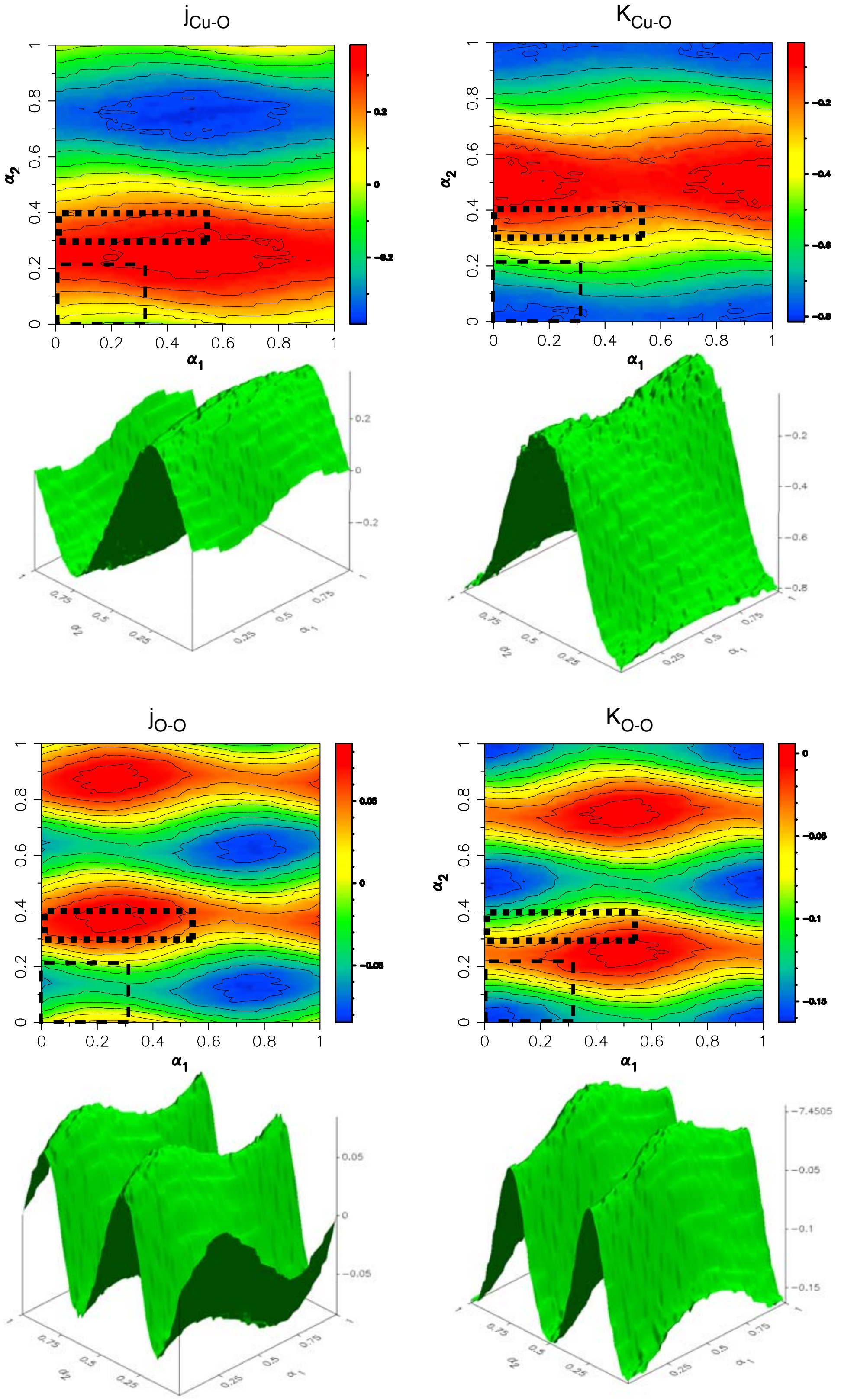

Figure B.2: Operator j and K measured in a wavefunction with flux parameters α_1 and α_2 (see text). The short-dashed box indicates the region where the current pattern is orientated like the θ_2 pattern by Chandra Varma. The long-dashed box indicates the region of parameters that is stabilized in the 3-band Hubbard model. α_1 and α_2 are in units of 2π.

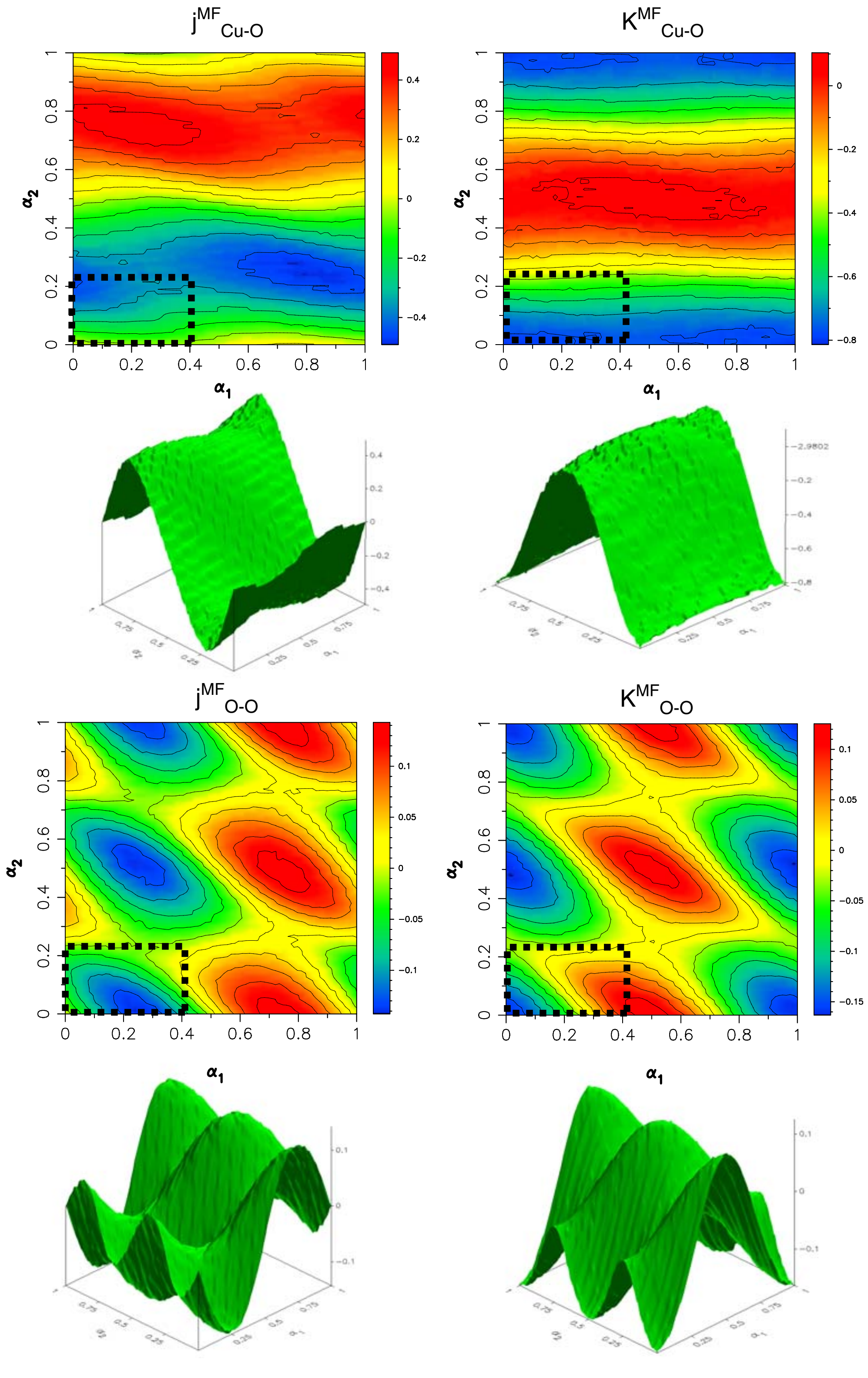

Figure B.3: Mean-field operators $\hat{j}^{MF}$ and $\hat{K}^{MF}$ measured in a variational wavefunction with flux variational parameters α_1 and α_2 (see text). The long-dashed box indicates the region of parameters that lead to an energy optimization in the 3-band Hubbard model. α_1 and α_2 are in units of 2π.

Cedric Weber

Ph.D. student in Condensed Matter Theory
Swiss Institute of Technology (EPFL / IRRMA)
Station 13, Room 337, CH-1014, Lausanne, Switzerland
Phone: +41 311 30 87
Cell: +41 78 714 47 24
web: http://www.cedric-weber.ch
email: cedric.weber@epfl.ch

Personal data

- **Name:** Cedric Weber
- **Date of birth:** January 12th, 1979
- **Citizenship:** Swiss
- **Marital status:** Single
- **Languages:** French, English, German

Referees, letters of recommendation

- Frederic Mila : Frederic.Mila@epfl.ch
- Thierry Giamarchi : Thierry.Giamarchi@physics.unige.ch
- Didier Poilblanc : Didier.Poilblanc@irsamc.ups-tlse.fr
- Giovanni Dietler : Giovanni.Dietler@epfl.ch

Current position

- Ph.D. student at the **Swiss Institute of Technology (EPFL)**, Lausanne, Switzerland, since May 2003.
- Currently working on complex strongly correlated electronic systems (three band Hubbard model) by using Variational Monte Carlo, Green Function Monte Carlo and Exact Diagonalization techniques.
- Supervisors: **Prof. Frederic Mila** (EPFL) & **Prof. Thierry Giamarchi** (University of Geneva).
- Thesis to be defended the 22th of August 2007.

Education

- Reviewer activity at Physical Review (B,L) since 2005.
- 2004: Research work at EPFL as a physicist researcher. Topics: *Monte-Carlo simulations of DNA dynamics, DNA collisions with obstacles during gel electrophoresis, DNA disentanglement*. Supervisor: Giovanni Dietler (EPFL), Andrzej Stasiak (University of Lausanne).
- **Degree in Physics** at the **Swiss Institute of Technology (EPFL)**, Lausanne, Switzerland. Thesis: *Phase Transition driven by Frustration in a 2D classical Heisenberg model*. Supervisor: Prof. Frederic Mila. Final grade: 6.0/6.0. Thesis defense: March 2003.
- 1997 - 2003: Undergraduate studies at EPFL, Lausanne, Switzerland. Final grade: 5.7/6.0.
- 2001: Summer work of three months at *Biofluid System* (Nyon, Switzerland) as a engineer physicist in the development/research sector of the company. Topic: developing medical devices such as blood transfusing machine and artificial respirators.

Teaching experience

- June 2006 : Expert for the exam of the lecture : *Advanced Quantum Mechanics II* of Dr. D. Ivanov, EPFL, Switzerland.
- February 2006 : Expert for the exam of the lecture : *Advanced Quantum Mechanics I* of Dr. D. Ivanov, EPFL, Switzerland.
- March 2006 - June 2006: Teacher assistant of Prof. F. Mila for his lecture on Quantum Mechanics I, EPFL, Switzerland.
- March 2006 - June 2006: Supervising a 4th year student for his project in the frame of the lecture of A. Pasquarello *Advanced numerical methods in Physics*. Topic: *Monte Carlo simulations of the classical compass model*.
- October 2003 - February 2006: Teacher assistant of Prof. A. Baldereschi for his lecture on *Fortran programming in Physics* to 2nd – 3rd year students, EPFL, Switzerland.

Grants and awards

- Ph.D. fellowship at the Swiss Institute of Technology, October 2003.

Ph.D. Lectures

- *Advance Solid State Physics I & II*, October 2002 – June 2003, held by Frederic Mila, Lausanne, Switzerland.
- *Atomic Optics*, May 2003 – June 2003, held by P. Meystre, Lausanne, Switzerland.
- *High-Tc Superconductivity*, March 2005 – April 2005, held by D. Pavuna, Lausanne, Switzerland.
- *X Training Course in the Physics of Correlated Electron Systems and High-Tc Superconductors*, October 2005, held by Pr. Thierry Giamarchi, Pr. Walter Metzner, Pr. Bernard Coqblin, Pr. Wolfgang von der Linden.

Computer skills

- **Computer languages:** FORTRAN 77, FORTRAN 95, and some knowledge of C++.
- **Parallel programming:** Good knowledge of MPI. Extensive experience in performing calculations on parallel machines (mizar.epfl.ch, pleiades.epfl.ch).
- **Techniques:** Lanczos diagonalizations, Monte-Carlo for classical spin systems, Variational Quantum Monte-Carlo, Green-Function Monte-Carlo, Auxiliary-field Quantum Monte-Carlo, Monte-Carlo algorithms for polymers.

Research interests

My current research interests are mainly concerned with **strongly-correlated electron systems and frustrated spin models**. In parallel, I was also interested by scanning tunneling microscopy experiments. The tools used include both numerical (exact diagonalization, classical and quantum Monte Carlo) and analytical (mean-field, slave boson approximations) techniques. My scientific activity has focused on the following fields (reference numbers relate to the *List of publications* hereafter):

1. **Physics of frustrated classical spin models**

    - **Phase transition driven by Frustration**. In connection with the physical properties of Li_2VOSiO_4, we have carried on extensive classical Monte Carlo simulations for the anti-ferromagnetic Heisenberg model with both nearest (J_1) and next-nearest (J_2) exchange couplings on the square lattice. The long-range magnetic order is known to be destroyed by thermal or quantum fluctuations at finite temperature (Mermin-Wagner theorem). However, it was found that frustration can induce a non-trivial phase transition related at a finite temperature related to a discrete symmetry breaking [1].
    - **Coupling to the lattice**. It is also relevant, when comparing with experiments, to study the coupling of the spin degrees of freedom to the lattice. Indeed, the Ising-like phase transition, that appears for $J_2/J_1>1/2$ in the pure spin model, was found to be still present and even strengthened by the spin-lattice coupling, and is accompanied by a lattice deformation from a tetragonal symmetry to an orthorhombic one. Evidences that the universality class of the transition does not change with the inclusion of the spin-lattice coupling was reported. Implications for the prototype for a layered J_1-J_2 model in the collinear region were discussed [5].
    - **Effect of static disorder**. Presently we are studying the effect of static disorder in a frustrated spin model, and presently we found that non trivial interaction between disorder and frustration occurs.

2. Model of strongly correlated electrons

- **Magnetism and Superconductivity in the t-J model on the triangular lattice**. We have investigated the phase diagram of the t-J Model on a triangular lattice using a variational Monte Carlo approach. We used an extended set of Gutzwiller projected fermionic trial wave-functions allowing for simultaneous magnetic and superconducting order parameters, which were extended by using Pfaffian matrices. We obtained energies at zero doping for the spin-1/2 Heisenberg model in very good agreement with the best estimates. Upon electron doping this phase is surprisingly stable variationally up to electronic density n=1.4, while the d+id order parameter is rather weak. For hole doping the coplanar magnetic state is almost immediately destroyed and the d+id superconductivity survives down to n=0.8. Moreover, there are evidences for a narrow spin density wave phase and ferromagnetism [6].

- **Bond-order wave instability in the t-J model on the square lattice**. Motivated by the observation of inhomogeneous patterns in some high- T_c cuprate compounds, several variational Gutzwiller-projected wave functions with built-in charge and bond-order parameters are proposed for the extended *t-J-V* model on the square lattice at low doping. In this work, we investigate, as a function of doping and Coulomb repulsion the relative stability of a wide variety of modulated structures. It is found that the 4×4 bond-order wave function with staggered-flux pattern (and small charge and spin current density wave) is a remarkable competitive candidate for hole doping around 1⁄8 in agreement with scanning tunneling microscopy observations in the underdoped regime of some cuprates. This wave function is then optimized accurately and its properties studied extensively using a variational Monte Carlo scheme. Moreover, we find that under increasing the Coulomb repulsion, the *d* -wave superconducting RVB wave function is rapidly destabilized with respect to the 4×4 bond-order wave function [8,9].

- **Scanning-tunneling microscopy.** Low temperature (3.9 K) scanning-tunneling spectroscopy on a Ag(111) surface has revealed that for some concentration of Cerium ad-atoms on-top of the surface, a superstructure (hexagonal) of ad-atom could be stabilized. Using a tight-binding model, we could relate the overall spectral structures to the scattering of Ag(111) surface-state electrons by the Ce ad-atoms. Also the site dependence could be related to the disorder induced by imperfections of the superlattice, and the opening of a gap in the local density of states could explain the observed stabilization of superlattices with ad-atom distances in the range of 2.3-3.5nm. For more details see ref. [2].

Parallel scientific activity

In parallel to my thesis scientific work, I have also research interests in complex biological systems, like DNA. The tools used in this activity are essentially numerical (Polymer Monte-Carlo simulations, 3D surface construction, bezier curve interpolation), and mathematics (Knot Topology, Fluid Dynamics) but also consist of some engineering (stereo-lithography technique). This scientific activity has focused on the following fields (reference numbers relate to the *List of publications* hereafter):

3. **Physics of DNA knots**
   - **DNA knot dynamics and collisions.** Gel electrophoresis allows one to separate knotted DNA (nicked circular) of equal length according to the knot type. At low electric fields, complex knots, being more compact, drift faster than simpler knots. Recent experiments have shown that the drift velocity dependence on the knot type is inverted when changing from low to high electric fields. We have presented a computer simulation on a lattice of a closed, knotted, charged DNA chain drifting in an external electric field in a topologically restricted medium. Using a Monte Carlo algorithm, the dependence of the electrophoretic migration of the DNA molecules on the knot type and on the electric field intensity is investigated. Moreover, we have observed that at high electric fields the simulated knotted molecules tend to hang over the gel fibres and require passing over a substantial energy barrier to slip over the impeding gel fibre. At low electric field the interactions of drifting molecules with the gel fibres are weak and there are no significant energy barriers that oppose the detachment of knotted molecules from transverse gel fibres [3,4,7]. At present time, macroscopic experiments of plastic models of DNA knots falling under gravity in a very viscuous medium are performed. Such experiments, performed at very low Reynolds number, could simulate the behaviour of DNA knots inside the biological cell moving under an electric field during gel electrophoresis.
   - **DNA disentanglement.** Type-2 DNA topoisomerases maintain the level of DNA knotting up to 80-times lower than the topological equilibrium that would result from random inter-segmental passages occurring within freely fluctuating DNA molecules. Keeping the level of DNA knotting below the topological equilibrium is not a paradox as these enzymes use the energy of ATP hydrolyzis for each inter-segmental passage. However, it is unknown how these enzymes that interact with a small portion of knotted circular DNA molecule can recognize whether a given intersegmental passage will rather lead to a simplification than to a complication of DNA topology. Over the years several different mechanisms were proposed to explain the selective simplification of DNA topology by DNA topoisomerases. We study at present time realistic simulations of DNA unknotting and find results in agreements with experiments for realistic geometries.

List of publications

1. *Ising Transition driven by frustration in a 2D classical model with continuous symmetry*
   C. Weber, L. Capriotti, G. Misguich, F. Becca, M. Elhajal, and F. Mila
   Physical Review Letters **91**, 177202 (2003)

2. *Scanning-tunneling spectroscopy of surface-state electrons scattered by a slightly disordered two-dimensional dilute "solid" : Ce on Ag(111)*
   M. Ternes, C. Weber, M. Pivetta, F. Patthey, J. P. Pelz, T. Giamarchi, F. Mila, and W.-D. Schneider
   Physical Review Letters **93**, 146805 (2005)

3. *Simulations of Gel Electrophoresis of DNA Knots*
   C. Weber, M. Fleurant, P. De Los Rios, G. Dietler
   World scientific, Knot and everything, vol.**36** (2005)

4. *Gel Electrophoresis of DNA Knots in weak and strong electric fields*
   C. Weber, A. Stasiak, P. De Los Rios and G. Dietler
   Biophysical Journal **90**, 3100-3105 (2006)

5. *Finite-Temperature properties of frustrated classical spins coupled to the lattice*
   C. Weber, F. Becca, F. Mila
   Physical Review B **72**, 024449 (2005)

6. *Magnetism and superconductivity of strongly correlated electrons on the triangular lattice*
   C. Weber, A. Laeuchli, F.Mila, T.Giamarchi
   Physical Review B **73**, 014519 (2006)

7. *Simulations of electrophoretic collisions of DNA knots with gel obstacles*
   C. Weber, P. De Los Rios, G. Dietler, and A.Stasiak.
   J. Phys.: Condens. Matter **18**, S161-S171

8. Bond-order wave-function for the t-J model on the square lattice
   C. Weber, D. Poilblanc, S. Capponi, F. Mila, and C. Jaudet
   Physical Review B **74**, 104506 (2006)

9. Checkerboard order in the t-J model on the square lattice
   D.Poilblanc, C. Weber, F. Mila, M. Sigrist
   cond-mat / 0605226

10. Interaction between static disorder and classical magnetism in a frustrated spin model
    C. Weber, F. Becca, A. Laeuchli, F. Mila
    A manuscript is under preparation

11. Orbital currents, magnetism and superconductivity in the three band Hubbard model
    C. Weber, A. Lauechli, T. Giamarchi, F. Mila
    A manuscript is under preparation

12. Model of selective simplification of DNA topology by DNA topoisomerases
    Y. Burnier, C. Weber, A. Flamini, A. Stasiak
    Accepted for publication at *Nucleic Acids Research*.

Talks, Posters and seminars

- **April 2003**. *Ising Transition driven by frustration in a 2D classical model with continuous symmetry,* Highly frustrated magnetism Conference, Poster, Grenoble, France.
- **March 2004**. *Scanning-tunneling spectroscopy of surface-state electrons scattered by a slightly disordered two-dimensional dilute "solid" : Ce on Ag(111)*, Swiss Physical Society Meeting, Poster and Talk, Neuchâtel, Switzerland.
- **February 2004**. *Ising Transition driven by frustration in a 2D classical model with continuous symmetry*, Talk, invited by S. Troyer, ETHZ, Zürich, Switzerland.
- **March 2004**. *Ising Transition driven by frustration in a 2D classical model with continuous symmetry,* Correlated electrons meeting, Talk, Lausanne, Switzerland.
- **April 2004**. *Macroscopic DNA knots sedimentation*, Group seminar, invited by John Maddocks, Lausanne, Switzerland.
- **May 2004.** *Scanning-tunneling spectroscopy of surface-state electrons scattered by a slightly disordered two-dimensional dilute "solid" : Ce on Ag(111)*, Poster, Cargese, Corsica, France.
- **October 2004**. *Simulation of DNA Knots*, invited talk, Chemin-Dessus, Switzerland.
- **December 2004**. *Scanning-tunneling spectroscopy of surface-state electrons scattered by a slightly disordered two-dimensional dilute "solid" : Ce on Ag(111)*, Talk, Meeting of PhD students of EPFL, Lausanne, Switzerland.
- **February 2005**. *Variational Study of Superconductivity in a geometrically frustrated compound,* Forum meeting at Geneva University, Talk, Geneva, Switzerland.
- **March 2005**. *Finite-Temperature properties of frustrated classical spins coupled to the lattice,* Group seminar, invited by C. Mudry, PSI, Villigen, Switzerland.
- **September 2005**. *Magnetism and superconductivity of strongly correlated electrons on the triangular lattice,* Poster, MaNEP meeting, Diablerets, Switzerland.
- **October 2005**. *Magnetism and superconductivity of strongly correlated electrons on the triangular lattice,* Group seminar, invited by D. Poilblanc, IRSAMC, Toulouse, France.
- **February 2006**. *Magnetism and superconductivity of strongly correlated electrons on the triangular lattice,* Swiss Physical Society Meeting, Talk, Lausanne, Switzerland.
- **October 2006**. Magnetism and superconductivity of strongly correlated electrons on the triangular lattice, Martin-Peter Colloquium, Talk, Geneva, Switzerland.
- **January 2007.** Invited Group Seminar (Werner Krauth) at *Ecole Normale Supérieure*, Paris, France.
- **February 2007**. Invited Group Seminar (Claudius Gross) at the *Frankfurt Universität*, Frankfurt, Germany.
- **March 2007**. Contributed talk at the *Swiss Physical Society Meeting*, Zürich, Switzerland.

Schools, workshops and conferences

- *High-Tc superconductivity*. Lecture of the *3ème cycle de physique en Suisse Romande* held by T. Maurice Rice, april 2004 , Lausanne, Switzerland
- Swiss Physical Society Conference - MaNEP Meeting, Neuchâtel, March 3 and 4, 2004
- Cargese, International Workshop on the Evolution of Quantum Effects from the Nanoto the Macroscale 17-22 may 2004
- *The Physics of Materials with Novel Electronic Properties,* MaNEP summer school, Saas-Fee, Switzerland, 6-11 September 2004
- *Slow dynamic and aging,* Lecture of the *3ème cycle de la physique en Suisse Romande* held by Jean-Philippe Bouchaud, November 2004, Lausanne, Switzerland
- *Theory and phenomena of unconventional superconductivity,* Lecture of the *3ème cycle de la physique en Suisse romande,* held by Manfred Sigrist, april 2005
- *Statistical mechanics : algorithms and computations,* Lecture of the *3ème cycle de la physique en Suisse romande,* held by Werner Krauth.
- *Summer School X training course in the physics of correlated electrons and high-Tc superconductors,* Vietri-sul-Mare (Italy), 3-14 october 2005, held by Thierry Giamarchi, Walter Metzner, Bernard Coqblin, Wolfgang von der Linden.
- *Swiss Physical Society - MaNEP Workshop, Les Diablerets, Switzerland, September 26-28, 2005.*
- *Probing the physics of low dimensional Systems,* MaNEP summer school, Saas-Fee, Switzerland, 11-16 September 2006.